Nulling interferometry for exoplanet detection: using a multimode interference coupler in a two dimensional chalcogenide glass platform

Harry-Dean Kenchington Goldsmith

30th of October 2019

A thesis submitted for the degree of Doctor of Philosophy
of the Australian National University.

Australian
National
University

Declaration

The work in this thesis is my own except where otherwise stated.

Harry-Dean Kenchington
Goldsmith

To my son, Quentin Pearsall, and my partner, Eliza-Jane Pearsall, for their love and support throughout my PhD. To Quentin, your smile and laughter have been a constant, and welcome, distraction through the last year, ever since you were born. To Eliza, without your hard work our lives would not be the same, and we are better off for it. None of this would have been possible without you.

To my dog, Marco. We will go to the dog park more often now that my thesis is complete. I promise to snuggle you in the evening before bed most nights, instead of working.

To my parents, Charlie Goldsmith and Penny Kenchington, and my brother, Max Kenchington-Goldsmith, I thank you for your support through the years. I would not be in the privileged position I am today without you.

Acknowledgements

This research was supported by the Australian Research Council (ARC) Centre of excellence for Ultrahigh bandwidth Devices for Optical Systems (CUDOS - CE110001018).

In addition, the 2017 Award for Space Plasma, Astronomy & Astrophysics aided in securing the required photo masks used in the final chapter of this thesis.

The assistance provided though facilities usage and staff support in the ANU node of The Australian National Fabrication Facilities is also acknowledged here.

The supervisors for this work are Stephen Madden, Michael Ireland and Nick Cvetojevic, each of whom have contributed their thoughts to this work and aided in both training me on various instruments and computer programs and consultation of key aspects included within.

Pan Ma and Kunlun Yan have both assisted me in this work by performing tasks involving the mask aligner tools. Pan Ma also trained me in using the Xenics Onca camera and aligning the mid infrared laser. They recently celebrated the birth of their first son Ethan. Congratulations.

Barry Luther-Davies, Craig MacLeod and John Bottega are also acknowledged here for their contribution to aligning the mid infrared laser, constructing many mechanical solutions for the experimental setup and fixing all the things that broke during my PhD.

Abstract

Astronomy has begun an uptake in photonic technologies to replace cumbersome, heavy optics, to achieve lighter systems that are robust to environmental and instrument noise. An application of one such change, from optics to photonics, is for beam combination in multi-telescope systems, and specifically; direct imaging of exoplanets using interferometry.

Currently, astronomers have detected over 3500 exoplanets. Due to the overwhelming luminosity of the host star, compared to that of the exoplanet, the majority of these detections used indirect imaging - inferring an exoplanets existence by measuring variation in the host star's light. Direct detection, however, uses the light from the exoplanet and is assisted by methods reducing the host star's light, like nulling interferometry.

Nulling interferometry achieves both a high-resolution image and a deep null depth (by using destructive interference over the star). Its resolution is limited by the distance between the farthest telescopes (the longest baseline). So that the contrast between the exoplanet and star is minimised this work is constrained to the astronomical L'-band where young, and thus hot, exoplanets have their blackbody spectrum peak.

The focus of this thesis was to design and construct a beam combiner that segregates the star and exoplanet light - the nulling interferometer. Using established ultraviolet lithography methods and plasma etching, a two-beam combiner on a photonic chip was constructed. These chips were fabricated using a combination of two chalcogenide glasses, made from networks of germanium, arsenic and selenium for the core and substituting sulphur for the cladding, which is transmissive through the mid-infrared up to approximately 12 µm with a high index contrast of 0.33.

From the start, a multimode interference coupler was chosen as the beam combiner for this work. This is a device that is unaffected by common fabrication errors and as such was shown to be reliable in various materials. The in-depth study shown in this work proved this to be the case for this material too. In addition, a version of the MMI with a broad bandwidth splitting ratio, over 400 nm, was discovered. This MMI was investigated thoroughly to understand the relationship between the excited light-modes in the slab and the increase in bandwidth. An investigation into whether the width of the MMI has any influence on the breadth of the bandwidth was undertaken, showing little relationship with a larger width. With smaller width MMI limited by the number of modes in the slab to generate this broad bandwidth special case.

The computed nulling interferometer for this work was made using a single multimode interference coupler as the two-beam (or telescope) combiner that was simulated to have a 40 dB (10^{-4}) null over a 400 nm bandwidth. Experimentally, using a single input and calculating the expected null performance, achieved 30 dB (10^{-3}) over a 300 nm bandwidth, centred at 4000 nm. Less than predicted but a benchmark for nulling interferometers in

the MIR.

Subsequent direct measurements of extinction, using two MMIs in a Mach-Zehnder interferometer configuration, could not ascertain such a null depth. These measurements were limited by scattered light from the beam combiner as well as imperfect fabrication larger than predicted, especially in the MZI arms. The issue was related to the small size of the waveguides used and increasing them to multimode waveguides, for a short period to limit multimode excitation, would provide a much more robust system. Taking these limitations, and the solution, into account these structures should be able to produce the predicted deep null over the specified bandwidth once these issues have been addressed.

To the author's knowledge, the extinction measurements in this thesis are the first of their kind and are a significant step towards measuring an exoplanet never before seen using nulling interferometry in the mid-infrared. The experiments on the beam combiners as 3 dB splitters show the expected null to be as deep as predicted, within error and highlight the difficulties in ascertaining exact measurements of extinction with modern technology and current fabrication techniques. Fabrication errors as they stand are the key issue that will need to be overcome in future work but are achievable with current technology.

Contents

List of Figures

List of Tables

Author's publications

[1] Kenchington Goldsmith, H.-D., Cvetojevic, N., Ireland, M., Ma, P., Tuthill, P., Eggleton, B., Lawrence, J. S., Debbarma, S., Luther-Davies, B., and Madden, S. J., "Chalcogenide glass planar MIR couplers for future chip based Bracewell interferometers," in [*Proc. of SPIE*], **9907**, 990730 (2016).

[2] Kenchington Goldsmith, H.-D., Cvetojevic, N., Ireland, M., and Madden, S., "Fabrication tolerant chalcogenide mid-infrared multimode interference coupler design with applications for Bracewell nulling interferometry," *Optics Express* **25**(4), 3038 (2017).

[3] Kenchington Goldsmith, H.-D., Ireland, M., Ma, P., Cvetojevic, N., and Madden, S., "Improving the extinction bandwidth of MMI chalcogenide photonic chip based MIR nulling interferometers," *Optics Express* **25**(14), 16813–16824 (2017).

[4] Kenchington Goldsmith, H.-D., Ireland, M., Ma, P., Wang, R., Luther-Davies, B., Madden, S., Noris, B., and Tuthill, P., "Photonic mid-infrared nulling for exoplanet detection on a planar chalcogenide platform," in [*Optical and Infrared Interferometry and Imaging VI*], Mérand, A., Creech-Eakman, M. J., and Tuthill, P. G., eds., 33, SPIE (2018).

his itur ad astra: With these, we go to the stars.

James Gregory, 1663 on his reflective telescope design.

his itur ad planetarum extra: With these, we go to the exoplanets.

Harry-Dean Kenchington Goldsmith, SPIE, 2016, Edinburgh

No one knew what I was talking about

Chapter 1

Introduction

Photonics is the physical study of light generated, detected or manipulated in a material. In a photonic chip, micro-structures are used to manipulate light. A waveguide is one such micro-structure that transmits and routes light through the chosen medium. These can be manufactured in glass (the generic term for a non-crystalline, amorphous solid) or other transparent materials. The sizes of these structures can be the same scale as the wavelength to be manipulated if not smaller. The use of photonic circuits is thus a method for shrinking an entire lab bench to a centimetre scale chip.

The study of photonic circuitry originates with fibre optics. In the late 1800s and early 1900s the passage of light, and the bending of light, through a glass fibre showed the world that the direction of light could be controlled continuously. It wasn't until the first successful transmission of an image [1, 2] that interest in the technology as a means to transfer information was generated. The availability of lasers provided the last technological feat that enabled the use of light in the telecommunication industry (previously dominated by radio and electrical technology). To this day, high-speed global telecommunication is arguably the largest driver of technology development in this field and underpins trillions of dollars in the global economy.

In 1977 the field of astronomy incorporated fibre optics into telescopes [3] for the first time. For many tasks that required light to be moved away from a telescope focal plane, fibre would be the substitute for bulk optics systems of lenses and mirrors. For example, when there are multiple components of a single telescope image that need to be isolated: Fibre optics enable each component to be directed to a different scientific instrument, such as a spectrograph [4] or a series of spectrographs.

From fibre optics, photonic chips are the logical next step for astronomy. Where previously fibre optics could not replace scientific instruments, like a spectrograph, photonic chips are being developed that can. These chips are robust, potentially insensitive to environmental effects, alignment-free, and light-weight, making them easier to handle, package, and control. This is especially advantageous when considering future astronomical instruments to be launched into space. Whether they compromise performance when compared to their bulk optic counterpart must be evaluated on a case by case basis but from the perspective of decreasing the cost to space flight, photonic chips have the advantage. The photonic chip allows for new scientific instruments that may have been too cumbersome to make with bulk optics or advances on current instrumentation that are limited due to their size.

Photonic circuitry is already in use in astronomy and making a significant impact in

the field. The instrument known as GRAVITY is installed at the Very Large Telescope Interferometer (VLTI) and is the first interferometer to detect an exoplanet [5]. The focus of this work is similarly "exoplanet detection via interferometry", the technology presented here however is not ready for on-sky testing and is a few generations (from a technology viewpoint) away from replicating the success of Lacour et al. [5].

For the definition of an exoplanet, it is prudent to understand that a planet is an object that has reached hydrostatic equilibrium (it is round), orbits the sun and has cleared the neighbourhood around its orbit, whereas an exoplanet does not orbit the sun but a distant star [6]. The terms exoplanet and planet will be used interchangeably in this chapter but the term exoplanet will be favoured throughout the thesis. The various methods of detection and characterisation of exoplanets are discussed in Sec. 1.1, with a focus on direct-imaging in Sec. 1.2. Section 1.3 will motivate exoplanet detection research by exploring what is known and unknown about planetary formation and the composition of exoplanets.

1.1 Indirect exoplanet discovery

Exoplanet detection is vital for our understanding of star system formation and planetary formation: how did the solar system form, is the solar system a typical star system, how do planets form in the ice line - the boundary where water can become ice around a star, and under what conditions can life exist on a planet? The importance of these questions was recognised in 2019 with the Nobel prize for physics [7] awarded for the first detection of an exoplanet around a solar-type star [8].

Exoplanet detection adds to the understanding of these fundamental questions. Some detections, however, add yet more questions: How can a Jupiter sized planet be closer to its host star than Mercury is to ours, why do most star systems have multiple exoplanets with Earth-sized or larger mass (whereas ours does not), what is the boundary between star and planet? For answers to these questions, it matters what star the exoplanet orbits and what other exoplanets are in the same system. Section 1.3 explores some of these questions in detail but to improve our understanding of planetary science a greater variety of exoplanets are required, specifically Earth-like exoplanets that orbit star's akin to our own. For that, it is important to know what methods of exoplanet detection exist, what their present limitations are and whether they can detect such Earth-like exoplanets in the future.

Only recently has humanity detected objects, other than binaries, orbiting distant stars. Objects like brown dwarfs (failed stars without the mass for prolonged hydrogen fusion), giant Jupiter sized exoplanets, and even smaller, Earth-like, rocky exoplanets (not around star's like our own sun) - these being the best candidates for habitability. A tree diagram of exoplanet detection methods is shown in Fig. 1.1 from Perryman et al. [9] and shows the plethora of detection methods and the number of exoplanets discovered in this way as of 2014. Here it is shown that direct detection has found only a few exoplanets and

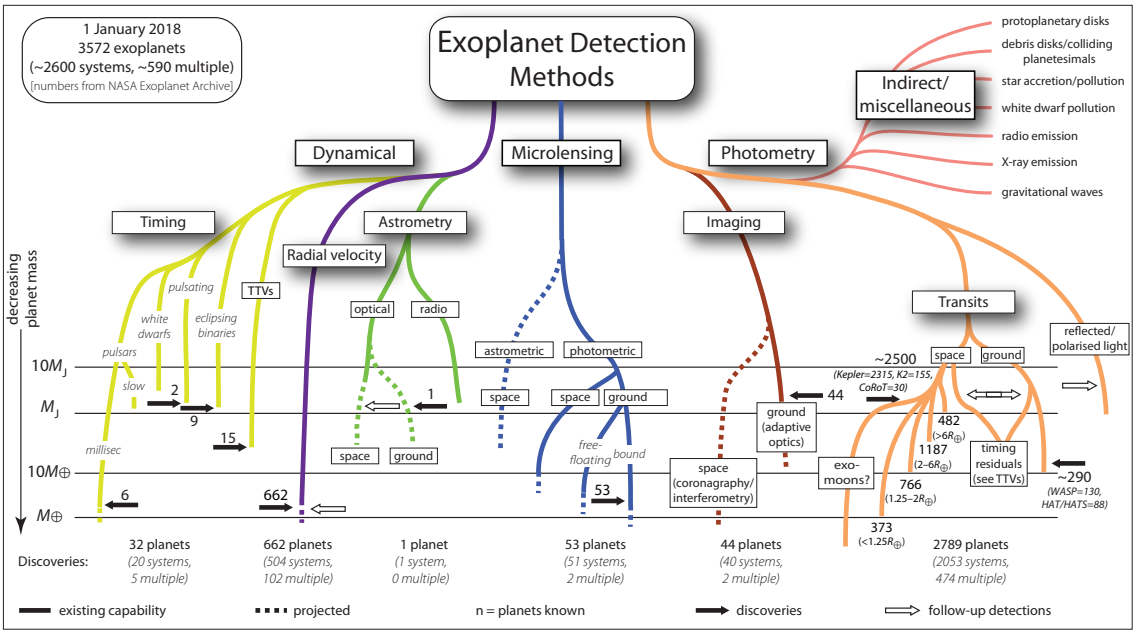

Figure 1.1: A colour tree of exoplanet detection methods and the number of exoplanets discovered using them [9].

that most of our understanding of other star systems has come from indirect detection methods.

Exoplanet discoveries have primarily been from indirect inferences using variations of the host star's light. Few discoveries use the exoplanet's light itself - a direct imaging detection - and only two have been detected using the reflected light of the host star.

There are currently many exoplanet detection methods, each with its advantages and disadvantages. Historically, the first exoplanet was found using the radial velocity detection method [10], followed by detection using pulsar timing [11]. The most common exoplanet detection method is the transit method which achieved its first detection in 1999 [12] and now boasts more than 3000 confirmed exoplanets[i]. Less prolific but equally as important is the gravitational lensing method of detection. It too was used to find exoplanets [14] with many exoplanet systems now detected using this method [15, 16]. Observations of an exoplanet via its emitted light, using a direct imaging method, did not occur until 2004 [17], opening up a new field of exoplanet research. A brief review of these exoplanet detection methods now follows.

1.1.1 Radial velocity detection

Indirect exoplanet detection has occurred since 1989 with the first exoplanet found around the star HD 114762 [10]. The exoplanet, HD 114762 b, was detected using the radial velocity method where a periodic Doppler shift of the host star's light was observed. A Doppler shift is when the star's light is shifted in frequency. On a cosmic scale, this is

[i] `https://exoplanetarchive.ipac.caltech.edu/docs/counts_detail.html` [13], accessed on 20/12/2018

indicative of stars moving away from the Earth (redshifted) or moving closer to Earth (blue shifted). A periodic Doppler shift is indicative of another celestial body (like a companion star or exoplanet) causing the star to orbit around a centre of mass that is not it's own. This results in a slight red shift or blue shift as the star moves away from the Earth or towards it respectively. The conservation of momentum:

$$M_* V_* = -mV, \tag{1.1}$$

where M_* is the mass of the star, m is the mass of the companion and V/V_* are the respective orbital velocities, governs this reflex motion - assuming all other objects in the vicinity are gravitationally insignificant. The centre of mass itself is the point in space where the sum of the two bodies' displacements, weighted by their masses, is zero. The star's radial velocity semi-amplitude (K_*), in metres per second, is given by:

$$K_* = \frac{28.4329\,\mathrm{m}\cdot\mathrm{s}^{-1}}{\sqrt{1-e^2}} \frac{m\sin i}{M_J} \left(\frac{M_* + m}{M_\odot}\right)^{-1/2} \left(\frac{a}{\mathrm{AU}}\right)^{-1/2}. \tag{1.2}$$

This relates the observed parameter, K_*, the eccentricity of the planet's orbit (e) and the period of the star (which is the same as the period of the exoplanet); to the mass of the exoplanet (m) as compared to the mass of Jupiter (M_J), and M_* as compared to the mass of Sol ($M_\odot$). The semi-major axis of the planet (a), in astronomical units (AU), is calculated using Kepler's third law. Thus eq. (1.2) can be rearranged to calculate the minimum mass of the exoplanet if the mass of the star is known, with a discrepancy due to the inclination angle i (from the $m\sin i$ term in eq. (1.2)).

The inclination angle of the exoplanet is a limitation and hampers the ability to detect exoplanets via the radial velocity method, evident in eq. (1.2), as otherwise detectable exoplanets will be missed due to the orientation of the star system.

Table 1.1: The relation of a celestial body's mass and the classification, in terms of Earth's mass ($M_\oplus$), Jupiter's mass (M_J) and our sun's mass ($M_\odot$), by Stevens & Gaudi [18].

Classification	Mass
Sub-Earth	$10^{-8} M_\oplus$ - $0.1\,M_\oplus$
Earth	$0.1\,M_\oplus$ - $2\,M_\oplus$
Super-Earth	$2\,M_\oplus$ - $10\,M_\oplus$
Neptune	$10\,M_\oplus$ - $100\,M_\oplus$
Jupiter	$100\,M_\oplus$ - $1\,M_J$ ($10^3\,M_\oplus$)
Super-Jupiter	$1\,M_J$ - $13\,M_J$
Brown dwarf	$13\,M_J$ - $0.07\,M_\odot$ ($73\,M_J$)
Stellar companion	$0.07\,M_\odot$ - $1\,M_\odot$

Alongside the first exoplanet discovered, HD 114762 b [10] in 1989, 61 Vir (confirmed in 2010 [19]) and γ Cep (confirmed in 2011 [20]) in 1988 [21] were also discovered. At the time of discovery, only brown dwarfs had previously been found and smaller objects were not yet thought to be detectable. HD 114762 b in particular challenged the idea that only brown dwarfs could be detected. The deciding factor in verifying whether an object is

an exoplanet is the calculation of its mass. Table 1.1 details the size distinctions between stellar objects as a general classification guide. Calculations of HD 114762 b's mass and Tab. 1.1 suggest this object is likely an exoplanet [22], with an uncertainty of the mass calculation due to the inclination (i) providing remaining doubt over its classification as an exoplanet.

Figure 1.2 contains every exoplanet detected using the radial velocity method. Note that exoplanets detected using another method are often measured again using the radial velocity method in order to measure their mass. These exoplanets are not included here.

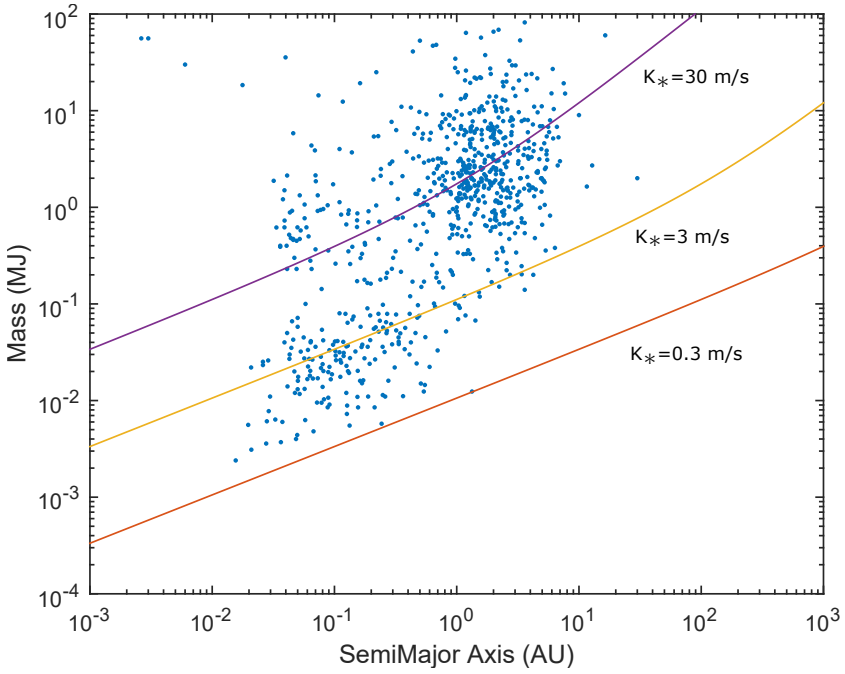

Figure 1.2: Every radial velocity detection from `http://exoplanets.org/` [13], accessed on 20/12/2018, with K_* from eq. 1.2 calculated for 30 m/s, 3 m/s and 0.3 m/s, using $e = 0$ and $M_* + m = M_\odot$.

From Fig. 1.2 the radial velocity method appears to favour Jupiter mass exoplanets at 1 AU (the same distance from the sun to the Earth). A cluster of closer Jupiter sized exoplanets, known as "hot Jupiters", appear in Fig. 1.2 but are not as prevalent compared to exoplanets with the same mass and orbits further than 1 AU.

The cluster of exoplanets in the super-Earth region ($m = 10^{-2}\, M_J$) at 1 AU and the Jupiter sized exoplanets at 10 AU supports the idea that smaller exoplanets should be located close to their host star and larger exoplanets further away. This is what we would expect by using our star system as a template. With this measurement technique, however, this trend may simply be selection bias.

The K_* contours, plotted through Fig. 1.2, indicate a relationship between m, M_* and a for the different exoplanet types. The exoplanets with a large gravitational influence, those with masses of about Jupiter's, follow the $K_* = 30$ m/s band whereas the lighter exoplanets, with masses of a super-Earth or Neptune, follow the $K_* = 3$ m/s band. The abun-

dance of these lighter Earth/Neptune exoplanets was predicted by Mordasini et al. [23] in a planet population synthesis model. The same model predicts another abundance of exoplanets at 3 to 4 AU at $10^{-3}\,M_J$ (about Earth's mass), requiring a detection limit below $K_* = 0.1\,\mathrm{m/s}$. This is some way below the $K_* = 0.3\,\mathrm{m/s}$ line in Fig. 1.2 which represents the current limit to radial velocity detection [24] - the limit being photon noise the instability of the host star. This limitation highlights the bias of the radial velocity detection method towards larger exoplanets.

As an example of what can and cannot be measured using current technology, consider whether Jupiter or Earth could be found using this method. Using eq. (1.2), Jupiter has a semi-major axis of 5.2 AU (which means the centre of mass of the Jupiter-Sol system is 0.0050 AU from the centre of the sun, which is larger than its radius of 0.0046 AU) placing Jupiter within detection range ($K_* = 12.7\,\mathrm{m/s}$). An Earth-like exoplanet, however, (at 1 AU and a mass of $0.0031\,M_J$) could not be found, having a $K_* = 0.09\,\mathrm{m/s}$.

There is an additional inherent limitation in the radial velocity method, that being the period of detectable exoplanets. For detection, the exoplanet must orbit a few times to limit the uncertainty in the measurement. Since the first-ever radial velocity detection occurred approximately 30 years ago, the maximum possible semi-major axis detected (using Kepler's third law) could be 100 AU if the host star was ten times the size of the sun (for only one orbit to have occurred). A more realistic calculation using say a seven-year observation time gives a limit between 17 and 36 AU on the radial velocity detection method. Note that for multiplanet radial velocity measurements exoplanets at larger periods may be inferred from numerical models [25], providing a high error method to overcome this limitation.

Although the radial velocity detection method has observed a plethora of exoplanets and served as a tool for determining the mass of exoplanets, it is currently limited by technology and observational time. The next detection method, gravitational lensing, does not suffer from the same limitations.

1.1.2 Gravitational lensing

Gravitational lensing uses the curvature of space around a significantly massive body to detect exoplanets. Massive objects bend the space-time around them which therefore alters the path of light directed to Earth from background stars. An approximately spherical body will provide a lensing effect, hence gravitational lensing, which directs more of the background star's light back to Earth. An exoplanet in orbit would also cause a manipulation of space-time that can direct even more light towards Earth. An example of light intensity versus time curve is included as Fig. 1.3 where the lensing of a background star causes an increase in intensity before dipping again, the exoplanet then causes a much thinner second peak over the broad peak generated by the gravitational lensing of the host star.

First proposed by Einstein in 1936, gravitational lensing was a mathematical note, published in response to conversations with R.W. Mandl as a purely theoretical event. It

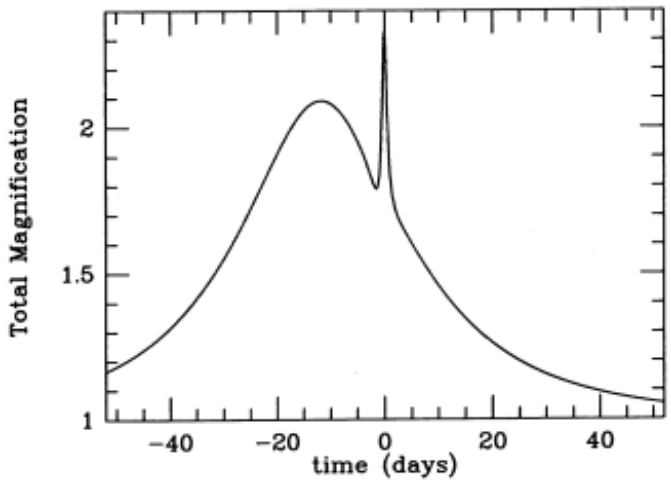

Figure 1.3: The light curve of a predicted microlensing event of an exoplanet [26].

was described by Einstein [27] as

> The light coming from star A traverses the gravitational field of another star B [...] from the law of deviation that an observer situated exactly on the extension of the central line $\overline{AB}$ will perceive, instead of a point-like star A, a luminous circle of angular radius β around the centre of B, where
>
> $$\beta = \sqrt{\alpha_0 \frac{R_0}{D}} \tag{1.3}$$
>
> [for an observer at distance D, a deviation of light α_0 and the distance between star B and place of deviation R_0]. The same will happen, if the observer is situated at a small distance x from the extended central line $\overline{AB}$. But the observer will see A as two point-like light sources, which are deviated from the true geometrical position of A by the angle β, [as per eq. (1.3)].

Controversially the theory of gravitational lensing appears in an earlier work by Chwolson [28] underneath Einstein's paper on a separate topic [29]. Chwolson discusses the gravitational influence of star A, behind star B to create "a mirror image" of star A, or, that star B would "appear surrounded by a ring". Like Einstein twelve years later there is, of course, a disclaimer that this work is likely only theoretical: "Whether the case of a fictitious double star specified here, I cannot judge."

In the 1990s the theory once thought only speculative became a method of detecting companions in a binary orbit for stars in the galactic bulge of our Milky Way galaxy [30]. The focus was initially on detecting brown dwarfs but soon moved to exoplanets [26]. The first exoplanet detection was made in 2004 [14]. The event was labelled OGLE 2003-BLG-235/MOA 2003-BLG-53 for the two independent observations made by the Optical Gravitational Lensing Experiment (OGLE) and the Microlensing Observations in Astrophysics (MOA) respectively.

Relatively few detections have been made using gravitational lensing and all are shown in Fig. 1.4. These measurements indicate that this method only works for exoplanets that

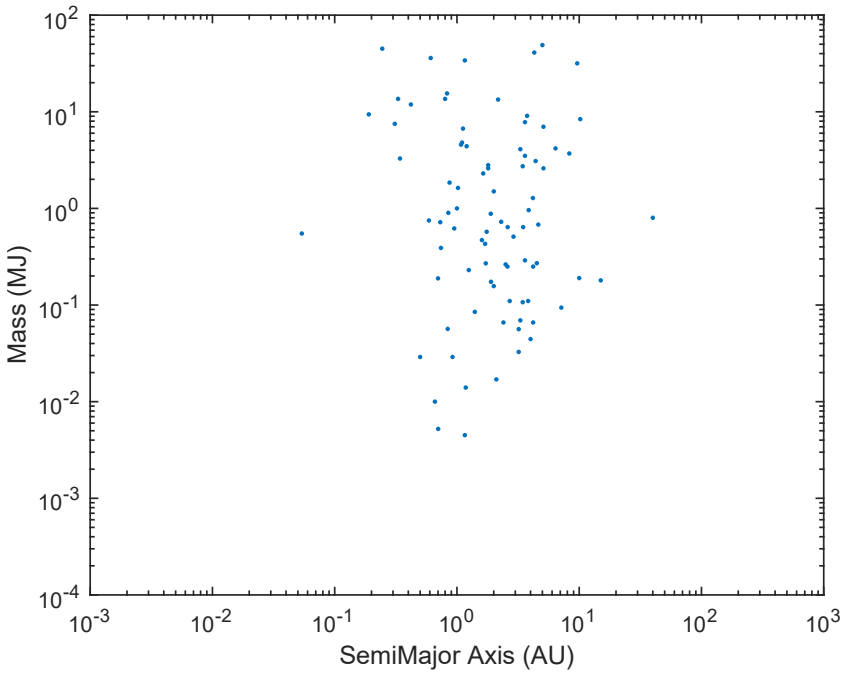

Figure 1.4: Exoplanets discovered using gravitational lensing from `http://exoplanets.org/` [13], accessed on 20/12/2018.

are between 1 and 10 AU (approximately) from their host star. Intrinsically this makes sense as the method requires that the exoplanet is spatially separated from its host star. The deflections would be more distinguished the further separated the exoplanet is, up to a separation where the light would not pass by the exoplanet [30]. The issue with microlensing is the degeneracy, as detection cannot produce unique parameters of the exoplanet. During a microlensing event with an exoplanet, the star to planet mass ratio can be determined but parameters like planetary mass and distance from the host star require accurate information on the star itself that cannot be found using a microlensing method as the host star is generally not seen. Follow up observations of the star are thus required. The GAIA project is one such large scale experiment [31].

Even with limited exoplanets detected using gravitational lensing, the method has furthered the field and added more data to test theories on planet formation and how star systems are created.

1.1.3 Pulsar timing detection

First detected in 1967 by graduate student Jocelyn Bell [32] during her PhD, pulsars are furiously spinning neutron stars that emit periodic bursts of light (in the radio band of the electromagnetic spectrum), the timing of which is precisely periodic [33]. Usually, they are found with a companion star from which they have been theorised to have siphoned their high angular momentum, but as was the case for Wolszczazan & Frail [11], they may instead have a series of exoplanet companions. This detection method is similar to that of the radial velocity detection method, observing the star's output variation in time, but

rather than looking at the Doppler shift of the star's light it is the timing of the pulses that determine whether an exoplanet is in orbit.

Currently, there are only six exoplanets detected using this method, and a host of brown dwarfs. After the first-ever exoplanet discovery [10] the next three were detected using Pulsar timing [11, 34]. An example of a pulsar timing detection is shown in Fig. 1.5 indicating multiple exoplanets in orbit of PSR B1257+12 [11], making it the first detected multi-planetary system around a star that is not our own.

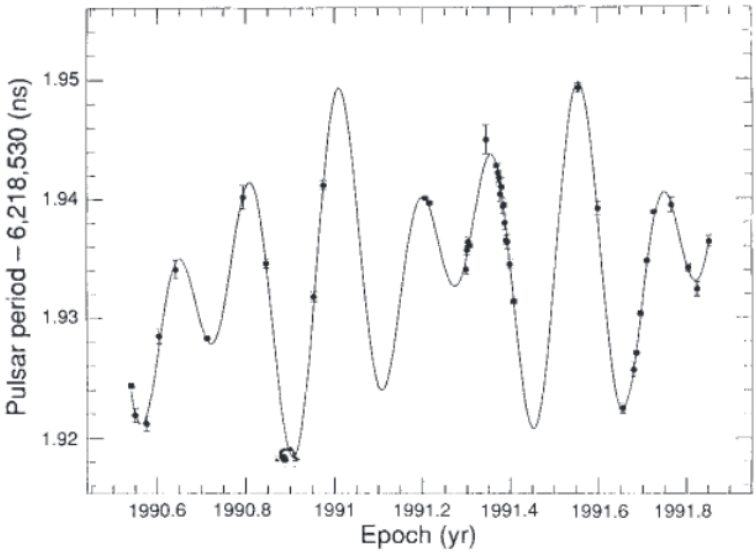

Figure 1.5: Pulsar detection by Wolszczan et al. [11]. The solid line is a simulation of a two exoplanet model of the star system.

Due to the rarity of pulsars detectable from Earth, few exoplanets have been detected around pulsars. There are, however, astronomers using this method to find pulsar companions and keeping this field active [35].

1.1.4 Transit detection

With over 3000 confirmed exoplanets detected, the transit method is by far the most prolific detection scheme. This method, first proposed for exoplanet detection in 1952 [36], relies on the exoplanet blocking its host star's light as the exoplanet passes between the Earth and the host star. This small reduction in starlight is periodic by nature and follow up observations are required, like for any periodic measurement, to confirm the transit. The brightness (B) dip from the exoplanet is calculated as the ratio of the projected area of the exoplanet to the projected area of the host star as seen on Earth:

$$B(\%) = 100 * \left(\frac{\pi R^2}{\pi R_*^2}\right) \tag{1.4}$$

where R is the exoplanet radius and R_* is the star's radius. This implies that larger exoplanets are favoured, as are exoplanets with shorter orbital periods due to the length of observation time required to make multiple measurements. The fundamental limitation

of this method is the orientation requirement for the detection. Exoplanets orbiting close to their host star benefit by having a larger range of inclination angles that will transit, which is another reason why these exoplanets are more likely to be detected.

Figure 1.6 shows each exoplanet detected using the transit method. The axes used are the (measured) exoplanet radius and (calculated) semi-major axis (from the measured period). Masses here are either from follow-up radial velocity measurements or inferred by the size and assumed density.

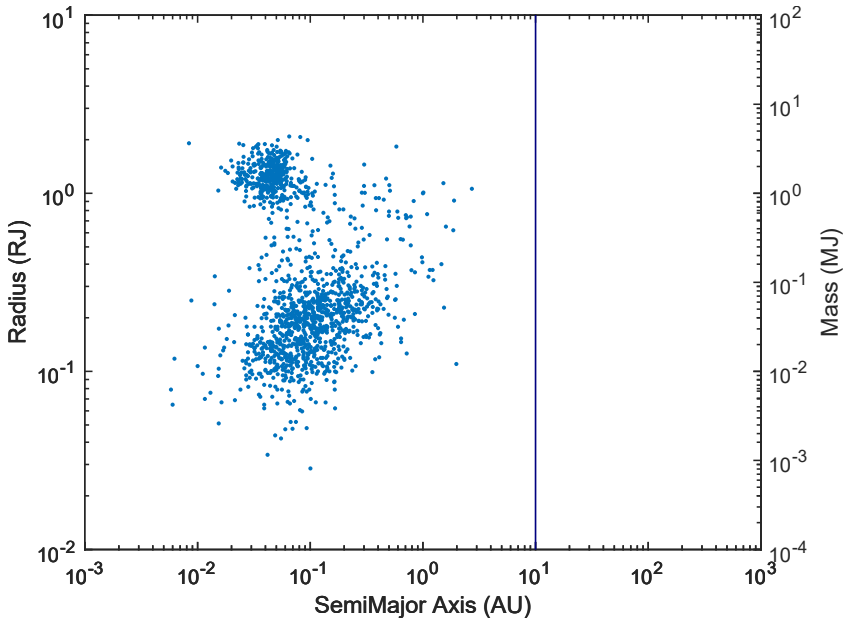

Figure 1.6: Exoplanets detected by the transit method from `http://exoplanets.org/` [13], accessed on 20/12/2018.

Figure 1.6 shows the previously noted detection bias for exoplanets that are close to their host star - between 0.01 to 1 AU. There are two distinct clusters of exoplanets found using this method: one being the "hot Jupiters" and the other including super-Earths and exoplanets with the mass of Earth. The more massive the exoplanet the more the host star's light would be dimmed, hence the prevalence of Jupiter sized bodies. However, such logic would imply a plethora of Jupiter sized exoplanets detected at a wide range of semi-major axes. The detection of exoplanets at a large separation from their host star is however limited by the observation time compared to the orbital period, as a confirmed detection requires multiple transits which limit a detectable exoplanet to a distance of approximately 10 AU from their host star. At larger separations there is also a higher probability that the orientation of the star system (the inclination i) will not be conducive to a transiting orbit, making the likelihood of detecting exoplanets lower the more distant their orbit.

A typical transit detection is shown in Fig. 1.7 which was the first-ever transit detection of an exoplanet [37]. As the exoplanet begins and ends its transit a partial shadowing effect occurs, causing the slopes on the transit part of the waveform in Fig. 1.7. The slight curve

in the transit is due to limb darkening, a result of the transit being offset from the host star's centre.

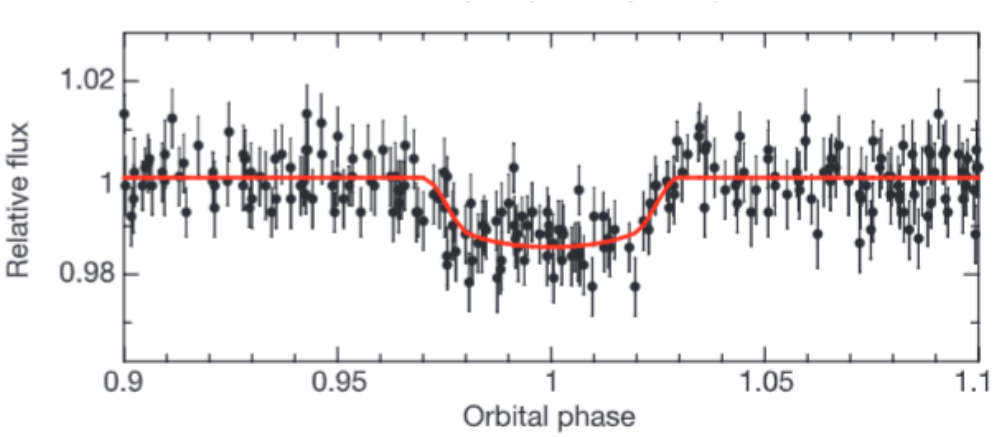

Figure 1.7: The transit detection of OGLE-TR-56 b with an accompanying red line to guide the eye [38].

Using the transit dip, the radius and period (and thus semi-major axis by Kepler's third law) of the exoplanet can be determined. Subsequent radial velocity measurements are required to determine the mass of the exoplanet.

The first dedicated space mission that used the transit method to find exoplanets was the Convection, Rotation et Transits planétaires (CoRoT) [39] which was followed by the Kepler mission [40]. These space missions have made the transit method the dominant method for detecting exoplanets, a trend which will be extended with the latest space mission, the Transiting Exoplanet Survey Satellite (TESA) [41], detecting its first exoplanet in 2018 [42]. Improvements to equipment and methodology will enable the transit method to continue to detect smaller, and thus fainter exoplanets, and potentially add exoplanets to Fig. 1.6 at the 1 AU, 0.001 M_J area, where an Earth-like exoplanet would exist.

1.2 Direct Imaging

Indirect measurements have successfully detected thousands of exoplanets, including exotic species like hot Jupiters, and characterised them by measuring the exoplanet's atmosphere (as explained later in Sec. 1.3.2).

The reason to undertake direct imaging is to discover exoplanets that cannot be detected indirectly and to search for exoplanets in star systems of any orientation. Providing an image of a star system will also satisfy a fundamental human desire to see exoplanets directly.

Direct imaging of exoplanets began in 2004 with the light from an exoplanet captured around the brown dwarf 2MASSWJ 1207334-393254 [17], as seen in Fig. 1.8. The detection method was a simple image of the star on the Very Large Telescope (VLT) in Chile, taken

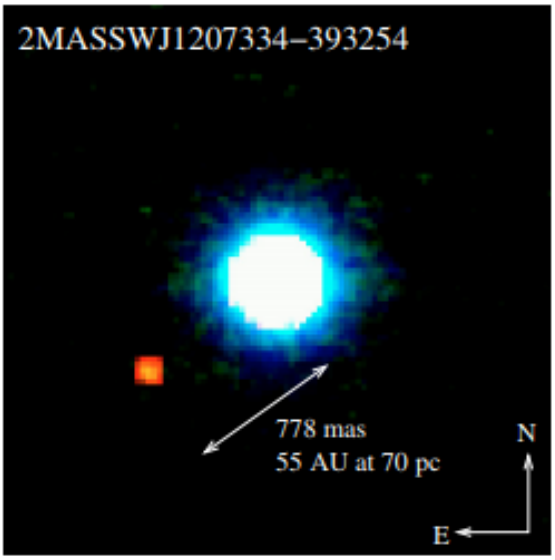

Figure 1.8: Composite image of the brown dwarf 2MASSWJ 1207334-393254 with a (red) companion exoplanet [17]. Three wavelength bands were used to construct the image: H (between 1.5 and 1.8 µm) for blue, Ks (1.9 to 2.5 µm) in green and L' (3.2 to 4.4 µm) for the red colouring, as summarised in Tab. 1.2.

with the COudé Near-Infrared CAmera (CONICA) and using the Nasmyth Adaptive Optics System (NAOS) [43] to rectify atmospheric disturbances (CONICA and NAOS are commonly referred to as NaCo when they are used together). Figure 1.8 is a composite image of four images each taken in different astronomical infrared (IR) wavelength bands, as detailed in Tab. 1.2. It shows the bright central star (a brown dwarf) and the exoplanet companion orbiting 55 AU away.

Table 1.2: Infrared filter system

Filter	Wavelength range (µm)
J	1.1 to 1.4
H	1.5 to 1.8
Ks	1.9 to 2.5
L'	3.2 to 4.4

Figure 1.8 illustrates three limitations of directly imaging star systems: the resolution of the image, the flux difference between the star and the exoplanet and the "seeing" - which is the time-dependent blurring effects of atmospheric turbulence in the image - during detection.

The star and the exoplanet are resolved in Fig. 1.8 due to their separation, but any light from exoplanets substantially closer (approximately 20 AU by the image's scale) would be encompassed by the host star. Using the four wavebands, as this image has done, is one method to dissociate star and exoplanet light. It is not hard to imagine, however, that the resolution is a key factor limiting this method of exoplanet detection. As angular

resolution (θ) relates as follows

$$\theta = \frac{1.22\lambda}{D} \tag{1.5}$$

to the wavelength (λ) and the telescope diameter (D) this limitation can be overcome by using larger telescopes.

Using multiple telescopes in an interferometric image would also increase the resolution as eq. (1.5) would no longer be dependent on the telescope's diameter but on the size of the baseline - the furthest distance between any two telescopes - of a telescope configuration.

Not as apparent in Fig. 1.8 is the difference in flux between the exoplanet and star. Exoplanets with limited flux may not be bright enough to be detected given the overwhelming glare of the star. Methods like coronagraphy and nulling interferometry (described in Sec. 1.2.1 and Sec. 1.2.2 respectively) overcome this limitation by blocking out the starlight.

Finally, this direct imaging technique requires adaptive optics (AO). An AO system, like NAOS, is used to correct for the "seeing". The purpose of an AO system is to restore as much as possible the instrument limited resolution of a telescope that is subject to both instrumental noise and atmospheric disturbances. In terms of exoplanet detection, improving the resolution reduces the spatial spread of the host star and enables the exoplanet to be sufficiently spatially separated from the host star. AO systems are typically comprised of an array of deformable mirrors built for a specific telescope and wavelength, like the 188AO system at the Subaru telescope [44] that uses a 188 electrode bimorph deformable mirror, shown in Fig. 1.9.

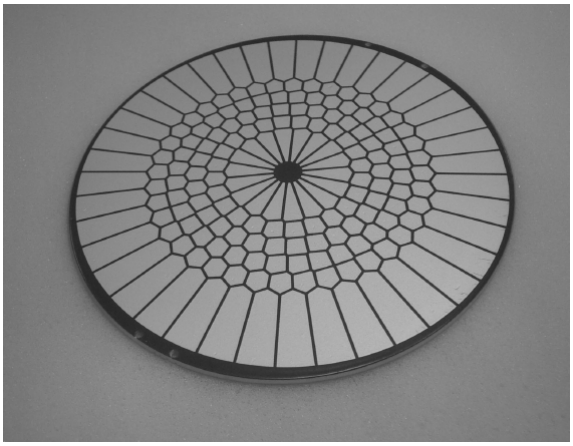

Figure 1.9: The electrode pattern for the 188AO system at the Subaru telescope [45]. The specific pattern indicates a non-uniform technique in correcting the atmosphere.

Current AO systems can only achieve so much and are often used as a single part of a larger detection system, the Subaru Coronagraphic Extreme Adaptive Optics instrument (SCExAO) [46] being an example of an AO instrument combined with a coronagraph (placed after the 188AO at the Subaru telescope).

The use of AO systems is widespread in astronomy. An example of an AO system being used to detect exoplanets is by Marois et al. [47] with the discovery of three exoplanets

orbiting HR 8799. Along with an AO system, this detection used two imaging methods: Angular Differential Imaging (ADI) and a coronagraph. ADI is a technique where the image-plane rotates with the sky causing the point spread function (PSF) of the central star to "blur" [48]. During this process, the exoplanets move around the star while the starlight overlaps and becomes a homogeneous signal. This property was used to decouple the exoplanets from stellar artefacts.

1.2.1 Coronagraph

The coronagraph was first designed as an opaque mask, situated in the focal plane of a telescope, to block sunlight and allow for the sun's corona to be imaged [49]. For exoplanet detection, a coronagraph is used to diminish starlight to find exoplanets around the star. This is achieved by using longer exposure times that would otherwise saturate and bloom the image with the starlight present.

Some modern coronagraphs no longer use opaque masks but translucent material [50] that changes the phase of the telescope's PSF rather than blocking the light as this yields a more efficient reduction of the starlight. This too only affects the centre of the PSF, the starlight, leaving the light entering the telescope at an angle, i.e. exoplanet light, to pass through unaffected.

The basic coronagraph [51] system has three components: an apodizer, the coronagraph itself and a Lyot stop. See Fig. 1.10 for a pictorial example of what these components do to starlight - represented as a rectangle function. An amplitude apodizer is used before the coronagraph, in the pupil plane, to convert the incident light into a smooth, high contrast, PSF (like a Gaussian) that can then be blocked with a hard-edged mask [52] (the coronagraph). Converting the PSF into a Gaussian at the pupil plane will produce a Gaussian function in the focal plane with the starlight in the centre. The coronagraph need only block the centre to reduce the starlight significantly. Without the apodizer the PSF has fringes, like an Airy function, requiring the coronagraph to block not only the centre but also these fringes - adding more complexity to the coronagraph's fabrication. A Lyot stop, named after the creator of the coronagraph, is a hard mask placed in the pupil plane after the coronagraph. It is a generally circular opening that only transmits the PSF's centre which removes the remaining starlight as additional stellar light is contained in the outside of the PSF in the pupil plane. The use of a Lyot stop allows the apodizer to produce a PSF with fringes (like an Airy function) and as a corollary allows for the use of smaller focal masks.

Coronagraphy can, in theory, measure Earth-like planets [53] if the coronagraph is fabricated perfectly (and employed under ideal experimental conditions). The Phase Induced Amplitude Apodization Complex Mask Lyot Coronagraph (PIAACMC) [51] is the optimal design for a coronagraph and should have the ability to resolve young massive planets in the near-infrared (NIR). This coronagraph, the stages of which are shown in Fig. 1.10, uses aspheric optics to apodize the beam before, or instead of, an apodizer mask. This provides an extreme contrast between the centre light and the side lobes. A reverse set of

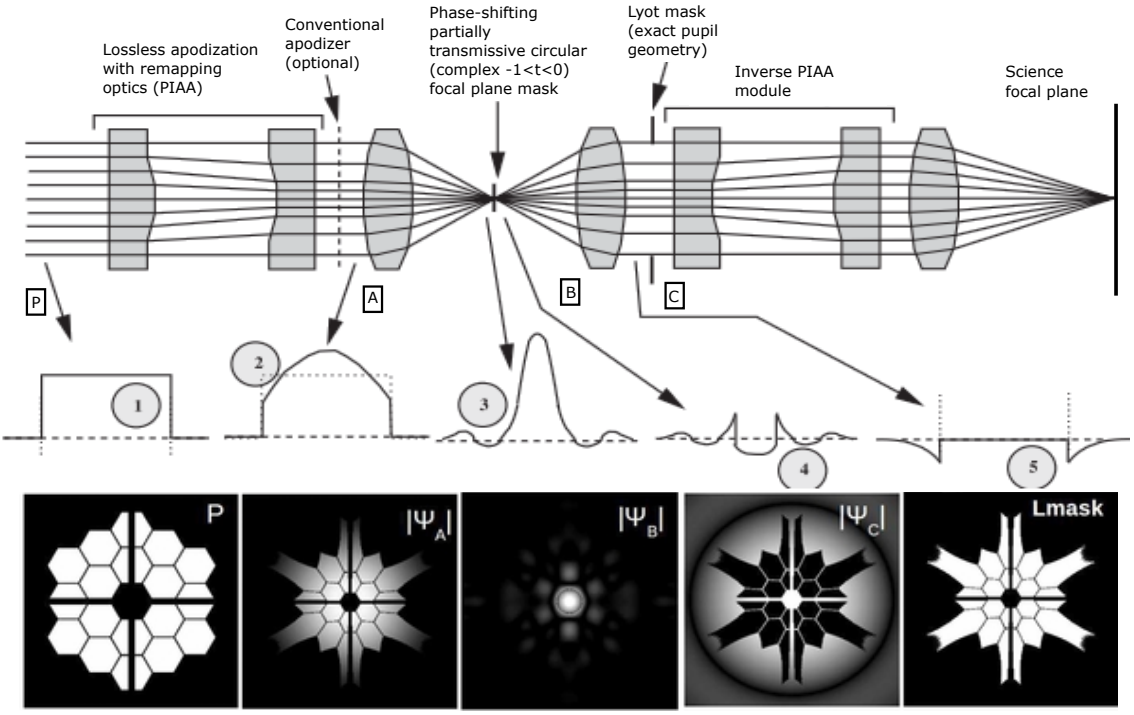

Figure 1.10: PIAACMC design with theoretical PSF and focal points, using (1) a rectangular function to describe incoming light of a star and the equivalent for (P) a full illumination of the Giant Magellan Telescope (GMT): (A) light apodized by aspheric optics (2) or a conventional apodizer, (3) the light in the focus plane before the coronagraph, (B and 4) after the focal plane mask the PSF has been both attenuated and phase-shifted by a translucent, complex, coronagraph, (C and 5) the resulting destructive interference from the focal plane mask in the pupil plane leaving only the fringes for the Lyot stop to mask out, (Lmask) the Lyot mask designed to only allow light in the area of destructive interference to be transmitted (i.e. light from off-axis sources) for the GMT [50, 51].

optics are used after the Lyot mask to cancel aberrations introduced by the initial optical apodization. It also uses a complex mask - a mask with transmission (t) between -1 and 0 where $t = 0$ for an opaque mask and $t = -1$ for a π-shifting phase mask - in the focal plane as the coronagraph.

The Lyot stop in Fig. 1.10 is not circular but instead fabricated especially for this telescope. This illustrates the drawback for coronagraphy - the fabrication. The current limitation for coronagraphy is the fabrication of each component: the apodizer, coronagraph and the Lyot stop. For the PIAACMC it is the fabrication of the aspheric optics, the complex coronagraph and the hard edges of the Lyot stop that limit the performance [51]. Once overcome, this system will be telescope specific which is not a drawback in itself but a general instrument has a much faster fabrication turnaround and can go directly from the test bench to the telescope.

A large star to exoplanet separation assists in exoplanet detection as each direct imaging method relies on distinguishing the exoplanet from the host star. Any exoplanet in a close orbit (typically multiple times Earth's orbit) are either in the speckle of the star's

light, as with ADI, or are blocked by the coronagraph itself.

Because of the difficulty with detecting exoplanets near their host star, the majority of candidates for direct detection are typically situated between 10 and 100 AU and predominately between 10 and 100 M_J. All exoplanets discovered so far, using direct imaging methods, are included in Fig. 1.11.

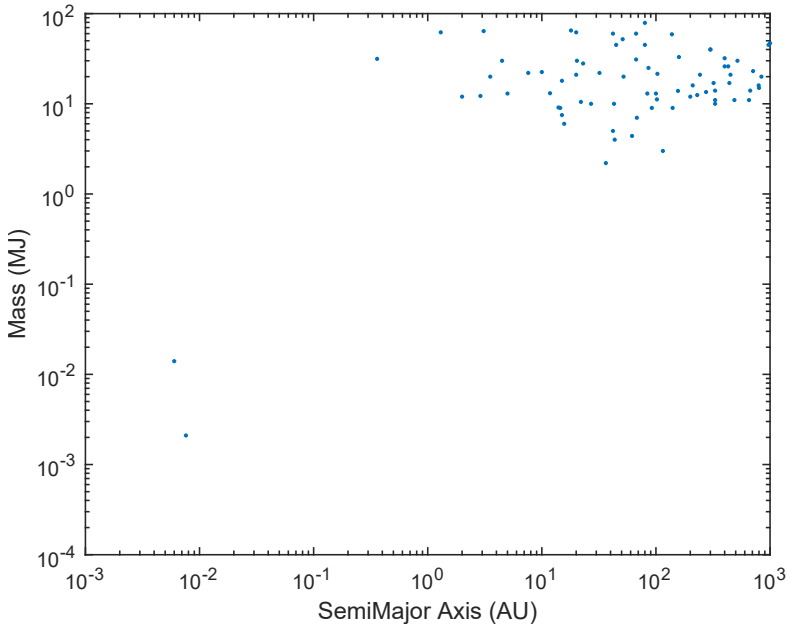

Figure 1.11: Exoplanet and brown dwarf companions detected using direct imaging from `http://exoplanets.org/` [13], accessed on 20/12/2018.

The exoplanets detected and shown in Fig. 1.11 have a large displacement from their host star and are large in mass. This is because the further away from the host star the easier the exoplanet is to distinguish. In addition, the more massive the exoplanet the larger the flux from the exoplanet itself. The exceptions to this are the two outliers of mass $10^{-2}\,M_J$ at 10^{-2} AU. These exoplanets reflected light periodically from their host star in what is best described as an "inverse transit detection" by the Kepler (space) telescope [54]. This type of detection may prove fruitful in the future but requires a robust analysis to determine whether it is comparable to the transit method in finding these types of exoplanets. Until then, coronagraphy remains the dominant method for direct imaging techniques in detecting exoplanets.

The theoretical limits of coronagraphy suggest that Jupiter sized exoplanets, if not Earth-sized exoplanets [53], with a semi-major orbital axis of < 5 AU could be detected with current technology [51] (assuming a contrast between star and exoplanet is 60 dB and the angular separation is $0.6\lambda/D$ or higher). However, there has been no direct image detection of objects with orbits less than Jupiter's (< 5 AU) with coronagraphy nor with mass less than Earth's demonstrating that the theoretical limit of coronagraphy has yet to be realised.

The advantage of using direct imaging methods over indirect methods is that direct

imaging methods are not limited to a single orientation of a star system. Transit and radial velocity detection methods are limited to detecting exoplanet that passes between the host star and the Earth, for example, whereas direct imaging does not. This should allow for more planetary systems to be detected in the long term. These methods are not limited to detecting exoplanets but also images of brown dwarf companions, binaries, dust around the stars and more importantly the gaps in the dust that could be caused by a large exoplanet (or brown dwarf) clearing an orbit around the star. An example of this is shown in Kalas et al. [55] with optical detection (the wavelengths 600 and 800 nm) of an exoplanet around Fomalhaut. The exoplanet is 115 AU away from its host star (semi-major axis) and appears to have sculpted the clouds around Fomalhaut. Whether an exoplanet can form at a distance of > 100 AU away from its host star (as a comparison Neptune is 30 AU from our sun) is under debate (although it is possible that the exoplanet migrated to this distance) [47]. Another example, closer to its host star, is the exoplanet orbiting β Pictoris, embedded in a disk of silicate and ice [56]. This exoplanet detection used the NaCo on the VLT but only in the L' astronomical band to take advantage of the light emitted by the exoplanet in a dim region of the host star's emission.

Exoplanets detected while in the process of construction give a new insight into planetary formation. These exoplanets can be found in transition disks while they are accreting material from the protoplanetary disk around their host star and thus create a suggestive gap in the disk [57]. PDS 70 b is one such exoplanet. It was imaged using the NaCo and the Spectro-Polarimetric High-contrast Exoplanet REsearch (SPHERE) at the VLT and the Near-Infrared Coronagraphic Imager (NICI) at the Gemini telescope [58]. Over the period of 2012 to 2016 the exoplanet was observed intermittently at a variety of IR wavelengths: 1.593 µm, 1.667 µm (H2, H3 bands), 2.11 µm, 2.25 µm (K band), 3.8 µm (L' band). As a result, it was found that PDS 70 b was a young exoplanet with a dusty or cloudy atmosphere, a radius greater than $1.3\,R_J$, a temperature of 1200 K and a semi-major axis of 22 AU.

Current exoplanet detection instruments used in direct imaging methods have yet to distinguish between light from an Earth-like exoplanet and any star nor have they detected exoplanets closer than 5 AU, even with an optimal coronagraph system to remove the starlight. Presently the best coronagraphs are limited by fabrication constraints [51] that reduce the detectable separation between the exoplanet and host star. Additionally, the size of the coronagraph scales linearly with wavelength so they are often created for a single wavelength and thus limited chromatically [50]. There is also the issue of AO instruments and whether they can effectively correct for interference caused by atmospheric disturbances. Another direct imaging method, interferometry, could be used as it is potentially achromatic, or achromatic over some limited bandwidth, with resolution limited not necessarily by a telescope's diameter but instead by the physical separation between two or more telescopes.

1.2.2 Interferometry

Interferometry has been used in astronomy since 1891 when Michelson [59] used two parallel slits over a single telescope to measure the diameter of Jupiter's moons via interference patterns. Interferometry, in astronomy, is the interaction of light from a single, segmented telescope or multiple telescopes. The purpose of which is to generate a high-resolution image [60] or Fourier components of an image. To use a single telescope the light is segmented before recombination. Segmenting the telescope image with sub-apertures (masking the mirror) allows for non-redundant baselines that enable each Fourier component to be related to a sub-aperture, allowing for tailored wavefront corrections [61].

As a comparison to coronagraphy, which is typically discussed in the literature as using a single telescope, interferometry uses multiple telescopes. The angular resolution (θ) is no longer limited to the diameter of a single telescope but instead by the baseline (B):

$$\theta = \frac{\lambda}{B} \tag{1.6}$$

for the wavelength (λ). This is how interferometry can create a higher resolution image (a single telescope resolution is described by eq. (1.5)).

Exoplanet discovery is not the only purpose of interferometry: the angular diameters of stars is another focus of stellar interferometry. This was originally shown in measurements at the Narrabri Observatory in the 1950s and 60s [62, 63] and is being conducted presently at the Center for High Angular Resolution Astronomy (CHARA) array [64]. Also at the CHARA array, interferometry is used to directly image binary stars [65]. Interferometry as a method of exoplanet detection was proposed by Bracewell [66] in 1978. The idea was to use a space telescope with multiple spatially separated mirrors to segregate starlight and exoplanet light in a bulk optics configuration. The suppression is similar to when using a basic coronagraph: the central light is blocked and the angular components of the PSF are allowed to pass through to a detector. The difference is that instead of employing a focal mask to block the starlight, destructive interference is used.

The ability to null starlight without nulling exoplanet light relies on the pathlength difference of light entering two or more telescopes being dependent on the angle at which the light entered the telescopes. This causes constructive and destructive interference fringes over the combined image with the starlight undergoing destructive interference. An example of the light and dark interference fringes on an image is shown in Fig. 1.12. From the figure, the fringes show the star in the centre of the angular instrument response function (of the telescope) and thus at a null. This allows the imaging of orbiting exoplanets, dust and binary companions in the light fringes around the star. This method is still dependent on whether there is a significant amount of transmitted light from the exoplanet as compared to the suppressed star. The possibility of an exoplanet being in a dark fringe, as shown in Fig. 1.12, is high and to account for this multiple exposures can be taken in a single observation night. As the Earth rotates, from the telescope's point of view, the exoplanet, or exoplanets, move around the star - in and out of light and dark

fringes.

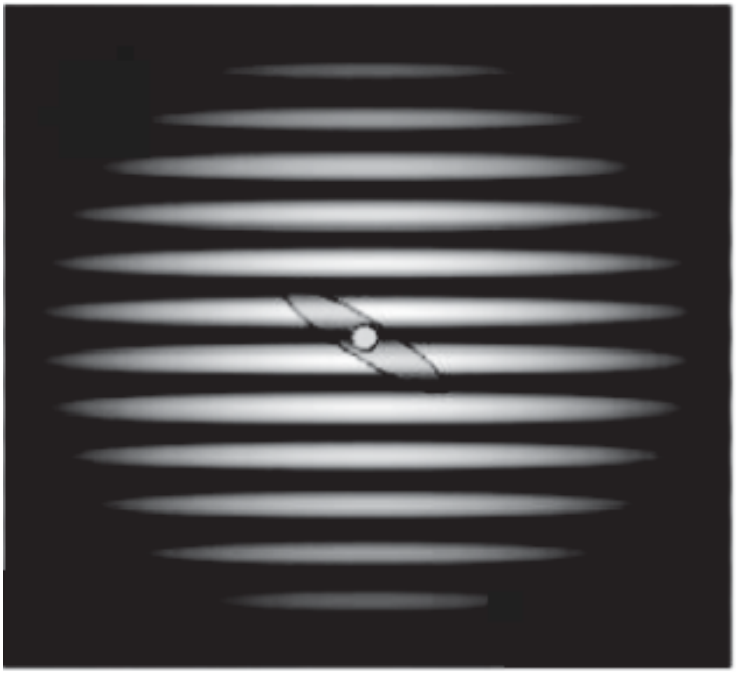

Figure 1.12: Interference fringes created by having two telescopes (one baseline) interfere [67] with the star in the centre and the orbit of an exoplanet around it.

The current interferometry telescopes, like the Keck Interferometer nuller (KIN) [68, 69] and the Large Binocular Telescope Interferometer (LBTI) [70], have yet to directly detect exoplanets. For example, the Hunt for Observable Signatures of Terrestrial Systems (HOSTS) at the LBTI [71], has presently only imaged zodiacal dust around stars [72, 73, 74].

This was until 2019 when Lacour et al. [5] imaged the exoplanet HR 8799 e using interferometry. The detection was made using a photonic chip called GRAVITY (see Chap. 2 for an illustration) on the four 8 m telescopes of the VLTI. It utilised the fringes of the interferometer and managed to suppress, with help from post-processing, 40 dB of starlight.

The first interferometric detection of an exoplanet was an accumulation of decades of research with numerous teams developing nulling interferometry methods. Figure 1.13 shows the null depth and bandwidth of various nulling interferometry testbeds, partially taken from [75]. Note that this figure has no data in the L band - where a gap in the CO_2 absorption of the Earth's atmosphere can be utilised for ground-based nulling interferometry.

Nulling the star is vital for interferometry to measure exoplanet light but equally as important is whether the AO systems on the telescopes can correct for atmospheric disturbances. This is a limiting factor for whether exoplanets at small separations can be detected using interferometry.

Space missions would not require advanced AO systems that the Earthbound telescopes

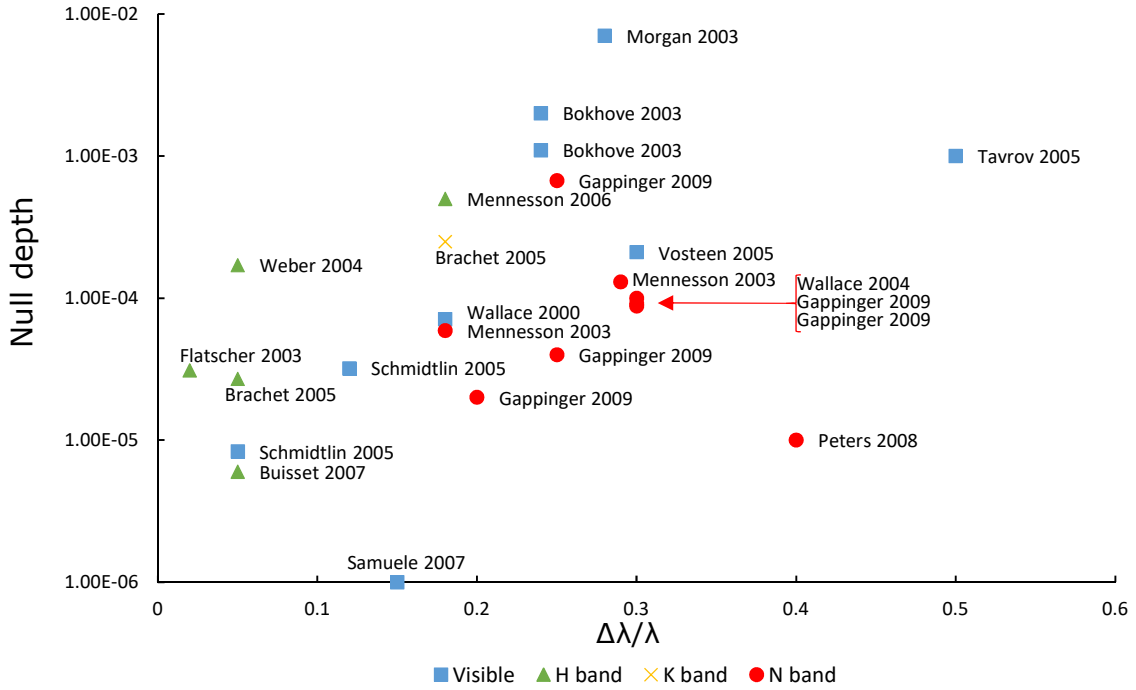

Figure 1.13: A snippet from Ref. [75] focusing on large bandwidth nulling interferometer testbeds. See original work for labelled references. Colour discriminates central wavelength: visible (blue), H band (green), K band (orange), N band (red).

would. The Darwin [76] and Terrestrial Planet Finder (TPF) [77] (or TPF-I for the specific interferometer mission [78]) missions were the planned space missions for nulling interferometry by the European Space Agency (ESA) and the National Aeronautics and Space Administration (NASA) respectively, both proposed just before the turn of the century. Inspired by the Bracewell nulling interferometer [66], both planned missions consisted of three to four mirrors, spatially separated, with a detector and a beam combiner. Rather than being sent to an orbit of 5 AU around the sun, as suggested by Bracewell, these missions were planned to be sent into Earth's orbit or Earth's second Lagrange point (a saddle point in the gravitational forces of the Earth and the Sun that would require weekly, but minor, corrections to maintain orbit) depending on funding. Presently, however, the Darwin mission has been cancelled [79] and the TPF no longer has an official launch date.

Rather than push for these space agencies to fund a large project like Darwin or TPF other, mid-range, space-based interferometers have been proposed. The Fourier-Kelvin Stellar Interferometer (FKSI) [80] and Pegase [81] were proposed as pathways to a larger space instrument in the future. These satellites would be able to image debris disks around stars and take spectra of known exoplanets which will not only test these systems in space but add to the breadth of research. A recent proposal, LIFE, is a nulling interferometer proposed as a replacement for Darwin or TPF. If it was to be taken up approximately 315 exoplanets could be detected using current technology [82].

Table 1.3 shows a brief history of interferometry highlighting the first direct detection of a brown dwarf, the two proposed space missions and their cancellations, leaving

Table 1.3: A brief history of interferometery in astrophysics, direct imaging and nulling interferometry.

Michelson	Measured the moons of Jupiter via interferometry	1891	[59]
Bracewell	Proposed a two telescope nulling space interferometer	1978	[66]
Angel & Wolf	Improved on the design for a four telescope version	1997	[83]
Darwin & TPF	Nulling interferometer space missions announced	~1998	[76, 77]
Chauvin	First image of an extra-solar object using Direct imaging	2004	[17]
TPF	Deferred indefinitely	2007	[84]
Darwin	Study ended: no further activity planned	2009	[79]
Lacour	Exoplanets measured using interferometry	2019	[5]
VIKiNG	Proposal for direct imaging using Kernel phase		[85]
LIFE	Proposal for an infrared nulling interferometer space mission		[86]
Roman	Nasa's Wide Field InfraRed Survey Telescope to be launched in 2025		[87]

interferometry without a planned space mission. Future direct detection space telescope WFIRST (now Roman) is still planned for launch in 2025 whereas interferometry has only had proposals for space missions, such as LIFE (a mid-infrared (MIR) space-based nulling interferometer) [86], and so ground missions are the only short- and medium-term option, such as VIKiNG (a Kernel-Nulling interferometer for the VLTI). This limits the detection capability to current AO technology, the null depth of interferometry techniques and the baselines of currently built telescopes. To improve two of these three limitations (decreasing the required null depth and decreasing the speckle due to atmospheric turbulence that would otherwise need an extreme adaptive optic to correct) one can work in the MIR. There are other benefits of working in the IR, detailed in the mission plans [78] for the TPF as follows:

> The wavelength region between 5 and 15 µm is rich in diagnostics for probing physical conditions in astrophysical environments. Emission from warm dust in the range 100 to 1,000 K, the characteristic temperature of grains located in and near the habitable zones of stars [...] probe of dust in star forming-cloud cores heated by young stars and clusters. [...] imaging of the region from 0.1 to 10 AU where planets form around Solar-mass stars located within a few hundred [parsecs] of the Sun, warm dust located from 10 to 1000 AU around massive stars located anywhere in the Galaxy, and the dust surrounding the Active Galactic Nucleus (AGN) and extragalactic star-forming regions in our locale in the Universe.
>
> A variety of molecular bands and solid-state features (arising from grains and ices) [...] This wavelength region contains bands produced by polycyclic aromatic hydrocarbons (PAHs), the bands of amorphous and crystalline silicate dust around 10 µm, and a variety of ice features due to water, carbon monoxide, carbon dioxide, and methanol, molecular vibration bands of many common organic and inorganic substances, fine structure lines of many elements and ions, and the spectral lines of atomic and molecular hydrogen.

Hence, constructing devices that operate in the MIR is vital for future space missions and the future of astrophotonics.

1.2.3 Detecting in the MIR

Many direct imaging measurements used MIR wavelengths, for example, Marois [47] in the detection of HR 8799 b, c, and d and Lagrange [56] in the detection of β Pictoris b. The advantage gained by working in the MIR is that exoplanets with temperatures of $\approx 1000\,\mathrm{K}$ have a black body peak at the 3 µm wavelength and thus the contrast between exoplanet and starlight is at a minimum (that is, the exoplanet is at the peak of its brightness whereas the star is in the tail of its blackbody spectrum). The magnitude (M)[ii] in the L' wavelength band of the exoplanet around β Pictoris was $(M_{L'} =)$ 11.2 [56] compared to $M_{L'} = 3.5$ for β Pictoris itself. Similarly for the exoplanets around HR 8799, $M_{L'} = 12$ compared to HR 8799 itself which had $M_{L'} = 2$ [47]. Hence for β Pictoris the difference in magnitudes is 31 dB ($\Delta M_{L'} = 7.7$) and for HR 8799 the difference is 40 dB ($\Delta M_{L'} = 10$).

To put these numbers into context Fig. 1.14 shows a simplified model indicating the difference in detectable light between a star (like our own) and two types of exoplanets: an Earth analogue and a Jupiter-like exoplanet with a temperature of 1000,/K (to represent a young, hot exoplanet), both at 10 pc. A 2 m radius telescope (set by the size in SpaceX's largest rocket's, the Falcon 9's, payload [88]) is used in this simulation to collect the exoplanet and starlight in space and the GMT is used for the Earth-bound detection simulation. The distance between the exoplanet and their host star is neglected in this model but the exoplanets are assumed to be resolved.

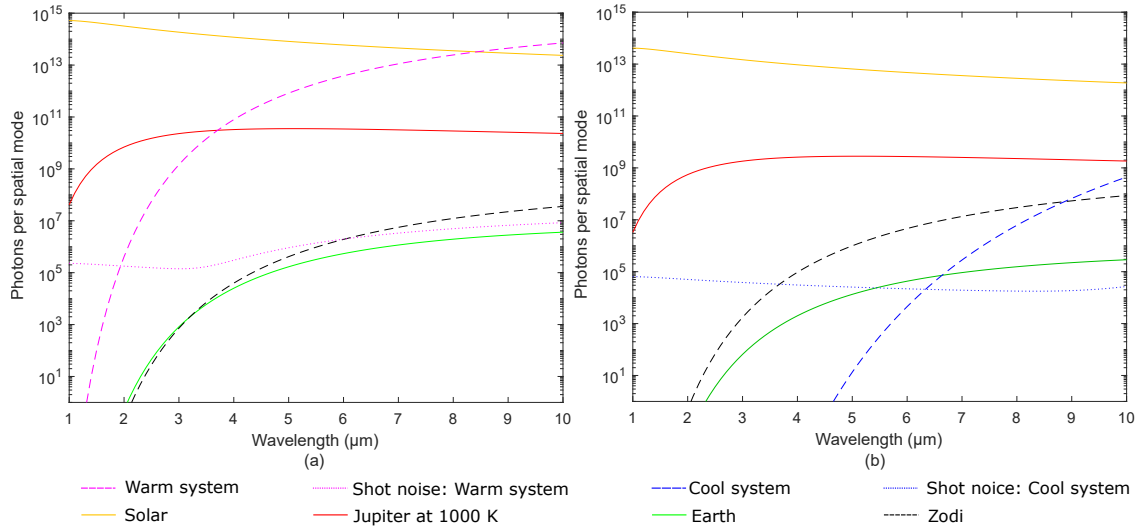

Figure 1.14: Obtainable photons in (a) a warm system and (b) a cool system. A cold system used a 2 m telescope and 24 h of total integration time. The warm system used an 11 m telescope and 10 h integration time. Both assumed a 35% efficiency, 10% emissivity and a 16% bandwidth. The Earth, Jupiter and Solar (in green, red and yellow solid lines) analogue were simulated 10 parsecs away. Jupiter's temperature has been increased to 1000 K to simulate a warm, young exoplanet. The noise (in dashed lines) from the telescope system at 280 K (magenta) and 80 K (blue) are shown alongside Zodiacal light (black). The shot noise limt (in dotted lines) represents the limitations of the respective systems with a 40 dB null over the star.

[ii] The astronomical magnitude as compared to the star Vega.

In this simulation the light from a G2 star (a star like our sun), Earth and Jupiter analogue is calculated based on the black-body emission formula. This was used to determine how many photons, collected by a 2 m space telescope or 11 m ground based telescope, are injected into a single mode fibre to be input into the nulling interferometer. The light emitted from the telescope system, and incident light from the Earth's atmosphere, was simplified to

$$\text{System} = \frac{2}{\exp((h * \nu)/(k_B * T)) - 1}$$

where h is Plank's constant ($6.626 \times 10^{-34}\,\text{m}^2\text{kg/s}$), ν is the central frequency (converted using $\nu = 3 \times 10^8 \times \lambda$), k_B is Boltzman's constant (1.38×10^{-23} J $*$ K^{-1}) and T is the background temperature. This is represented in Fig. 1.14 twice, once for an Earth based telescope ($T = 280\,\text{K}$) and one at Lagrange point two ($T = 80\,\text{K}$). An efficiency (representing the amount of light that would reach the endpoint camera) of 35% is given for both. The Zodiacal light emission (reflection is ignored) around Earth is calculated with an emissivity of 5×10^{-8} [89].

The shot noise is the assumed limitation for this theoretical astronomical detection[iii]. In Fig. 1.14 this is calculated for the case where the Zodiacal light, the star with 40 dB of light suppression (equivalent to the difference in light between HR 8799 b, c and d and HR 8799) and the telescope system emission are the only source of unwanted photons, and calculated as:

$$\text{Warm}_{\text{shot noise}} = \sqrt{\text{System } 280\,\text{K} + \text{Zodiacal light} + \text{sun} \times 10^{-4}}$$
$$\text{Cool}_{\text{shot noise}} = \sqrt{\text{System } 80\,\text{K} + \text{Zodiacal light} + \text{sun} \times 10^{-4}}$$

for a ground based telescope and space based telescope respectively.

The simulated background light from Fig. 1.14 shows the limits of what can be detected, noting that the longest integration time for a telescope on Earth is 10 h whereas the space-based telescope has no such limitation and was set to 24/,h. On Earth, the warm system light dominates the shot noise (the signal being 10^8 times lower than the thermal background) to the extent that an Earth analogue (at 10 pc) cannot be detected at any wavelength. In space, where the system temperature is at 80 K, the shot noise is limited by the nulled light, not the system noise, making an Earth-like exoplanet around a G2 star detectable at wavelengths longer than 5.5 µm.

A 1000 K Jupiter sized exoplanet is above the shot noise limits for all wavelengths shown making it detectable in the IR. This temperature was used as it reflects a young exoplanet, but it also relates to the proximity of an exoplanet to its host star. This means that Earthbound telescopes can focus on young Jupiter sized exoplanets before a space mission is launched with the capability to detect smaller exoplanets.

The relationship between luminosity and proximity to the host star is investigated by Burrows [90]. An exoplanet at a semi-major axis of 0.2 AU has the same suppression

[iii] This assumes the camera will be cooled using liquid helium, to remove thermal noise, with lock-in via a phase modulator.

requirement (for equal intensity) as above, with larger separations requiring larger star suppression: 60 dB for 1 AU separation and 90 dB for 15 AU. The dependence on separation is due to the heating, via irradiance, of the exoplanet by the star. In addition, the closer the exoplanet the more starlight is reflected making measurement in the visible light spectrum potentially viable - at a wavelength of 500 nm (noting that the robust library of silica photonics can be used at this wavelength potentially making nulling interferometry easier) only 70 dB of suppression is required for a 0.2 AU Jupiter sized exoplanet for both to be at equal intensity.

Due to irradiance hot Jupiters should be prime candidates for nulling interferometry. The difficulty comes from the displacement between the exoplanet and its host star (to maintain a high temperature, on the order of 1000 K, the hot Jupiters are required to be close to their host star [91]) and the telescope's baselines have to have a high enough angular resolution to resolve the exoplanet from the star. Instead of looking for old exoplanets that are potentially not resolvable due to their proximity to their host star, massive young exoplanets that are still hot from accretion [47], and are hence luminous in the MIR, become the best candidates for nulling interferometry. Figure 1.15 shows the luminosity of exoplanets, compared to their age and mass, indicating that young exoplanets are much more luminous than their older counterparts.

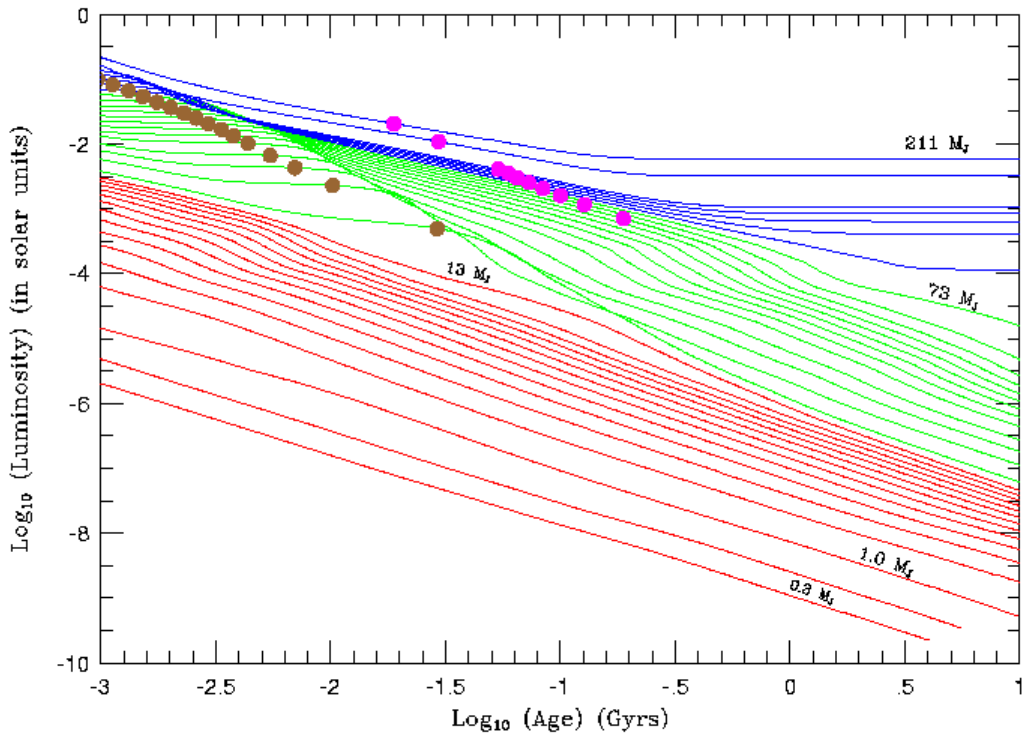

Figure 1.15: The luminosity of giant exoplanets (red), brown dwarfs (green) and sub-solar mass stars (blue) over time [92]

In addition to the luminosity shown in Fig. 1.15, younger exoplanets may have an ac-

cretion disk still coalescing into it. This may emit infrared light brighter than an exoplanet without an accretion disk [93] making them much easier to detect.

The benefits of looking in the MIR go beyond that of simply imaging the exoplanet. By identifying molecular abundances [94] one can infer evidence of life on the exoplanet. Using infrared light can even distinguish between a rocky surface and one made of ice [95] leading to a better understanding of how exoplanets form around stars.

1.3 Open questions in exoplanet astronomy

The detection and subsequent investigation of exoplanets are the key to many unresolved questions in astrophysics. Already there is a veritable zoo of exoplanets - of various sizes, atmospheric content, surface composition and proximity to the host star, and each detection improves the scientific understanding of planetary formation.

1.3.1 Planet formation

Planetary formation is a complex process where the dominant physics at play in each step is still a mystery. Before the discovery of exoplanets, the theories of star system evolution focused on the solar system by necessity - small rocky planets close to the star, a ring of asteroids and larger gaseous planets further away [96].

The first few exoplanets discovered immediately questioned whether the solar system was a typical star system as their masses were between 0.1 and 10 M_J and they had orbital periods of between 3 and 10 days - examples of hot Jupiters [97]. However, these seem to be an anomaly in detection as it was found that more than 50% of solar-type stars have an exoplanet with a period of 100 days, or less, and a mass of $\leq$ 30 Earth masses [98]. Noting that Mercury has an orbit of 88 days this is not in itself surprising. The study by Mayor et al. [98] suggest that 50% of solar-type stars have a super-Earth or Neptune sized exoplanet in close orbit, with an additional 14% of solar-type stars with any detectable close in exoplanet (like hot Jupiters). This makes the solar system (which has no super-Earth, Neptune or Jupiter-sized exoplanet with a 100 day period or less) an outlier.

The question of where in the star system exoplanets like hot Jupiters and super-Earths form is still open. There are three main competing theories of how long term exoplanet orbits are established - *in situ*, migration and scattering.

In situ formation has no movement of exoplanet orbits, leading to massive exoplanets forming in the inner-most region [99] of the stellar nebula, initially by accreting solid particles and later through rapid accretion of gas from the protoplanetary disk [100]. This theory lends itself well to exoplanet systems bound close to their host star (all exoplanets in the system with a period of $<$ 200 days) and the creation of super-Earths [101]. Hot Jupiters are the key to this theory as they supposedly keep a planetary system tidally locked. They consume all exoplanets that are near to their host star that is not tidally locked [97] making them unique in their proximity to their star.

The theory of exoplanet migration suggests that exoplanets with short periods slowly

(in an astronomical time scale) moved inward from larger orbits. The mechanism for migration is the tidal influence of protoplanetary disks or nebula on the exoplanet either during planetary formation or once the exoplanet has reached hydrostatic equilibrium [102, 103, 104]. This theory is not limited to Jupiter sized exoplanets, as exoplanets classified as super-Earths or Neptunes that have a small displacement from their host star may have migrated after formation. Migration often implies that exoplanets should not be alone in their planetary system [105].

Once exoplanets have formed, leaving minimal dust and gas to instigate migration, migration may still occur due to resonance between the established exoplanets [106, 107, 108]. Resonance is a ratio between orbital periods of exoplanets around the same star (not limited to exoplanets as satellites around a planet also can be in resonance with other orbiting satellites) where an integer value makes the system inherently stable [109].

Planetary scattering is another model that deals with fast exoplanet movement (in the astronomical time scale), where exoplanets undergo chaotic motion leading to angular momentum transactions which significantly change their orbits. Focusing on planetary systems with established bodies in hydrostatic equilibrium, their orbits may become chaotic and unstable. Such orbits can lead to large planets coming gravitationally close to each other such that angular momentum is exchanged between the planets, causing a scattering effect off of each other. This can occur in a planetary system after exoplanets form a resonance, with off-resonance exoplanets the target for potential scattering events. These events often lead to a planetary ejection [110] from the system but otherwise provide a rearrangement of planets in a star system. One indicative sign of a scattering event is higher than expected eccentricities in the exoplanets' orbits that cannot be predicted by the mass distribution of the original protoplanetary nebula [111].

With more detection of star systems and the exoplanets within, these star system formation models can be tested and refined. Direct imaging of star systems will provide an entire picture of a star system with multiple exposures (over multiple months to years) providing information on the orbital dynamics of the exoplanets.

1.3.2 Atmospheric models and the search for life

Detecting exoplanets is only the start of what is required for planetary evolution and creation models: the atmosphere is also required for the understanding of a star system's history. The atmosphere content can also indicate the likelihood of life on an exoplanet, especially an Earth-like planet (in terms of mass) in the "habitable" zone of its host star. There are many chemical biosignatures, like oxygen (O_2), methane (CH_4), carbon dioxide (CO_2) and ozone (O_3) [112], that are detectable in the exoplanet's atmosphere. Figure 1.16 shows the spectra of the Earth as an example with the absorption features of the chemicals above as well as Nitrous Oxide (N_2O).

Figure 1.16 provides an indication of what a habitable exoplanet's spectra would be but also how difficult observation of exoplanets are from within the Earth's atmosphere. Water vapour has a large proportion of Earth's absorption features followed by CO_2, blocking

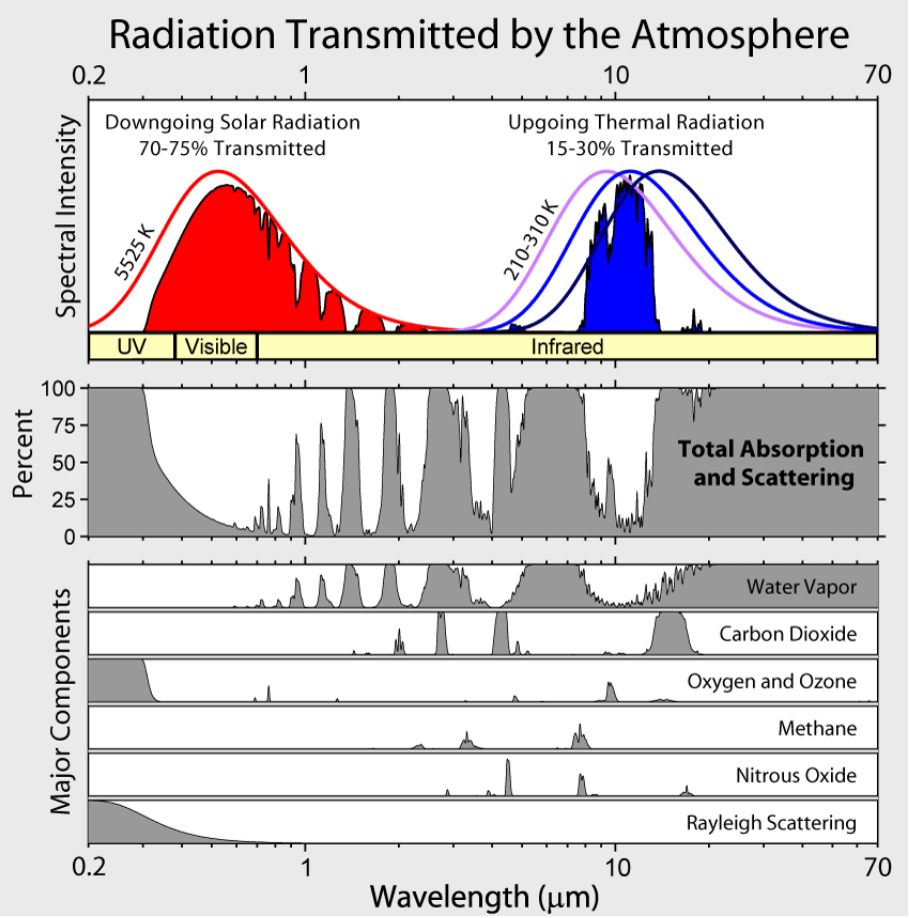

Figure 1.16: Solar light transmitted through the Earth's atmosphere (red) and emitted light from the Earth's atmosphere (blue) with transmission (through the Earth's atmosphere) spectra of listed chemicals: H_2O, CO_2, O_3 + O_2, CH_4, N_2O and elastic scattering of solar light from the atmosphere (Rayleigh Scattering) [113].

light from reaching surface-bound telescopes. At a wavelength of approximately 4 µm (in the astronomical L' band) is one of many gaps in the total atmospheric absorption. At this wavelength, however, there is also a reduction in thermal and solar radiation. This provides a window through Earth's atmosphere in the MIR that can be exploited for exoplanet detection. Also note the large gap in Earth's atmosphere between 8 and 10.5 µm. This gap does not exist in inhospitable worlds like Venus due to sulphur dioxide (SO_2) which then reacts to form sulphuric acid (H_2SO_4) which is corrosive to tissue and even metal [114].

Measuring the chemicals listed in Fig. 1.16 is vital for detecting exoplanets that harbour or could sustain life. Water is commonly used as a benchmark for whether life can exist on a celestial body, be it an asteroid, moon or exoplanet. As an example, water abundance was measured by Kreidberg et al. [115] for the 2 M_J exoplanet WASP-43 b.

For a direct indication of life (as it exists on Earth) one looks for O_3. This is a key feature for the existence of plant life [112]. To be sure the O_3 was not formed via other processes (like photodissociation of O_2), O_2 and CH_4 measurements are also used for

verification. The reason for singling out O_3 however is to highlight that the main O_3 peak is in the MIR and as such not as easy to detect as the other chemical species that absorb in the visible and NIR (see Fig. 1.16 for further detail). This work's focus is on the MIR and is just one step, in a long line of steps, towards having spectroscopic measurements in the MIR of exoplanet atmospheres.

Finding evidence of life is important but not the only reason to measure exoplanet atmospheres. These measurements also improve our exoplanet formation models. As an example of exoplanet detection, and consequent investigation, consider the exoplanet GJ 436 b. Stevenson et al. [116], during observation with the Spitzer Space Telescope [117], measured the atmosphere at the following wavelengths: 3.6, 4.5, 5.8, 8.0, 16, and 24 µm during the exoplanet eclipse - which is an event opposite to a transit involving the exoplanet going behind the star and comparing that measurement with the exoplanet in view. The purpose of the detection was to determine the abundance of carbon monoxide (CO), CO_2 and CH_4 - which, with a dip at the 3.6 µm wavelength, was lower than expected - on the exoplanet. From these measurements Hu et al. [118] modelled an atmospheric evolution of Neptune sized exoplanets, close into their host star, that formed with either an abundance of helium or hydrogen. The models predict that an exoplanet that began its life with a helium dominated atmosphere would account for a low CH_4 whilst maintaining a high CO and CO_2 abundance. Note that this conclusion came after various models of the atmospheric chemistry [119, 120], metallicity [121] and tidal heating [122]. This was further explored by Morley et al. [123] with the determination that "hot Neptunes" are a diverse species that cannot simply be grouped together. Hence detecting the atmosphere of a single exoplanet has spawned multiple models, added to our understanding of exoplanet creation and increased our knowledge to the point of requiring better classifications of a particular subspecies of an exoplanet.

It is not just the atmosphere that can be detected. Using MIR and NIR spectroscopy the rocky or water-ice surface of an exoplanet could be detected [95]. With each detection of Earth-like exoplanets, models of the composition of such exoplanets become more refined, with the mass and radius being all that is required to generate an approximation of the core composition [124].

1.4 Thesis Direction

1.4.1 Motivation

The established exoplanet detection methods favour the detection of massive exoplanets that are either close to their host star - using transit and radial velocity detection - or at a great distance (>10 AU) - using direct imaging. A new method is required to find exoplanets in the middle ground, around the ice line (where water can condense into solid ice grains) of stars like our own. This is where the only known habitable planet (Earth) exists and is thus the first place to search for habitable worlds in other star systems.

The importance of exoplanets here cannot be understated. Knowing the population

density of exoplanets at the ice line (of various stars) strongly constrains planet formation theories. The ability to measure the chemical absorption in the atmosphere of these exoplanets, as a test for habitability, would then directly influence the predictions of extraterrestrial life abundance in the universe.

Removing stellar light is essential for detecting Earth-like exoplanets. Nulling interferometry can be used to remove 40 dB of stellar light, a requirement proposed in Sec. 1.2.3, to make Earth-like exoplanets visible to direct detection. A beam combiner is proposed here that can, in theory, remove up to 40 dB of stellar light over the entire L' band.

To detect Earth-like exoplanets the best contrast between the host star and exoplanet is at 10 µm wavelength. The technology to manufacture a nulling interferometer here has yet to be realised. In the astronomical L‘ band however, a plethora of technologies exist that can be used to make the first iteration of nulling interferometer. These can be tested on Earth-bound telescopes, looking through a gap in Earth's CO_2 layer to find hot, young Jupiter-like exoplanets. This is before moving the technologies to the far-infrared where the Earth's glow is most bright.

1.4.2 Outline

Chapter 2 looks to interferometry as the solution to detect exoplanets in this region. The range of current technologies in photonics, materials that transmit in the MIR and compromises of the waveguide fabrication techniques are discussed. The chapter focuses on the photonics aspect of interferometry as these are preferable in a space interferometer from a cost perspective but potentially also in terms of reducing instrumental noise.

A multimode interference coupler (MMI) was selected for this work as the beam combiner in a basic interferometer. Detailed in Chap. 3 the robust fabrication tolerance of this coupler [125] extends to its innate ability to split light evenly between two output ports. Taking advantage of this ability, and inherent linearity is how a photonic 3 dB coupler (a device that evenly splits light) can be used as an interferometer - specifically, a nulling interferometer that reduces the host star's light sufficiently to image the exoplanet.

The bulk of this chapter is dedicated to the fabrication tolerance of the MMI selected for this thesis. These are unique insight into why this MMI is preferable over other beam combiners for the material selected that suffer during fabrication.

The wavelength range at which an MMI can be used as a nulling interferometer was potentially a limiting factor for this device. The literature exploring the MMI does not address this limitation, nor does it look to the MMI for a broad bandwidth response, to the author's best knowledge, as this is not a common significant requirement. In Chap. 4 an investigation into an MMI with a broad bandwidth null of starlight was undertaken. This work is specific only for broad bandwidth applications, such as detecting reflected/emitted light from an exoplanet to determine the atmosphere composition. The result is an MMI that, in theory, can achieve a 40 dB extinction over the entire astronomical L' band.

The materials chosen for the MMI fabrication are discussed in Chap. 5. Due to the desire to work in the MIR (to take advantage of the transparency of the atmosphere

caused by a gap in the CO_2 absorption tail) chalcogenide glass was selected for this work. Previously in the Laser Physics Centre at the Australian National University, the same chalcogenide glass was used to create low loss ring resonators [126] and thought to be a good starting point for this work. Chapter 5 details the complexity in making a low loss, fully etched, waveguides for an interferometer in the MIR.

The performance of the MMI itself is explored in Chap. 6 and 7 as a 3 dB coupler and a nulling interferometer respectively. To the author's best knowledge an MMI of this type, using this material, has never been explored in this manner before. The results show that the fabricated MMI splits light as predicted by simulations but a deep null over a wide bandwidth is yet to be achieved.

A broadband MMI may be the key to a single photonic chip for future space missions, assuming it can be made with low loss, have a high fabrication tolerance and a splitting ratio that is constant for wide bandwidth. Although not all of this was achieved in this work the result of this thesis is an MMI that behaves as simulated, has a broad bandwidth at an even splitting ratio and can be made to have a deep null at select wavelengths.

Chapter 2

Astrophotonics

In astronomy, bulk optics and fibre optics are being used for instrumentation. At present there is a push to add photonic systems, moving further into operating in the infrared, to astronomical instruments - replacing bulk optic components or entire benches. An example of this is in beam combination [127], pupil-remapping [128] and a test-bed for the cancelled DARWIN mission utilised a photonic chip to achieve a 50 dB null [129].

As a result of photonics becoming prevalent in astronomy, space missions will begin to reduce in cost and become more robust and stable due to massive optics on the order of kilograms being replaced with monolithically integrated devices up to 1000 times lighter.

Where possible photonics will eventually replace bulk optics: reducing the cost of space missions, increasing the tolerance to environmental and instrumental noise, and increasing the stability due to the massive optics being reduced to a monolithically integrated device up to 1000 times lighter. This is not to say that the transition will be simple nor does it mean there will not be a trade-off with efficiency, but in time, photonics will play a key role in the next generation of telescope instruments.

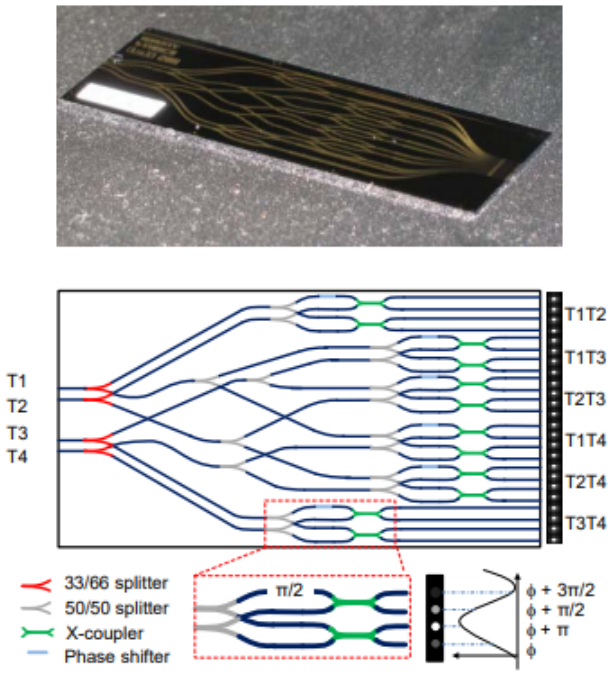

Figure 2.1: Beam combiner used at GRAVITY (a 4-beam interferometric combiner at VLTI [130]). TOP: Photo of the IO installed in GRAVITY, BOTTOM: the schematic of the four port interferometer.

Already photonics is being used on telescopes: GRAVITY is an interferometric instrument at the Very Large Telescope Interferometer (VLTI) [130] using a four-port beam combiner, shown in Fig. 2.1, on a silica on silicon (SiO_2-on-Si) platform. Before that rather than photonics fibre optics were used: the Fiber Linked Unit for Optical Recombination (FLUOR) used fibres to achieve multi-telescope interferometry at the Infrared and Optical Telescope Array (IOTA) [131] before being moved to the Center for High Angular Resolution Astronomy (CHARA) Array [132] and updated to include a photonic beam combiner. In both cases, y- and x-junctions were used (on-chip at the CHARA and with fibre at the IOTA) for beam splitting and combining. Beam combination alternatives are discussed in detail in Sec. 2.2.

Fibre optics have been utilised to transport or reformat light from telescopes into science instruments but this can lead to spurious phase shifting due to environmental factors and instrument and telescope vibration. Eliminating fibres means using bulk optics through the telescope system until a final photonic chip is used for recombination, splitting or other purposes before redirecting the light into a scientific instrument.

Consider the following hypothetical situation: An interferometric photonic chip has the light from multi-telescope systems launched into it. For this to be achieved multiple steps are taken. For a single telescope, a segmented mirror [61] is used to split the light into multiple "telescopes" which allows for the phase of the light to be manipulated, using a compensating system [133] a broad bandwidth of light with the same phase is directed into the chip. The light is then directed into the photonic chip. It has insertion loss from the chip and loss from the chip itself, but as a contrast to fibres, it is robust to the environment. Light from the photonic chip is then sent directly into the science instrument either through a lenslet array or by a short segment of optical fibre [128].

Looking further afield an additional step could be to use a photonic chip to segment star and exoplanet light. The exoplanet port (where the star is at a null) can then be linked to the spectrograph so that the atmosphere of an exoplanet can be measured. The starlight can also be used for calibration purposes. Photonic spectrographs have already been manufactured for use in the near infrared (NIR), with a prototype reported by Cvetojevic et al. [134] for detecting hydroxide (OH) in the Earth's atmosphere between the wavelengths 1465 and 1785 nm.

Considering all that photonics can already achieve it is not unreasonable to predict that a single photonic chip [135] will be able to null starlight and send exoplanet light through to a spectrograph, adapting to multimode fibres if needed (with photonic lanterns). However, more work is required to achieve this outcome. This thesis focuses on the nulling interferometer part of this vision, limiting the scope to only a two telescope interferometer for simplicity, with scope to push the technology to multiple ports for multiple beams inspired chip (four beams if using the VLTI for instance).

One such all-in-one photonic solution is the nulling plus sensing photonic chip currently designed for the Very Large Telescope Interferometer (VLTI) known as VLTI's Infrared Kernel NullinG instrument (VIKiNG) [85]. A schematic is shown in Fig. 2.2 illustrating

the two-step process: nulling stellar light via interferometry and retrieving the kernel phases.

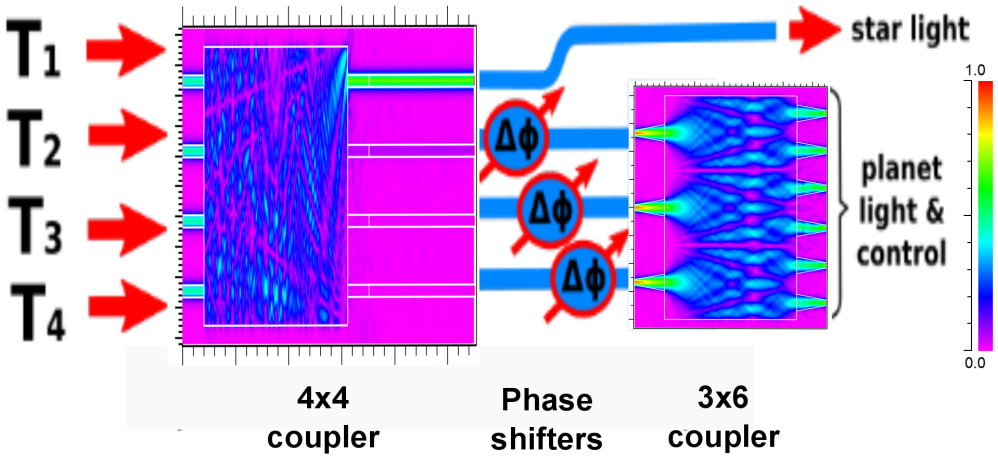

Figure 2.2: Two stage Kernel null photonic chip schematic, adapted from Martinache et al. [85], with simulations of a 4x4 (nuller) coupler and a 3x6 (sensing) coupler stage using the beam propagation software in RSoft (see Sec. 3.3.1). Multimode interference couplers were used for these simulations because they were the main theme of this thesis. The two simulations are scaled individually, the nuller to an output port of 1 intensity and the sensing coupler to three input ports of 1 intensity. Between the two stages are phase modulators that are designed to eliminate background fluctuations.

The kernel phase is a property of the focal plane image, like the closure phase, that is immune to noise. In fact, what has classically been considered closure-phase is a special case of kernel-phase that is limited to non-redundant aperture masks [136] which the kernel-phase itself is not. Unlike closure-phase, kernel-phase is not robust to large wavefront errors and so telescopes under the Earth's atmosphere will need extremely sensitive AO systems [136], making a kernel-nulling device a great candidate for space telescopes.

There are many individual components to the Kernel-Nuller in Fig. 2.2, the first being the nuller itself. This combines the light from four telescopes (or one segmented telescope) to create a null in three output ports, forcing the starlight into the topmost port. A cascade of 2x2 couplers in what is termed a Bracewell nuller configuration [3] works to this end.

The sensing device is used to recombine the nulled output ports. The purpose of this device is to identify the output intensity combinations that are robust to instrument noise. This is the kernel information of the Fourier-phase [85]. For a 6-output port device, the three kernels are simply the combinations of ports $1-2$, $3-4$, $5-6$.

The input ports before the sensing device of the Kernel-Nuller are modulated on-chip to correct for background fluctuations. Chromium heaters, discussed in Chap. 7, can be used for this purpose and are also an integral component to have an active phase control entering the sensing device after the nulling device.

This is only one example of what can be achieved in a photonic system that would otherwise be cumbersome in a bulk optics system. It is explained here because of the parallels with this work: the Kernel-Nuller is the natural progression after the basic two

telescope nulling interferometer due to its inclusion of the sensing device. Whether this will be made for the mid-infrared or near-infrared the choice of material is vital.

2.1 Materials

Previously in this thesis (Sec. 1.2.3) it was proposed not to work at the telecommunication band (1550 nm) but in the mid infrared (MIR) to have better contrast between exoplanets and their host stars. To work in the MIR, the most prevalent material in photonics, silica, cannot be used as it is opaque past 3.5 µm [137]. Table 2.1 at the end of this section includes the extended list of materials suitable for working in the MIR from 2 µm up to 12 µm discussed here.

Silicon-on-Insulator (SOI) is a common combination in photonics. It has a limited transparency window from $1.2 - 3.7$ µm with a high loss region between $2.6 - 2.9$ µm. This material was included in Tab. 2.1 as a baseline to compare the other materials too. The benefit of SOI is the robust library of architecture it has to offer. As an example, specific to the MIR, Nedeljkovic et al. [138] constructed a multimode interference coupler (MMI) - a 3 dB coupler that uses optical interference to split light - to perform at a wavelength of 3.8 µm. In the same paper, it was also suggested that the transmission window of SOI can be increased to a wavelength of 7 µm by undercutting the insulator (SiO_2) layer underneath the Si waveguide, making a "suspended waveguide" [138] which makes SOI a potentially viable material in MIR photonics. However, due to the large refractive index of Si, a single-mode waveguide would have widths on the nanometre scale - making fabrication difficult. This could be overcome by cladding the waveguide, to reduce the refractive index difference, but the common cladding material (SiO_2) provides no significant improvement to this issue.

Silicon-on-Sapphire (SOS) replaces the SiO_2 in the SOI configuration to increasing the transmission window further to a wavelength of 5 µm. The refractive index difference between Si and sapphire (Al_20_3) is 1.7, with a Si waveguide having a difference of 2.5 with an air over-cladding. This high refractive index difference means that the bend radius of any waveguide (to maintain negligible loss) is extremely small but it also means that single-mode waveguides are also small, leading to high fabrication requirements for a good quality (low loss) waveguide. As a trade-off, the Si waveguide can be coated in a cladding material to decrease the refractive index contrast and limit possible impurities from an air cladding. Cladding with SiO_2 reduces the transparency window to that of SOI [137], although by manipulating the size of the waveguide a reasonable loss of < 2 dB/cm has been achieved at a wavelength of 5 µm implying that under particular circumstances SOS can be used in the MIR. The key issue, like in SOI, is that the refractive index difference between core and cladding is too high.

Silicon-Germanium (SiGe) waveguides do not suffer from the need to use SiO_2 as they use Si as a substrate and an over-cladding, which is transparent until approximately 7 µm. Without the over-cladding the transmission can be extended to 16.7 µm [137] assuming the

impurities of the SiGe combination can be removed at the interface of the Si substrate [139]. Waveguides have successfully been manufactured with and without Si cladding to produce a loss of 1 dB/cm [140] and 0.3 dB/cm [141] respectively, at a wavelength of approximately 4 µm.

Lithium niobate ($LiNbO_3$) is an option for replacing SiO_2 as a substrate due to its transmission out to 5 µm. Notably, waveguides of As_2S_3 (a chalcogenide glass discussed further in Chap. 5) have been deposited, and dry etched, on a substrate of $LiNbO_3$ to take advantage of the similar thermal expansion coefficients ($LiNbO_3 = 15 \times 10^6/°C$, $As_2S_3 = 21.4 \times 10^6/°C$, $SiO_2 = 5 \times 10^7/°C$) to aid in waveguide fabrication [142]. A loss of 0.33 dB/cm at a wavelength of 4.8 µm can be achieved in this way.

Plasma etched $LiNbO_3$, with a SiO_2 cladding, has achieved low loss, 0.4 dB/cm at 1550 nm. It has a minimum bend radius of 80 µm [143] making the platform competitive in the sense that compact designs can be made. However, the use of SiO_2 limits the wavelength range and an alternative cladding material will be required to move the technology into the MIR.

Proton exchange, where lithium ions are exchanged with hydrogen ions, is another high index contrast $LiNbO_3$ technology. It has been shown to have a low loss in the visible [144] and at 1550 nm [145] which should translate through to the MIR.

Low index contrast waveguides can also be fabricated in $LiNbO_3$ by titanium diffusion (Ti:$LiNbO_3$), creating an index contrast of 0.0136 [146] which allows for larger, single-mode waveguides. The cost for such a low index difference being a larger bend radius or suffer high bend losses.

The materials mentioned so far all use two-dimensional architecture: the glass has either been deposited on a substrate to form waveguides (as is the case for chemical vapour deposition) or layers have been deposited and etched (in a standard lithography process) leaving only waveguides. A three-dimensional architecture is when a waveguide is written inside the bulk material. An example of this is femtosecond writing in ZBLAN.

ZBLAN is made by heating the combination ZrF_4-BaF_2-LaF_3-AlF_3-NaF to a temperature on the order of 1000 K which is past the point at which each material forms a liquid. The melt is then cast into a block and slowly cooled [147]. The waveguides are laser inscribed into the bulk using a femtosecond laser [128, 148] which creates a localised refractive index change of 9×10^{-4} [149]. This is significantly smaller than for two-dimensional structures and requires photonic chips of much greater lengths, due to the increase of bend radius for negligible loss per bend, for similar photonic devices.

The transmission window of ZBLAN is limited to approximately 7 µm. To extend the transmission window to beyond 10 µm - a scientifically significant area for exoplanet detection as discussed in Sec. 1.3.2 - chalcogenide glass (ChG) may be the best option.

ChGs are glasses of sulphur, selenium or tellurium that have formed networks through covalent bonds with other (non-oxide) elements (generally in the III or IV group of the periodic table). As an example, As_2S_3 forms a predominantly 2-D network using the As-S bond [150] with some cross-linking to make a stable material. Rudolf Frerichs [151] was

the first to publish an investigation into a ChG for uses in infrared transmission, focusing on As_2S_3. His report followed from the Schultz-Sellack publication in 1870 that included a quantitative observation of As_2S_3's infrared transmission [152]. This material pushed beyond the transparency window of oxide glasses and into the infrared, and allowed glass to be made that was transparent in a regime typically dominated by oxide absorption [153]. The transmission spectra in Fig. 2.3 shows the throughput for each ChG generic species.

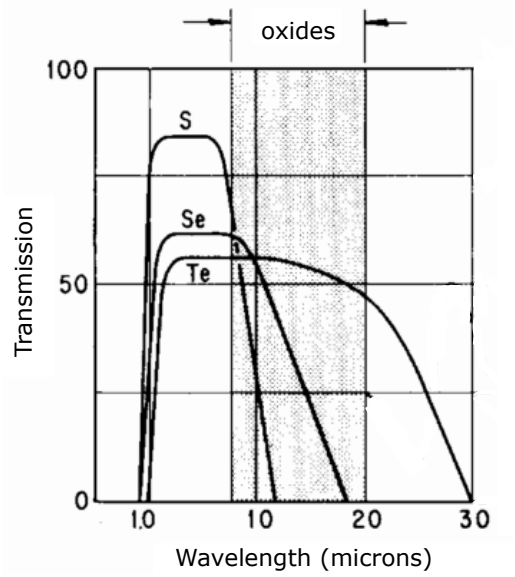

Figure 2.3: The transmission spectra of S, Se and Te in the infrared regime from [153]. The shaded region is dominated by oxide impurities.

ChGs too can use three-dimensional architecture, through the combination of gallium lanthanum sulphide (GLS) and femtosecond writing [154] at a similar refractive index change as ZBLAN and a loss of 0.25 dB/cm. ChG can also be deposited via evaporative deposition to create two-dimensional architecture with a refractive index difference on the order of 0.3 [155] with a loss down to 0.33 dB/cm [156]. This latter index provides a bend radius of approximately 200 µm for negligible loss and single-mode waveguides of approximately 1 µm (in the MIR), which is on the cusp of what can be fabricated for "low cost" equipment.

The final materials to be discussed here are indium phosphide (InP) and aluminium gallium arsenide (AlGaAs). InP has a transmission spectrum limited to 900 nm in the IR [169] but has been used for a variety of IR applications: in the construction of laser diodes [170] to multiplexers [171], with a plethora of technology that can be found in the review paper by Smit et al. [166]. What is lacking (to the author's best knowledge) is a low loss, single-mode waveguides in InP that would be useful for MIR interferometry. In comparison, AlGaAs has achieved low loss waveguides (of 0.45 dB/cm at 2.4 µm) using a suspended AlGaAs on Si platform [168]. In addition, an AlGaAs-on-insulator platform has displayed low loss but like the Si-on-insulator the waveguides are sub-micron in width and suffer from strong light fields in the waveguide-cladding interface [167]. Using the suspended AlGaAs platform a supercontinuum from 2.3 to 6.5 µm was generated [168]

Table 2.1: Transparent materials in the MIR.

Material	Transmission window (µm)	Material deposition	Waveguide fabrication	Reference
SOI	$2.9 - 3.7$	Bond and polish back	Plasma etching	[137]
SOS	$0.2 - 5$	Epitaxial growth	Plasma etching	[137][157]
SiGe/Si	$1.9 - 7$	Evaporation or Chemical vapour deposition		[137][158] [159]
ZBLAN	$0.2 - 7$	Melt and quench	Femptosecond writing	[147, 149]
$LiNbO_3$	$0.4 - 5$	Czochralski technique	Thermal in-diffusion Proton exchange	[146, 160, 161] [144]
ChG	$3 - 12$	Melt and quench or Physical vapour deposition	Femptosecond writing or Plasma etching	[154, 155, 162, 163] [156, 164, 165]
InP	< 0.9	Epitaxial growth	Plasma etching	[166]
AlGaAs	$1 - 6.5$	Epitaxial grown or Wafer bonding	Plasma etching	[167, 168]

showing that the infrared will be accessible with single-mode waveguides in the future, once surface roughness is reduced [167] or a low index contrast becomes available.

From Tab 2.1 only one glass has transmission past 10 µm - ChG - enabling this technology to be moved up to the 10 µm wavelength in future work. As was briefly mentioned in Chapter. 1 this region is used for detecting O_3 in potentially habitable worlds and to more easily image Earth-like exoplanets.

In addition, ChG has already produced single-mode waveguides in high index contrast materials [156] and low index contrast materials [154]. The loss of waveguides in both technologies has been measured below 0.3 dB/cm and so either option is justified for future work. The physical vapour deposition technology has been selected for this thesis as it can produce compact devices that can be extended without increasing the total length of the chip beyond a few centimetres. Additional background on ChG is included in Chap. 5.

2.1.1 Active mateirals and glasses

As mentioned above in the Kernel-Nuller example, active phase control is required for future space nulling interferometry missions. The selection of glass will influence how the phase is controlled: Using ChG, additional lithography will be required to add this functionality, compared to an active material like $LiNbO_3$ which already has this functionality.

$LiNbO_3$ uses the electro-optic effect to rapidly switch the refractive index (n) of a waveguide, of length (L), and, since the optical distance is $n \times L$, the phase of the waveguide can be altered rapidly.

However, to take advantage of the high index and low loss, physical vapour deposition ChG was selected for this work. The electro-optic effect requires the glass to be thermally

poled with up to 8 pm/V having been achieved in initial studies [172]. This process is beyond the scope of this thesis, without significant investment in time and money, and instead we will be using the thermal-optic effect - a more established process. These are similar in that they both produce index change whereas one uses an electric field and the other uses a change in temperature to change the index. A simple approach to selectively heating the waveguide is to add resisters alongside the waveguides. These act as heaters when a current is passed. This limits the speed at which the phase can change due to the time it takes for the resisters to heat and for the heat to penetrate through to the waveguide.

2.2 Nulling interferometers

Integrated Optics (IO) was proposed for interferometry in 1997 [127] utilising y-junctions for light splitting (and reverse y-junctions for beam combination). Figure 2.4 details the two beams combiner photonic chip described by Kern et al. [127] with equivalent IO for a four beam combiner, similar to the GRAVITY combiner in Fig. 2.1, that would provide six interferometry ports - one for each baseline - instead of the single baseline in Fig. 2.4. Another configuration of four ports was proposed by Angel & Woolf [83] as an addition to the work by Bracewell's two telescopes nulling interferometer [66].

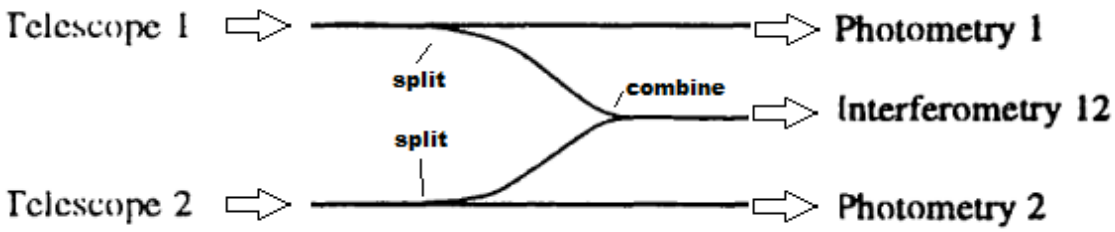

Figure 2.4: The first proposed two telescope combination IO chip [127], comprising of two y-junction splitters, to tap light into a photometry port, and one reverse y-junction combiner for the interferometry port.

The optical characterisation of the configuration in Fig. 2.4 was undertaken by Haguenauer et al. [173]. This type of interferometer was found to have a strong dependence on the combiner with an x-junction or MMI (also referred to as a multimode interferometer [173]) having a larger throughput than the chosen y-junction combiner. Using a y-junction, however, provides wavelength independence. This highlights the key issues with beam combination: transmission and bandwidth.

2.2.1 X- and Y-junction

An x- or y-junction, as the name suggests, is a combination of two waveguides with two or one output ports respectively, forming an 'x' or 'y' shape. An x-junction is shown in Fig. 2.5. Rather than a 3 dB coupler an x-junction is commonly used as a crossing

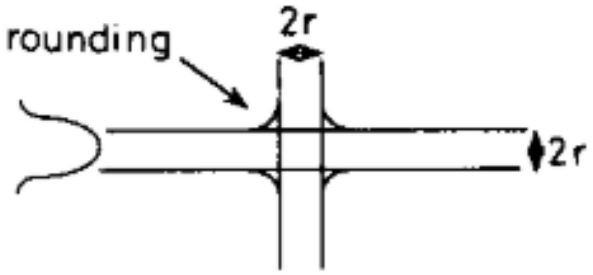

Figure 2.5: The x-junction from MacKenzie [174], indicating rounding at the waveguide junction.

point between two overlapping waveguides with minimal cross-talk. This occurs when the waveguides are at an angle of 90° [174]. At acute angles, however, cross-talk occurs [175] enabling the x-junction to be used as a combiner, or splitter, depending on the number of input launch fields. Loss in an x-junction comes from the rounding at the taper tips, as shown in Fig. 2.5. This leads to high uncertainty in the performance of the x-junction as a combiner because each iteration of the combiner could provide a different coupling ratio [176] due to this rounding.

The same fabrication uncertainty occurs in a y-junction. A reverse y-junction (two input ports and one output port) utilises the symmetric response of the y-junction (one input port and two output ports) to produce a broad bandwidth 50:50 splitting ratio [177]. By its design, any light rejected by the combiner (starlight for example) will scatter out of the device rather than diverted to an adjacent output port. This restriction will be limiting if this light is used for calibration (for example). The preferred combiner for nulling interferometry is the evanescent coupler as it has no corners that may make the coupler unreproducible.

2.2.2 Evanescent coupler

An evanescent coupler (often referred to as a directional coupler in the literature) has two waveguides in close proximity without touching. A directional coupler that has touching waveguides is referred to as a zero-gap coupler. A mode overlap between the two waveguides allows for a supermode to form, encapsulating the waveguides. The combination of the individual waveguide modes and the supermode creates a superposition that has the light "beating" from one waveguide to the other periodically. The evanescent coupler as a 3 dB splitter was successfully demonstrated in a four telescope configuration, inspired by Angel & Woolf [83], at a wavelength of 1550 nm, made with SiO_2 [178] and in the MIR (specifically at 3.7 µm) made with GLS [162]. The limitation of the directional coupler is the tolerance to the spacing between the waveguides, the sensitivity of which is subject to the materials used but may prevent an equal splitting.

As waveguide losses as low as 0.25 dB/cm [179] have been demonstrated in GLS, in the MIR, it becomes a promising material for astronomical applications, in particular nulling interferometry. The few nulling interferometers made in GLS have been tested,

to the author's best knowledge, as 3 dB couplers only. A coupling ratio from 30:70 to 70:30 has been demonstrated for bandwidth over 500 nm [162]. Producing a coupler with a constant ratio, without a 1% deviation, over a large bandwidth in the MIR, to the author's knowledge, has yet to be published. This is an important step for a beam coupler to achieve as it determines the amount of starlight that can be removed from an image. There is no fundamental limit of the directional coupler as demonstrated in ZBLAN: with a waveguide loss of 0.2 dB/cm, a 75:25±6% splitting ratio over 500 nm [149] was achieved using an evanescent coupler. This still did not produce a 1% deviation but it is the first step in creating an evanescent coupler that can.

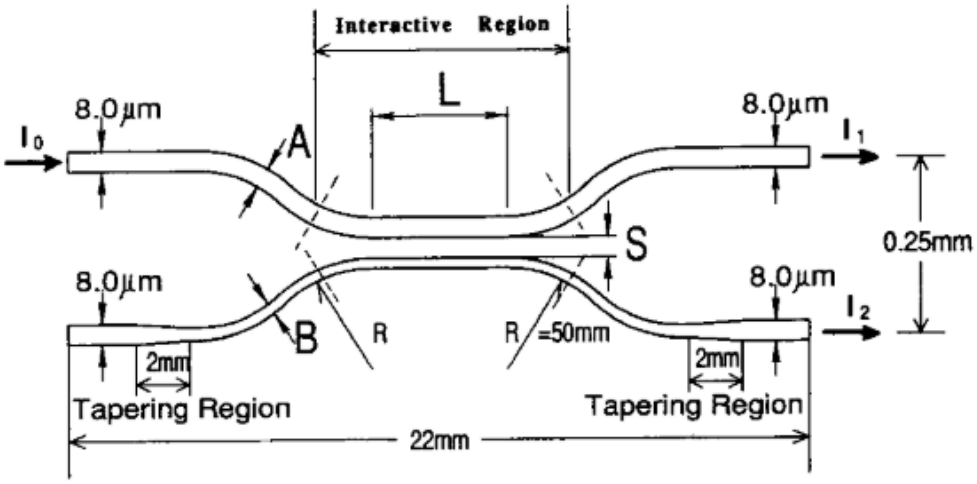

Figure 2.6: A tapered velocity coupler from Takagi [180] (Fig.3): a directional coupler that has one arm's width (B) reduced (from a width of A) to alter that waveguide's propagation constant during the interaction region, where the waveguides are spaced (S) apart for the required duration (L).

Producing an achromatic response for directional couplers is well documented in the literature. A few examples are included here. A tapered velocity coupler is shown in Fig. 2.6 which changes the waveguide's width [180] in the coupling length portion of the directional coupler, which in turn varies the modes in each waveguide as a function of position. This method is not limited to width but height too [181]. The super-mode that connects the two waveguides (similar to a higher-order mode that would have existed had the two waveguides been split from a single waveguide) interferes with the waveguides' fundamental mode, giving an oscillating effect between the waveguides [181]. This was used to control the power splitting of the coupler and allows an arbitrary choice of power splitting ratio with a specific choice of tapering [182]. Asymmetric directional couplers [180] use a difference in width (or a difference of refractive index) between the two waveguides of the directional coupler to control the coupling ratio. This is achieved by explicitly setting the propagation constants of the two waveguides to not be equal and setting the coupling ratio small so that the light coupling between the waveguides is suppressed. A 50:50±5 split has been achieved in SiO_2 (specifically SiO_2 - TiO_2 clad in SiO_2 deposited via flame hydrolysis [183]) between $1.3 - 1.55\,\mu m$ [184]. A three coupled waveguide [185] can also

be used, where an additional fixed-width waveguide is placed between the waveguides in a typical symmetric directional coupler. This acts as a tapered velocity coupler to control the power split.

With all of these designs, the result is a similar achromatic coupler that could be used as a beam combiner in a nulling interferometry system. Where these systems fail is in their tolerance to typical fabrication errors: a slight change in width will drastically alter the splitting ratio of the directional coupler and its broad bandwidth response [180].

For nulling interferometry specific projects, a recent type of asymmetric directional coupler (where the bend into the coupling junction of the two waveguides is non-symmetric) has been manufactured in GLS with a 50:50±3% coupling ratio over a 250 nm bandwidth [186]. In this thesis an MMI will be added alongside the direct coupler, also made in ChG but of different material composition, as a potential 3 dB coupler for nulling interferometry applications.

2.2.3 Multimode interference coupler

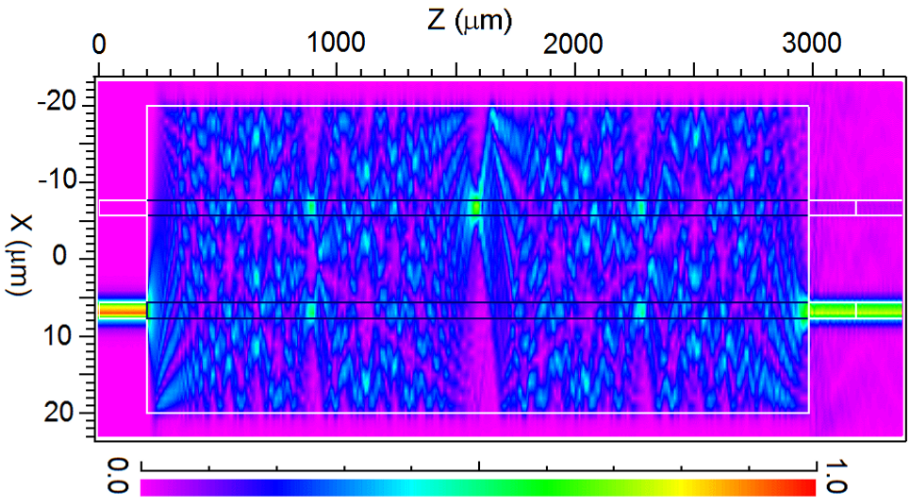

Figure 2.7: An MMI simulation using the beam propagation software RSoft BeamPROP [187]. The black lines inside the MMI cavity are for simulation purposes only.

An MMI is the final coupler to be discussed. A simulated MMI is shown in Fig. 2.7 which splits light by having multiple modes undergoing constructive and destructive interference [176]. Figure 2.7 shows that the light periodically forms localised points of intensity. From the input point, the original image diffracts and interacts with itself through the cavity and forms into two intensity points (at 1/4L where L is the total length of the cavity), one reflected intensity point (at 1/2L), two intensity points again (at 3/4L), and a final recreation of the original image (at L). It is by calculating the position of these splits (governed by the Talbot length [77, 188]) that the MMI can be made into a 3 dB coupler (or any NxM coupler for that matter).

The advantage of an MMI over the directional coupler is that it is highly tolerant of fabrication errors [125]. In addition, there are no sharp edges critical to the design, like

the point of contact in a y- and x-junction, that limit the confidence in the fabrication process [176]. That is not to say that the MMI doesn't contain any sharp corners: the rectangular MMI cavity becomes rounded in standard fabrication as does the interface between the waveguide and this cavity. This limitation is one of resolution but the performance of the MMI is robust to this error. A precursor to the work of this thesis [164] showed that for two competing 3 dB couplers, an MMI and a symmetric directional coupler, the MMI had a coupling ratio closer to 50:50, over a $1.5-1.6\,\mu m$ bandwidth, but the directional coupler had less total loss. An increase in the MMI bandwidth was explored by Maese-Novo [189] using subwavelength gratings inside the MMI cavity with a subsequent broad bandwidth response experimentally verified [190]. Whether this method is fabricationally robust has yet to be experimentally quantified. Using the standard MMI as a broad bandwidth coupler to the author's best knowledge, especially in the infrared regime, has yet to be fully investigated.

2.3 Summary

A choice of using ChG to fabricate the interferometer is one that allows for light transmission past the 10 µm wavelength where ozone could be detected in an exoplanet's atmosphere. The wavelength considered for this work is 4 µm. This is to take advantage of the transmission window in Earth's atmosphere if this technology was to be used on existing telescopes. Future work, that focuses in the 10 µm wavelength regime will benefit from this work with components designed in Chap. 4 and 7 but due to the previous technology showing promising results at 4 µm this work too focuses on the 4 µm regime.

The ChG selected is one shown in previous work to deposit at the same index as the bulk glass. It has no electro-optical properties and will need heaters placed over the waveguide to actively change the phase of the light, via the thermal-optical effect, for use in a large device like VIKiNG.

The selected 3 dB coupler for this work is an MMI, chosen because it is tolerant to standard lithographic errors. An MMI compared to other couplers, like a directional coupler, will always have a higher loss (assuming bother are made perfectly) over a broad bandwidth. Its fabrication tolerance to standard lithographic errors may, however, give it an advantage. For this work, a total loss - insertion loss, coupler loss, waveguide loss - of 3 dB was used as a metric for success (over the entire L' band).

The purpose of this work is to analyse the MMI's ability to split light evenly. Explicitly, to confirm the splitting ratio of the MMI is robust to fabrication tolerances. This will first allow the extinction depth to be calculated and verified before the MMI itself can be assessed as a two-port beam combiner for nulling interferometry.

The design parameters, and the analysis of transmission and splitting ratio, of the MMI, are investigated in Chap. 3 with detail given to the length and width selection. The wavelength dependence is left to Chap. 4 where improvements on the design are explored.

Chapter 3

Multimode interference coupler

This chapter includes work already published:

Kenchington Goldsmith, H.-D., Cvetojevic, N., Ireland, M., and Madden, S., "Fabrication tolerant chalcogenide mid-infrared multimode interference coupler design with applications for Bracewell nulling interferometry," *Optics Express* **25**(4), 3038 (2017).

A multimode interference coupler (MMI), sometimes referred to as a multi-mode interferometer in the literature, is a photonic device that excites multiple modes, typically > 10, in a wide waveguide segment, referred to as the MMI cavity. Light launched into such a cavity undergoes self-interference, combining constructively and destructively, such that at particular lengths the light forms a series of localised intensity maxima that can then be segregated into multiple output waveguides. Hence an MMI can be used as a splitting device. The fundamental principles determining the nature of the splittings are related to experiments undertaken by Talbot [188]: the localised intensity maxima being the Talbot images and the combination within the cavity akin to the Talbot carpet. These experiments were conducted using white light (from the sun) passed through a diffraction grating and illustrate the wavelength dependence of this self-interference effect. It is only by extension, and further research, that these experiments have been related to an MMI.

3.1 Talbot Imaging

As initially described by Talbot [188] light incident on a grating exhibits a fundamental self-interference such that multiple regions of localised intensity maxima form at specific positions in the direction of the beam propagation. This was described in Talbot's paper as "white light split into lines of alternating colours (magnified with a lens for visibility)". These colours would oscillate into focus as the lens moved towards and away from the grating:

> The appearance was very curious, being a regular alternation of numerous lines or bands of red and green colour, having their direction parallel to the lines of the grating. On removing the lens a little further from the grating, the bands gradually changed their colours and became alternately blue and yellow. When the lens was a little more removed, the bands again became red and green. And this change continued to take place an indefinite number of

times, as the distance between the lens and grating increased.

In 1881 it was determined that the position of the colours' foci follows the simple pattern of

$$L = a^2/\lambda$$

where a is the pitch of the grating and λ is the wavelength of the light [191], and L is known as the Talbot length.

This interference can be described using a pinhole array, represented schematically in Fig. 3.1 by Bryngdahl [192] in 1973. The figure shows that light, after interacting with the pinhole array, has well-defined regions of intensity maxima that are evenly spaced in the x-axis direction.

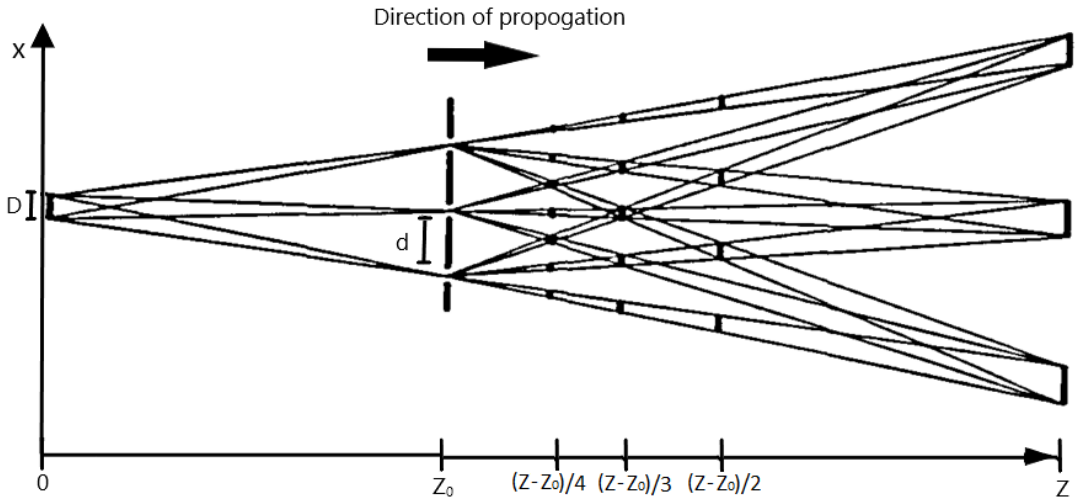

Figure 3.1: Fresnel images for self-imaging as illustrated by Bryngdahl [192].

The theory behind Fig. 3.1 shows that if an emitting object (of size D) is incident on an array of pinholes (with a spacing of d) then it will create light and dark fringes as a consequence of Fresnel diffraction [192]. From Fig. 3.1 with three pinholes, identical representations of the initial image at D appear at position Z, this being termed a Fourier image. There are also fringe patterns at $(Z - Z_0)/2$ for four localised intensity maxima, then five and six closer into the pinhole array. These are referred to as Fresnel images, representations of the initial image D with a $1/N$ reduction in size, where N is the number of local intensity maxima between iterations of the Fourier image. Assuming a 2D grid of square pinholes the position of these local maxima is calculated using

$$\frac{1}{Z_0} + \frac{1}{Z} = \frac{2\lambda}{3(\eta + N/m)d^2}$$

with η (the iteration of the Fourier image) as an integer and m being the repeat occurrence number of that particular N, where m and N are integers such that they have no common factors [192]. The Talbot effect is not limited to free-space optics and the same effect would occur in an optical fibre or graded refractive index film [192]. The equation would

now introduce a refractive index term (n) becoming

$$Z = \frac{2mnd^2}{N\lambda} \tag{3.1}$$

where d is now the size of the cross-section and η has been replaced entirely with N/m [176]. As an example of how light would propagate under self-interference, a single localised intensity maxima or Fourier image, $N = 1$, is obtained at every m interval ($m = 1, 2, 3, ...$) whist two local intensity maxima or Fresnel images, $N = 2$, are only at odd values of m ($m = 1, 3, 5, ...$); whereas three Fresnel images, $N = 3$, only occur at values of N not divisible by 3 ($m = 1, 2, 4, 5, ...$); and so on and so forth.

An MMI exploits the Talbot effect as discussed above in a structure that allows for more than the fundamental mode to be excited in the slab (as specified above, > 10 modes is standard). It uses self-interference inside a finite domain with reflective boundaries rather than simply allowing the light to evolve in free space as in Fig. 3.1 and hence follows eq. (3.1). A MxN MMI splits light from M (not the same m as before) input ports into N output ports (the same N as before). For simplicity the number of output ports is hereafter set to the number of localised intensity maxima and, unless otherwise specified, only one input port (of M ports to select from) of the MMI is illuminated at any one time (i.e. a splitter configuration rather than a beam combiner).

3.2 MMI theory

Figure 3.2: The base 2x2 MMI used in this these, complete with tapers (of width W_a and length L_a), taper positions of $\pm x_c$ and cavity width (W) and cavity length (L).

A 2x2 MMI is shown in Fig. 3.2. With an electric field launched into one port, this MMI can be used to split light evenly with minimal loss. Equal splitting, at a single wavelength, for now, requires the light to propagate through the MMI such that Talbot style self-imaging produces two localised intensity maxima at the output. The theory of light propagation in an MMI is described in Refs. [176, 193, 194, 195] and summarised here using an approximate two-dimensional analytical model (using the MMI slab width in the x direction, wave propagation along the z axis and neglecting the y axis representing

the height).

Figure 3.3 shows the MMI cavity with individual mode fields that are excited in the cavity represented as sine waves. Note that these fields extend beyond the walls of the cavity to an effective width (W_e) - calculated below - determined by the width of the fundamental mode. The position of the input ports into the MMI is at $\pm W_e/6$ which is vital for the restricted interference MMI that will be used in the work. More information is provided in Sec. 3.2.2.

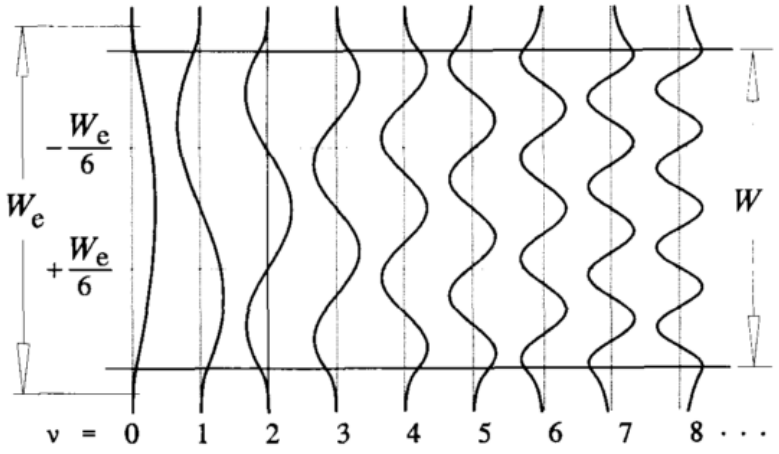

Figure 3.3: An MMI schematic, from Ref. [176], illustrating the modes excited in the slab. Each are approximated as a sinusoid [196] with an exponential decay at the boundary.

The wavefront (Ψ) at the start of the MMI cavity ($z = 0$) is equal to the excitation field:

$$\Psi(x,0) = \sum_{\nu=0}^{\nu_{\max}-1} c_\nu \psi_\nu(x), \tag{3.2}$$

expressed as the sum over all modes (ν) supported by the cavity for each mode fields (ψ_ν), illustrated in Fig. 3.3, multiplied by their respective excitation coefficients (c_ν):

$$c_\nu = \frac{\int \Psi(x,0)\psi_\nu(x)dx}{\sqrt{\int \psi_\nu^2(x)dx}} \tag{3.3}$$

The cut off for a mode to exist in the MMI slab is determined by the angle of incidence is less than the critical angle for total internal reflection. A simple estimation for what modes are excited in the slab uses the "V number" for the set wavelength (λ), the two refractive indices, core (n_{core}) and cladding (n_{cladding}), and slab width (W):

$$V = \frac{2\pi}{\lambda} W \sqrt{n_{\text{core}}^2 - n_{\text{cladding}}^2} \tag{3.4}$$

such that $V > \nu\pi$ [197] must be satisfied for a mode to propagate in the slab [198]. Note here that the term *mode* is agnostic to transverse electric (TE) and transverse magnetic (TM) modes. This is because for symmetric waveguides (clad with the same index on both sides and hence no birefringence) the cut off for TE and TM is the same.

The superposition of the excited modes fluctuates as the light travels through the MMI cavity, hence the length dependency of Ψ. Using the model discussed below the wavefront as it passes through the slab is shown in Fig. 3.4.

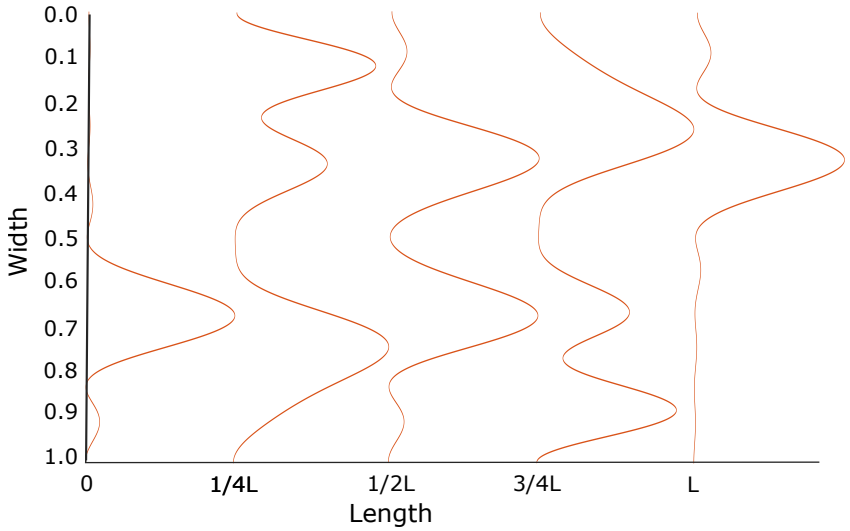

Figure 3.4: An MMI schematic showing the wavefront intensity at various points along the MMI slab of length L, where L satisfies the condition $\Psi(x, L) = -\Psi(x, 0)$. For the paired interference case, described in Sec. 3.2.2, L is equal to the beat length, described in eq. (3.8). The modes used in this calculation are limited to four, each being illustrated in Fig. 3.3, as to be agnostic to W which was normalised in these calculations.

The schematic in Fig. 3.4 shows the evolution of the wavefront with the position. At $L = 0$ the launch field is shown as a single peak with a symmetrical wavefront produced at $L = L$. A 50:50 split occurs at $L = 1/2L$, whereas the quarter splits show no structure due to the mode limitations placed on the model. Further investigation into the mode contributions on Ψ in the MMI slab is contained in Chap. 4 but only in terms of increasing the bandwidth response.

The model in Fig. 3.4 used a sinusoidal approximation of the launch field into the MMI (i.e. ψ_ν for eq. (3.2) were set as sinusoids). For simplicity, an approximation was also made that the modes are contained to a width of W (normalised to $W = 1$ for the model). The validity of the latter approximation is investigated here.

For high index contrast waveguides, the field is essentially confined to the core region. Note that this approximation was not used in Fig. 3.3 but it will be used in all future figures. This means that the mode fields can be represented as harmonic functions with zero values at the cavity boundaries. To illustrate this as a reasonable approximation, consider the equation for the fundamental mode width, from the solution to Maxwell's equations:

$$W_e = W + \frac{\lambda}{\pi}\left(\frac{n_{\text{cladding}}}{n_{\text{core}}}\right)^{2\sigma}(n_{\text{core}}^2 - n_{\text{cladding}}^2)^{-1/2} \tag{3.5}$$

where $\sigma = 1$ for TM and 0 for TE. This is derived from the shift in light interacting with a prism at a critical angle, from Goos [199], between TE and TM light, with the equivalent

for a slab waveguide at any incident angle, as described by Kapany & Burk [200] (see their equation 3.130, where the effective geometrical thickness of the waveguide is increased depending on the polarisation).

The equation indicates that the effective width of the MMI (W_e), compared to the fabricated width of the MMI (W), is different for TM and TE modes. Using the refractive index values n_{core} and n_{cladding} in this work (2.609 and 2.279 respectively at a wavelength of 4 µm [156]) the difference between the fabricated W and the W_e is as follows:

$$W_e - W = \frac{4}{\pi}\left(\frac{2.279}{2.609}\right)^{2\sigma}(2.609^2 - 2.279^2)^{-1/2}$$

$$\Delta W = 0.76\,\mu\text{m for TM and } 1.00\,\mu\text{m for TE.}$$

Thus for a W of 45 µm the TM width is 44.24 µm and the TE width is 44 µm, making a width difference between TE and TM width of 0.24 µm (0.55%). This change in W_e to actual width is small but potentially not insignificant. The width dependence of an MMI for both TE and TM will need to be checked in simulation to be sure light behaves similar, or similar enough, for the intended experiments (see Sec. 3.4).

3.2.1 General MMI relations

The wavefront propagation, used for Fig. 3.4, is calculated as the prorogation of eq. (3.2). It is the phase propagation constants, which is zero in eq. (3.2), for each mode that causes the wavefront to change. The mode phase factor is a complex number: $\exp(i(\omega t - \beta_\nu L))$ with the variables of angular frequency (ω), time (t), propagation constant (β_ν) at any length L. Rather than dealing with a problem that has a time variable, the standard convention is to work in terms of length. This is achieved by assuming the time dependence is implicit and using the dispersion equation derived from a step-index slab waveguide [194]:

$$\left(\frac{(\nu+1)\pi}{W_e}\right)^2 + \beta_\nu^2 = \left(\frac{2\pi n_{\text{core}}}{\lambda}\right)^2$$

with n_{core}, W_e and λ as before. Using the binomial expansion, the propagation constant is expressed as:

$$\beta_\nu = \frac{2\pi n_{\text{core}}}{\lambda} - \frac{\pi\lambda(\nu+1)^2}{4n_{\text{core}}W_e^2}. \tag{3.6}$$

An additional length term is utilised to remove the propagation constant from the phase factor, known as the beat length (L_π). This term is defined as the distance for the first two modes to acquire a π phase difference (following the nomenclature of power exchange from one port to the other in a standard directional coupler) [176]:

$$L_\pi \triangleq \frac{\pi}{\beta_0 - \beta_1}. \tag{3.7}$$

Note that, from eq. (3.6),

$$\begin{aligned}\beta_0 - \beta_\nu &= \left(\frac{2\pi n_{\text{core}}}{\lambda} - \frac{\pi\lambda}{4n_{\text{core}}W_e^2}\right) - \left(\frac{2\pi n_{\text{core}}}{\lambda} - \frac{\pi(\nu+1)^2\lambda}{4n_{\text{core}}W_e^2}\right) \\ &= \frac{\pi\nu(\nu+2)\lambda}{4n_{\text{core}}W_e^2}.\end{aligned}$$

Which is then used to change eq. (3.7) to be in terms of n_{core}, λ and W_e:

$$L_\pi = \frac{4n_{\text{core}}W_e^2}{3\lambda} \tag{3.8}$$

which is similar to eq. (3.1) for the Talbot length in a fibre.

Using eq. (3.8), Ψ can be expressed in terms of L, instead of t, at $z = L$:

$$\Psi(x, L) = \sum_{\nu=0}^{t-1} c_\nu \psi_\nu(x) \exp\left[i\frac{\nu(\nu+2)\pi}{3L_\pi}L\right]. \tag{3.9}$$

This equation allows for the wavefront to be investigated at any arbitrary MMI length to determine the relation between L and localised intensity maxima formation. For example, Fourier images are formed when the condition $\Psi(x, 0) = \Psi(x, L)$ is satisfied.

An example simulation is shown in Fig. 3.5. It shows the equivalent beam propagation, using RSoft BeamPROP (a 3-D modelling software of beam propagation, see Sec. 3.3.1 for more details), similar to Fig. 3.4 but without the restriction of modes and twice the length. Note that $\Psi(x, 0) = -\Psi(x, L_\pi) = \Psi(x, 2L_\pi)$. This relation is explained in the forthcoming equations.

The MMI's input (and output) waveguide position, along the x direction in Fig. 3.5, is crucial (details to why are contained in Sec. 3.2.2).

To calculate the relationship between the localised intensity maxima and the length of the MMI consider that to have the input wavefunction repeated at $\Psi(x, L)$, that is to say

$$\sum c_\nu \psi_\nu \exp\left[i\frac{\nu(\nu+2)\pi}{3L_\pi}L\right] = \sum c_\nu \psi_\nu, \tag{3.10}$$

the phase factor must fulfil the criteria

$$\exp\left[i\frac{\nu(\nu+2)\pi}{3L_\pi}L\right] = 1 \text{ or } (-1)^\nu \tag{3.11}$$

for all values of ν. For positive solutions to eq. (3.11) a direct replica is produced, whereas negative solutions represent the case where the Fourier image is reflected about the x axis. The reason for the $(-1)^\nu$ in eq. (3.11) is to represent that the reflective and replica images repeat, in intervals of π: the positive solutions of eq. (3.11) occurring at $2n\pi$ and the negative solutions at $(2n+1)\pi$, leading to the solution to eq. (3.11):

$$L = m(3L_\pi) \tag{3.12}$$

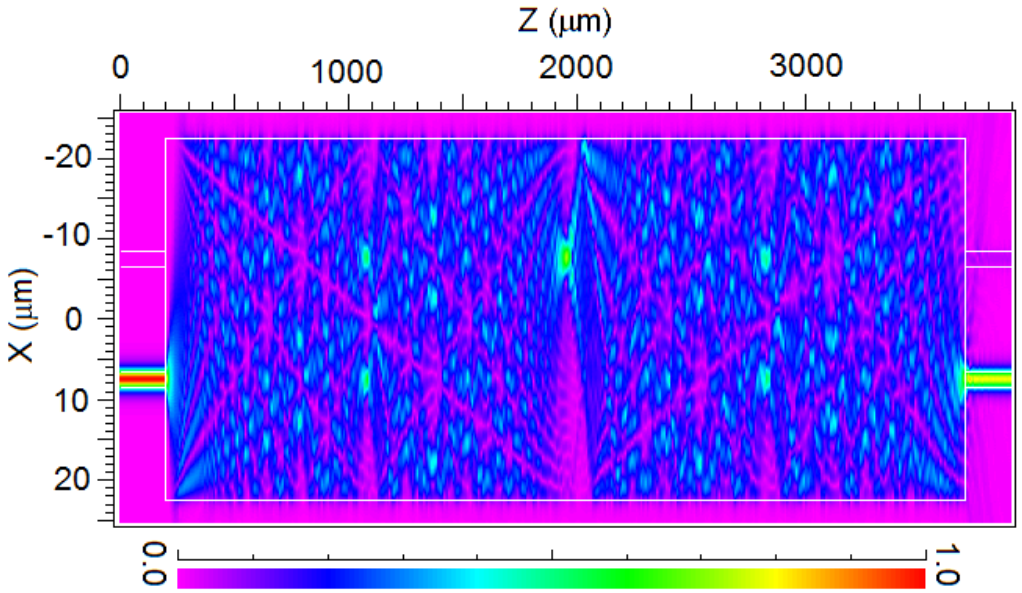

Figure 3.5: A reproduction of Fig 2.7: a 2x2 MMI undergoing paired interference (see Sec. 3.2.2) generated using Rsoft BeamPROP for two beat lengths (i.e. $2L_\pi$). Notice the parallels to Fig. 3.4 for $L = 0, 0.5L_\pi, L_\pi$ (where $L_\pi = 1750\,\mu\text{m}$ or Z= 1950 µm). The difference at $0.25L_\pi$ and $0.75L_\pi$ are due to the four mode restriction to recreate the wavefront in Fig. 3.4.

for even and odd values of m respectively.

An extension of the relationship is to include N replicas of the input wavefunction at a reduced intensity ($1/N$ of the initial wavefunction intensity) at various positions L in the length direction of the MMI and evenly spaced along the width W - similar to the Fresnel images in the Talbot effect. For N images the relation

$$L = \frac{m}{N}(3L_\pi) \tag{3.13}$$

is used and follows the same principle of even and odd images, for m and N with no common factors.

Understanding these relations provides us with tools to create any MxN MMI. This includes polarisation splitters, from eq. (3.5); multiplexers, from eq. (3.12); and 3 dB splitters, from eq. (3.13). For the latter, only one input port is required and two if it is also used as a combiner, and as such, can take advantage of special cases of the MMI.

3.2.2 Special cases

There are two special cases in MMI design that exhibit so-called restricted interference. The special cases are referred to as paired interference and symmetric interference. The idea is that under certain, curtailed, geometric conditions the position of Fourier images, as calculated by eq. (3.13), appear closer: at length L_π rather than $3L_\pi$ for paired interference and $3/4L_\pi$ for symmetric interference, with Fresnel images benefiting from the reduction in length as well.

Consider eq. (3.11), and the periodicity of the exponential term. The equation indicates that to produce a Fourier image ($\Psi(x,0) = \Psi(x,L)$) the exponential must be either 1 or -1. By eq. (3.13) this occurs for $L = 3L_\pi$ because $\nu(\nu+2)$ is an integer. For $L = L_\pi$ however this is not the case and for $\nu = 2, 5, 8, ...$ the exponential term is $= \pm 0.5$ but for all other ν the term is $= \pm 1$. The implication here is that if $c_{\nu=2,5,8,...} = 0$ then $\Psi(x,0) = \Psi(x,L) = 0$ for $\nu = 2, 5, 8, ...$, effectively disregarding the exponential term for these ν, and thus provides a Fourier image at L=L_π. The mathematical verification of this "Restricted Multimode Resonance" is contained in appendix A of Ref. [176].

One method of stifling the excitation of the modes $\nu = 2, 5, 8, ...$ is to launch an even symmetric field into the cavity from waveguides placed at $x_c = \pm W/6$ (only being applicable for two input waveguides, hence the term paired interference) from the centre of the MMI ($x_c = W/3$ or $x_c = 2W/3$ from the corner) [194]. This configuration is highly advantageous for a 3 dB splitter as it reduces the MMI length and increases the fabrication tolerance [196]. Quick verification of this is to show that the variance of the MMI:

$$\frac{|\partial\lambda|}{\lambda_{\text{opt}}} = 2\frac{|\partial W|}{W}\frac{|\partial L|}{L}$$

has a length dependence and hence achieving the same result at a reduced length decreases the variance [125].

This reduction in length is extendable to Fresnel images too and changes eq. (3.13) to

$$L = \frac{m}{N}L_\pi. \tag{3.14}$$

Symmetric interference is like paired interference and similarly reduces the length of the MMI, but by a quarter [201], by utilising the relation:

$$\text{mod}_4[\nu(\nu+2)] = 0 \text{ for even } \nu$$

in the exponential term of eq. (3.11). To achieve the symmetric interference, by forcing $c_\nu = 0$ for all odd ν, the input wavefunction is placed in the middle of the MMI which limits the number of input waveguides to one [194]. For interferometry, additional inputs are required, by definition, and symmetric interference will not be applicable for this section of the project but may be useful in future work when constructing tap-couplers which can be used to maintain an equal intensity entering the beam combiner.

This model provides a physical understanding of how an MMI works and the ability to probe different parameters to see if they radically change the MMI's performance - both in terms of transmission and also as a 3 dB coupler over a wide bandwidth. This is utilised in Chap. 4 to investigate how suppressing specific modes - similar to how the restricted and symmetric interference designs suppress modes - can increases the 3 dB splitting response of an MMI over a wide bandwidth.

3.3 The nominal design

Selecting an MMI that fulfils the requirement for restricted interference (selecting a taper position of $x_c = \pm W/6$) simultaneously reduces the MMI length and increases the fabrication tolerance [125, 196]. The W (and by extension L) of the MMI is still a free variable and the question arises as to how to maximise transmission, whilst maintaining an accurate power split and high fabrication tolerance.

As discussed in Chap. 2, the extinction levels and bandwidth over which they are maintained are demanding for stellar interferometry to reduce starlight and measure the light emitted from an exoplanet. It is, therefore, crucial to creating a device design that is robust to typical fabrication process variations whilst achieving the required performance. Discussed later in Sec. 3.4, the applicable variables for the MMI from eq. (3.8) are the L, W_e (approximated as W for initial calculations of L) and n_{core}. The wavelength in eq. (3.8) is not a variable from a fabrication standpoint. Changing any one of these variables will change the wavefront within the MMI resulting in the two localised intensity maxima not forming at the desired position. For the dimensional variables, L and W, a fabrication tolerance of $\pm 0.1\,\mu\text{m}$ is expected from the lithography and mask making processes used in-house, and for the refractive index, a difference of ± 0.005 is the maximum observed from the evaporative deposition process used at the Laser Physics Centre (at the Australian National University).

3.3.1 RSoft: modelling software

In this thesis, software from Synopsys, Inc., Optical Solutions Group [187]: RSoft, was exclusively used to design photonic devices in various geometries before manufacturing. RSoft is at the centre of what Synopsys, Inc. provides, with the base program the Component Design Suite (CAD) and many modules stemming from it. From here the inbuilt modules can be used to simulate light modes and the propagation of light in a constructed 2-D or 3-D photonic device. The CAD allows users, through a graphical user interface, to set the materials of the photonic device, design the photonic structural geometry, set the initial variables of the simulation (like launch fields, boundary conditions and a limited ability to restrict what modes can be excited in the device) before using a modular simulation engine that is linked directly to the base software to run a simulation.

Each simulation module is compatible with the others, allowing the output of one simulation to be the input of another. For example, using the finite element simulation (FemSIM) module the fundamental modes of a waveguide can be simulated and in a subsequent simulation, a mode from that simulation can be launched into a photonic chip (it does not need to be of the same geometry) with the propagation of the mode intensity tracked through a larger photonic structure (in the beam propagation or BeamPROP module). In this thesis, FemSIM and BeamPROP are used to calculate modes in a 2-D cross-section at any point in our photonic chip geometry and simulate the propagation of light in various photonic chip geometries, either using light calculated through FemSIM

or via the BeamPROP software module itself.

The FemSIM module uses a finite element method to calculate modes in a 2-D cross-section. This is not limited to modes propagated in a waveguide structure but also leaky modes such as substrate radiation mode coupling and radiation from bends. Using a non-uniform and irregular mesh allows for structure with small features to be used and is highly effective when simulating the modes in a hybrid structure or a geometry with many leaky modes. It operates in a full vector model suitable for high index contrast devices, as simulated in this work.

BeamPROP is a finite difference 3-D beam propagation (BPM) software module. It is used to simulate how light propagates through structures that vary in the propagation direction incorporating full vector effects to accurately model high index contrast devices including modal coupling and structure induced cross polarisation coupling effects. In combination with the CAD interface, it also provides a visual aid as to how modes propagate in the geometry.

In addition to FemSIM and BeamPROP a MultiPhysics engine can be utilised to incorporate electro-, thermo-, and stress-optic effects in the model. This is used in Chap. 7 to modulate the optical path length between waveguides to induce phase change before being input into an MMI, applications of which are for "on-chip" phase modulators.

3.3.2 Modelling the MMI

These simulations require an initial wavefront to launch into the input waveguide. To produce a launch field RSoft FemSIM was used to create a 2D field for both the TE and TM fields. In the event where the waveguide dimension, refractive index or wavelength changed via an iterative simulation the inbuilt computed launch field in BeamPROP itself was used instead. For simulations that did not require a computed launch field the FemSIM calculation was used to reduce simulation time and avoid any fatal errors that occurred from BeamPROP caused by non-convergence of the launch field computation which would immediately halt a lengthy automated parameter sweep.

From Sec. 3.2 the special case of the 2x2 MMI was emphasised to reduce the length of the MMI to $1/2L_\pi$ (for two localised intensity maxima), the reduction in length is advantageous in terms of size, loss, tolerances and stability.

The W is a key factor as, from eq. (3.8), W and L are linked by a quadratic relationship. Thus each W should have a single optimum L, both in the theoretical sense of eq. (3.8), but also in terms of the important measurable attributes, i.e transmission (the ratio of total light output compared to the original input) and the accuracy of the 3 dB splitting, often referred to as the imbalance, calculated in this work using

$$\text{Imbalance} = \frac{\mathrm{P}_{\text{cross}} - \mathrm{P}_{\text{bar}}}{\mathrm{P}_{\text{cross}} + \mathrm{P}_{\text{bar}}} \tag{3.15}$$

where the cross port is the diagonal port from the input, the bar port is directly opposite the input and P is the power in the port. The optimum imbalance is zero.

The extinction is similarly calculated from the output ports:

$$\text{Extinction} = -10\log_{10}\frac{\mathrm{P}_{\text{cross}}}{\mathrm{P}_{\text{bar}}} \tag{3.16}$$

and when referring to a 3 dB coupler this term is the unbalance [125]. For this work, the extinction is used when discussing the MMI as a beam combiner and the imbalance used when discussing the MMI as a 3 dB splitter. Since the result of this work is to create a nulling interferometer and this section's focus is the imbalance it is best to provide context for the imbalance numbers.

Figure 3.6 compares the imbalance expressed in coupler percentage terms (an imbalance of 2% means that the coupling ratio of the MMI is 49:51 or 51:49) against the predicted extinction for the same MMI used as a two telescope beam combiner, phase matched for optimal extinction.

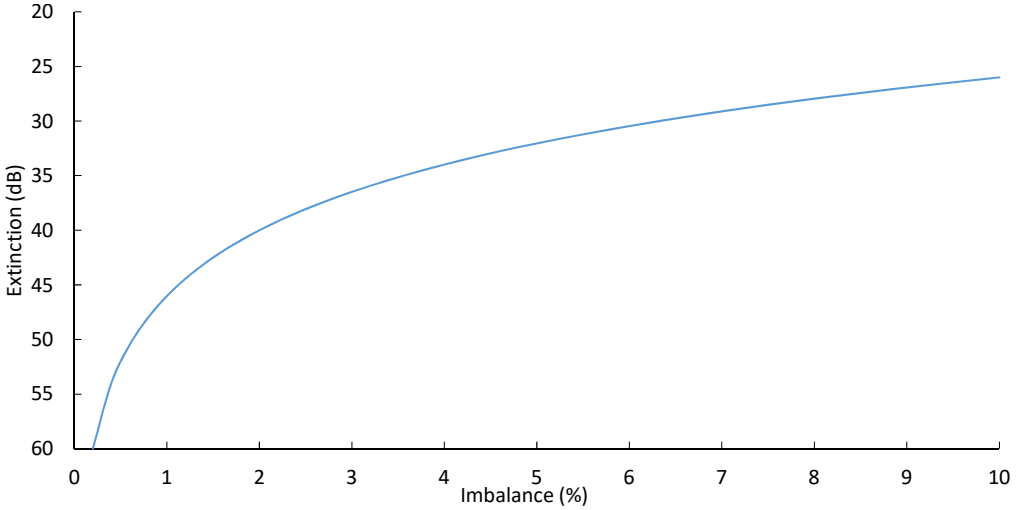

Figure 3.6: The implied extinction for a measured imbalance, both derived from the coupling matrix in eq. (3.18), for coupling coefificients [0.49:0.5) and the phase difference between input waveguides set to 90° (for the extinction measurements). The line is approximated as the power formula Extinction (dB) = $45.67 \times \text{Imbalance}(\%)^{-0.23}$ for convenience. For a quick reference from imbalance to extinction use: 0.2% = 60 dB, 0.65% = 50 dB, 2% = 40 dB, 6.3% = 30 dB.

To calculate the relationship in Fig. 3.6 begin with the unitary matrix:

$$\mathbf{U} = \exp\left(\frac{i\phi}{2}\right)\begin{bmatrix}\cos(\theta)\exp(i(Z_+)) & \sin(\theta)\exp(i(Z_-))\\ -\sin(\theta)\exp(-i(Z_-)) & \cos(\theta)\exp(-i(Z_+))\end{bmatrix} \tag{3.17}$$

where $\cos\theta$ is the coupling coefficient of the MMI and $Z_\pm$ are phase parameters that of the matrix that, like the coupling coefficients, are unique to the MMI. *phi* here is purely a rotation of the electric field and is cancelled out on transitioning into the measured intensity of the MMI.

The coupling matrix for a generic input of $[I_1, I_2]$ is defined as such:

$$U\begin{bmatrix} I_1 \\ I_2 \end{bmatrix} = \begin{bmatrix} I_1\cos(\theta)\exp(i(\phi/2+Z_+)) + I_2\sin(\theta)\exp(i(\phi/2+Z_-) \\ -I_1\sin(\theta)\exp(i(\phi/2-Z_-)) + I_2\cos(\theta)\exp(i(\phi/2-Z_+)) \end{bmatrix}$$
$$\Rightarrow^* \begin{bmatrix} I_1^{*2}\cos^2(\theta) + I_2^{*2}\sin^2(\theta) + \cos(\theta)\sin(\theta)[I_1 I_2^* \exp(i(Z_+ - Z_-)) + I_1^* I_2 \exp(i(Z_- - Z_+))] \\ I_1^{*2}\sin^2(\theta) + I_2^{*2}\cos^2(\theta) - \cos(\theta)\sin(\theta)[I_1 I_2^* \exp(i(Z_- - Z_+)) + I_1^* I_2 \exp(i(Z_+ - Z_-))] \end{bmatrix} \tag{3.18}$$

where * indicates a change into intensity i.e. $|E|^{*2}$.

Using the input matrix $[1, 0]$ provides the parameters for the MMI as a splitter to compute the imbalance:

$$U\begin{bmatrix} 1 \\ 0 \end{bmatrix} = \begin{bmatrix} \cos(\theta)\exp(i(\phi/2+Z_+)) \\ -\sin(\theta)\exp(i(\phi/2-Z_-)) \end{bmatrix} \Rightarrow^* \begin{bmatrix} \cos^2(\theta) \\ \sin^2(\theta) \end{bmatrix}$$

and $[1, i]$ provides the values of an MMI as a beam combiner to compute the extinction:

$$U\begin{bmatrix} 1 \\ i \end{bmatrix} = \begin{bmatrix} \cos(\theta)\exp(i(\phi/2+Z_+)) + i\sin(\theta)\exp(i(\phi/2+Z_-) \\ -\sin(\theta)\exp(i(\phi/2-Z_-)) + i\cos(\theta)\exp(i(\phi/2-Z_+)) \end{bmatrix}$$
$$\Rightarrow^* \begin{bmatrix} 1 + 2\cos(\theta)\sin(\theta)\sin(Z_+ - Z_-) \\ 1 - 2\cos(\theta)\sin(\theta)\sin(Z_+ - Z_-) \end{bmatrix}$$

Hence the coupling ratio of an MMI, with the phase difference of the output ports, can be related to the extinction. For simplicity Fig. 3.6 used a phase difference $(Z_+ - Z_-)$ of 90° rather than the measured phases of the electric field for an MMI as a splitter. For a real device, the input phase must be matched to complement this phase difference (as will be discussed in Chap. 4.

As an aside, the phase of each output lobe of the overall field exciting a specific output waveguide was calculated in Ref. [195] as

$$\phi_q = q\pi(N-q)\frac{M}{N} \tag{3.19}$$

where $q = 0, 1, ..., N-1$ describes the sequence number of the output waveguide (numbered depending on the position of the input waveguide, if input from the bottom waveguide the number is top down and vice versa) and M and N are the same as Sec 3.2. As an example consider the 2x2 MMI; as a coupler $N = 2$ and $M = 1$ which leads to $\phi_0 = 0$ and $\phi_1 = \pi/2$. This is why, to create an extinction, the input ports in eq. (3.18) are 1 and i.

This means that the MMI requires a 90° phase difference at the designed wavelength. Away from this wavelength, as stated above, the phase shifts and must be corrected to achieve the deep extinction.

In this thesis calculations of the extinction use the relation provided in Fig. 3.6 which has the implicit assumption that the input phases complement the phase difference.

3.3.3 Optimal widths and lengths

The W and L being free variables meant they were the first design criterion to be met. The other variables, that determine the localised intensity maxima position (from eq. (3.8)), already set: n by the choice of material (2.609) (see Chap. 5 for details on the selected materials) and the desired wavelength (4000 nm) by the astronomical wavelength band. Another free parameter that could be chosen was the waveguide width at the MMI interface, which tapers from the 2 µm waveguides, hereby referred to as the taper width (W_a). Previous research for much lower index contrast materials had identified that there is an optimum W_a that provides simultaneously the highest throughput and lowest imbalance (an imbalance close to zero) at the design wavelength, that being three tenths the W [164, 196]. This was chosen to be the W_a for these simulations. The taper length was set to 200 µm to maintain a smooth taper that did not excite higher-order modes (discussed more in Sec. 5.2.1). Optimising this parameter is not a key part of this work but there is a brief discussion on the taper length and optimising the imbalance (at a transmission cost) contained in Sec. 4.4.

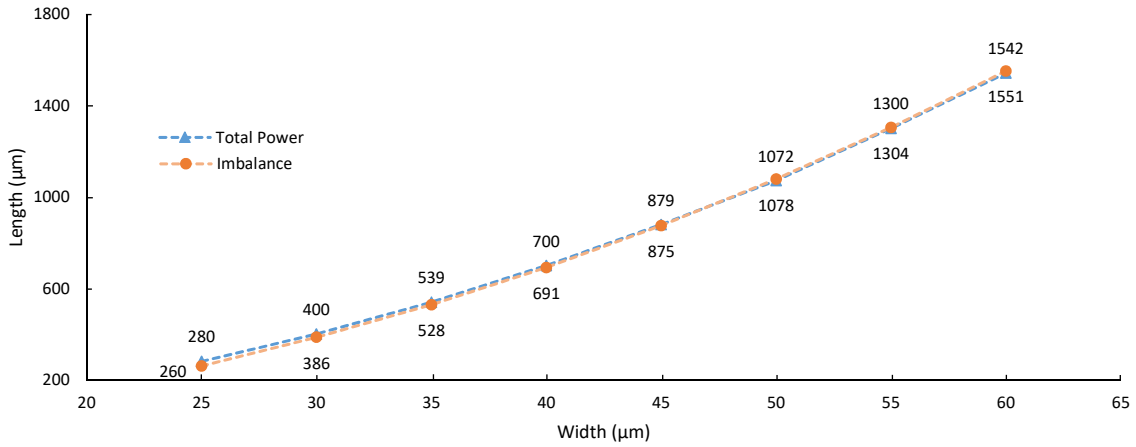

Figure 3.7: The optimum MMI cavity length, based on total loss and imbalance between outputs, at various MMI cavity widths. Numbers above points are the optimum length in microns for transmission, and below for imbalance to provide a higher degree of precision.

The calculated L, from eq. (3.8), were used as starting points in the MMI simulations with selected W $(25 - 60\,\mu\text{m})$ to find the best transmission and imbalance for a quasi-TE mode. The results are displayed in Fig. 3.7 and whilst the optimum L for transmission and imbalance are similar they are not equal. At a W of approximately 45 µm the two optimum L are the closest to equal.

The difference in the lengths is key here and is plotted explicitly in Fig. 3.8 for both quasi-TE and quasi-TM input modes.

Based on the results, the nominal MMI cavity had width 45 µm and length 875 µm.

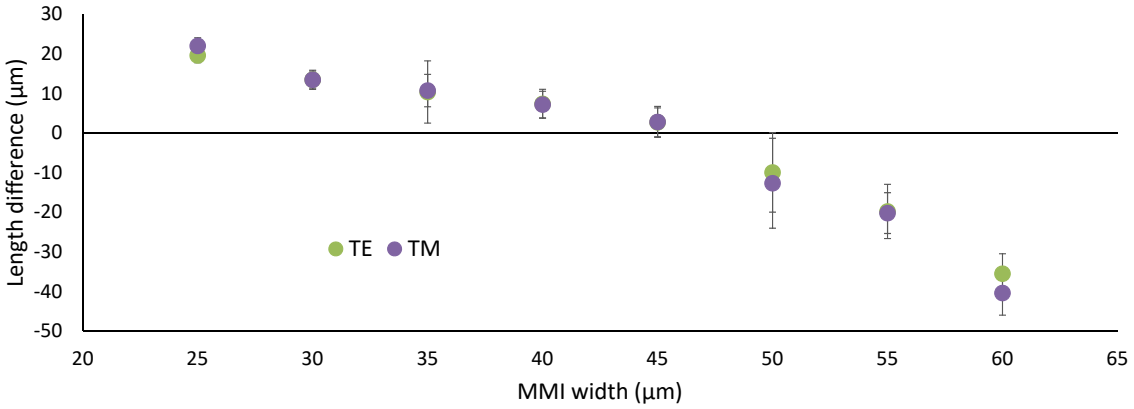

Figure 3.8: The difference in MMI cavity optimum lengths for transmission and imbalance versus MMI cavity width.

3.3.4 Light coupling between the MMI taper

A minimum MMI width of 25 µm was selected due to evanescent coupling between the input and output tapers. This coupling changed the imbalance curve, similar to simulating two unequal launch fields into the MMI cavity.

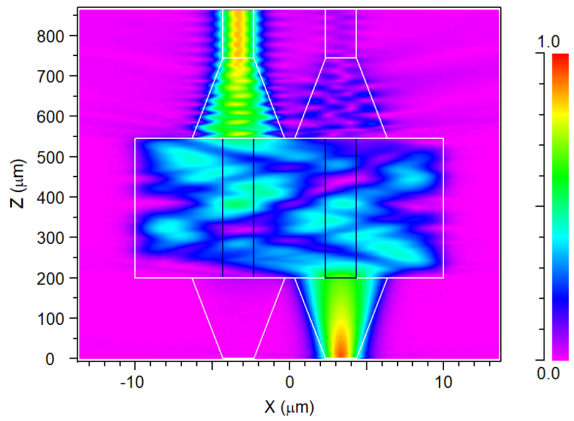

Figure 3.9: BeamPROP simulation of an MMI with $W = 20\,\mu m$, with light input into the bottom right taper. Note the minute light entering the waveguide from a taper with no input field (about 0.6% of the input field).

This was simulated using RSoft BeamPROP (an example of which is included in Fig. 3.9) with Tab. 3.1 highlighting the width 20, 25 and 45 µm for tapers of length 200 µm.

Table 3.1: Light leakage from one taper to the other before the MMI cavity.

W (µm)	W_a (µm)	Separation (µm)	Coupling (%)
20	6	6.7	0.6
25	7.5	8.3	0.06
45	13.5	15	0.0001

Table 3.1 shows that the degree of evanescent coupling at 20 µm is two orders of

magnitude higher than the 25 µm W. The separation of the waveguides decreases as the W decreases hence the evanescent coupling increase.

The coupling length of two parallel waveguides is described here:

$$L = \frac{1}{2}\frac{\lambda}{n_1 - n_2} \tag{3.20}$$

where $n_{1,\,2}$ are the effective index of the first two supermodes. This was calculated for the separations above shown in Fig. 3.10 at positions 0, 50, 100, and 200 µm along the taper.

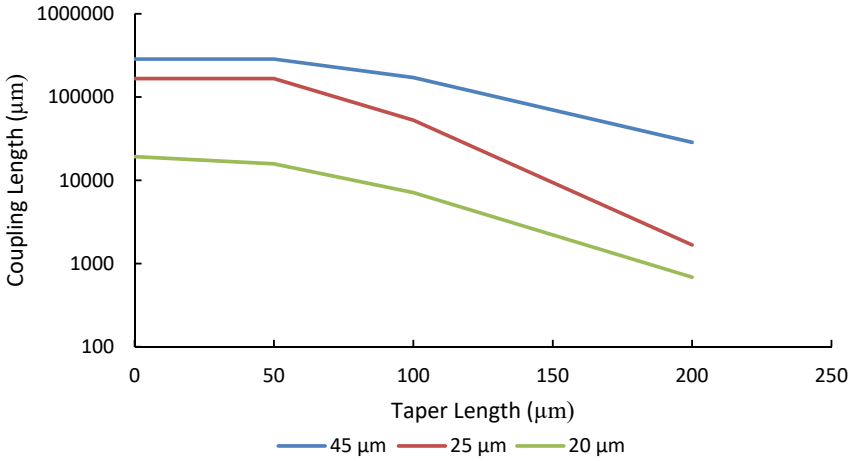

Figure 3.10: The coupling length, calculated using eq. (3.20), with the effective index of the supermode simulated using FemSIM at lengths 0, 50, 100, 200 µm for W = 20, 25 and 45 µm (green, red, blue respectively). The TM modes are displayed with a similar graph for TE.

Figure 3.10 shows that the larger separation waveguides have the lowest evanescent coupling (as expected). The separation of the waveguides before the taper is such that the evanescent coupling is minimal (on the order of cm) and as the taper width increases (and the mode becomes larger) the evanescent coupling increases (to hundreds of µm) which is why it has begun leaking light into the other taper (as per Tab. 3.1). The shortest separation has a coupling length of approximately 600 µm at the end of the taper and so integrating over the entire taper provides the evanescent coupling.

Note here that by changing the taper length the evanescent coupling can be reduced to (near) zero and so smaller MMI could be utilised if required - with appropriate increase in waveguide separation until tight bends just before the MMI tapers. Because larger MMI widths are practical here, and there is no significant increase in performance or transmission (specifically for a single MMI) apparent when using a smaller width MMI this work will limit its focus to W = 45 µm.

3.4 Fabrication tolerance

To determine whether an MMI is viable to be used as a beam combiner for nulling interferometry, the fabrication tolerance of the MMI must be analysed. The fabrication tolerance

of an MMI is discussed in Besse et al. [202] and more recently Morrissey et al. [203] published a fabrication tolerance analysis of a 1x2 MMI in indium phosphide (InP). However, the focus in these papers was the width and length of the MMI. This section adds to their work for a 2x2 MMI in ChG, extending the analysis to refractive index, core height and the gap between the up-taper into the MMI, and shifting the focus from tolerances in transmission to imbalance.

Judging from Fig. 3.6, an imbalance of ±2% implies that if used as a two telescope beam combiner the MMI would produce a 40 dB extinction over the starlight. This is used as a key indicator of whether the MMI is within tolerance. The transmission of the MMI, as mentioned before, has already been explored. A loss of 10% (equivalent to 1 dB) would not make the MMI the dominant source of loss in this work (as discussed in Chap. 5) and is used as the limit allowed to the transmission in this analysis.

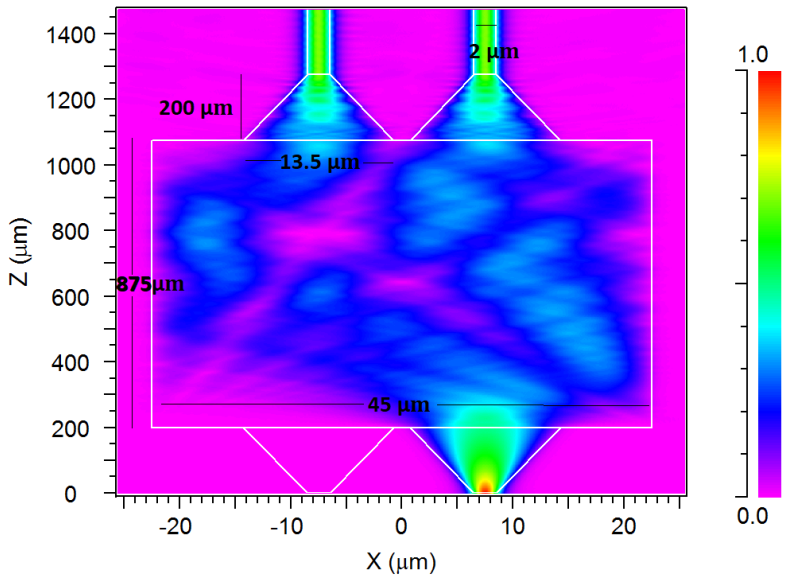

Figure 3.11: An Rsoft BeamPROP simulation image of the nominal design 2x2 MMI.

$L = 875\,\mu\text{m}$ was chosen to optimise the imbalance, though the polarization dependence also has to be considered. The base MMI design is shown in Fig. 3.11 with the TE major electric field component evolution through the MMI used as an illustration of how light behaves in an MMI.

By choosing 875 µm the imbalance for the TE mode is predicted to be 0% and the TM mode 0.25% however there are fabrication tolerances to consider. Firstly, the photomask has an inherent error when writing. A typical photomask writer achieves a critical dimension (CD) tolerance of ±0.1 µm at the feature sizes involved, this being a random error. Secondly, during lithographic printing and dry etching there can be overall growth or shrinking of the entire pattern by ±0.1 µm. The impacts of these effects need to be considered. Looking closer at the beat length in eq. (3.8)

$$L_\pi = \frac{4}{3}\frac{n_{core}}{\lambda_0}W^2.$$

These variables would be expected to be the most effective at reducing the MMI performance: any fabrication errors in L, W or n_{core} may produce a deviation of the required 50:50 coupling or reduce the throughput of the MMI. The errors associated with W, L and W_a are concerning the photonic mask fabrication, with an error of $\pm 0.1\,\mu\text{m}$. The total outline of the MMI (which is inclusive of W, L and W_a) is also expected, with the same error of $\pm 0.1\,\mu\text{m}$. These are independent variables and have been analysed separately below, and then combined in a Monte Carlo simulation to predict the real device performance.

3.4.1 Length tolerance

Having chosen the W and L for optimum imbalance the question arises to the effect on the transmission and imbalance. Figure 3.12 plots the TE and TM transmission at a W of $45\,\mu\text{m}$ against L. The expected fabrication error in the L is $0.1\,\mu\text{m}$ and yet, from Fig. 3.12, even a $4\,\mu\text{m}$ length difference away from the optimum L has no significant effect on transmission.

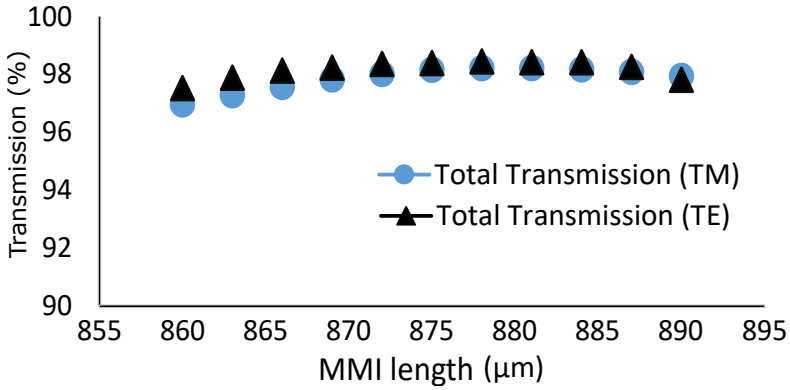

Figure 3.12: The throughput of the MMI of width $45\,\mu\text{m}$ for length 860 to $890\,\mu\text{m}$

The imbalance on the other hand, plotted in Fig. 3.13, indicates that there is only one L for which the imbalance is zero, and no L for which the TE and TM imbalances are both zero simultaneously.

For the TE mode, $875\,\mu\text{m}$ is optimum and for TM, $880\,\mu\text{m}$. The dilemma thus is to decide whether to change L to a length between the two optimum lengths. As both these numbers are within the 98% transmission band it was decided that choosing L such that one polarisation imbalance would be zero was better as it offered the possibility of perfect nulling by selecting that polarisation. This provides the opportunity to determine how good the measurements and device performance could be.

Computed from Fig. 3.13, the imbalance deviation from the fabrication tolerance of an MMI of $L = 875\,\mu\text{m}$ was $\pm 0.009\%$ for TE and $\pm 0.013\%$ for TM. As will be shown in the other tolerance analyses this is not a significant concern.

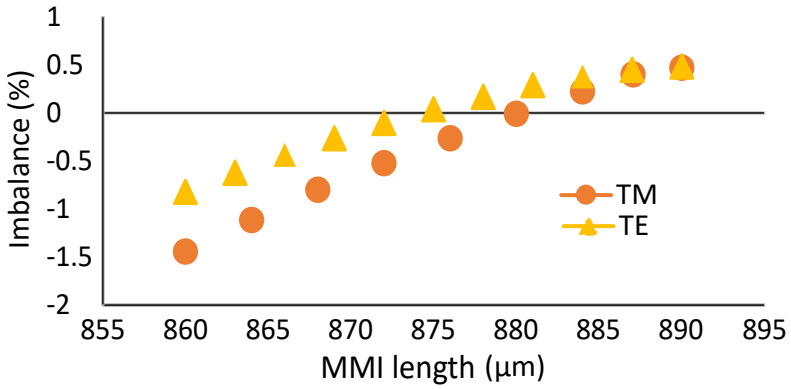

Figure 3.13: The imbalance of the MMI of width 45 µm for length 860 to 890 µm

3.4.2 Width tolerances

Given the direct link between L and W for the optimum performance, and the fact that L is much greater than W, then the performance was expected to show considerably greater sensitivity to W. Figure 3.14 shows the transmission as a function of W at $L = 875\,\mu m$, and Fig. 3.15 shows the imbalance as a function W.

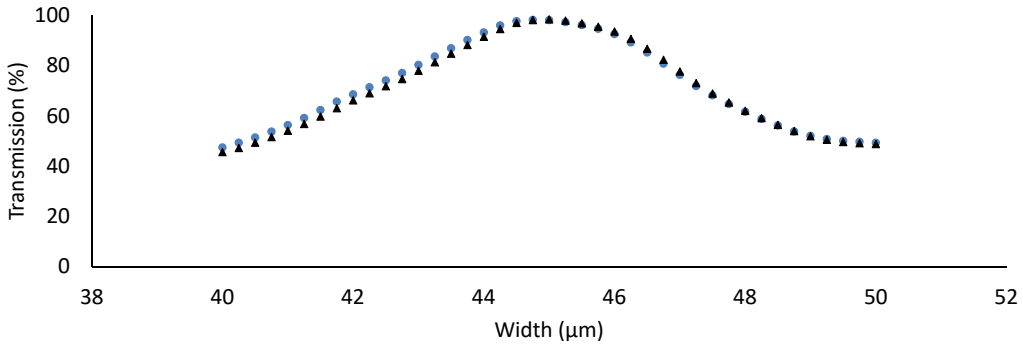

Figure 3.14: The total power through the MMI versus width at a constant length of 875 µm.

Transmission is not significantly affected for the typical fabrication tolerance levels displaying symmetric variation of -0.35% of the 98% maximum figure. This is true for both TE and TM modes. The width variation appears to be indifferent to the change in mode. This is possibly due to the small effective width change from eq. (3.5) that detailed the change of width due to the polarization of light.

With a CD tolerance of $\pm 0.1\,\mu m$ the imbalance variation around the nominal $W = 45\,\mu m$ design is $\pm 0.24\%$ for TE and TM modes, which is considerably more sensitive than for the same length variation.

3.4.3 Index change tolerances

The refractive index of the core (n_{core}) and cladding ($n_{cladding}$) films will remain constant throughout a single device or a small group of devices (at least over a device <1 mm long), however, there will be intra- and inter-wafer variations. Experience with the films involved

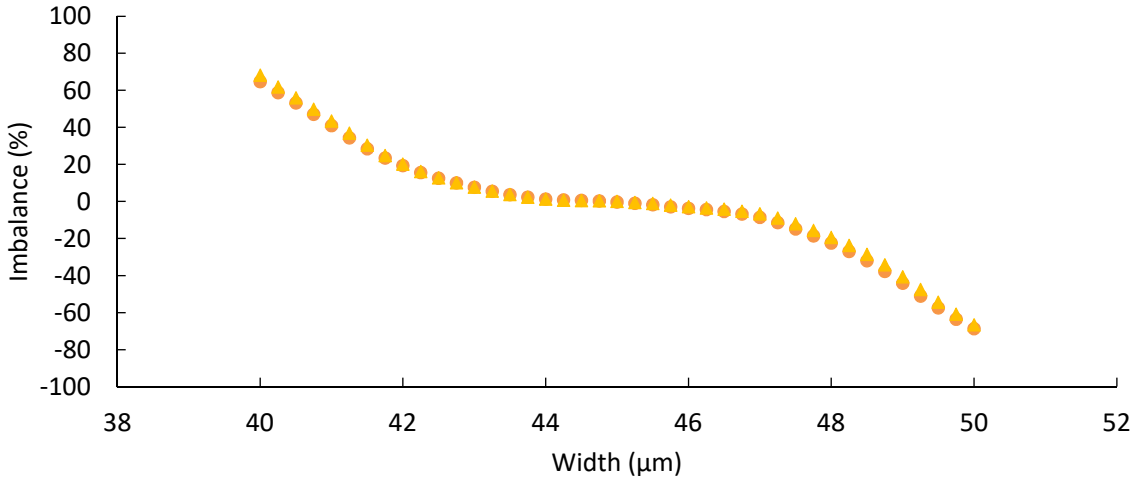

Figure 3.15: Imbalance versus MMI width at a length of 875 µm.

over many depositions indicates a total variation of 0.01 (± 0.005) in n is the worst case. The dependence on n was not expected to be as dire as that of W as minor index contrast changes do not change the proportion of power in the core significantly.

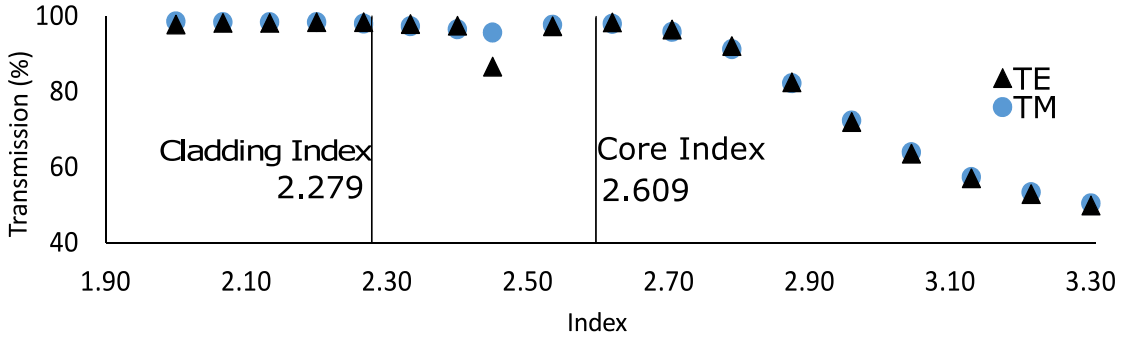

Figure 3.16: MMI transmission, in both TE and TM mode, for the cladding index between 2.000 to 2.400 (design value is 2.279) and the core index from 2.450 to 3.300 (design value is 2.609), whilst maintaining the design value for the index not being varied.

Figure 3.16 plots the transmission of the MMI design for n_{cladding} from 2.0 to 2.4 and n_{core} from 2.4 to 3.3. This range is larger than necessary and was chosen to examine whether any large patterns emerge from the relation between index and transmission or imbalance. For reference, the vertical lines show the design n for the optimised device in Sec. 3.4 and the value used when varying the other index. The transmission does not drop below 95% for a n_{cladding} with a lower refractive index than the nominal 2.279 value and sees only very minor change for higher values. Given the worst-case variation of ± 0.005 the performance of the MMI is essentially independent of n_{cladding}.

Variation of the core refractive index is also plotted in Fig. 3.16. The n_{core} does change the L_π according to eq. (3.8) and, as a result, changes in transmission occur on both sides of the nominal value. The variation in transmission for the ± 0.005 index variation is $\pm 0.05\%$ - a negligible change.

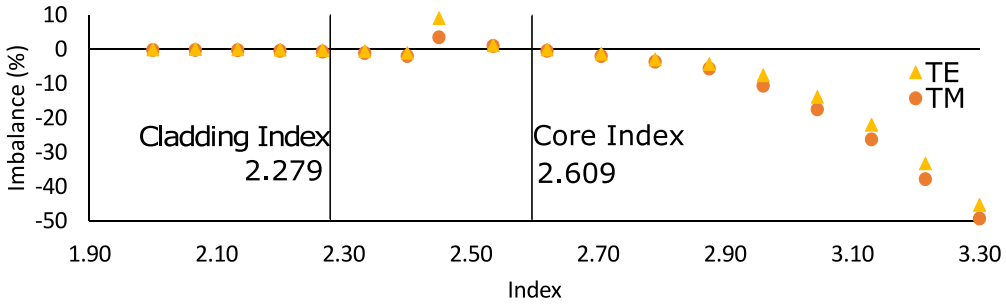

Figure 3.17: MMI imbalance for the same core and cladding indices as in Fig. 3.16.

The imbalance is presented in Fig. 3.17. As would be expected, the performance is relatively insensitive to the n_{cladding} exhibiting an imbalance variation of $\pm 0.0015\%$ for both TE and TM modes per ± 0.005 around the design point (2.279). The n_{core} was expected to effect the imbalance more than n_{cladding} due to eq. (3.8). From Fig. 3.17 the design point of n_{core} is 2.609 and the imbalance change is $\pm 0.09\%$ per ± 0.005 of index change for both TE and TM modes, about half the sensitivity of the MMI width to typical tolerances.

3.4.4 Core height tolerances

Moving away from the variables related to L_π the remaining device geometry variable yet to be addressed is the core height. This is determined by the deposited core film thickness. This suffers intra-wafer variations of typically below 0.1% and a run to run variations of 1% under optimised conditions. Figure 3.18 shows the transmission dependence with change in the core height.

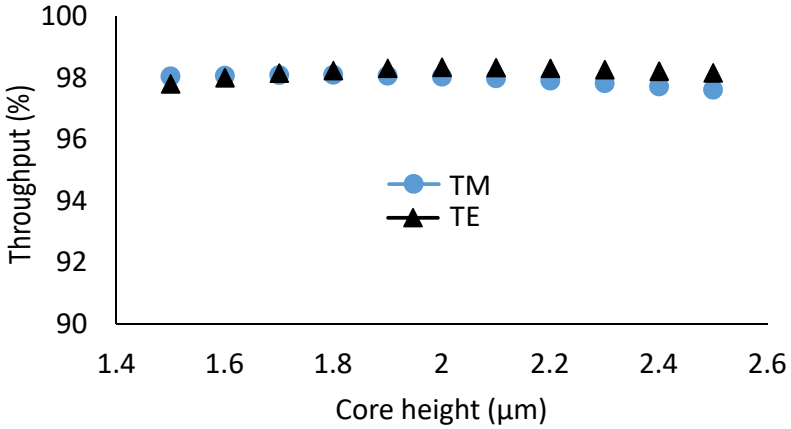

Figure 3.18: The transmission of the MMI versus the thickness of the core film.

The transmission is robust against drastic changes in the core height, as shown in Fig. 3.18, and essentially unchanged for the typical thickness variations expected under normal circumstances. Note that this simulation did not include any bends in the input or output waveguides before and after the MMI respectively. Had there been bends, due

to the higher-order modes for thicker cores and the reduced mode index for thinner cores, there may have been additional, minor, losses. Figure 3.19 shows the imbalance as the core height is varied.

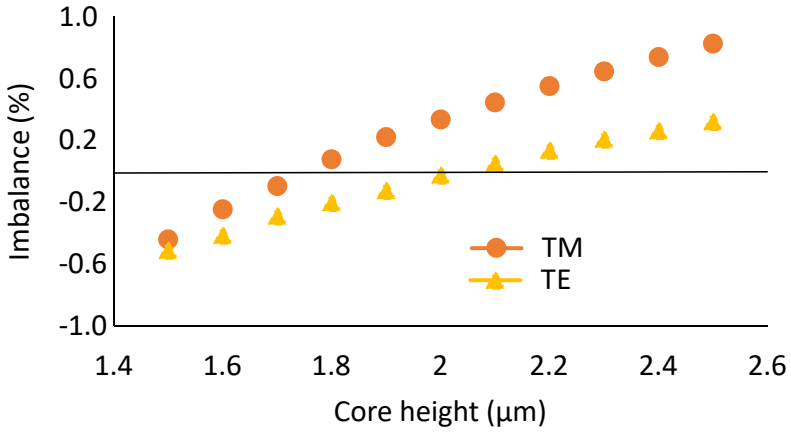

Figure 3.19: MMI imbalance versus MMI core height.

From the Fig. 3.19 the imbalance diverges away from an equal splitting at the set height of 2 µm for TE and 1.7 µm for TM. It could be argued that a height of 1.5 µm should have been designated for the MMI as the imbalance for TE and TM are equal here. However, it is unclear how this would affect the transmission of the waveguide (not the MMI as shown in Fig. 3.18) as Chap. 5 will show: a 2 by 2 µm waveguides has significant loss and decreasing the height would have more propagation loss.

The range shown in Fig. 3.19 is much larger than the expected fabrication tolerance. For the ±10 nm achievable accuracy the change in imbalance is ±0.011% for TE and ±0.0010% for TM - minimal as compared to the other geometry variables.

3.4.5 Taper width: Truncating the taper

For the prior simulations a $W_a = 0.3W$ (= 13.5 µm) was used with the tapers centred at $1/6W$ (a position ±7.5 µm from the centre of the MMI). This width was chosen based on previous works on the W_a and the effect they had on the MMI transmission and imbalance with the claim that this arrangement would have high transmission and a low maximum imbalance [196]. This was similar to the MMI examined by Morrissey et al. [203], however, they highlight a $W_a = 0.25W$ also provided a high "coupling efficiency". This is investigated further in Chap. 4.

An increase in the W_a reduces the gap between the tapers at the interface with the main cavity of the MMI. At $W = 45$ µm and $W_a = 13.5$ µm the gap is 1.5 µm. This raises a question as to the available resolution of the lithography process in terms of accurately resolving this part of the structure, as the effects of truncation here do not seem to have been explored in the literature.

With an irregular taper that fills in the gap between the input tapers and output tapers respectively, as shown in Fig. 3.20, the imbalance varies from positive to negative in both

TE and TM.

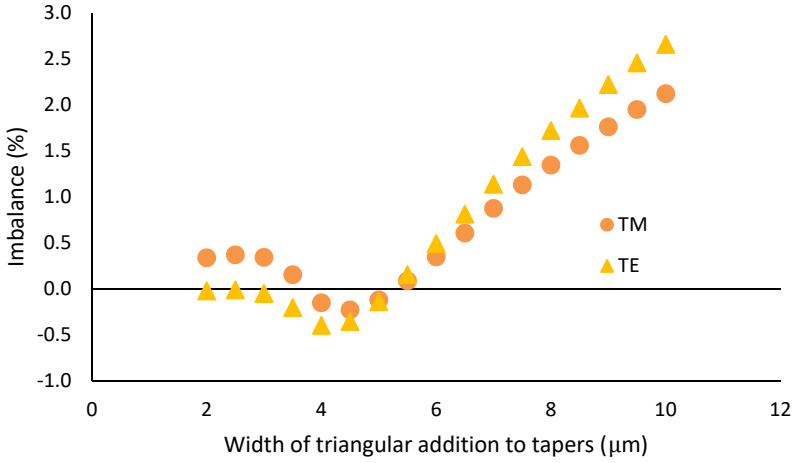

Figure 3.20: The imbalance of the MMI with iterative increases in the truncated taper width, shown in Fig. 3.21.

From Fig. 3.20, between the 2 µm truncated taper width to 4 µm the imbalance reaches -0.5% before becoming positive as the truncated taper width increases. A computer-aided design (CAD) of this truncated width is included in Fig. 3.21. It is unclear what to expect in the fabrication tolerance for this part of the lithography. As an estimate consider when the tapers are connected, at a truncated taper width of 4 µm in Fig. 3.21, the imbalance here changes by -0.38% for TE and -0.49% for TM, from Fig. 3.20. This is the largest effect on the imbalance in the variables examined so far, implying that keeping the gap clear is imperative. If, we assume that the lithography is the same as the MMI width and MMI length (±0.1 µm) then this imbalance shift is reduced to 0.004% but it is impossible to know ahead of time that this will be the case.

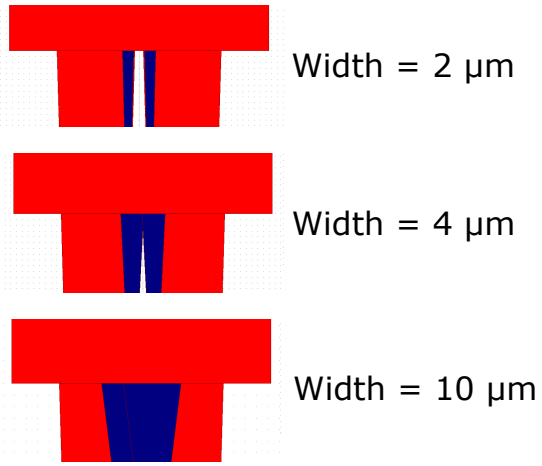

Figure 3.21: An artificial truncation (blue) at widths of 2 µm, still within the 13.5 µm taper (red), 4 µm, the truncation combines, and 10 µm. The truncated taper is 40 µm long inside the regular tapers (200 µm long) at ±1.9 µm from the centre of the MMI.

3.4.6 Taper width: Width tolerance

In addition to core material filling the gap between the tapers, there is the risk in this region of forming an air void when over-cladding is applied by physical vapour deposition methods. Whilst the lithographic resolution issue can be overcome by using sufficiently advanced projection lithography tools (though at a significant cost), the void issue is more complex to ameliorate. Increasing the gap will certainly make avoiding air pockets easier. With this in mind, it was decided to test the effects on device performance of varying W_a. The first simulation of the W_a was to keep the input taper constant and vary the output taper to see whether the imbalance or transmission was affected. The transmission drops quickly, as shown in Fig. 3.22, falling below 90% at a taper with of 9 µm. Varying both taper widths maintains a transmission above 90% until a $W_a = 6$ µm.

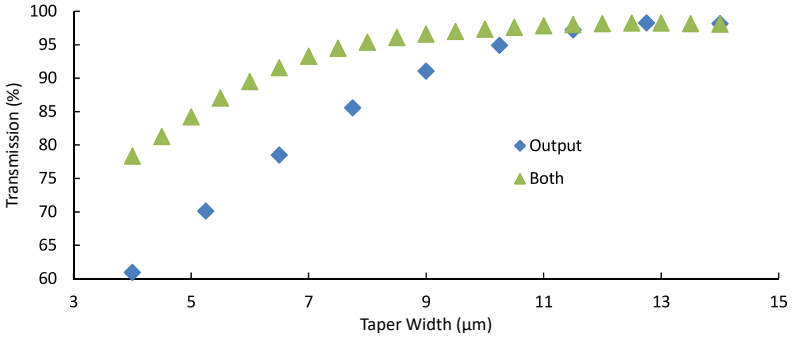

Figure 3.22: MMI transmission for output taper width variation (blue diamonds) or both input and output tapers being varied (green triangle) for a 45 µm wide, 875 µm long MMI at a wavelength of 4 µm.

Maintaining an input $W_a = 13.5$ µm and reducing the output W_a increases the loss because the light is not wholly captured by the output taper. From the simple Talbot imaging arguments, the local intensity maxima at the output are Fresnel images of width 1/N the size of the original image, N = 2 in this case. The indication here is that a minimum output taper width of half the input taper should suffice. Figure 3.22 indicates that it does not. At an output width of 7 µm (almost half 13.5 µm) there is 20% loss. The loss is due to a mismatch between the modes in the wavefront at the end of the MMI (an image of the original input) and those that can be excited into the taper. More work is required to understand this further but for now, it is sufficient to mandate the input and output W_a be equal.

Figure 3.22 shows a monotonic decrease in the transmission with a decrease in W_a when varying both the input and output tapers simultaneously. This is due to the larger W_a allowing for higher-order modes to be coupled into the taper [196]. These modes would have to couple into the fundamental mode of the 2 by 2 µm waveguide to maintain this high transmission. Chapter 4 delves into the complicated nature of mode coupling in the MMI cavity and the taper widths but does not provide a definitive answer to why this would be the case.

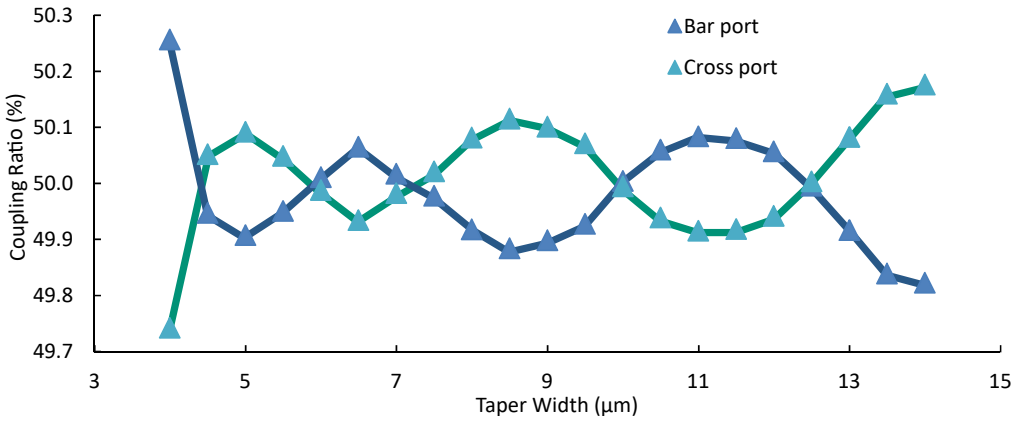

Figure 3.23: Individual output port coupling ratios for the nominal MMI that varied both input and output tapers where the bar port is blue, the cross port in teal and the lines between them to guide the eye.

How the taper variation affects the splitting ratio is a highly complicated function that is explored in Chap. 4, however, consider a simplistic start here with Fig. 3.23 showing the coupling ratio of an MMI with a varying W_a. This figure uses TE light only for simplicity. The maximum divergence in Fig 3.23, from a 50:50 split, is 50.3:49.7 (0.6%). However, the interesting part of this figure is the periodic structure with no fewer than five crossings of the 50:50 coupling ratio.

From Fig. 3.23 the two output ports, despite oscillating, remain relatively equal as W_a reduces. Comparatively the imbalance is shown in Fig. 3.24 for both TE and TM, with the oscillations now around zero instead of 50:50. This indicates that there are several different high performance operating points (the zero points) and the W_a could be selected accordingly. It was this that prompted the investigation in Chap. 4 with the additional benefit of potentially having a taper width structure that has a large gap that could be fabricated and then filled with the over-cladding material.

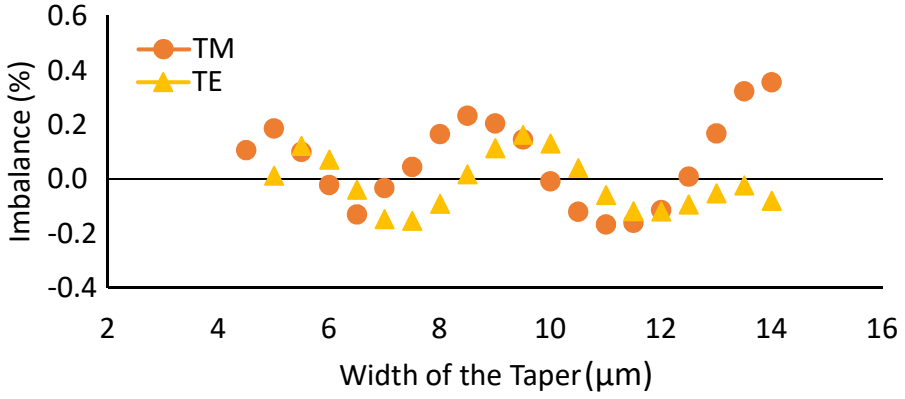

Figure 3.24: Imbalance due to the simultaneous change of taper width of the input and output port, from Fig. 3.23 with the extreme ratio at 4 µm disregarded for aesthetic reasons, for an MMI of width 45 µm and length 875 µm.

Figure 3.24 indicates that many taper widths will provide an imbalance of zero, however, the TE and TM values appear to never align on a zero point and more work is required to find an overlap for TE and TM at a minimal imbalance. For the taper width itself the tolerance of ±0.1 µm has little effect on the imbalance. For TE the difference is -0.025±0.004% with a much larger difference of 0.32±0.02% for TM.

3.4.7 MMI outline variation from lithography and etch biases

The previous simulations showed that the MMI's dimensions of W, L, n_{core}, n_{cladding}, W_a and core height vary the imbalance and transmission from their optimum, designed values. The transmission barely changes from the 98% peak, and as such is not an issue to dwell on, but the imbalance exhibits more significant variations.

An accurate simulation of the lithography and etch bias, however, does not vary a single dimension but all dimensions at once (specifically W, L and W_a that all have common fabrication error mechanisms). Each would be expected to have the same ±0.1 µm variation for any given fabrication run. Figure 3.25 shows the impact of the fabrication tolerance of the outline, the etch bias, on the imbalance. The transmission was omitted as there was negligible transmission change.

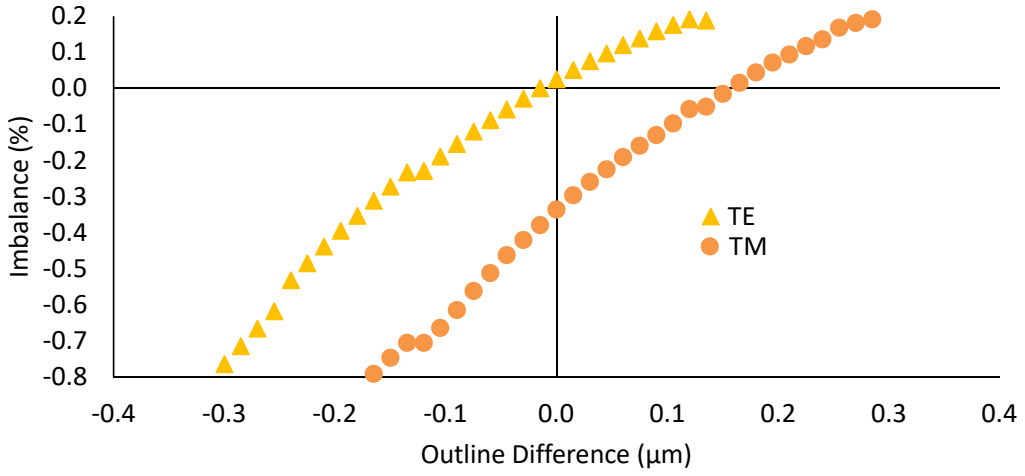

Figure 3.25: The simulated imbalance for the TE and TM modes when the outline of the MMI: the length, the width, and the taper width are varied.

Explicitly, the outline is a change in W, L and W_a by the same amount. For example, an outline change of +0.1 makes an MMI with $W = 45.1$, $L = 875.1$ and $W_a = 13.6$ µm and -0.1 makes an MMI with $W = 49.9$, $L874.9$ and $W_a = 13.4$. From Fig. 3.25 when simulating the TE mode the imbalance change is $0.0^{+0.17}_{-0.35}$% away from zero for the expected CD change of ±0.1 µm and $-0.32^{+0.25}_{-0.35}$% for TM. As such the effect on the TM mode is greater, likely because it was already away from zero and subject to the tail end of the nonlinear imbalance function that would exaggerate the fabrication tolerance calculation.

This error is significantly higher than the individual dimensional variables: the maximum change in taper width is 0.02% for TM (negligible for TE), ±0.24% for the change

in width (TE), and ±0.013% for the change in length. The width is likely the main contribution to the outline imbalance deviation.

3.4.8 Wavelength dependence

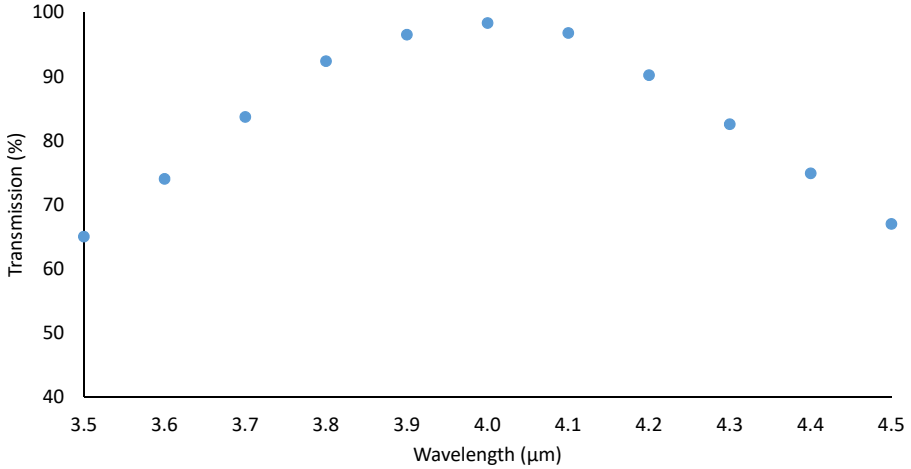

Figure 3.26: MMI transmission as a function of wavelength for the nominal MMI base design of 45 µm width MMI 875 µm length.

Although the wavelength is not a fabrication variable, it is nonetheless a quantity of operational interest when nulling performance is considered. Considering eq. (3.8), L_π has an inverse dependence on the wavelength and as such would be expected to have a significant effect on the transmission and imbalance. The transmission was simulated in Fig. 3.26 showing a large wavelength dependence as expected.

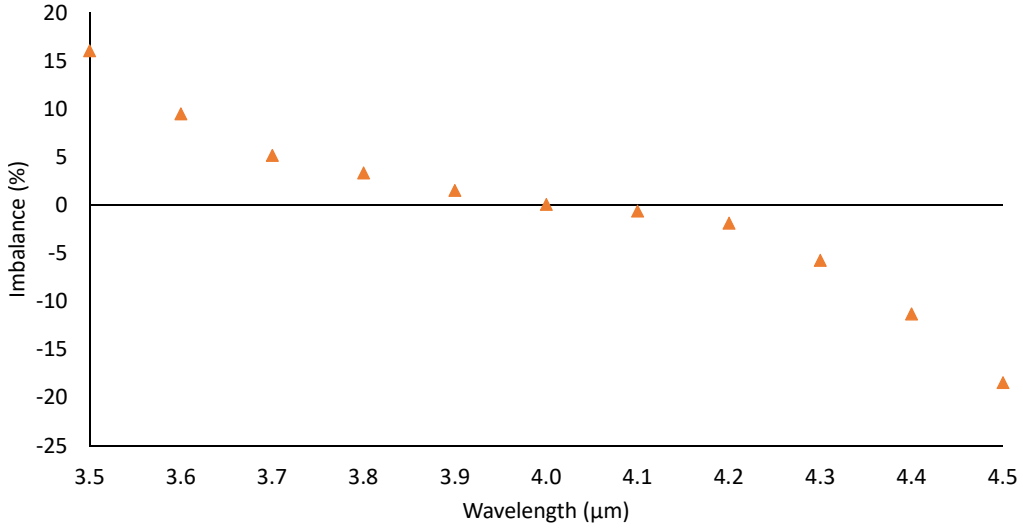

Figure 3.27: Change in the MMI's imbalance due to the wavelength.

Around the 4 µm nominal centre operating point the transmission behaves symmetrically, $98 \pm 6.5\%$ for ±200 nm of optical bandwidth.

The imbalance shows a drastic asymmetric change away from the 4 µm point. Around the range of interest, 3.8 to 4.2 µm, a first-order approximation provides the linear proportionality constant of 0.0126%/nm. For a benchmark of 40 dB the 2% imbalance condition must be met. Hence, over this operational bandwidth an even splitting bandwidth of 150 nm has been achieved.

This change in wavelength is an exploration of where the local intensity maxima forms in the MMI. Figure 3.28 shows the field evolution in the MMI at two wavelengths on either side of the design wavelength. The two localised intensity maxima expected at $1/2L_\pi$ form early in the 4.2 µm example and do not appear to form at all in the 3.8 µm example.

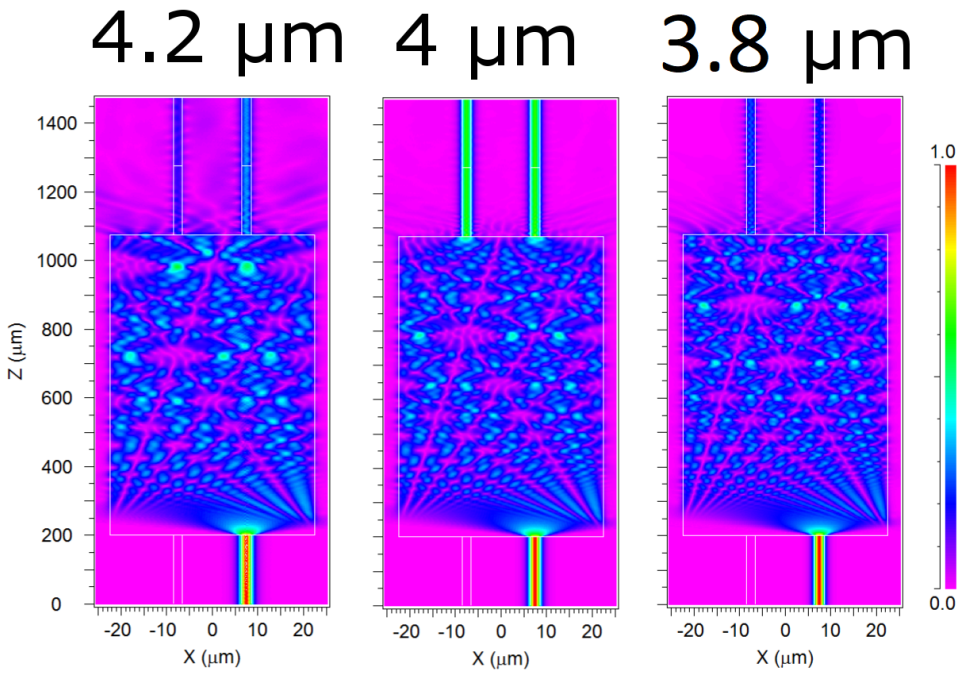

Figure 3.28: MMI simulations with a 2 µm taper width 45 µm width and 875 µm length for the wavelengths of 4.2 µm, 4.0 µm and 3.8 µm.

3.5 Summary

For the nominal MMI design the transmission does not drop below 98% (0.09 dB) which is much higher than the transmission through the waveguide, see Chap. 5 for more detail, and as such is not the limiting factor for loss through the system.

The imbalance is crucial to the performance of the MMI as a beam combiner and the effects of the various possible sources of fabrication tolerance error on the imbalance are summarised in Tab. 3.2.

The wavelength tolerance analysis was not included in these design parameters as it is not controlled in fabrication, however, it should be noted that over the 400 nm bandwidth a 5% imbalance occurs which is much greater than any tolerance in the fabrication. This is explored further in Chap. 4 and a design feature to flatten the imbalance is shown.

Table 3.2: Fabrication tolerances

Source	± TE imbalance change (%)
Mask error length (±0.1 µm)	0.013
Mask error width (±0.1 µm)	0.240
Mask error taper width (±0.1 µm)	0.004
Outline lith/etch bias (±0.1 µm)	0.350
Filling the gap between tapers (touching)	-0.5
Core index (±0.005)	0.060
Cladding index (±0.005)	0.002
Core thickness (±0.01 µm)	0.011

From Tab. 3.2 the biggest change in the imbalance is caused by imperfectly rendering the gap between the tapers at the interface to the MMI cavity. If the resolution of the lithography is insufficient such that the tapers merge before reaching the MMI cavity, then a 0.5% error in the imbalance could occur, but assuming the outline lithography and etch bias is all that changes the taper widths then 0.35% is the maximum imbalance error that could occur.

A Monte Carlo simulation was conducted to show the extent of the fabrication errors on the predicted extinction of the MMI, shown in Fig. 3.29. The simulation was restricted to an MMI of $W = 45 \pm 0.1$ µm with a random outline error between ±0.1. The simulation does not take into account the phase of the input beams and instead assumes they have been phase matched.

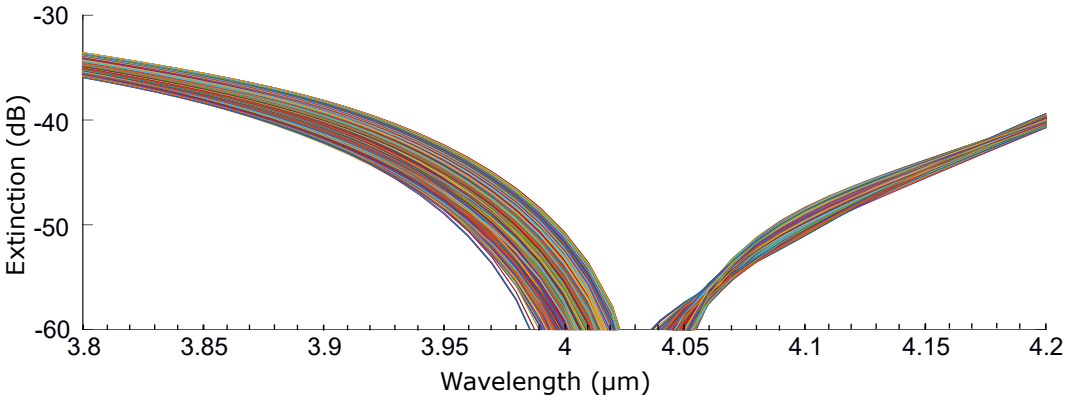

Figure 3.29: The extinction curves of 1000 MMI with an outline between ±0.1 µm randomly selected and an MMI width of 45 ± 0.1.

The simulation shown in Fig. 3.29 takes the coupling coefficients, for TM light, generated by the outline simulation from RSoft BeamPROP and calculates the extinction in the null port of the MMI for a pair of equal amplitude in phase inputs as a function of wavelength. The matrix in eq. (3.18) was used for the extinction calculations. Note that TM light was selected as the optimum design was for TE light and hence this simulation was designed to illustrate the limitation of this device.

Figure 3.29 shows that the MMI null area (below 60 dB) can vary from 3.98 µm to 4.05 µm. The centre is pointedly not at 4 µm. This is likely due to the choice of 875 µm

as the light used in this simulation is TM instead of TE (see Sec. 3.4.1). The fabrication tolerance simulations show that an MMI is a robust design for a high performance 3 dB coupler. A broad bandwidth for a high extinction, however, was not realised with this base MMI design. Indeed Fig. 3.29 suggests only a 20 nm bandwidth for 60 dB extinction. A 40 dB extinction, however, should extend from 3.95 to 4.15 µm making a 200 nm extinction bandwidth. The next step is thus to improve the bandwidth of the MMI base design. To do so, W_a simulations, which offered multiple high-performance areas in Sec 3.4.6, are investigated to determine if these are better options than the "established" design with $W_a = 0.3W$.

Chapter 4

Investigating the MMI bandwidth response

This chapter includes work already published:

Kenchington Goldsmith, H.-D., Ireland, M., Ma, P., Cvetojevic, N., and Madden, S., "Improving the extinction bandwidth of MMI chalcogenide photonic chip based MIR nulling interferometers," *Optics Express* **25**(14), 16813–16824 (2017).

The multimode interference coupler (MMI) presented in Chap. 3 was 45 µm wide (W) by 875 µm long (L), corresponding to on optimised transmission and imbalance curve for transverse electric (TE) light. A taper width (W_a) of 13.5 µm was used for these MMI as it corresponded to the optimum design from Hill et al. [196] that stated that an MMI access waveguide width of ($W_a =$) $0.3W$ provided the best transmission. Chapter 3 focused on the fabrication tolerance of such an MMI, with Sec. 3.4.6 highlighting a previously unknown rapid oscillation response in the coupling ratios as the MMI simulation varied W_a. The transmission was only moderately affected by this oscillation in imbalance, dropping from 99% to 80% as W_a decreased from $W_a = 0.3W$ (13.5 µm) to twice the input waveguide width (4 µm). For this reason, it was not investigated at that time. The cause of this oscillatory behaviour in the imbalance is the focus of this chapter.

The fabrication tolerance of the tapers was a key aspect of the total fabrication tolerance of the MMI, to the extent that it was included in the outline variable of the Monte-Carlo simulation. The gap between the tapers at the interface with the MMI cavity was of enough concern that it was simulated in Sec. 3.4.5 but found that there was limited impact on the imbalance curve over the ±0.1 fabrication tolerance. To achieve a large shift away from zero imbalance the taper was truncated to an extreme beyond that of standard fabrication tolerances of the typical lithography procedure. Such fabrication errors are incurred during the making of poor quality photonic masks and are an example of how extreme truncation can occur. Because of this a smaller W_a, which has no risk of producing an air gap, may be a better match for the fabrication process selected for this work (see Chap. 5 for more detail on fabricating the MMIs). This is another reason to investigate various W_a and their bandwidth response.

4.1 Initial bandwidth response

The impact of W_a on the MMI imbalance as a function of wavelength was not studied in Chap. 3, and to the author's best knowledge has not been subsequently investigated since Hill et al. [196]. Arguably the paper by Morrissey et al. [203] did discuss MMI wavelengths and imbalances but the focus was specifically for a 1x2 MMI and the effect of optimising W_a, not specifically regarding optimisation processes. Their work may extend to all MMIs but this has yet to be proven.

Following from Chap. 3, that looked at a single wavelength, a full vector beam propagation method (BPM) study using RSoft BeamPROP was undertaken to determine the wavelength dependence of the imbalance (and transmission to understand any potential tradeoffs) for a range of W_a in the aforementioned nominal MMI design: $W = 45\,\mu m$, $L = 875\,\mu m$ and taper length $= 200\,\mu m$. The wavelength range used was 3500 nm to 4500 nm which encompasses the astronomical L'-band but also provides additional context for the experimental studies where wide-band tuning from 3100 to 5000 nm was available for testing devices, as will be discussed in Chap. 5.

The MMI transmission with different W_a is shown in Fig. 4.1. From Fig. 4.1 an increase

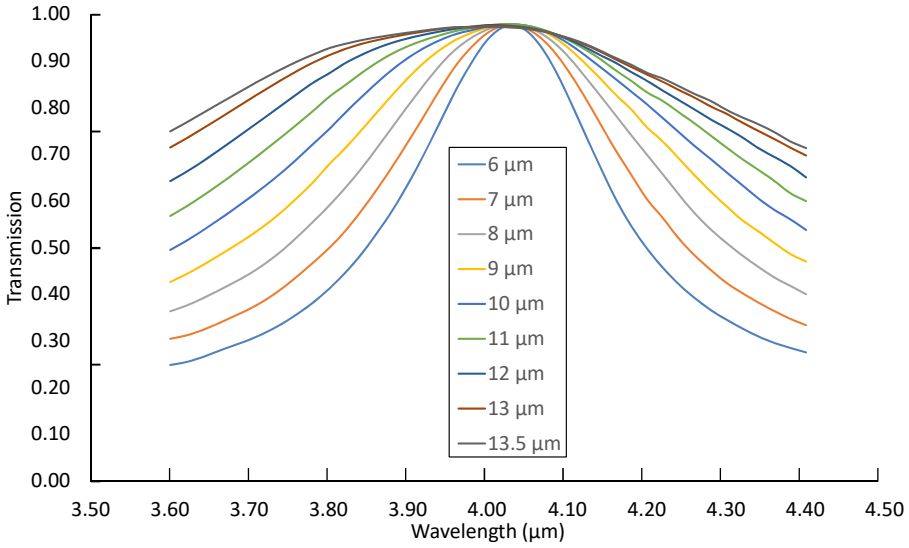

Figure 4.1: MMI transmission versus wavelength at different W_a for an MMI of $W = 45\,\mu m$ by $L = 875\,\mu m$.

in W_a corresponds to a wider transmission bandwidth, with $W_a = 13.5\,\mu m$ having the lowest loss at all wavelengths. As shown, for $W_a = 13.5\,\mu m$, the loss stays above 80% transmission (1 dB of loss) for a bandwidth $\pm 0.3\,\mu m$ around the design wavelength where it has lowest loss. The smallest, $W_a = 6\,\mu m$, has the narrowest transmission band with loss of more than 1 dB occurring within $\pm 0.1\,\mu m$ of the design wavelength.

Presented in Fig. 4.2 are the imbalance curves for $W_a = 6$ to $13.5\,\mu m$. They show a significant difference between tapers with the larger W_a passing through zero imbalance once and the smaller with multiple passes of zero imbalance. Figure 4.2 shows that as the tapers get smaller the imbalance curves show signs of additional structure with side-

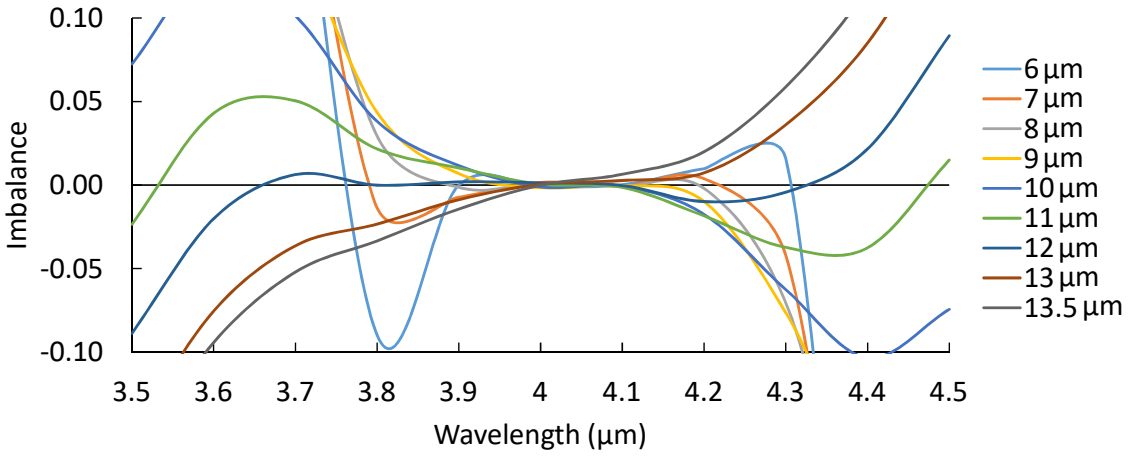

Figure 4.2: MMI imbalance versus wavelength for MMI and W_a listed in Fig. 4.1.

lobes or "wings" forming and producing multiple crossings of zero imbalance. $W_a = 6\,\mu\text{m}$ highlights the extra structure in its imbalance curve and the multiple crosses of zero imbalance. At the wavelengths, 3.6 µm and 3.8 um (and reflected past the zero imbalance point of 4 µm) are the wings in the imbalance curve where the second point is bound between two zero imbalance crossings leading to multiple crossing that are barely seen at this resolution.

For an understanding of Fig. 4.2's significance on the extinction bandwidth the imbalance data was converted to an equivalent extinction using Fig. 3.6. Repeating the method of converting imbalance to extinction: The null in an MMI is the result of launching two equal amplitude coherent fields into the input ports of the MMI with an appropriate phase such that destructive interference occurs in the chosen nulled output port. To understand how the imbalance and extinction are linked, consider the coupling matrix scalar field approximation from before in eq. (3.18) with the phase dependence removed for simplicity:

$$a \begin{bmatrix} \sqrt{1-k} & i\sqrt{k} \\ i\sqrt{k} & \sqrt{1-k} \end{bmatrix} \begin{bmatrix} \text{Input1} \\ \text{Input2} \end{bmatrix} = \begin{bmatrix} \text{Output1} \\ \text{Output2} \end{bmatrix}$$

where a is the total power through the MMI and k is the coupling ratio, both with an implicit wavelength dependence. Equation (3.18) is in terms of electric field and so the intensity is found by multiplying the output matrix by its complex conjugate.

Using eq. (3.18) to calculate the extinction is different as light is input into both arms with a 90° phase shift between them (an input matrix of $[1; i]$ in electric field terms) to cause destructive interference at the central wavelength. Away from the central wavelength the required phase various and must be matched by the electric field terms to form a deep null. For this chapter the phase match is assumed. Given the extinction definition:

$$\text{Extinction (dB)} = 10 \log_{10} \left(\frac{\text{Output1}}{\text{Output2}} \right) \tag{4.1}$$

then the extinction in terms of the coupling ratio may be derived as:

$$10\log_{10}\left(\frac{1-2\sqrt{k}\sqrt{1-k}}{1+2\sqrt{k}\sqrt{1-k}}\right)$$

where the phase term is assumed to cancel with the input fields.

The parameter k can be simulated through RSoft BeamPROP via one launch field into the MMI. Calculating the extinction this way provides the deepest extinction as it implicitly assumes the phase is matched. This is the preferred method as calculating the extinction directly, by launching two input ports into the coupler, has disadvantages. Matching the phase requires complete knowledge of the MMI and so requires not only a prior simulation of the MMI as a coupler but also the phase difference in the output ports to be fed back into the model. In addition, the null port is limed to numerical noise comparable to the actual extinguished light level in a high-performance nuller and requires much longer run times than an imbalance simulation to determine k. This longer simulation time is required to firstly use a smaller Z step size to overcome the numerical noise and secondly to use a longer model domain. A longer domain is required to match that of the actual chip and capture the effects of stray light radiated from the MMI slab after it dissipates realistically. This is required to simulate the actual chip facet output. The extinction simulation arguably provides a more accurate representation of what will be measured in the real device, but in what follows it is assumed that any radiated light is suppressed as it would be by suitable design for a real, high-performance device. Hence it is convenient to simulate the imbalance and calculate k instead. Thus for the extinction, using the above equations, k was simulated in RSoft BeamPROP using an input of $[1;0]$ with the transmission (α) normalised out using

$$\frac{\text{Output1}}{\text{Output1}+\text{Output2}}=\frac{\alpha k}{\alpha k+\alpha(1-k)}=k.$$

Note here that the numerical noise is still present in these simulations but due to the difference in scale it was negligible in the determination of k. It does beg the question of how accurate k needs to be in determining the extinction of an MMI and as such whether the numerical noise has a significant impact on this accuracy. This is a question dealt with for real devices, in Chap. 6, but not for the simulations.

Figure 4.3 shows the extinction bandwidths for the same selection of W_a as Fig. 4.1 for the extinction levels of 40, 50 and 60 dB. Due to limited numbers of wavelength points due to the long run times, the error in the bandwidth was estimated at ± 0.02 µm. Note that the wavelength range for this simulation was restricted to between 3.6 µm to 4.4 µm, which was not wide enough to measure extinction bandwidth at a 30 dB extinction for every W_a.

Figure 4.3 in no uncertain terms shows that $W_a = 0.3W = 13.5$ µm is the worst choice in W_a for a wide extinction bandwidth response. Rather, a choice of $W_a = 6$, 8 and 12.5 µm is optimal as these have the widest extinction bandwidths for the 60 dB

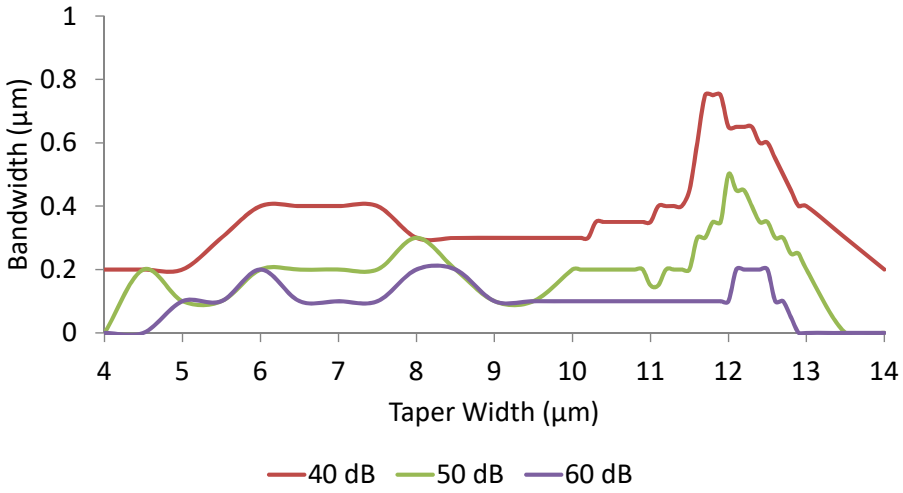

Figure 4.3: The extinction bandwidths of base design MMIs, calculated using the imbalance curves shown in Fig. 4.2 and connected assuming a smooth curve between points, at indicated extinction levels, with a smaller step size about the 12 µm region.

extinction level. For 50 dB the $W_a = 6$ µm peak disappears and the $W_a = 12$ µm peak begins to show a significantly wider bandwidth than the others. At the lower extinction level (40 dB) the $W_a = 8$ µm peak is reduced to that of the surrounding W_a making this peak meaningless for low extinction bandwidth requirements, the $W_a = 12$ µm peak however becomes the dominant region of high extinction bandwidth. Regardless, Fig. 4.3 shows that 8 and 12.5 µm (and possibly 6 µm, see Sec. 4.5 for more details) are the W_a to chose from for a wide-band extinction at 60 dB and 12 µm is best if the extinction need only be 50 dB or lower. These are the W_a selected for investigation with an attempt to determine why they have a high extinction bandwidth and the $W_a = 13.5$ µm does not.

The imbalance curves for the same MMI but with $W_a = 8$, 12 and 13.5 µm are shown in Fig. 4.4. In respect to W these W_a can be rewritten as $0.18W$, $0.27W$ and $0.3W$ respectively. In Hill et al. [196] $0.3W$ and $0.2W$ wide taper widths were shown to have a low imbalance and Morrissey et al. [203] indicated that an MMI with $W_a = 0.25W$ or $0.29W$ has a good "coupling efficency", but neither compared the bandwidth response of W_a to the optimum MMI in terms of transmission - one with $W_a = 0.3W$.

The imbalance plots are shown in Fig. 4.4 indicating the contrast in shape with W_a. The imbalance curve for an MMI with $W_a = 13.5$ µm for example shows a monotonic increase with increasing wavelength with only a single zero-crossing. By default, this means it can only have a narrow, high extinction bandwidth. The MMI with $W_a = 8$ and 12 µm imbalance curves are highly non-monotonic and have multiple zero crossings with small amplitude oscillations around zero imbalance in the band of interest. It is this feature that gives them their large, high extinction bandwidths. The 8 µm curve also exhibits large imbalance side-lobes that rapidly rise away from the operational band of the device. Why these imbalance curves have this functional dependence and whether this is a more general trend are questions of interest for this chapter.

In Sec 4.4 and 4.5 RSoft BeamPROP is used to simulate the taper length dependence

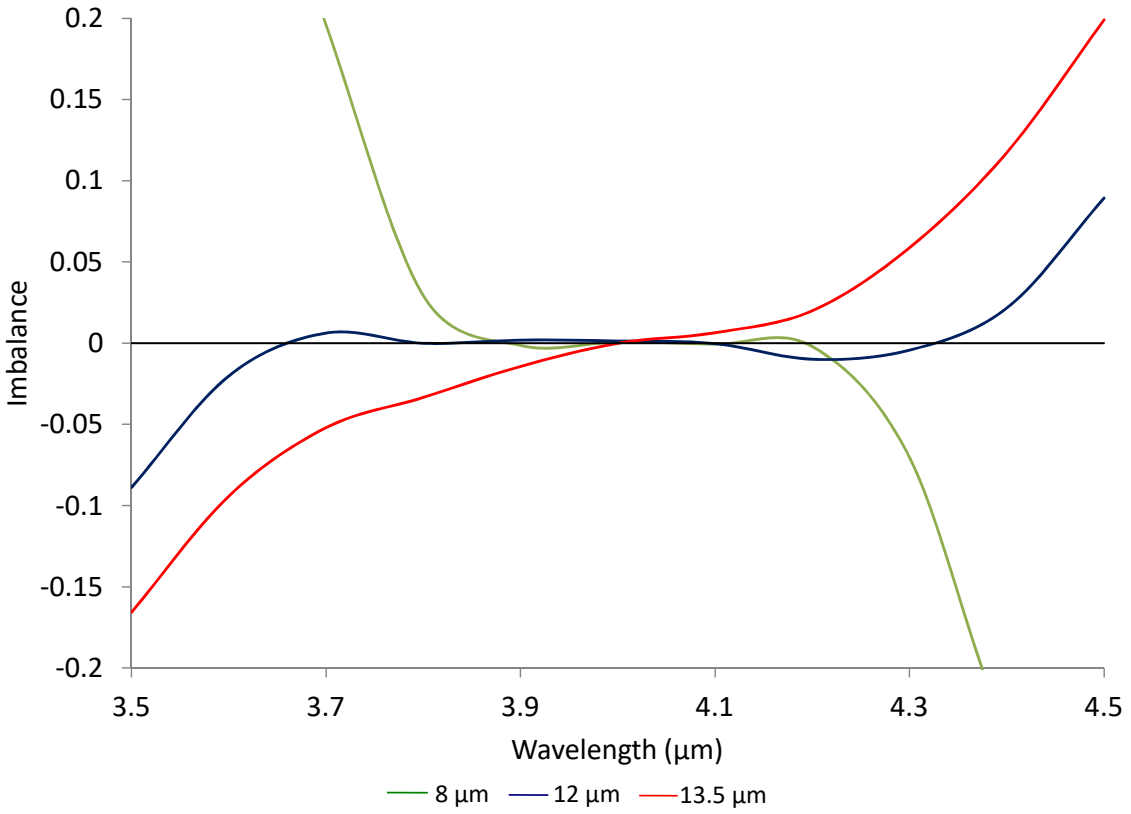

Figure 4.4: The imbalance curves of MMI with W_a = 13.5, 12 and 8 µm calculated in RSoft BeamPROP.

for these extinction bandwidths and the W_a dependence for MMI with varying W respectively. For a realistic investigation of what is occurring inside the MMI, regarding mode excitation due to W_a, using the approximate model from Chap. 3, with a W_a dependence added, is required as RSoft BeamPROP lacks functionality in this regard.

4.2 Adding taper width to the MMI model

Whilst BeamPROP provides an accurate simulation of the whole device, it provides little to no understanding of the physical mechanisms that lie behind the attained performance. To achieve insight, it is necessary to use the theory set up in Chap. 3 to construct the wavefront at the end of the MMI cavity. This allows for the wavefront to be deconstructed into each mode (approximated as a sine function) to investigate the effect of each mode on the imbalance curve. The theory described in Chap. 3 had no functional dependence on W_a but using a launch field that does provides the required dependence [196].

Beginning with an approximation that the MMI modes simplify to a sinusoid with zero field outside the MMI cavity, the modes are represented as

$$\psi_\nu(x) = \sin\left[\pi(\nu+1)\frac{x}{W}\right] \tag{4.2}$$

for all supported modes (ν) in W (along the x direction where beam propagation is in the

z direction).

The input field is also assumed as sinusoidal, again with no field outside the taper. An offset, so that the taper is centred at position x_c (which will be set to $W/3$ later), is used and the width is set to W_a. Hence at $L = 0$ the equation describing the overall wave inside the MMI, eq. (3.9), is replaced with

$$\Psi(x, 0) = \sin\left[\frac{\pi(x - x_c + W_a/2)}{W_a}\right]. \tag{4.3}$$

Thus the overlap function from eq. (3.3) is

$$c_\nu = \frac{4W_a}{\pi W(1 - (\nu+1)^2\left(\frac{W_a}{W}\right)^2)} \cos\left[\pi(\nu+1)\frac{W_a}{2W}\right] \sin\left[\pi(\nu+1)\frac{x_c}{W}\right]. \tag{4.4}$$

The performance of the MMI can now be modelled as a function of W, L, W_a and wavelength with relatively straightforward fast execution code. The assumption of each mode as a sine wave, however, implies the results will be in error compared to the RSoft BeamPROP model and the experimental results. This model will be used instead to approximate the RSoft model and show changes based on the removal of modes excited in the MMI cavity and not as a comparison to experimental results.

4.2.1 The excitation coefficients

The selected $W_a = 8$, 12 and 13.5 µm are now investigated, for the MMI as before, concerning what modes are excited and how each mode is weighted when combined to form the total wavefunction at the end of the MMI cavity. Explicitly the MMI dimensions (related to eq. (4.4)) are: $W = 45$ µm and $x_c = W/3$.

Note that the V number approximation, eq. (3.4), was again used to approximate the number of modes in the MMI cavity:

$$V = \frac{2\pi}{\lambda} W \sqrt{n_{\text{core}}^2 - n_{\text{cladding}}^2},$$

This predicts 29 modes are excited in the cavity. The excitation coefficients from eq. (4.4) are presented in Fig. 4.5 up to the 29^{th} mode.

Figure 4.5 is the graphical interpretation of eq. (4.4). For each W_a the restricted mode interference condition, $c_{\nu=2,5,8,\ldots} = 0$, is met by $x_c = W/3$ [194]. Further investigation into this figure and the graphical interpretation of each component in eq. (4.4) will provide reasons for why the imbalance shapes are as they are, and may answer why the extinction bandwidth is increased for MMI with $W_a = 8$ and 12 µm compared to an MMI with $W_a = 13.5$ µm.

The first and potentially the most significant difference between the W_a shown in Fig. 4.5 is the additional zero excitation coefficient in the 13.5 µm data at $\nu = 9$. The impact on the wavefront is investigated later but having one less mode in the final wavefront would intrinsically have a significant effect on the coupling ratio and hence the imbalance.

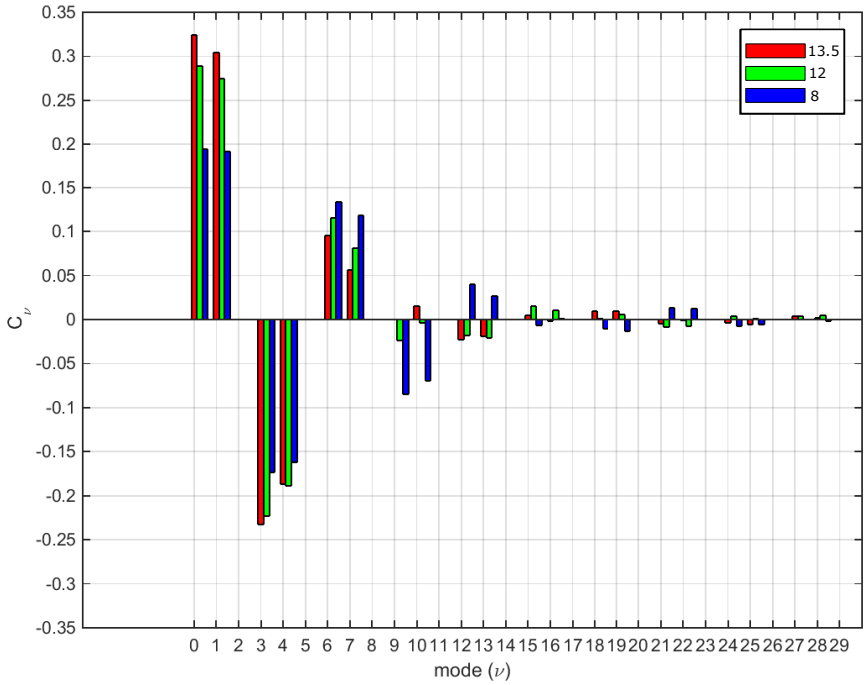

Figure 4.5: MMI slab mode excitation coefficients at $W_a = 13.5\,\mu m$ (optimum transmission), $12\,\mu m$ (optimum bandwidth for a 40 dB and 50 dB null), and $8\,\mu m$ (optimal bandwidth for a 60 dB null).

From observation of Fig. 4.5 other significant trends include the sign of the excitation coefficients and whether they are equal at various ν. This difference could be the reason for the "wings" in the imbalance curve. A reason to suspect this is that between $\nu = 10$ and 24 the excitation coefficient's sign for the MMI with $W_a = 12\,\mu m$ and $13.5\,\mu m$ (that have imbalance curves without "wings") are opposite to the MMI with $W_a = 8\,\mu m$ (that has an imbalance curve with "wings"). Noting that the lower modes having higher excitation coefficient magnitudes, and that past the 24^{th} there is likely no significant effect on the imbalance curve, and that before the 10^{th} mode the initial, global, structure of the imbalance curve is being established; these modes are significant to the construction of the $W_a = 8\,\mu m$'s imbalance curve and could indeed cause a shift in the extinction bandwidth.

Why Fig. 4.5 appears the way it does is explained by investigating the two terms in eq. (4.4) that have a W_a dependence: the cosine term and the denominator of the leading multiplicative term. The sine term is similar for all W_a and thus is not expected to be significant in increasing the extinction bandwidth with a change in W_a.

4.2.2 The cosine term

The cosine term of eq. (4.4) is shown in Fig. 4.6. Mathematically it was expected to be zero for each $\nu = W * n/(W_a) - 1$, where n is an odd number and ν is a positive integer. Only the MMI with $W_a = 13\,\mu m$ fits this formula (with an integer response) at $c_{\nu=9} = 0$. There is one more zero mode, $c_{\nu=29} = 0$, but that is also a global zero due to the sine

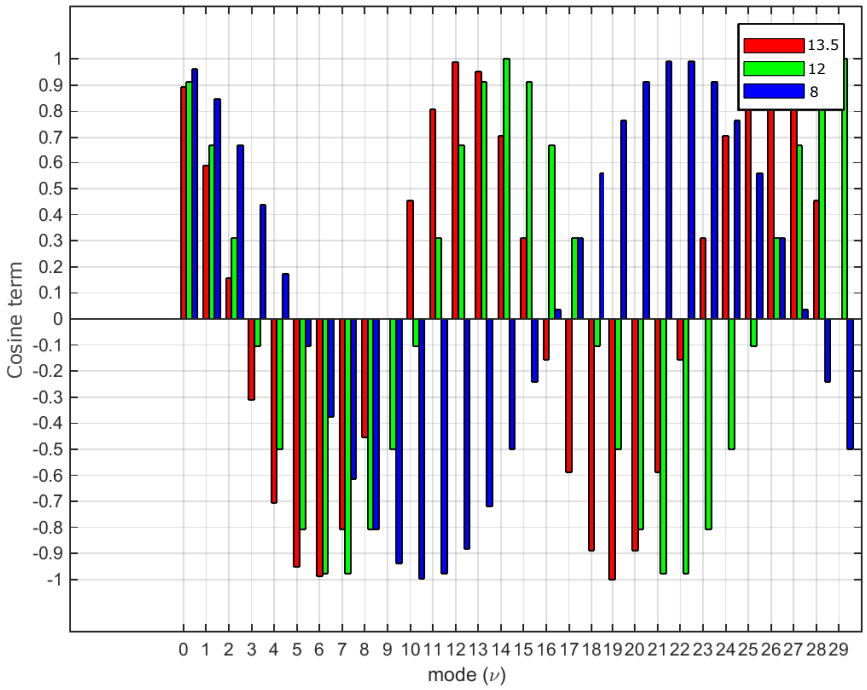

Figure 4.6: The cosine term, see eq. (4.4), of the MMI slab mode excitation coefficients at $W_a = 13.5$, 12 and 8 µm.

term of eq. (4.4) and hence not different between W_a.

As mentioned above the excitation coefficient sign difference between the MMI with $W_a = 13.5\,\mu m$ and the others may be integral to the structural difference between the resulting imbalance curve. From Fig 4.6 the turning point for each W_a, where the curve swaps between the positive and negative regime, is determined by the $\nu = W * n/(W_a) - 1$.

From Fig 4.6, the first significant turning point is at $\nu = 9$, for the MMI with $W_a = 13.5\,\mu m$. It is here where the sign of each subsequent excitation mode is opposite to that of an MMI with $W_a = 8\,\mu m$. A similar argument can be made with an MMI with $W_a = 12\,\mu m$ at $\nu = 10$: leaving the $W_a = 8\,\mu m$ curve alone in the negative regime. This opposition in sign is not balanced until the 23^{rd} and 26^{th} mode, by observation of Fig. 4.5, but this is not solely due to the cosine term.

A potentially significant find from Fig. 4.6 is that for $W_a = 8\,\mu m$ the second crossing of zero is close to $\nu = 16$ (exactly at $\nu = 15.875$). This explains why the excitation coefficient is small - $C_{\nu=16} = 0.0008$. The fact that it is not zero is significant in that this mode exists in the final wavefront in the MMI, however, it may require further investigation in determining whether the diminishing of this mode, in particular, has a significant impact on the imbalance curve. Such an investigation is undertaken in Sec. 4.3 below.

The significance of the staggered crossing areas relates to how the modes interfere - constructively or destructively - at the end of the MMI cavity. The sign change based on the cosine term, noting that the sine term is similar for each W_a and will not provide a sign variation, alters how the higher-order modes interfere with the fundamental modes.

It is this shift that is investigated here and potentially what is causing the imbalance to become flat away from $W_a = 13.5\,\mu m$.

4.2.3 The denominator term

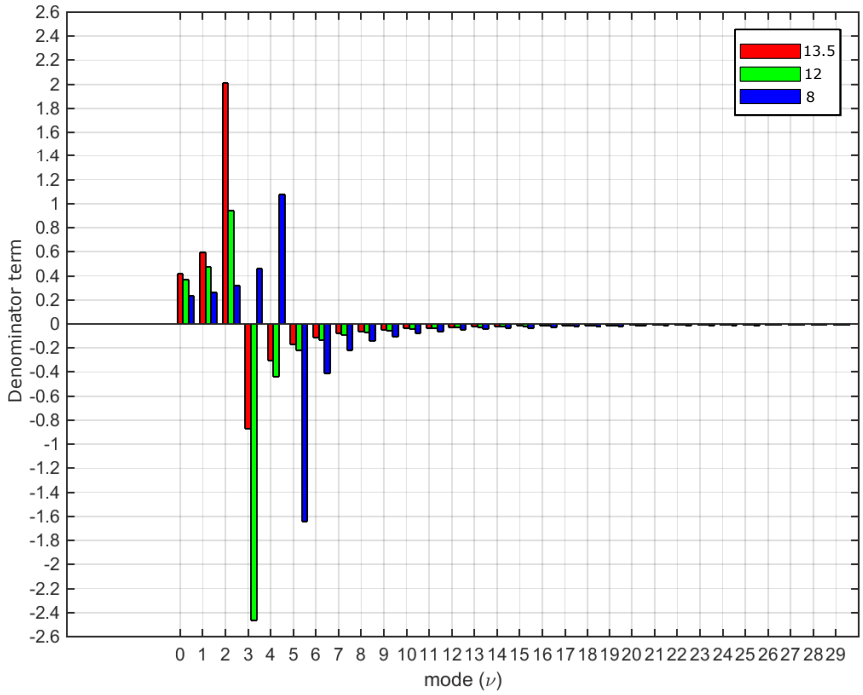

Figure 4.7: The reciprocal of the denominator term in the MMI slab mode excitation coefficients equation, from eq. (4.4), at $W_a = 13.5\,\mu m$, $12\,\mu m$, and $8\,\mu m$.

The first few modes, before the first cosine zero crossings in Fig. 4.6, are similar in that they have a large excitation value regardless of W_a, shown in Fig. 4.5. This is due to the nature of the denominator in the leading multiplicative term in eq. (4.4). The reciprocal of the denominator term is plotted as a function of ν in Fig. 4.7. If the W_a is a divisor of W then this term tends towards a positive infinity as $n^- \to 1$ in the equation $\nu = W * n/(W_a) - 1$ (the equation for the cosine term going to zero) and a negative infinity as $n^+ \to 1$. Whether this term goes to infinity depends on whether the sine and cosine terms go to zero at this point. If so then the model will go to zero and if either do not then it will go to infinity. As none of the W_a has their inverse term goto infinity this is not investigated in this work but it is highlighted here for future simulations to investigate whether this singularity is in some way physical and if so whether it can be used to control the imbalance curve.

Figure 4.7, for the W_a simulated, only serves to show two things: higher-order ν will be constrained to almost zero, which was already known from Fig. 4.5, and for the few inverse terms before $c_\nu \to \pm\infty$ work against the cosine terms to maintain an equal sign between all W_a. The latter implying that all three W_a have a similar "base" to build their imbalance curves from.

The implication here is that the initial modes dominate the behaviour of the MMI and that smaller MMI would behave similarly, as only the larger modes would not be excited. This ceases to be true when only a few modes are excited. This raises the question of how does the MMI couple light with limited modes: When only $0 > \nu > 10$ are excited in an MMI cavity (if it still is an MMI with so few modes), for example, how would the imbalance curve behave? It is this that is investigated next: what is the effect of each ν on the imbalance curve?

4.3 The effect on the imbalance when removing selected modes

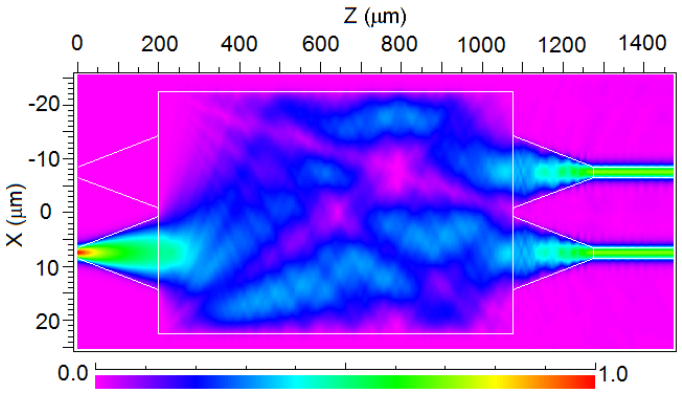

Figure 4.8: MMI with a single input resulting in a 3 dB splitting. Light propagates from left to right.

The imbalance is the normalised subtraction of the two output ports. Fig 4.8 highlights how the light propagates through the MMI and into the output ports. To recreate this, and calculate the light at the output ports eq. (3.9):

$$\Psi(x, L) = \sum_{\nu=0}^{t-1} c_\nu \psi_\nu(x) \exp\left[i \frac{\nu(\nu+2)\pi}{3L_\pi} L\right],$$

is used, and now with a taper width dependence added from eq. (4.4). For simplicity the calculation takes place at the end of the MMI cavity, $L = 875\,\mu\text{m}$, rather than at the end of the output tapers. The effect of the taper limitation of this simplification is discussed in Sec. 4.4 below.

Equation (3.9) is created through multiple equations: The excitation coefficient (c_ν) is found using eq. (4.4), the sine approximation from eq. (4.2) is used for $\psi(x)$ and the exponential term is simply calculated at $L = 875\,\mu\text{m}$. Each $\psi(x)$ was calculated individually before being added together, this allowed for selected modes to be removed. For the imbalance calculations Ψ was calculated only across the width of the output tapers (x_c),

restricting the x axis to

$$\begin{aligned} \text{port 1 co-ordinates} &= \frac{45}{3} \pm \frac{W_a}{2} \\ \text{port 2 co-ordinates} &= 2 * \frac{45}{3} \pm \frac{W_a}{2} \end{aligned} \tag{4.5}$$

where 45/3 and 2*45/3 are the positions of the input and output tapers (x_c) for the restricted interference MMI.

Partitioning the wavefront as per eq. (4.5) provides the electric fields of both output ports and thus the imbalance can be calculated. Imbalance calculations for the standard MMI with $W_a = 8$, 12 and 13.5 µm are shown in Fig. 4.9 with an RSoft BeamPROP model as a comparison.

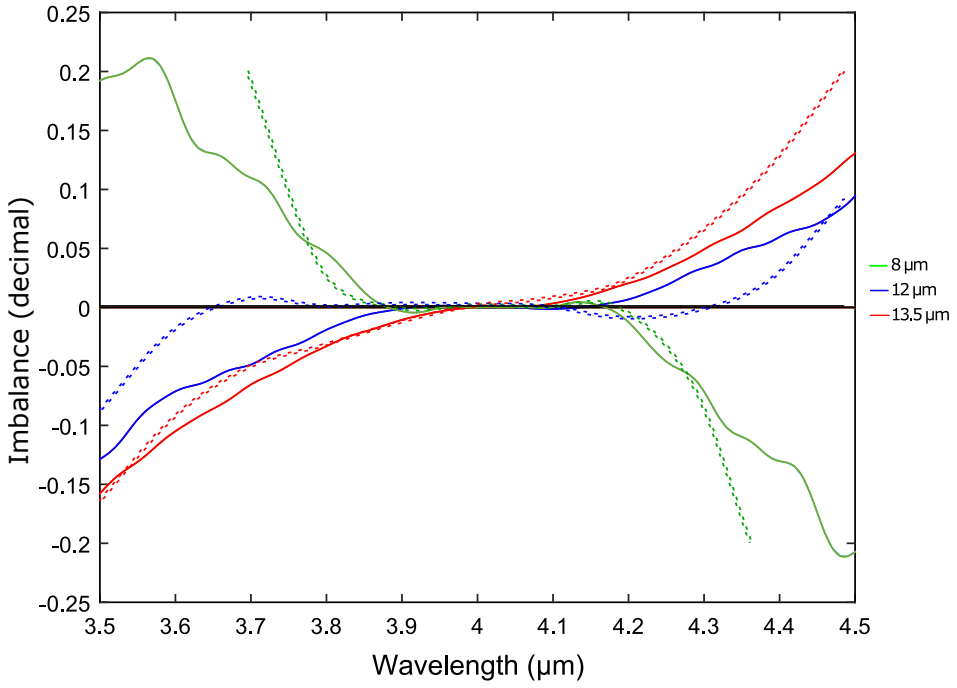

Figure 4.9: The calculated imbalance based on the wavefront using eq. (3.9) with the same MMI simulated using RSoft BeamPROP (dotted lines).

Comparing simulation approaches in Fig. 4.9 the approximate calculations reproduce the shape of the imbalance curves as simulated in RSoft BeamPROP, but not the bandwidths around zero imbalance. Thus this method cannot predict the W_a to extinction bandwidth relation. As such it can only be expected to provide insight into the behaviour of the devices.

Now that an approximation of the imbalance response has been generated, the impact of removing selected modes on the shape of the imbalance curve can be investigated. Note here that removing all higher-order modes is equivalent to shrinking the width of the MMI, with the corresponding length change. Removing select modes is not physical, other than the example explained above that removes the 9^{th} mode, but a useful tool to understand the effect of the mode on the imbalance curve.

Focusing on $W_a = 8\,\mu\text{m}$, Fig. 4.10 shows the imbalance curves from the approximate model for the $W_a = 8\,\mu\text{m}$ with selected mode ranges removed.

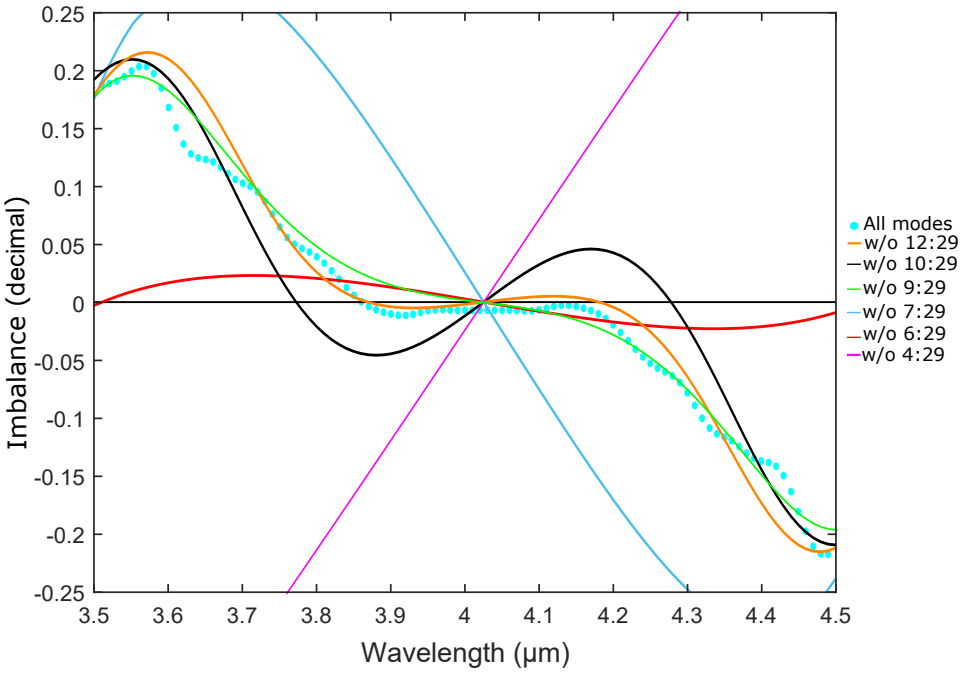

Figure 4.10: The calculated imbalance based on the wave equation, eq. (3.9), for an MMI with $W_a = 8\,\mu\text{m}$.

Looking back at Fig. 4.5, from approximately $\nu = 12$ the modal excitation coefficients diminish significantly and this is reproduced in Fig 4.10 with the imbalance curve with $\nu \geq 12$ removed almost indistinguishable from the imbalance with all ν included. The figure shows that the "shape" of the imbalance curve remains the same until $\nu \geq 10$ are removed and shift the first (and last) zero-crossing away from $4\,\mu\text{m}$. This lowers the "wings" significantly below zero. Removing an additional mode, $\nu = 9$, the "shape" appears to be similar to when all ν are included with an important exception: the imbalance only crossing zero once. With more ν removed the "shape" changes more and more from the original until all but the first four ν remain and the imbalance resembles that of an MMI with $W_a = 13.5\,\mu\text{m}$ more than the imbalance curve of an MMI with $W_a = 8\,\mu\text{m}$ and all modes included.

For the $W_a = 12\,\mu\text{m}$, the equivalent figure is included as Fig. 4.11. The higher order excitation coefficients are diminished beyond $\nu = 10$ from Fig. 4.5. Figure 4.11 reproduces this with the mode filtered imbalance curves with $\nu \geq 10$ removed and all ν included imbalance curves overlapping well.

Unlike with the $W_a = 8\,\mu\text{m}$ removing the 9^{th} term for $W_a = 12\,\mu\text{m}$ increases the bandwidth and it is the exclusion of ν beyond the 6^{th} mode that has the imbalance cross zero only once. Removing the 7^{th} mode too changes the shape of the imbalance so that the "wings" have significant excursions from zero. Note here that our previous publication [204] explored the removal of the 9^{th} mode, coming to the conclusion that

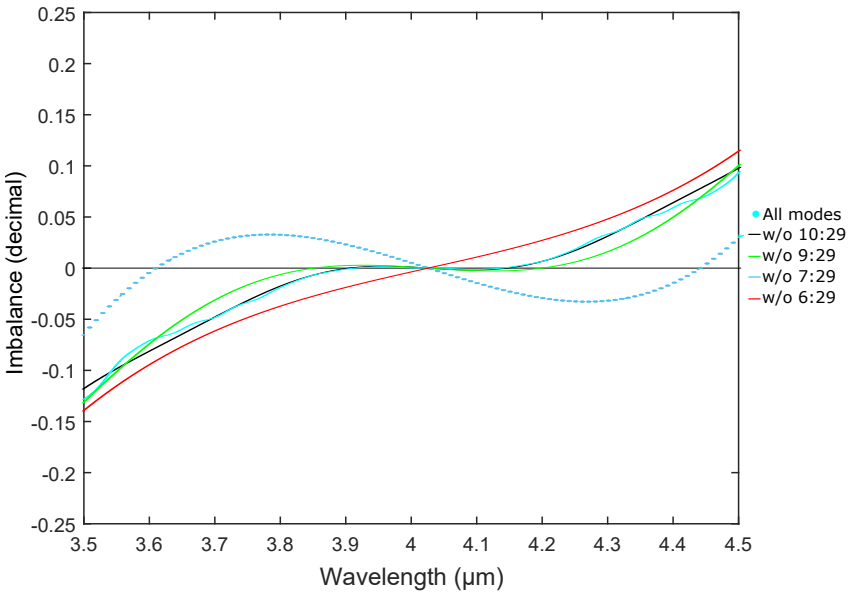

Figure 4.11: The calculated imbalance based on the wave equation, eq. (3.9), for $W_a = 12\,\mu\text{m}$.

the 9^{th} mode was vital for flattening the imbalance curve around zero for an MMI with $W_a = 12\,\mu\text{m}$. Although this is true for the MMI with an $W_a = 8\,\mu\text{m}$ it cannot be said to be as important for $W_a = 12\,\mu\text{m}$ based on the calculations included here. The difference between the model used in Ref. [204] and this thesis is that an overlap calculation to the fundamental mode of the output taper was used to generate the imbalance curves in the paper whereas the integration of the wavefront directly is used here. The model in this thesis points to a dependence on the odd modes, in general, having a significant effect on flattening the imbalance curve rather than just the 9^{th} mode as was suggested in the paper.

The secret to a larger imbalance may be in the odd modes in the MMI. These modes are significant because they are asymmetric. As such they have opposing signs at the output tapers and so the odd modes serve to increase the field on one taper and reduce it in the other: As the wavelength scans - at wavelengths close to, but shorter, than the design central point - the odd modes are phased such that they compensate the negative imbalance. With a similar effect for the wavelengths directly after the design central point (the design central point being 4000 nm in these calculations). Hence the flattening of the imbalance.

The imbalance of the odd ν are shown in Fig. 4.12 for an MMI with $W_a = 8\,\mu\text{m}$. Calculating the imbalance of a particular ν is the same as for an entire wavefunction (in eq. (3.9)) but with the sum over all ν limited to $\nu = 0$ and the selected ν. The odd ν, in Fig. 4.12, provide a periodic imbalance. Note that a similar imbalance curve can be generated for a $W_a = 12\,\mu\text{m}$ however all the imbalance curves are diminished due to lower c_ν and thus harder to differentiate. The implication of Fig. 4.12 is not that the even ν contribute nothing: $\nu = 10$ especially is vital, shown in Fig. 4.10, as without it the "wings" of the imbalance curve move away from zero and decrease the bandwidth; it is more than

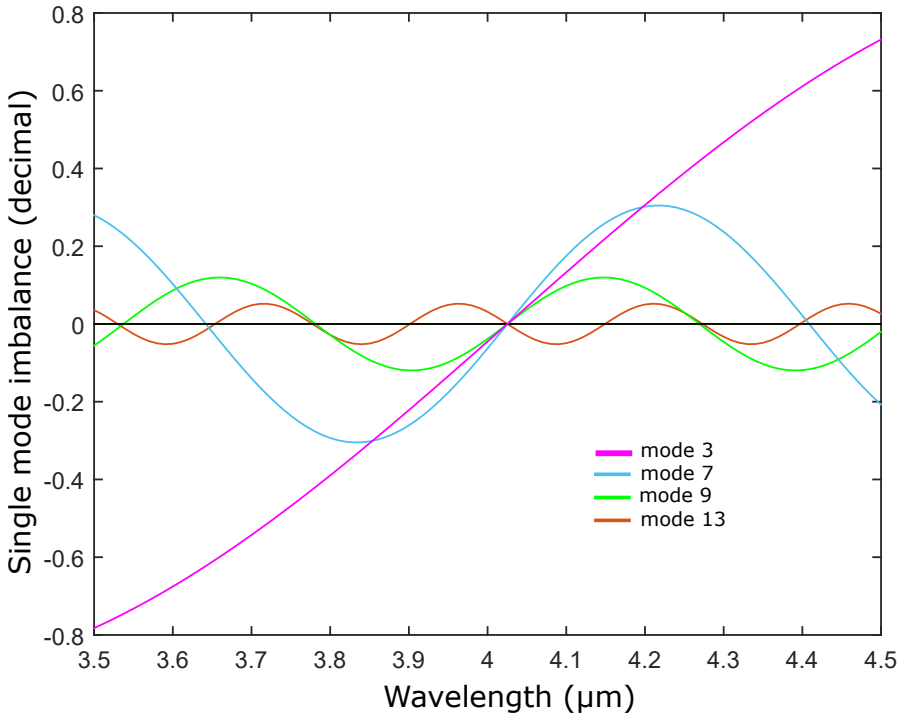

Figure 4.12: The calculated imbalance based on the wave equation, eq. (3.9), for $W_a = 8\,\mu\text{m}$ with only the fundamental mode ($\nu = 0$) and the selected ν of 3 (in pink), 7 (in blue), 9 (in green) and 13 (in brown) excited respectively.

the asymmetry of the odd ν allows for a change in the periodicity of the imbalance, as the equivalent image in Fig. 4.12 with even ν listed would show nothing but a horizontal line at zero - illustrating the odd modes vary independently offering some control over the imbalance curve by removing them. This asymmetric change affects the "shape" of the imbalance curve and can either flatten the imbalance at the zero crossing or push the "wings" away from zero.

As an example of the odd ν asymmetry, return to the argument of the 9^{th} mode and compare Fig. 4.13a to Fig. 4.13b, the prior containing a series of imbalance curves of MMI with $W_a = 12$ to $8\,\mu\text{m}$ and the later the same without $\nu = 9$. Using these figures the effect of $\nu = 9$ is examined. When $\nu = 9$ is included, each imbalance curve crosses zero imbalance and stays close to zero until crossing zero again whilst maintaining symmetry. With $\nu = 9$ removed, the imbalance curves shift from a symmetric horizontal shape to a diagonal with the only exception of $W_a = 12\,\mu\text{m}$. Note that for Fig. 4.13a the $c_{\nu=9}$ is decreasing as the W_a increases and so the influence of this odd ν decreases with increased W_a only serving to increase the bandwidth for $W_a = 12\,\mu\text{m}$.

This section has focused on how the bandwidth can be wider for tapers compared to the optimum, in terms of transmission, $W_a = 13.5\,\mu\text{m}$. Looking at the individual ν excited in the MMI slab, $\nu = 9$ is missing in $W_a = 13.5\,\mu\text{m}$ and without $\nu = 9$ an MMI with $W_a = 8\,\mu\text{m}$ has a diminished bandwidth. The same cannot be said for $W_a = 12\,\mu\text{m}$ but instead it is $\nu = 7$ that decreases the bandwidth. Although more work is required to

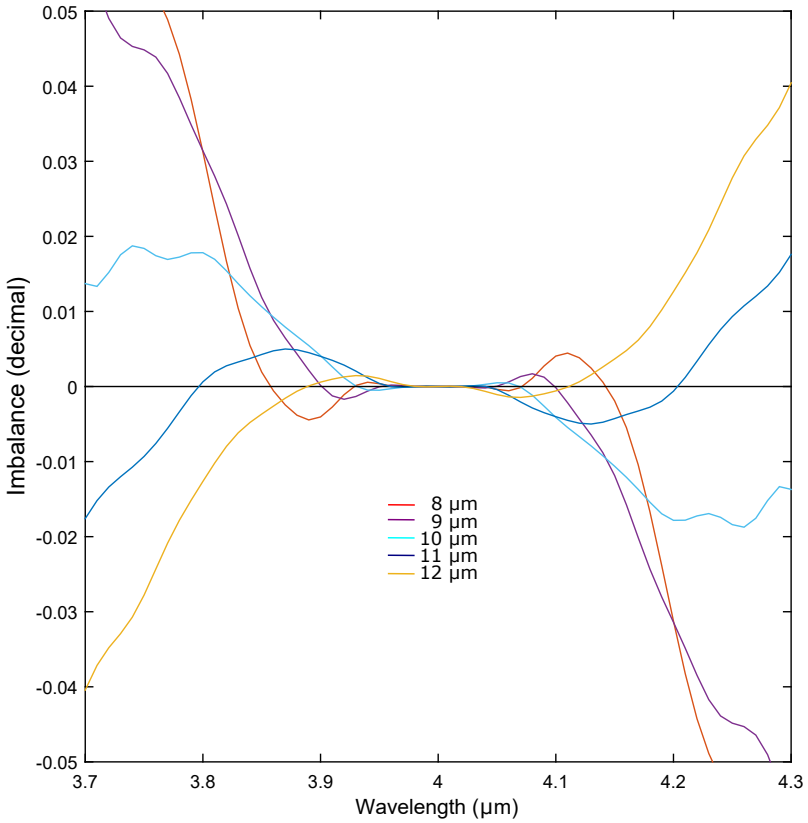

(a) Imbalance curves of MMI with $W_a = 8\,\mu\text{m}$ to $12\,\mu\text{m}$.

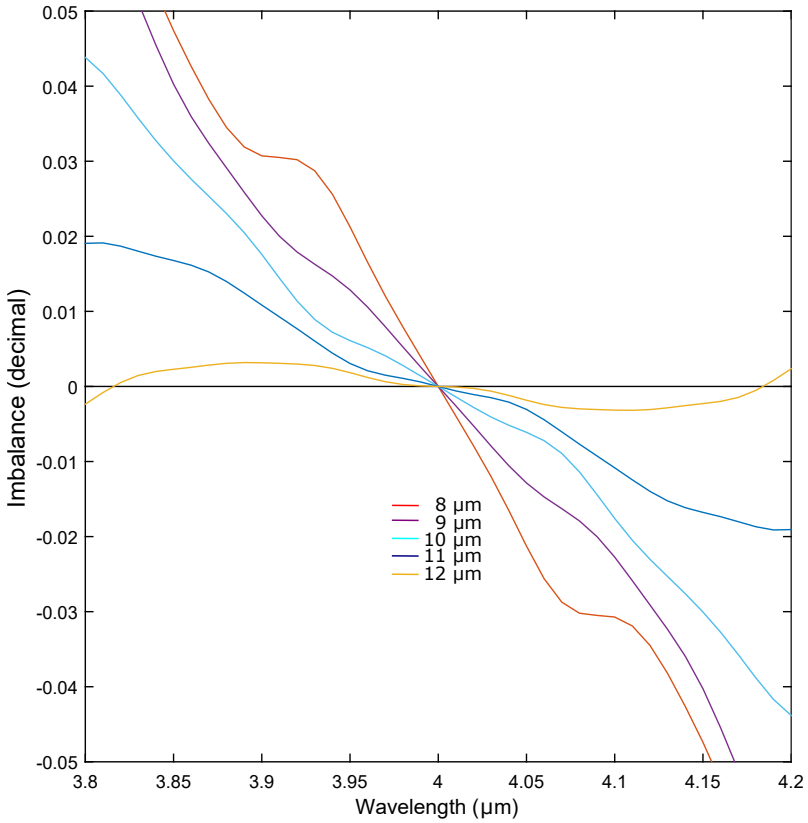

(b) Imbalance curves of MMI with $W_a = 8\,\mu\text{m}$ to $12\,\mu\text{m}$ with the $\nu = 9$ missing.

utilise these results in a meaningful way - artificially removing ν in a real device, similar to how placing the input ports at $W/3$ removes $\nu = 2, 5, 8...$, to extend the bandwidth. One idea is to decrease the higher-order modes by decreasing the width of the MMI cavity. It has been shown in this section that the higher-order modes do not affect the overall shape of the MMI but they do reduce additional structure and removing them should provide a flat imbalance curve and potentially an increase in the extinction bandwidth. This is explored using RSoft BeamPROP in Sec. 4.5 as the model provided so far is agnostic to W.

4.4 Taper lengths

The analysis to date has ignored any mode coupling effects or additional loss due to the output taper. This simplification was made under the assumption that the mode interactions within the taper and the subsequent 2 µm wide waveguide has no significant impact on the MMI's imbalance. Whether this assertion is accurate will not be conclusively stated in this thesis and further investigation into this matter is required. The dependence on the outgoing waveguides is subject to impurities in the core layer such as pillars of the cladding material grown into the core material that could induce scattering loss and thus provide a further imbalance in one arm. This is taken into account in the experimental data analysis in Chap. 6. It won't, however, change the "shape" of the MMI imbalance curve.

For the behaviour of the light inside the tapered area, between the input and output waveguides and the MMI cavity, and whether it changes the MMI's imbalance curve, an anecdotal (simulated) experiment was conducted using RSoft BeamPROP (as the previous model in this chapter has no taper length dependence). The base MMI, $W = 45$ µm with $W_a = 13.5$ µm, was again utilised.

Figure 4.14 shows the selected imbalance curves for an MMI with taper length = 20, 40, 80 and 100 µm, to best illustrate the change in curve.

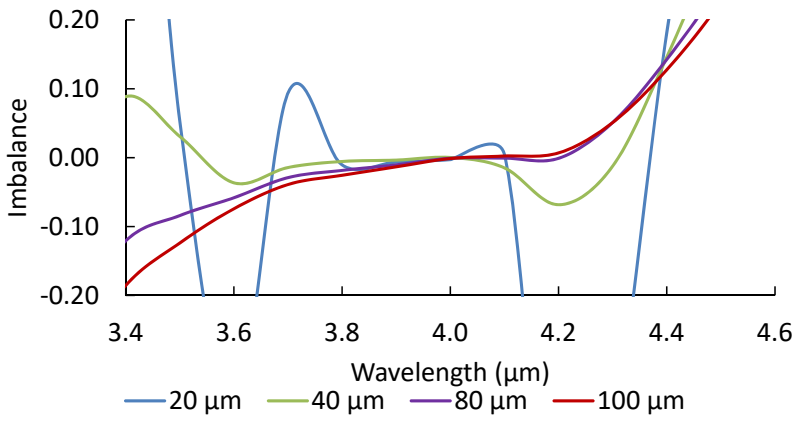

Figure 4.14: The imbalance curve of an MMI with $W = 45$ µm, $L = 875$ µm, $W_a = 13.5$ µm and taper lengths 100 (red), 80 (purple), 40 (green) and 20 µm (blue).

The imbalance curves in Fig. 4.14 show that the shorter taper length change the curve's "shape" significantly: flattening the imbalance around zero for the 40 µm taper length simulation and adding "wings" in the 20 µm taper length simulation. An explanation as to why these are so different to the original (200 µm taper length imbalance curves) may lay in the excited modes of the input taper and the modes that can couple into the output taper. Focusing on the input taper Fig. 4.15 shows the 1/e width (explained in Sec. 5.2.1) of the combined electric field at the taper's interface, not the MMI.

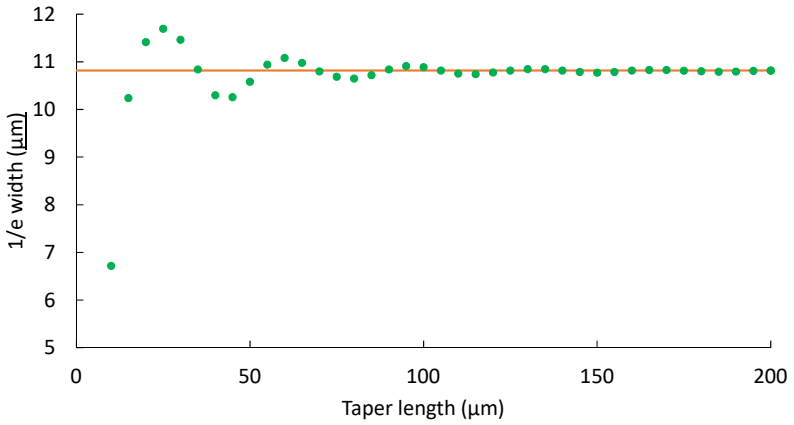

Figure 4.15: The mode size (the 1/e width to be precise) of the combined electric mode at the interface between the taper and the MMI cavity from a taper length of 5 to 200 µm (green circles). The line at 10.9 µm is the 1/e width for a 200 µm long taper.

Figure 4.15 shows an oscillatory behaviour of the 1/e width with an increase in taper length. This change in width is a result of mode coupling, initiated by sidewall scattering. Identifying these modes and contrasting them, as was done for the taper width in Sec. 4.2, may provide further insight into how the imbalance curve of an MMI can be flattened with implications into the extinction depth of that MMI.

From the previous section, there was no expectation that an MMI with $W_a = 13.5\,\mu\text{m}$ will be able to produce a large extinction bandwidth. Using the manipulation of the taper length it appears, from Fig. 4.14, that a flat imbalance response could be achieved between the MMI with 40 and 80 µm taper lengths but further optimisation is required to achieve this. With what is provided here it is possible to achieve 200 nm extinction bandwidth at 60 dB. Figure 4.16 is the calculated extinction depth for the MMI with taper length of 80 µm and 100 µm using the imbalance curves from Fig. 4.14. Note here that the 40 and 20 µm taper lengths are not used because their "wings" cut their extinction bandwidth shorter than the 100 µm taper length extinction bandwidth and thus not worth discussing further.

The extinction curves in Fig. 4.16 compare the "typical" extinction curve provided by the 100 µm taper length and the flat bottom of the 80 µm taper length. Note that the flat bottom curve is not centred at the designed "optimum" wavelength (4 µm), like the typical extinction curve is, indicating an asymmetry in the modes, with wavelength, potentially interfering together destructively to cause the deep extinction bandwidth. Shapes like

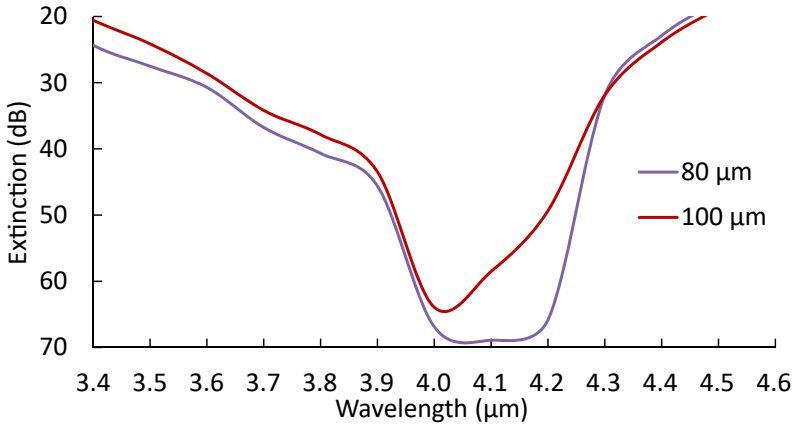

Figure 4.16: The extinction curves for taper lengths 100 (red), 80 µm (purple) curve of an MMI with $W = 45\,\mu m$, $L = 875\,\mu m$ and $W_a = 13.5\,\mu m$.

these are, assuming they are physical, what can be taken advantage of to increase the extinction bandwidth for the MMI.

The improvement in extinction bandwidth may correlate to a substantial loss in transmission, as seen for $W_a = 8\,\mu m$. The loss of the MMI for the taper lengths specified so far are shown in Fig. 4.17.

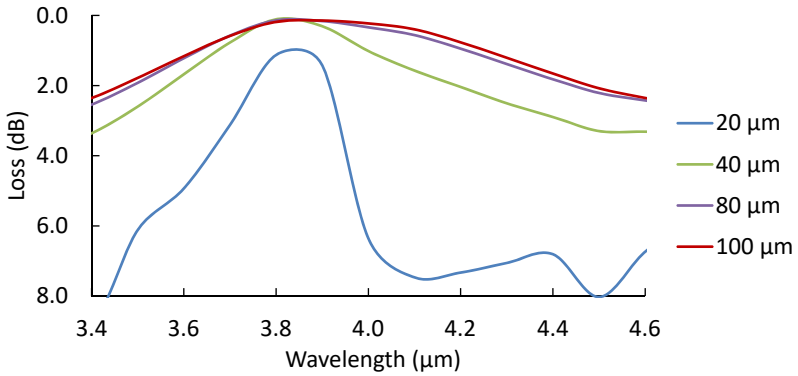

Figure 4.17: The loss, compared to 100% transmission, for an MMI with $W = 45$, $L = 875$, $W_a = 13.5\,\mu m$ and a taper length of 100 (red), 80 (purple), 40 (green) and 20 µm (blue).

Figure 4.17 shows that the 80 µm taper length appears to have minimal additional loss to the 100 µm taper length whereas the smaller taper lengths have substantially more. The indication here is that it is possible to find a taper length that has an increased extinction bandwidth and almost no additional loss.

The equivalent taper length scan was undertaken for the 8 µm taper width with the imbalance curves of 100 µm and 20 µm taper lengths shown in Fig. 4.18.

The shape of the imbalance curves, shown in Fig. 4.18, barely alters between the two taper lengths. There is an additional flattening of the curve in the shorter taper length of 100 nm but nothing as dramatic as for $W_a = 13.5\,\mu m$. Further work may choose to investigate this but $W_a = 8\,\mu m$ already has substantial loss over a large bandwidth and thus already an alternative to an MMI with $W_a = 12\,\mu m$ and does not necessarily need

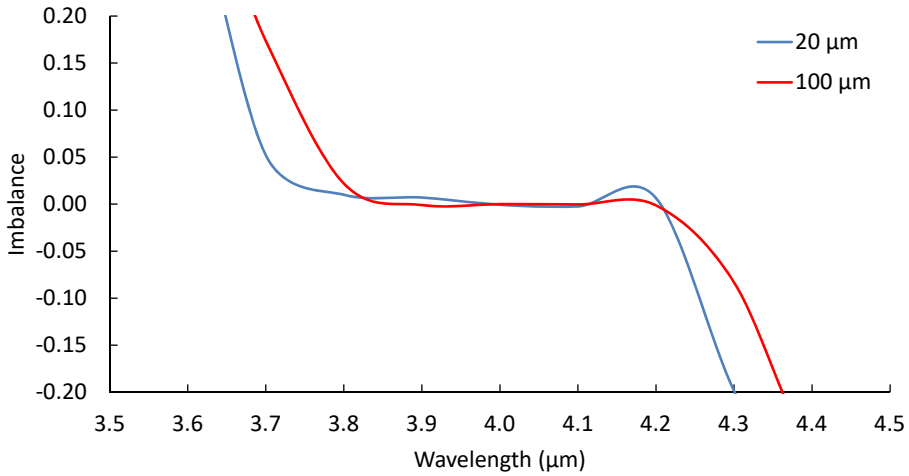

Figure 4.18: The imbalance curve of an MMI with $W = 45\,\mu m$, $L = 875\,\mu m$, $W_a = 8\,\mu m$ and a taper length of 100 µm (red) and 20 µm (blue).

improving in this area - if the transmission had been increased than this would have made an MMI with $W_a = 8\,\mu m$ more attractive. The purpose of this figure is to illustrate that the imbalance curve can undergo flattening at any W_a and that future work could utilise this response.

4.5 Extinction bandwidths of MMIs at other widths

So far this chapter has revealed that at the cost of transmission the extinction bandwidth can be increased with a change to W_a. The question is then posed as to how general a trend the W_a response is and if additional improvements can be made to the extinction bandwidth by changing the W (and proportionately L) of the MMI. This idea was also hinted at in the previous section (Sec. 4.3) when it was shown that the imbalance curves for $W_a = 8\,\mu m$ and $12\,\mu m$ have little dependence on higher-order modes and reducing them makes the imbalance curve smooth.

Using RSoft BeamPROP, the coupling values (k) from eq. (3.18) were found to calculate the extinctions of MMI designs listed in Tab. 4.1 for extinction depths of 30, 40, 50 and 60 dB.

Table 4.1: The widths, lengths and taper widths used in the following simulations. The step size in taper widths was 0.5 µm.

Width (µm)	Length (µm)	Taper Range (µm)
30	385	4 - 10
35	528	4 - 11
40	691	4 - 13
45	874	4 - 14
50	1078	4 - 16

RSoft BeamPROP is used here as an accurate bandwidth is required and the mathematical model in Sec. 4.3 cannot reproduce the same bandwidth as BeamPROP.

4.5.1 Extinction bandwidths

The extinction bandwidths at 30, 40, 50 and 60 dB was calculated for the different MMI designs and are presented below. Note that wide bandwidth data for the 30 dB extinction are inaccurate as insufficient spectral range was used in the simulations, but the trends with W_a are still reliable due to the low bandwidth W_a.

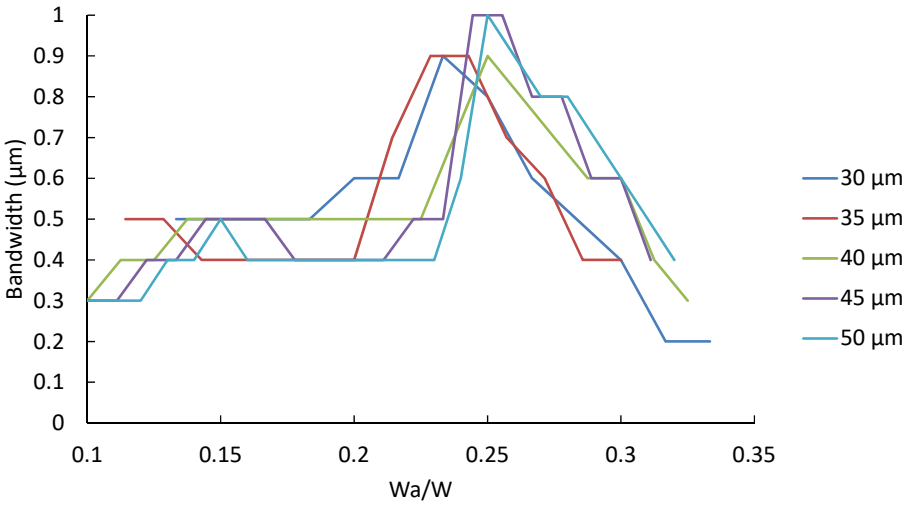

Figure 4.19: The bandwidth of each W at various W_a where the null depth is deeper than 30 dB.

To begin the analysis on the extinction bandwidth the 30 dB extinction depth for various W_a, shown in Fig. 4.19, was explored. This figure shows that each W has a single wide bandwidth peak and all are at a ratio of $W_a/W = 0.25 \pm 0.02$. For $W = 35$, 45 and 50 µm there is potentially a second smaller peak at $W_a/W = 0.15 \pm 0.02$ but it is much lower than the other peak. For these simulations, the wavelength step size is 100 nm due to the large number of time-consuming simulations required leading to potential inaccuracies in determining the exact bandwidth. However, focusing on the position of the high bandwidth area and accepting that more accurate simulation is needed to obtain the actual value then the error for the taper position was calculated as ± half the W_a step size divided by the W.

Figure 4.20 contains the extinction bandwidth curves for the same five W as before but for a 40 dB extinction depth. Each curve has a large peak at $W_a/W = 0.26 \pm 0.01$, similar to the 30 dB graph, and all but the $W = 30$ µm MMI have a second peak at $W_a/W = 0.16 \pm 0.01$. The $W = 50$ µm MMI extinction data appears to have a third peak (the three peaks being at $W_a/W = 0.27$, 0.17 and 0.14 respectively). This provides the three standard taper widths to check for the following extinction data.

Increasing the extinction to 50 dB provided the familiar peaks at $W_a/W = 0.27$ and 0.18 ($W_a = 13.5$ and 8 µm for $W = 45$ µm), shown in Fig. 4.21.

For a 50 dB extinction depth, each curve has two peaks with the first at $W_a/W = 0.26 \pm 0.01$ and the second at $W_a/W = 0.175 \pm 0.005$. There is an additional peak in the $W = 50$ µm MMI curve at $W_a/W = 0.1$. Due to this appearing in the 40 and 50 dB data sets this peak could be the start of a new set of wide bandwidth W_a at low extinctions,

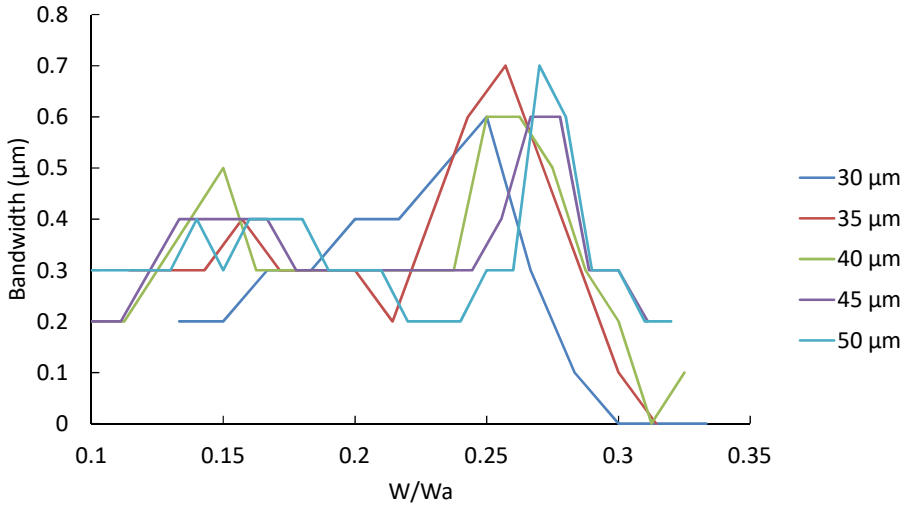

Figure 4.20: The bandwidth of each W at various W_a where the null depth is deeper than 40 dB.

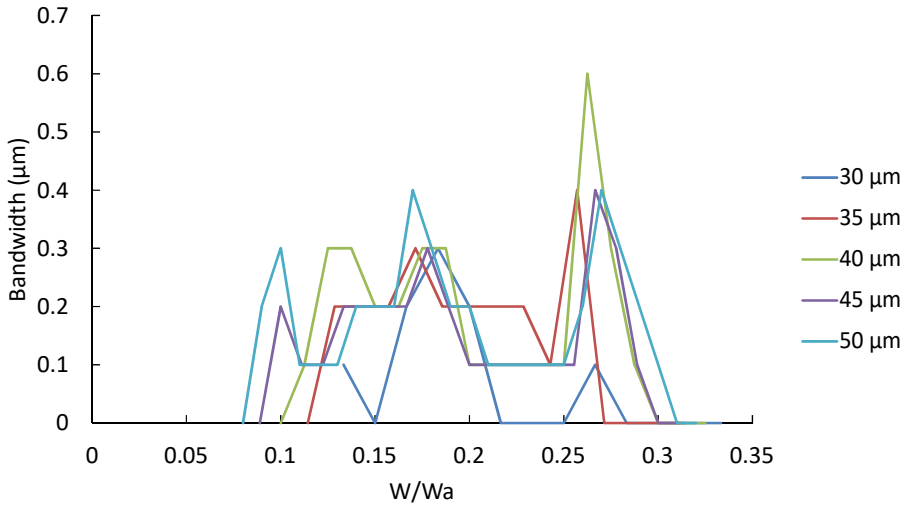

Figure 4.21: The bandwidth of each W at various W_a where the null depth is deeper than 50 dB.

however, there is not enough data, especially at other MMI widths, to confirm this theory. As expected the bandwidth of each peak is lower with each increase in extinction depth, except for the first peek of the $W = 40\,\mu m$. This peak is 200 nm higher than the other peaks displayed in Fig. 4.21 which is unique as all other peaks, in their group, are within 100 nm of each other.

Figure 4.22 shows the bandwidths at an extinction depth of 60 dB. The figure shows that the W_a/W ratio of 0.17 becomes the dominant peak in the bandwidth curve, except for $W = 45\,\mu m$ that still has a larger peak at $W_a/W = 0.26$ - reaching 300 nm bandwidth.

At this depth only two MMI have curves 300 nm wide: $W = 35$ and $45\,\mu m$. This is contrary to the previous, more detailed, simulation of Fig. 4.3 which shows a 160 nm bandwidth for an MMI with $W = 45\,\mu m$ and $W_a/W = 0.27$. This difference has arisen due to the coarser wavelength step size in the data of Fig. 4.22 (100 nm versus 20 nm respectively). With the smaller step size it was found that at 3900 nm and 3920 nm the

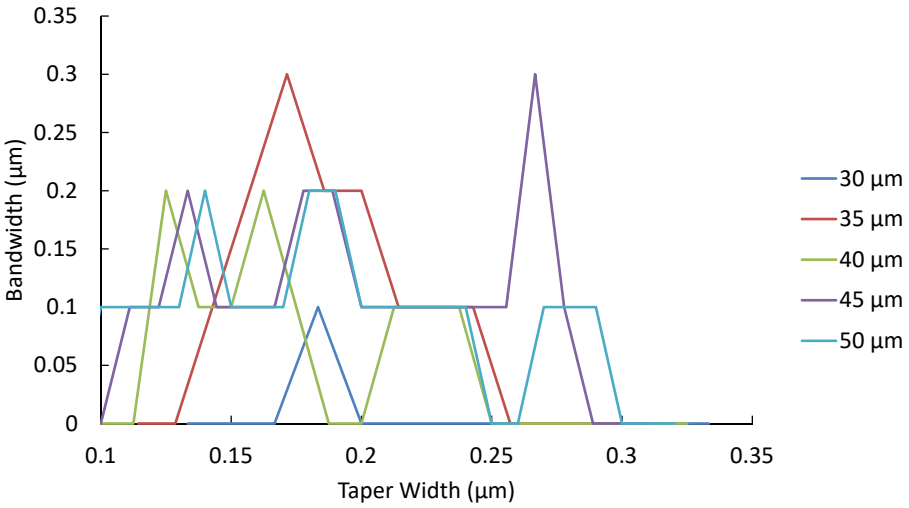

Figure 4.22: The bandwidth of each W at various W_a where the null depth is deeper than 60 dB.

extinction depth was 59 dB and so there are actually two "dips" below 60 dB of 160 nm and 120 nm width which would not have been picked up with the lower resolution scan. Additionally the lengths of the two simulated MMIs in Fig. 4.3 and Fig. 4.22 were 874 µm and 875 µm respectively and as a result the data at 3900 nm for the MMI with $L = 874$ µm is 60.5 dB. Depending on whether it is acceptable to have some level of inaccuracy in the extinction the bandwidth in Fig. 4.22 is either 300 nm or 160 nm.

In summary, there are two areas on interest for a wide bandwidth at a deep (≥ 40 dB) extinction depths: $W_a/W = 0.27$ and 0.18. These are explored further to understand any trade-off in transmission as compared to $W_a/W = 0.3$.

4.5.2 General shape of the generic taper widths

To understand the unique extinction curves at the three W_a of interest (0.3, 0.27 and 0.18), and whether there is an inherent fabrication intolerance in using a smaller taper width, the extinction curves have been shown below for each W detailed above. The extinction depth at the previous labelled "optimum for transmission" taper width ($W_a/W = 0.3$) is shown in Fig. 4.23 for $W = 35$ to 50 µm.

For each W the extinction curves in Fig. 4.23 drop to a mathematical infinity at $\lambda = 4$ µm. Each extinction curve similarly begins a steep descent to a high extinction from 3.9 µm and comes back at 4.1 µm. There is a hint that $W = 50$ µm has a wider extinction bandwidth, especially at a 40 to 50 dB depth. The centre of these extinction bandwidths, however, is no longer at 4 µm. This may be due to the mode coupling of the higher-order modes excited in this MMI. The centre shift is necessarily detrimental to the experiments it is simply something to keep in mind when the MMI is used in conjunction with an L'-band filter on a telescope to optimise transmission and null of the host star's light.

Unlike for $W_a/W = 0.3$ the extinction curves for $W_a/W = 0.27$, shown in Fig. 4.24, do not all have the same shape. This figure includes the $W = 45$ µm simulation that has a nearly 400 nm bandwidth at 60 dB with the extinction curve "wing" splitting the

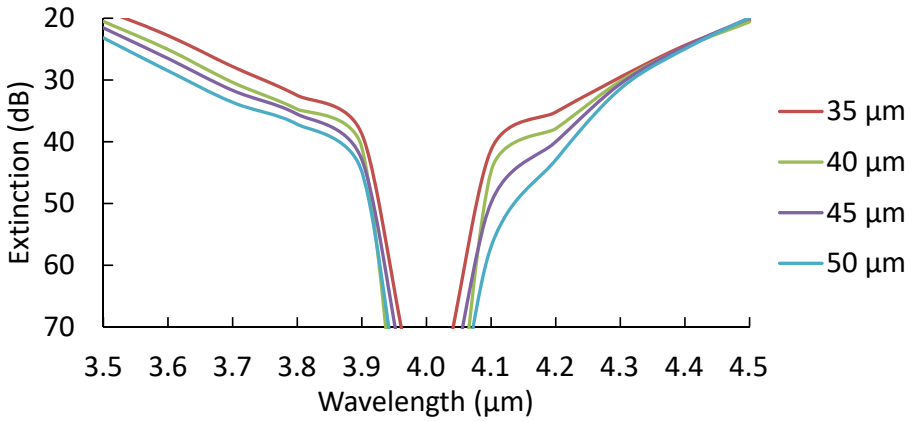

Figure 4.23: The extinction curves of MMI with $W = 35$ to 50 µm and $W_a/W = 0.3$.

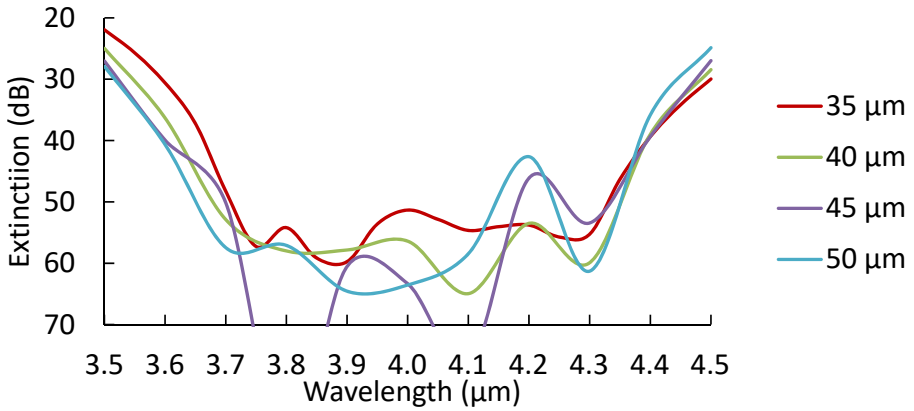

Figure 4.24: The extinction curves of MMI with $W = 35$ to 50 µm and $W_a/W = 0.26 \pm 0.01$.

bandwidth at 3.95 µm. In opposition to Fig. 4.23 the smaller W have an increase in bandwidth, but only for the 50 dB extinction. This is likely because each combinations of W and W_a/W was not optimised for any particualr null depth, focusing more on the specific ratio of W and W_a/W. Any W dependent increase or decrease in the bandwidth is investigated in greater detail below.

Figure 4.25 has the equivalent extinction curves for $W_a/W = 0.18$. Each curve has a the same basic shape, with notable exceptions in $W = 35$ and 40 µm that have evidence of model interference altering the extinction curve and, in the $W = 40$ µm case, decreasing the extinction bandwidth. From Fig. 4.25, $W = 50$ µm appears to have a deeper extincting depth than the other W but potentially a smaller bandwidth. The loss of light in each W_a is shown in Fig. 4.26, signifying the trade-off for an increase in bandwidth.

Figure 4.26 was calculated using an average loss for the MMI used above, with W between 35 and 50 µm and $W_a/W = 0.3$, 0.27 and 0.18, with error bars showing the range in the loss. The loss due to the W_a has been shown before but it has been included here to show that the trade-off for increased bandwidth is the same for each W, within the uncertainty shown in the figure.

Figure 4.27 is a collection of the data shown above, specifically comparing the W_a and

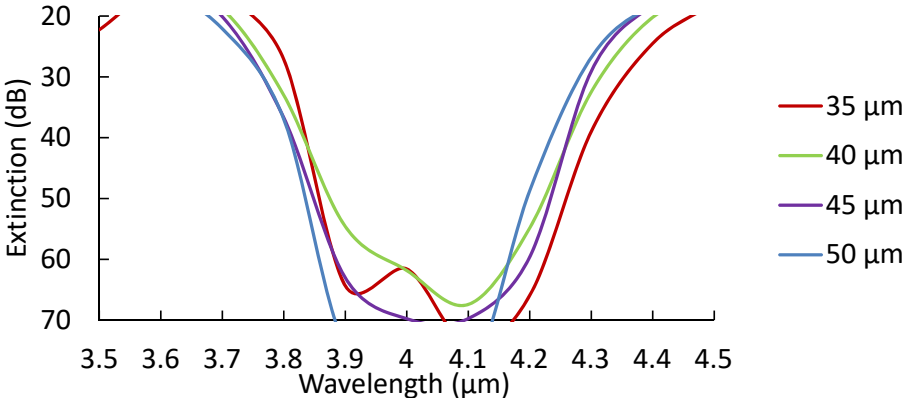

Figure 4.25: The extinction curves of MMI with $W = 35$ to $50\,\mu\text{m}$ and $W_a/W = 0.18 \pm 0.01$.

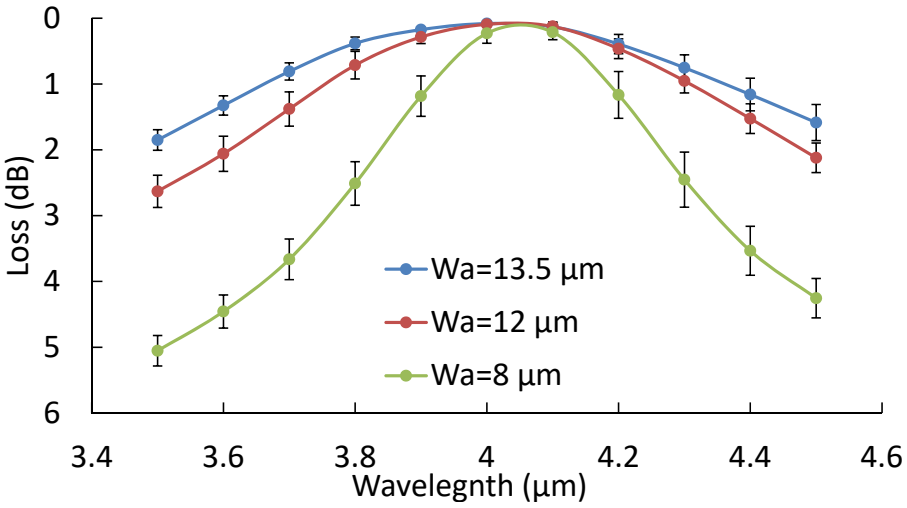

Figure 4.26: The average loss for an MMI with $W = 35$ to $50\,\mu\text{m}$ (with the two smaller W transmissions outperforming the larger by a small margin) and $W_a/W = 0.3$ (blue), 0.27 (red) and 0.18 (green). The solid lines are to guide the eye and error bars are to indicate the upper and lower range of transmission.

W for the tree large extinction bandwidths (reevaluated for each extinction depth). Note here that not all MMIs have three large extinction bandwidths, as discussed in Sec. 4.5.1, and when only one or two are available they are grouped according to the other data that needs to be represented.

For Fig. 4.27 the three distinct W_a/W are colour-coded: red for the first ratio, blue for the second and green for the third. The colour coding and the reference to first, second and last is an attempt to not bias the reader that the ratio is set at $W_a/W = 0.3$, 0.27 and 0.18. Instead, looking at the first ratio, there is possibly an increase in W_a/W as W increases whereas the second and third W_a/W remain constant (on average) with W. The latter has a high error in this sense due to the third peak's absence in some data sets.

Figure 4.28 investigates the optimised W_a/W for each extinction, for all W. It shows that there is a small upward trend in the position of all three W_a/W with an increased extinction. The indication is that there is no universal taper width that provides max-

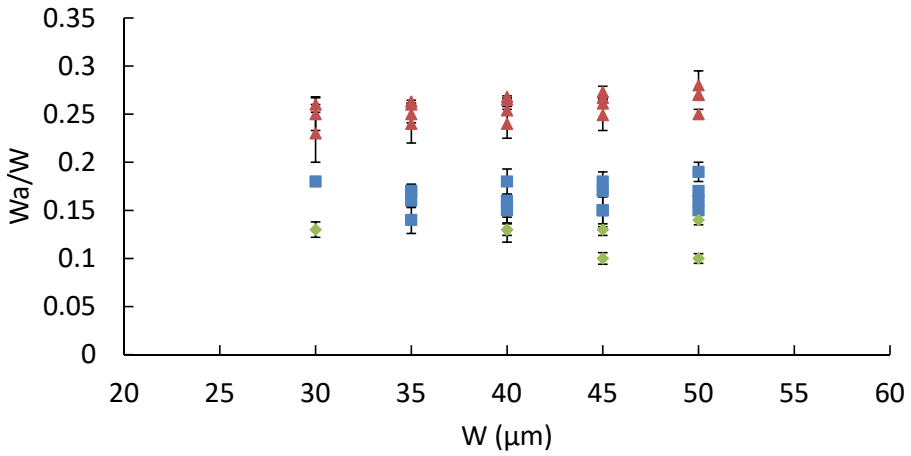

Figure 4.27: Relationship of W_a/W and W for maximum bandwidth. The three W_a/W ratio are shown separately in largest (red), second largest (blue) and lowest (green) for each extinction data set: 30, 40, 50 and 60 dB.

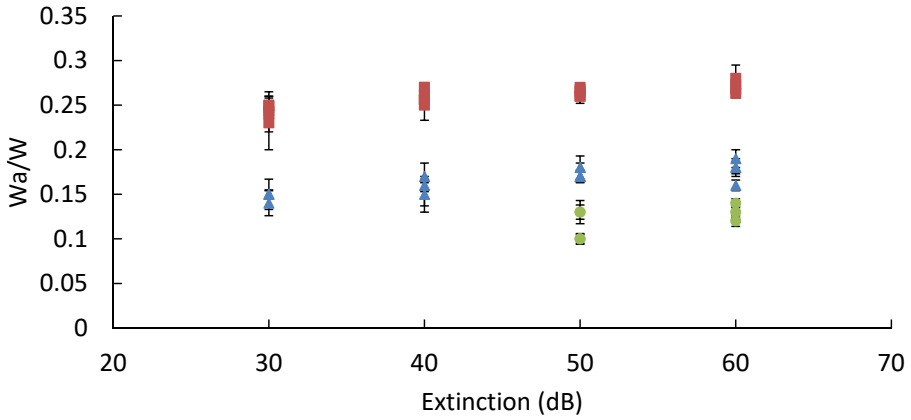

Figure 4.28: The three W_a/W ratio, in red, blue and green as per Fig. 4.27, versus extinction, for each W data set: 35, 40, 45, 50 µm.

imised bandwidth for each extinction depth. This does not mean however that a taper optimised for 60 dB bandwidth would have a low bandwidth for say a 30 dB extinction: It would simply not be the optimum taper width to achieve the widest bandwidth.

4.6 Summary

In this chapter the extinction bandwidth response to W_a, for a $W = 45$ µm design, has been investigated. It was found that using $W_a = 8$ or 12 µm would provide between 40 and 50 dB of extinction over a 400 bandwidth. The most likely explanation, proposed in this chapter, for why an extended bandwidth response was achieved at these W_a is due to the interaction of the odd modes that are excited in the MMI cavity. In particular, the removal of the 9^{th} mode was identified as a potential reason for why an MMI with $W_a = 13.5$ µm does not have a large bandwidth at any significantly deep extinction.

The taper length was anecdotally explored to show that potential increases in the ex-

tinction bandwidth are possible for $W_a = 13.5\,\mu m$ without significant loss in transmission.

The increase in extinction bandwidth due to W_a were explored further and shown to be agnostic to the W of the MMI cavity. A significant increase in extinction bandwidth, however, could not be obtained by changing the W (and W_a accordingly).

Experimental verification of this increase in extinction depth is contained in Chap. 6 and 7. They will first illustrate the extended imbalance response around zero imbalance for $W_a = 8$ and $12\,\mu m$ and then show the null of an MMI with $W_a = 8$, 12 and $13.5\,\mu m$.

Before that, however, the material used for these devices was tested. Chapter 5 measures the waveguide throughput and details the difficulties in fabricating simple devices in ChG let alone a more complicated device like an MMI.

Chapter 5

Fabrication

This chapter contains work already published:

Kenchington Goldsmith, H.-D., Cvetojevic, N., Ireland, M., Ma, P., Tuthill, P., Eggleton, B., Lawrence, J. S., Debbarma, S., Luther-Davies, B., and Madden, S. J., "Chalcogenide glass planar MIR couplers for future chip based Bracewell interferometers," in [*Proc. of SPIE*], **9907**, 990730 (2016).

The focus of this chapter is on the chosen material for this thesis and fabricating waveguides in this material. The choice of material was influenced by the astronomy requirement of transmitting mid-infrared (MIR) light. The IR spectrum was highlighted as an area of interest for direct imaging in Chap. 1 to decrease the contrast between young (and thus hot) exoplanets and their host star. This is because the light emitted by the exoplanet (calculated from the black body curve) is at a maximum here. In addition, there are gaps in the atmosphere throughout this regime, explained in Sec. 1.2.3, and choosing a wavelength corresponding to a gap provides Earthbound telescopes with a chance to measure exoplanets.

Constructing a photonic chip to transmit light in the MIR implies the standard silica (SiO_2) waveguides, limited to wavelengths less than 4 µm, cannot be used. Instead, chalcogenide glasses (ChG) are utilised. As discussed below, ChG is transparent in the IR and can have a tailored refractive index such that single-mode waveguides can be fabricated to maintain an appropriately small bend radius with negligible loss.

A brief history of ChG is included in Sec 5.1, including the specific combination of ChG chosen for the experiments in this thesis, with the bend radius and junction loss included in Sec. 5.2.2. The calculations specific to the waveguides used in this thesis, in terms of simulating waveguide dimensions to construct a single-mode waveguide, are included in Sec. 5.2. The deposition methods and experimental setup for measurements of the waveguides and beam combiners in this thesis are contained in Sec. 5.3 and 5.4 respectively. The measured transmission properties of the waveguides are included in this chapter under Sec. 5.5, and the beam combiner measurements (as a 3 dB coupler) are in Chap. 6.

5.1 Chalcogenide glass

The chalcogen group (group VIa of the periodic table) contains oxygen (O), sulphur (S), selenium (Se), tellurium (Te) and polonium (Po). Whilst O is technically a chalcogen and ChG such as TeO_2 exist, generally, oxide-based glasses are excluded from the family of ChGs. Instead, they are considered to be glasses that contain a major constituent element of S, Se or Te [205], and in some instances Po [206], that are combined with other elements or non-oxide species. In 1953 it was proposed that, like oxides, sulphides may form stable structures with elements known to be network formers, found in group IV and V of the periodic table [151]. Hence elements such as arsenic (As), germanium (Ge), antimony (Sb), phosphorous (P) and silicon (Si) are used to form various glasses [207] as well as gallium (Ga) in group III of the periodic table [205].

Binary glasses such as As_2S_3, GeS_2 and As_2Se_3 are well known and naturally occurring examples but ternary, quaternary, and above, compositions (e.g. GeAsS and GeAsSbS) are also available and offer greater flexibility in what glass to select based on that glass' properties. For this work, glasses are evaporated from their bulk form onto a wafer. This process is explained later but to fabricate a bulk glass the elemental components (or in some cases appropriate quantities of suitable compounds) are sealed into a quartz ampoule under vacuum, melted together, and held well above the melting temperature in a rocking furnace to homogenise before being rapidly cooled (typically by immersing the ampoule in water) to form a metastable solid.

If a ChG contains a fourfold coordinate atom in addition to the network former, e.g. Ge, a fully three-dimensional network is formed. The mean coordination number (MCN), calculated as the product sum of the individual element's valency in the glass multiplied by their abundance, is used to relate the network structure to the physical properties [208] of the glass. Work by He & Thorpe [209, 210] related ChG properties to their MCN and the glass phases: a "floppy" polymeric glass is defined as one with MCN < 2.4, and a "rigid" amorphous solid glass having MCN > 2.4, where MCN $= 2.4$ is said to be the transition between the two states. MCN related properties, like the transition temperature (Tg) - the temperature at which the glass is neither solid nor liquid but in a highly malleable transitional state - of $Ge_xAs_ySe_{1-x-y}$ was investigated by Wang et al. [211]. Broadly speaking glasses with $2.4 >$ MCN > 2.6 are inherently stable [212] - a property that determines whether the glass deposits at the same refractive index as the bulk material. The combination of Ge-As-Se specifically was found to be stable at an MCN $= 2.45$ [213]. The glass $Ge_{11.5}As_{24}Se_{64.5}$ is one such glass with a similar MCN $= 2.47$. At this MCN the Tg is 200°C and, as it is stable, the glass maintains its (linear) refractive index when thermally evaporated to deposit thin films [211, 213] - which is the method of deposition used in this work. Investigations relating the MCN to properties of ChGs have been undertaken for a variety of glasses, such as the combination Ge-As-S [214]. For the specific configuration $Ge_{11.5}As_{24}S_{64.5}$ (which also has an MCN $= 2.47$) it was found to have a Tg within 2% of the Se equivalent glass [215]. Due to the Tg being similar and having an MCN close to 2.45 (in the stress-free intermediate phase) it would be expected to deposit

similarly to the Se equivalent glass. The combination of this S and Se glass is thus ideal for creating mid-infrared waveguides using thermal evaporation based thin film deposition because of their similarity and because they do not require any steps post evaporation to rectify their refractive index.

The importance of this cannot be overstated. It means that the material does not need to be annealed either through heat, which may cause cracking of the film and ruin the waveguide, or using light, which may not penetrate through each layer or create index gradients in the material.

At the standard telecommunications wavelength of 1550 nm, ChGs have had excellent results with Madden et al. [216] reporting a loss of 0.05 dB/cm for a polymer clad ChG waveguide over 22 cm long. Furthermore, a sub-micron (750 nm wide) waveguide was fabricated with a higher (but still low) loss of 0.42 dB/cm showing that high throughput was possible in waveguides with minimised modal dimensions.

For the MIR, the loss of rib waveguides, constructed with $Ge_{11.5}As_{24}Se_{64.5}$ as the core material and $Ge_{11.5}As_{24}S_{64.5}$ as the undercladding material, was published by Ma et al. [156] with a thin fluorocarbon layer and air cladding, in 2013. Minimum losses of 0.3 dB/cm at 5 µm were measured in a wavelength scan between 3 and 5 µm. Yu et al. [217] modified the structure, in 2016, with an angle deposited top cladding of $Ge_{11.5}As_{24}S_{64.5}$, reporting a loss of 0.55 dB/cm. A fully etched 2.5 by 2.5 µm waveguide, with an undercladding of $Ge_{11.5}As_{24}S_{64.5}$ and air overcladding, was measured in a ring resonator with a loss of 0.84 dB/cm and as a straight waveguide at 0.60 dB/cm in 2015 [126] at a wavelength of 5.2 µm.

Table 5.1: ChG materials that have been used to create waveguides in the MIR with the corresponding fabrication method to create said waveguides.

Material	Fabrication method	Citation
$Ge_{11.5}As_{24}S_{64.5}$ on $Ge_{11.5}As_{24}Se_{64.5}$	Evaporative deposition and reactive ion etching	[126, 156, 217]
Ga-La-S	Femtosecond laser writing	[154, 186]
As_2Se_3	Photodarkening	[218]
$Te_{82}Ge_{18}$ on $Te_{75}Ge_{15}Ga_{10}$	Thermal coevaporation and reactive ion etching	[219]

Table 5.1 lists a few current chalcogenide materials and waveguide fabrication technologies being used to create waveguides for the MIR wavelength regime. Previous work at the Australian National University has focused on evaporative deposition and reactive ion etching to produces waveguides in $Ge_{11.5}As_{24}S_{64.5}$ on $Ge_{11.5}As_{24}Se_{64.5}$ [156] but has also used ChG like As_2S_3 and $As_{24}Se_38S_{38}$ [220] to generate waveguides via nano-imprinting for 1550 nm wavelength purposes. Work from other labs includes work previously mentioned in regards to fabricating beam combiners in the MIR for interferometry [186] using gallium lanthanum sulphide (GLS). Loss measurements of this glass were undertaken by Madden et al. [154], using ultrafast laser inscription, of 0.25 ± 0.05 dB/cm at a wavelength of 3.39 µm.

To extend the wavelength deeper into the MIR S-based ChGs are neglected in favour of Se and Te that have measured transmission tails far into the IR. For example, As_2Se_3 was found to have a loss of 0.5 dB/cm at 8.4 µm using a photo darkened waveguide, with an under cladding of As_2S_3 and air overcladding [218]. ChG fibres of $Te_{76}Ge_{21}Se_3$ have been made with low loss up to a wavelength of 14 µm, the lowest loss of 0.08 dB/cm (7.9 dB/m) being at the wavelength 10.5 µm [221, 222]. Telluride waveguides ($Te_{82}Ge_{18}$ on a $Te_{75}Ge_{15}Ga_{10}$ substrate) have also been constructed using standard photolithography and ion etching with a loss of 6.6 dB/cm at 10 µm [223]. Yu et al. [217] also successfully produced supercontinuum radiation beyond 10 µm using $Ge_{11.5}As_{24}Se_{64.5}$ on $Ge_{11.5}As_{24}S_{64.5}$, and so the transmission of this glass could reach further into the infrared with low loss. Despite this, to the author's best knowledge the loss (in dB/cm) of a single-mode waveguide has yet to be published in this glass at wavelengths around 10 µm - making this work for future study. The risk for this glass, however, is that a low-loss, fully-etched (keeping zero birefringence), single-mode waveguide at 10 µm may be too small to fabricate and new glasses may be required.

The materials chosen for this thesis are $Ge_{11.5}As_{24}Se_{64.5}$ and $Ge_{11.5}As_{24}S_{64.5}$. Despite a large range of ChGs to choose from, such that almost any index contrast could be selected, these materials were chosen because they have a low loss in various waveguide geometries [126, 156, 165] and their thin-film refractive index is the same as the measured bulk ChG refractive indices without the need to anneal the films [213, 215]. This is important as the stresses built-in by thermal annealing are known from prior work at the Laser Physics Centre at the Australian National University to lead to film cracking for thicknesses exceeding 1.5 µm. This is due to ChGs having a large coefficient of thermal expansion and undergoing structural reorganisation resulting from the normalisation of the bond structures.

The selected ChGs have the same MCN and thus similar properties making them ideal to use together. Their linear refractive indexes are 2.29 and 2.65 at 1550 nm, for the S and Se glass respectively [215], which corresponds to refractive indices of 2.279 and 2.609 at 4000 nm [156] providing a core to cladding index contrast of 0.33 at 4000 nm. This was calculated using the Sellmeier equation, eq. (5.1), that was fit to measured data from variable angle spectroscopic ellipsometric measurements [224] of the bulk glasses across the MIR.

$$\begin{aligned} n^2_{\mathrm{Se}}(\lambda) &= 1 + \frac{5.78525\lambda^2}{\lambda^2 - 0.28795^2} + \frac{0.39705\lambda^2}{\lambda^2 - 30.39338^2} \\ n^2_{\mathrm{s}}(\lambda) &= 1 + \frac{4.18011\lambda^2}{\lambda^2 - 0.31679^2} + \frac{0.35895\lambda^2}{\lambda^2 - 22.77018^2} \end{aligned} \tag{5.1}$$

The selection of ChG has limitations: the waveguides are sub-wavelength in the MIR and so small that they are close to what can be fabricated at the Australian National University (the cutoff being 1.3 µm). This may lead to large scattering loss and must be investigated (see Sec. 5.5). The advantage, however, is that there is negligible bend

loss, as will be shown in Sec. 5.2.2, for tight bend radii of 200 µm. From an astronomic interferometry perspective, a tight bend radius is required to offset the output waveguides from scattered, coherent, light from the input waveguides, as well as from scattered light from the coupling device. This is an advantage over say using GLS glass which fabricating waveguides using femtosecond writing, with a refractive index difference of 0.01, that cannot manufacture a glass slab large enough to account for their large bend requirements and as such cannot remove scattered coherent light from their output ports. By selecting the $Ge_{11.5}As_{24}Se_{64.5}$ and $Ge_{11.5}As_{24}S_{64.5}$ combination we are future-proofing our work against scattered light. The issue of scattered light is addressed experimentally in Chap. 6 where side-steps are utilised to measure the MMIs without coherent, scattered light.

5.2 Waveguide design

A 2 by 2 µm waveguide was selected for this work as it only permitted the fundamental transverse electric (TE) and transverse magnetic (TM) modes to propagate down to 3800 nm in wavelength. The intensity distribution of this mode is shown in Fig. 5.1 for a wavelength of 4000 nm. Due to the symmetry of the waveguide, it is a polarisation degenerate structure. As the deposition occurs on wafers at room temperature, no stress-induced birefringence is expected and so this combination is a good candidate for waveguide design in interferometry.

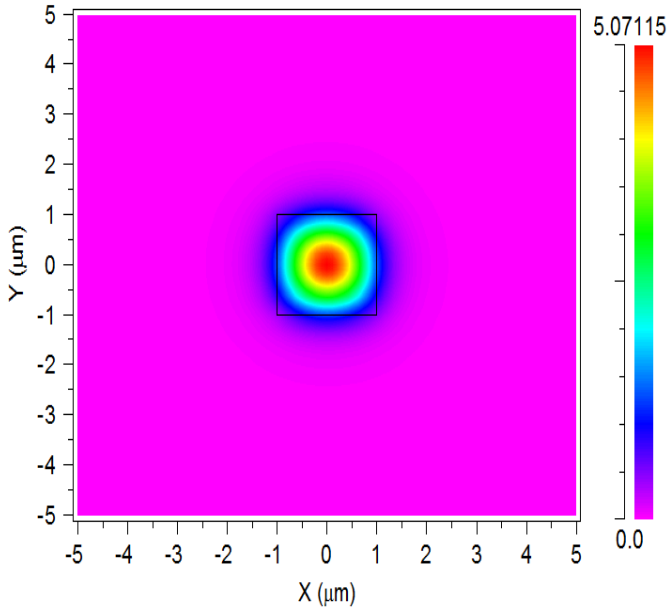

Figure 5.1: Pointing vector, simulated in RSoft FemSIM full vector mode, for the fundamental TE (or TM) mode in a 2 by 2 µm waveguide.

To input light into this waveguide, the mode field and input field must match. This structure has a $1/e^2$ mode field diameter of 2.6 µm (at a wavelength of 4000 nm).This matches the central lobe of an Airy disc formed in the air at 4000 nm, with a numer-

ical aperture (NA) of 0.79, or a Gaussian with minimal truncation (greater than 95% transmission) with an NA of 0.82.

Due to this project targeting astronomical applications, it was pertinent to rationalise whether a waveguide of such a small width, with a high NA, could interface with a telescope without significantly complex coupling optics or a high transmission loss due to a mismatch in NA.

5.2.1 Tapered input

As mentioned above, to match the mode of a 2 by 2 µm waveguide, an input lens with an NA of approximately 0.8 is required. Whilst single element, high NA, aspheric lens are commercially available for the MIR [225], with high throughput and diffraction-limited performance over limited fields, microlens array equivalents are not. These would be used to input telescope light into the final photonic chip design. Additionally, the use of a high NA implies difficult anti-reflection coatings and tight alignment tolerances, all of which is less than ideal given the environment in which the chips have to function on a telescope. For the chips to be practical they will ultimately need to accept light from a modest (< 0.3) NA system where suitable microlens array devices are already available and alignment tolerances are comparatively relaxed. To attain high-efficiency coupling, by lowering the NA of the system, a tapered core width and height configuration can be used [226].

The two fabrication options are a fully 3-D taper with simultaneous width and height changes, or a pair of 2-D tapers: one in width, and one in height. The 2-D taper pair is considered alongside the 3-D taper as it eases mechanical alignment tolerances imposed by the fabrication methodology for the vertical taper [179]: for a 3-D taper, the lithographic alignment of the horizontal taper must overlay precisely with the mechanically keyed vertical taper thereby requiring very tight (but not unreachable) tolerances on the dimensions of the shadow mask used, whereas the 2-D taper pair has a pseudo arbitrary spatial separation between the two. The challenge is to keep the light confined in the fundamental mode of the now multimode input waveguide to avoid mode coupling leading to coupling loss into the 2 by 2 µm single-mode waveguide used elsewhere on the chip.

Both device types mentioned above were modelled with RSoft BeamPROP in full vector mode. Figure 5.2 shows simulations of a full 3-D and 2-D taper pair (vertical then lateral tapers) transforming a 10 by 10 µm waveguide fundamental mode to a 2 by 2 µm waveguide mode.

A 10 by 10 µm waveguide was simulated as a coupling option as it has a beam spot of (1/e) 8.3 µm which corresponds to an NA of 0.37 for an Airy disc formed in air and 0.42 for Gaussian. This provides a lower NA lens requirement, with a higher positional tolerance, for a reasonable deposition procedure.

The model shows the tapers as asymmetric in the vertical plain (y) to reflect a real-world device. To achieve vertical tapering the deposition of the core material is interrupted after 2 µm so that a shadow mask can be inserted above the chip, as demonstrated by

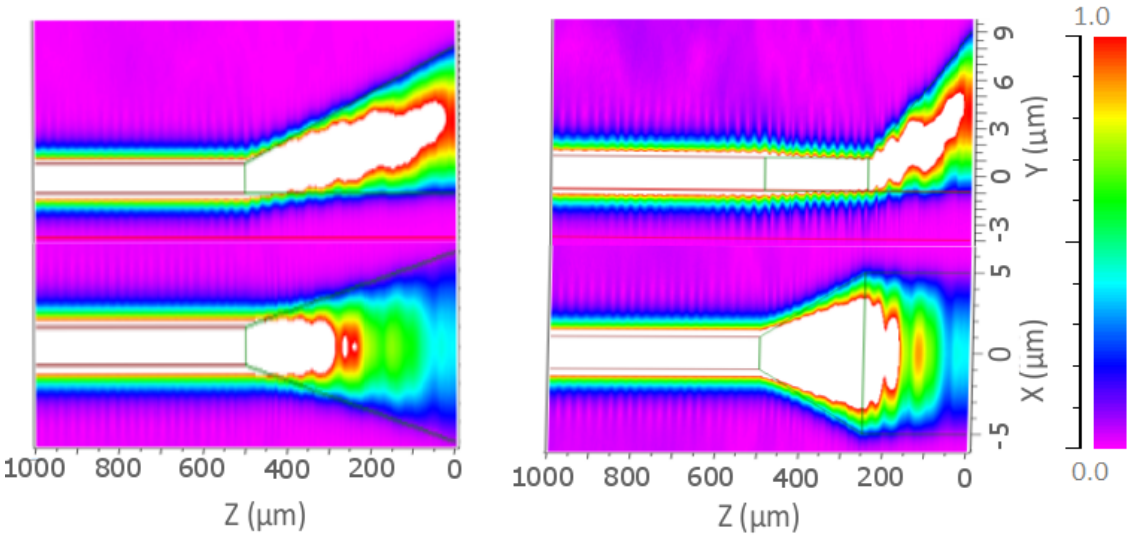

Figure 5.2: The electric field propagation for a 3-D taper: using a single, simultaneous width and height taper (left) and a dual 2-D taper pair (right). Upper images are vertical cross sections through core centre (y vs z), lower images are horizontal (x vs z). Both reduce the waveguide from 10 by 10 µm to 2 by 2 µm, with the 2-D taper pair reducing in the vertical (y) direction first then lateral (x). The beam propagation is from right to left.

Madden et al. [179]. The mask blocks all material during the subsequent deposition except over the taper. A shadow mask tapered to a fine point provides a partial shadow over the wafer creating the vertical taper as shown in Fig. 5.2.

The loss due to the transformation, for the three wavelengths 4.2, 4 and 3.8 µm, is shown in Fig. 5.3. The measurement was taken by overlapping the end face of the taper with the fundamental mode of a 2 by 2 µm waveguide, normalised to the input launch field, and assuming all other light is lost. The length of the tapers was varied in 50 µm increments to ascertain an optimal length for the mode transformation.

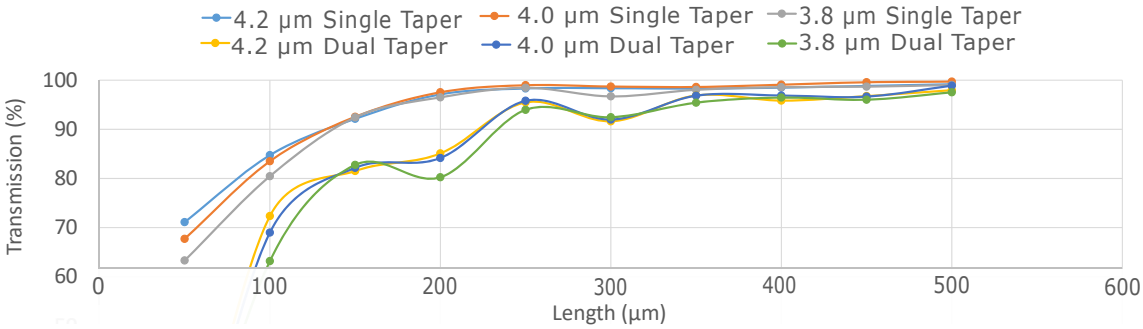

Figure 5.3: Simulated transmission for the two taper designs, from Fig. 5.2 at various wavelength.

Figure 5.3 shows that the 3-D taper has a monotonic increase in transmission with taper length, indicating negligible mode coupling and would allow for a device twice as short as the 2-D taper system for the same transmission of $\sim 95\%$. For taper lengths > 250 µm, the 3-D taper is essentially loss-less. The main issue is in the fabrication tolerances, which requires the lithographic mask for the waveguide width definition to be aligned to the

mechanically defined vertical taper to a tolerance $< 10\,\mu m$. This is a non-trivial exercise as the taper deposition mask is usually mechanically machined and so there are large (by microfabrication standards) tolerances at play and deposited alignment fiducials are necessarily large and of low edge sharpness due to the tapering. The fallback option is the 2-D taper system where the vertical tapering is separated from the width tapering resulting in significantly relaxed lithographic alignment tolerances. However, as can be seen in Fig. 5.3, there is non-monotonic behaviour occurring as a function of length which is a clear indicator of mode coupling occurring. The magnitude of this is acceptably small resulting in only slightly lower transmission (96% vs 99.5%) than the full 3-D taper length of $400\,\mu m$. Thus the 2-D taper, regardless of requiring more space on the chip, is acceptable and the photonic chip construction will benefit from a simpler fabrication step.

5.2.2 Light loss due to bends

Bending waveguides, as with optical fibre, will always induce loss. The dominant causes of bend loss are radiative out propagating parts of the previously guided field of the straight waveguide and the junction loss. The bend loss is the outcome of light previously experiencing total internal reflection incident on a bent section of the waveguide. This light subsequently reflects at an angle less than the critical angle causing the light to be lost [227]. From a mode field perspective, the radiative out propagating loss is due to the portion of the guided light outside the critical radius distance which must travel faster than the speed of light in a vacuum to bend with the rest of the mode. As this is impossible the light is instead radiated away. This bend loss has an exponential dependence on bend radius [228] with the critical radius also varying with wavelength. For junction loss, from a mode field perspective, the loss is caused by a mismatch in the guided field of the straight segment and the guided field in the bent segment. Thus it is crucial to get the right design to avoid large losses. Using RSoft FemSIM the radiation loss dependence on the bend radius for a mode in a 2 by $2\,\mu m$ waveguide was found based on a conformal transform methodology to simulate the bending [229]. The radiative loss calculations, shown in Fig 5.4, used the imaginary part (k) of the effective index ($n + ik$) generated by FemSIM:

$$\begin{aligned} \text{Loss (dB/cm)} &= 10 \log_{10}(e) \left(\frac{4\pi k}{\lambda} \right) \\ \text{Loss (dB/turn)} &= 2\pi R \text{ Loss (dB/cm)} \end{aligned} \tag{5.2}$$

(where R is the bend radius) and $4\pi k/\lambda$ is the attenuation coefficient. The junction loss was calculated from the overlap integral between the fundamental guided mode of the bend and the guided mode in the straight waveguide. Note here that radiative loss is measured in dB loss per full 360° turn and junction loss is measured as dB loss per junction.

Figure 5.4 displays the radiative loss per turn for bend radii ranging from 100 to $150\,\mu m$ - where the simulation becomes unreliable due to the loss being much lower than the junction loss - and the junction loss out to a bend radius of $300\,\mu m$. The simulations used the largest operating wavelength of $4.2\,\mu m$ to account for the maximum loss

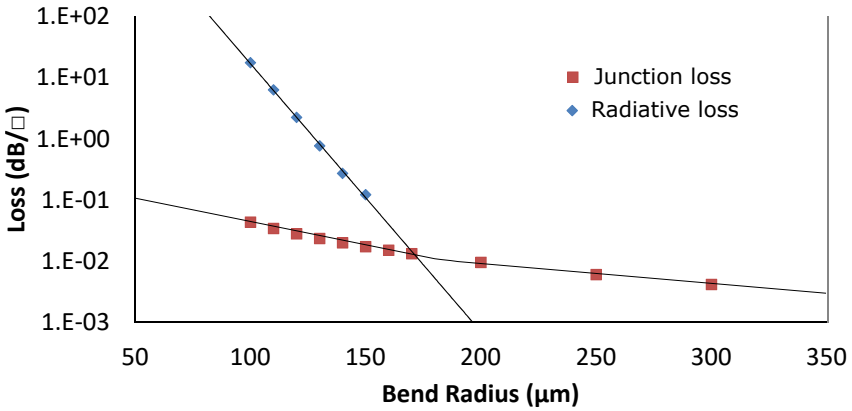

Figure 5.4: Radiative loss (blue), where □ = turn, and junction loss (red), where □ = junction, vs bend radius. A linear line through the radiative loss provides the equation $dB/\text{turn} = 40800\exp(-0.101\text{R})$ and the quadratic line through the junction loss (approximated as the linear function from 200 to 300 µm) provides $dB/\text{junction} = 0.106\exp(-0.011\text{R})$, where R is the bend radius. These simulated points were taken at the extremity of the required bandwidth (4.2 µm) as a worst case measurement.

in the required wavelength range. Initially, the radiative loss dominates the bend loss with the exponential gradient decreasing at a rate of 0.1 dB/turn/bend radius. At a bend radius of approximately 170 µm the loss of two junctions required for a single bend becomes dominant, hence the bend loss would decrease approximately exponentially at 0.011 dB/junction/bend radius. Thus, to ensure low bend losses at the extremes of the operating bandwidth, a bend radius of 200 µm was selected providing an expected loss of 0.02 dB per bend (primarily due to junction loss).

It is important to note that the smaller the bend radius, the more compact complex circuit structures can be made. Thus, a bend radius in the hundreds of microns allows for photonic chips manufactured on a centimetre scale rather than tens of centimetres. Moreover, if the bends use a smoothing function so that the bend radius decreases adiabatically from the ends of the bends towards the centre of the bend [230] then the junction loss can be essentially eliminated. The length of the bends increases dramatically by using an adiabatic incrementation - using an Euler bend, for example, would double the length but a Bézier curve would triple, at a minimum, the length. For this thesis adiabatic bends were not used as the junction loss was deemed acceptable, however, future work that has a more stringent condition on loss should utilise suitably designed adiabatic bending such that the increased propagation losses do not significantly outweigh the reduced junction losses and the circuits remain compact.

As a part of the test chip design, race track based spiral structures were included to provide a set of three lengths on the chip to enable estimation of propagation losses via an "on-chip" cutback measurement (i.e. fitting the loss versus length curve). Figure 5.5 shows the geometry used for an on-chip cutback measurement.

The added length provided by the spirals in Fig. 5.5 are 2.3 cm, 3.7 cm and 4.9 cm compared to a 1.5 cm straight waveguide. Each spiral has the same number and design of

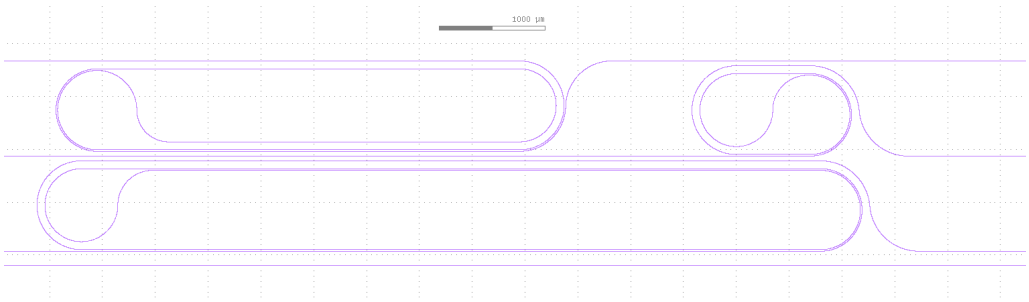

Figure 5.5: On chip cutback geometry, with spirals of 2.3 cm, 3.7 cm and 4.9 cm as compared to the 1.5 cm straight waveguide.

bends (and joints) and so has to have the same bend loss (if any), thus allowing for a true propagation loss measurement without the need to cleave the chip thereby both destroying the original chip, to create two new chips, and also introducing potential inaccuracies due to cleaving quality.

5.2.3 Light lost in waveguide propagation

For the main application of this work, astrophysics, a 20% (1 dB) loss is acceptable to be comparative to bulk optics equivalent devices such as beam splitters and beam combiners, in the MIR. The loss in a waveguide, without tapering and bending, is the metric used to justify photonic chips as bulk optic replacements and so identifying and estimating waveguide losses is essential to this work. Waveguide propagation loss has two major constituencies: scattered light and chemical absorption.

Scattered light occurs at the interface between the core and cladding material and is caused by the inhomogeneity of the sidewall. A common cause of inhomogeneous sidewalls takes place during the reactive ion etching procedure where the protective photoresist etches away, inconsistently, at the edge of the waveguide. This exposes the area underneath to the etching plasma whilst leaving the neighbouring areas unaffected.

Another cause of scattering is macro defects in the material. These defects are dust grains, or clumped ChG particles, that build up during deposition to form “pillars”. These pillars cause cladding material to appear in the core layer, making scattering centres in the waveguide.

At present, the loss due to scattering is unknown and will need to be evaluated after depositing the material (counting scattering centres) and after the reactive ion etching process (for sidewall roughness).

The loss due to chemical absorption is frequency dependent. The dependence stems from the composition of the glass and continence therein and cannot truly be known unless measured. High purity examples in the FTIR show low chemical absorption levels, sub 1 dB/cm. Note here that Ge-As-Se fibres have been made with losses down to 90 dB/km [231] and so purification steps can reduce this loss considerably.

In previous work at the Australian National University Ma et al. [156] produced rib waveguides with losses down to 0.3 dB/cm, close to the estimation above, and so this will

be assumed lost loss for this work.

Now that the glass has been discussed and the waveguide design explained the deposition and fabrication process can be described.

5.3 Deposition

The fabrication of waveguides for the experiments discussed in this thesis is similar to that in Ma et al. [126, 156] and Yu et al. [217] for the combination of ChG materials in the above simulations. The ChG waveguide fabrication process consisted of four main steps: evaporating the glass, photolithography, etching and additional evaporation of glass for an angled cladding.

The initial step was the thermal evaporation of ChG onto a wafer carousel - that held four wafers, had a 30 cm diameter and had a centre of carousel to centre of wafer length of 8 cm - in an Angstrom Engineering Inc. EvoVac chamber. A picture showing the inside of the chamber at the Laser Physics Centre at the Australian National University is included in Fig. 5.6. After pumping to a base pressure of typically 1.2×10^{-7} Torr, evaporation occurred at pressures fluctuating between 0.5 and 2 $\times 10^{-6}$ Torr. A resistively heated tantalum (Ta) baffled boat or a quartz crucible in a Radak furnace [232], 49 and 46 cm below the wafer carousel respectively, was used to heat the material to ~ 200°C. The quartz crucibles were used to evaporate the $Ge_{11.5}As_{24}Se_{64.5}$ at a rate of 1.52 Å/s and the Ta baffled boat [233] was used for the $Ge_{11.5}As_{24}S_{64.5}$ glass with a rate of 1.9 Å/s. These rates were calculated after deposition, by comparing the deposition time to the deposited film's thickness. During deposition, etch-rate monitors were used to track the film's thickness and a feedback loop was used to ensure the average etch-rate matched the preset value by altering the temperature of the material.

A baffled boat was used for the $Ge_{11.5}As_{24}S_{64.5}$ so that the target was never exposed to the source at a varying temperature. Instead, the material was melted slowly from the two separate cavities and into the main chimney via an indirect path [233]. This is to prevent spitting and streaming that would cause pinholes on the wafer surface.

Despite using optimised conditions there were visible defects, particle growths, in micrographs taken for both the S glass and Se glass films - more so for the S glass than Se. These dots are generated by a range of imperfections on the SiO_2 wafer, dust grains for example, or from material in the chamber that was not properly removed before deposition. Condensation of the material during deposition is another possibility and would be dependent on the deposited glass: explaining why the S glass is affected more than the Se. It is not clear, however, that condensation would occur more in the S glass than the Se.

Another possible reason for the discrepancy between the two deposited glass films' surface morphology is "clumping" - elements in the glass forming unintended molecular species such as S_8, As_4S_4 or As_4S_3 [214]. These areas would seemingly grow during the deposition and form what is seen under the optical microscope.

The exact reasons for the particle growth have not been mentioned in previous publi-

cations (Ref. [156, 217] for example) and is yet to be elucidated in this work. The quality of these films, however, is not the focus of this work and is a subject of ongoing research.

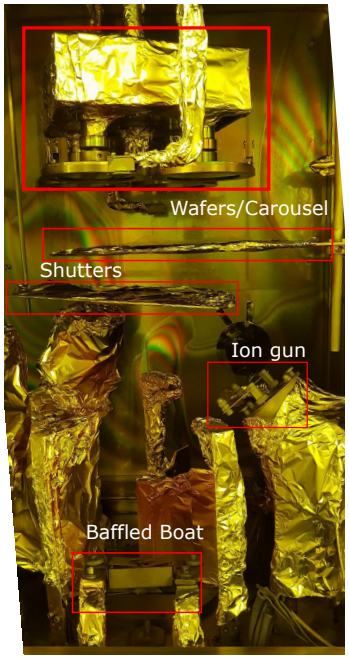

Figure 5.6: The inside of the Cothermal Angstrom Engineering Inc. EvoVac chamber. Labelled are the baffled boat, shutters, carousel and ion gun, the quartz crucible is hidden behind the aluminium foil used to protect the inside of the chamber from contamination between runs.

Figure 5.6 shows the evaporation chamber with the baffled boat at the bottom of the image and the wafer carousel loaded with four wafers 40 cm above the boat at the top of the image. The silicon wafers used are 100 mm in diameter and a 5 µm layer of thermally grown SiO_2 was used as a buffer layer to the high index Si substrate. At an index of 3.5, the Si would otherwise radiatively strip light from the core layer by evanescent coupling [126]. The optical field is quite small and the index contrast is high at the ChG to SiO_2 interface, and so with a 3 µm thick ChG under cladding the losses from absorption in the SiO_2 are negligible [126]. This saves significantly on both the time and quantity of glass required to grow the otherwise much thicker underclad layer required [126] and also reduces the risk of cracking during subsequent waveguide processing.

Shutters (labelled in Fig. 5.6) mask the wafer during the initial deposition temperature ramp-up and stabilisation, and when the required thickness has been reached. A quartz microbalance monitor was used to measure the deposition rate (hence, the thickness deposited at any one time). An ion gun (labelled) was active for 60 s before the deposition to clean the surface of the SiO_2 wafer and assist in the adhesion between the SiO_2 and the bottom ChG layer. It used an argon (Ar) beam at 15 sccm[i], discharge of 71 V, emission of 0.5 A and a base pressure of 1.2×10^{-3} Torr. It was not, however, active during film deposition in an ion assist role to prevent metallic contamination of the films from the filament.

[i] standard cubic centimetres per minute

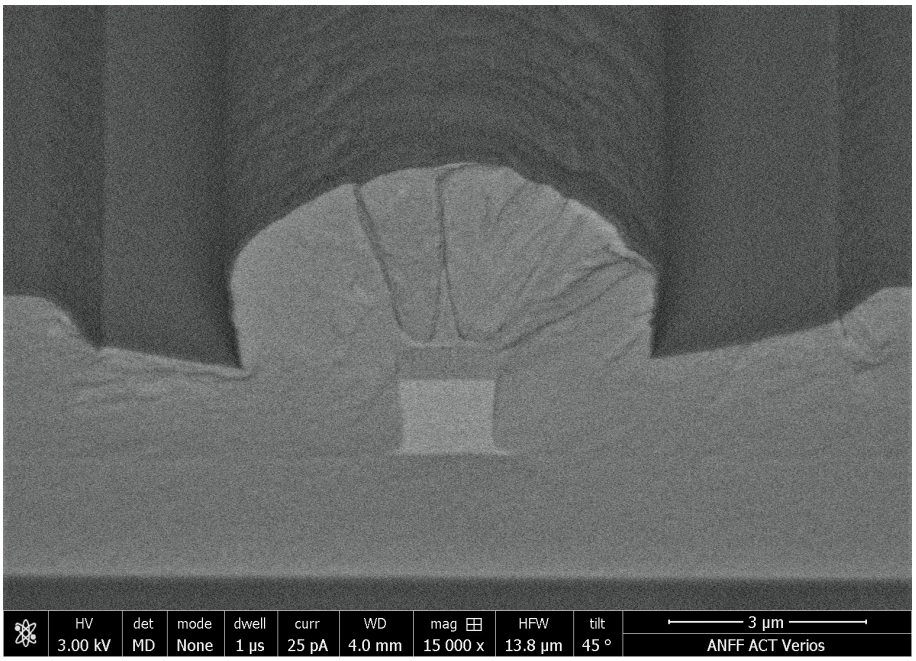

Figure 5.7: A scanning electron micrograph of a 2 by 2 µm fully etched waveguide with 3 µm of overcladding.

A scanning electron micrograph (SEM) of a fully deposited waveguide cross-section is shown in Fig. 5.7.

An under cladding of 3 µm of $Ge_{11.5}As_{24}S_{64.5}$ was deposited first followed by 2 µm of $Ge_{11.5}As_{24}Se_{64.5}$ as the core material. A further 1 µm cap of $Ge_{11.5}As_{24}S_{64.5}$ was then deposited to form a protective layer over the core to prevent any chance of processing induced contamination of the top surface of the waveguide.

For the photolithography step, a 1 µm thick film of standard positive photoresist (Clariant AZ MIR 701) was spun onto the wafer. The positive resist was exposed to broadband ultraviolet light in a Canon MPA-500 FAB one-to-one projection mask aligner with a chromium-on-glass photomask used to define the pattern. The standard developing procedure (AZ MIF 312 for one minute puddle development) was used to remove the exposed photoresist from the wafer.

Using an inductively coupled plasma (ICP) reactive ion etching tool, the glass layers were etched 3 µm deep using a CHF_3 plasma at 25 sccm flow, 10×10^{-3} Torr pressure, 20 W (Watts) of table power and 500 W ICP power. This recipe was well established from previous work by Ma et al. [156] and Yu et al. [217]. The etch rate was approximately 300 nm/min for the $Ge_{11.5}As_{24}S_{64.5}$ and 330 nm/min for $Ge_{11.5}As_{24}Se_{64.5}$. The etch rates were measured by a Jobin-Yvon SOFIE etch rate monitor using the interference fringes in the reflected light from a 677 nm laser, and calculated using an averaged refractive index of 2.7, during the etching process.

Once the core layer had been etched the photoresist was stripped by dry etching with 30 sccm of O_2, 2 sccm of Ar and 3 sccm of CHF_3 with an ICP power of 300 W, 20 W of table power and otherwise similar conditions to the ChG etch. To fully remove the photoresist

and any additional material that deposited as hydrogenated fluorocarbons from the CHF_3 plasma etch [234] a 4.5 min dry etch was required. The gas composition includes a small amount of CHF_3 to remove any As_2O_3 or GeO_2 that formed during the O_2 photoresist stripping, and the Ar addition is to assist as a physical sputter cleaning of the surface. This recipe is known from previous work at the Laser Physics Centre to strip cleanly without leaving residues or surface oxides, however only for a maximum etching length of 1.5 min as a second step to a wet etching process. Previous works used wet etching (DMSO, followed by water and IPA rinses) to remove the resist after a 30 second plasma clean to remove the CHF_3 etch residue and any hardened photoresist layer. In this work, dry etching was used to limit the time the wafer was out of the vacuum and to reduce the exposure to potentially hydrogen (H) and hydroxide (OH) contaminates (namely water).

After creating the fully etched waveguide, angled deposition at about 55° [235] incidence angle was used to deposit an over-cladding of $Ge_{11.5}As_{24}S_{64.5}$ to create the 0.33 index contrast in the two-directions (horizontal and vertical). Waveguide chips were then produced by hand cleaving of the Si substrate using a diamond scribe to provide a cleave initiation point.

The dependence of the sidewall deposition profile on incidence angle is shown in Fig. 5.8 for several angles of deposition between the baffled boat and wafer surface [235].

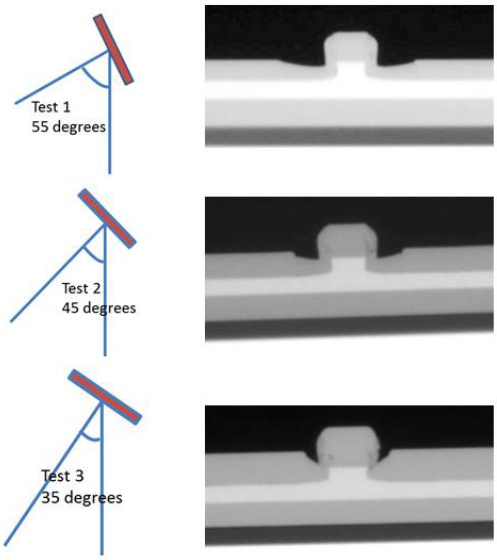

Figure 5.8: From the thesis by Yu [235], the difference in overcladding profile over a rib waveguide at different angles of incidence between the baffled boat and the wafer.

Past an incidence angle of 50°, the cladding appears to be uniform in the area immediately surrounding the waveguide taking into account the shadowing effect of the waveguide core itself which is responsible for the shallow depressions on either side of the core. The 35° image in particular shows the shadowing "wings" that at normal incidence would otherwise cause voids in the cladding close-in to the waveguide core as the film grows. With

an increase in incidence angle these "wings" progressively move away from the waveguide and become flattened. Although the top image in Fig. 5.8 is saturated, the 55° has the best cladding profile, with the flattest "wings" out of the three images shown.

Each deposition of over-cladding was undertaken with the wafer rotating at 10 rpm around its centre but otherwise stationary for the evaporation source. This created an even distribution on all sides and provided a void-free approximately uniform thickness cladding around the waveguide core (see Yu et al. [217] for further details). For waveguides and MMIs fabricated in this thesis, the incident angle was fixed at 57° for all over-cladding depositions. An SEM with a much higher resolution than the optical images is shown in Fig. 5.7. In this image, it is clear that there are no gaps left in the over-cladding that would expose the mode to a low index material (such as air).

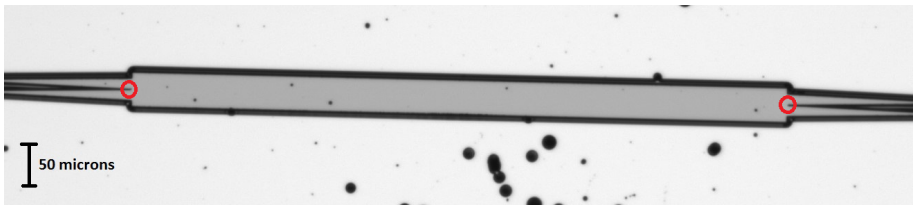

Figure 5.9: A micrograph of an MMI 875 µm in length, 45 µm in width and a fabricated taper into the main cavity starting from the single mode waveguide width of 2 µm to a 13.5 µm width over a 200 µm length. The red circles are to highlight the gap between the tapers at the interface with the MMI.

Waveguides were not the only devices fabricated for this work. MMIs were also designed and fabricated using the same combination of material and deposition method. A micrograph of an MMI is displayed in Fig. 5.9.

The same over-cladding, as in Fig. 5.7, was deposited over the MMI. The small gap at the waveguide interface with the main MMI cavity, as seen in Fig. 5.9, may not fill in during the over-cladding. A preliminary test was undertaken by over-cladding a sunken triangle, the results shown in Fig. 5.10. It indicated that the angled deposition fills in small gaps with a cost of thickness. Only at the tip of the triangle is the thickness reduced considerably and this must be considered in the MMI design.

Testing whether fabrication steps create what is expected is a fundamental part of this thesis. This extends to the MMI and whether the gap between the tapered waveguides leading into the main MMI cavity is large enough so that the over-cladding will leave no air gaps - an issue investigated in Fig. 5.10.

5.3.1 MMI fabrication

After fabrication three MMI with different taper widths (W_a) were imaged with a microscope, as was the photonic mask used in the lithography fabrication step, to investigate the actual shape of the MMI fabricated and verify the design data used for the simulation. These images are included in Fig. 5.11.

Figure 5.11 indicates that the largest W_a has such a small gap between tapers that the

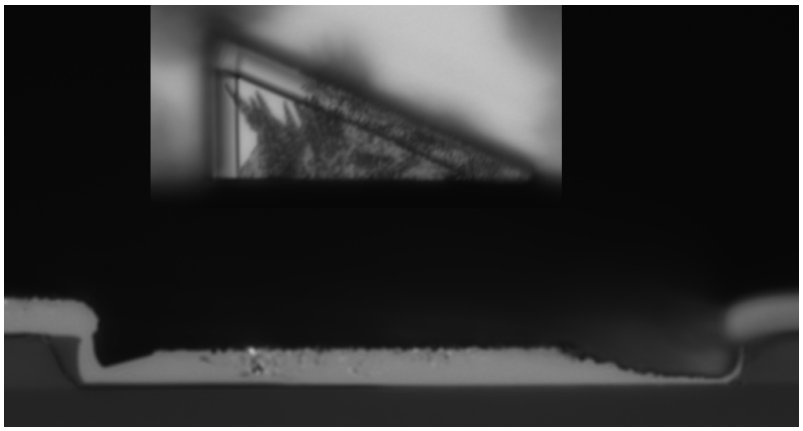

Figure 5.10: A micrograph of an etched triangle cross section and top down view (upper box) that was filled with As_2S_3 using angled deposition.

rounding in the corners of the mask may be enough to significantly change the shape of the fabricated MMI, causing the tapers to join. RSoft BeamPROP was used to compute the transmission, and imbalance curves, in a facsimile of the fabricated MMI design. This will still be an idealised case as there are no particles or other contaminants in the simulation.

The first change to consider, when investigating the rounding of the taper interface into the MMI cavity, is the effect on the MMI's imbalance curve. Figure 5.12 contains the comparison between the nominal simulation previously used in this work and the fabricated facsimile.

From Fig. 5.12 the change in imbalance curve, due to the rounding of the taper edges, is minimal at the bandwidth corresponding to a high extinction (imbalance close to zero) between 3800 and 4200 nm. The shift at the extremities is to be expected as the change in the tapers is equivalent to slightly increasing the W_a. The imbalance curves corresponding to the MMI with $W_a = 13.5$ and 12 µm, from Fig. 5.12, have a larger shift than the MMI with $W_a = 8$ µm. The MMI with $W_a = 12$ µm may even have a wider extinction bandwidth due to the shift. The reason for this substantial shift is because the gap between the tapers is smaller and as such light may couple between the tapers before entering the MMI cavity. This effect may need to be investigated further as it would have a significant effect on the imbalance and may lead to further optimisation in regards to the taper width and length.

The main issue that Fig. 5.12 cannot show is whether the over-cladding can fill the gaps shown in Fig. 5.11. This will only be an issue for the MMI with $W_a = 13.5$ and will cause a decrease in transmission. Whether the imbalance will be affected will be seen in Chap. 6.

5.3.2 As-Se-S deposition

Early in waveguide testing in the MIR, it was found that a parasitic mode was excited in the cladding material when the light launched into the waveguide excited the TE core mode. Figure 5.13 is an image taken with a Xenics Onca camera of TE and TM laser light sent through the same 2 by 2 µm waveguide, fabricated as described above.

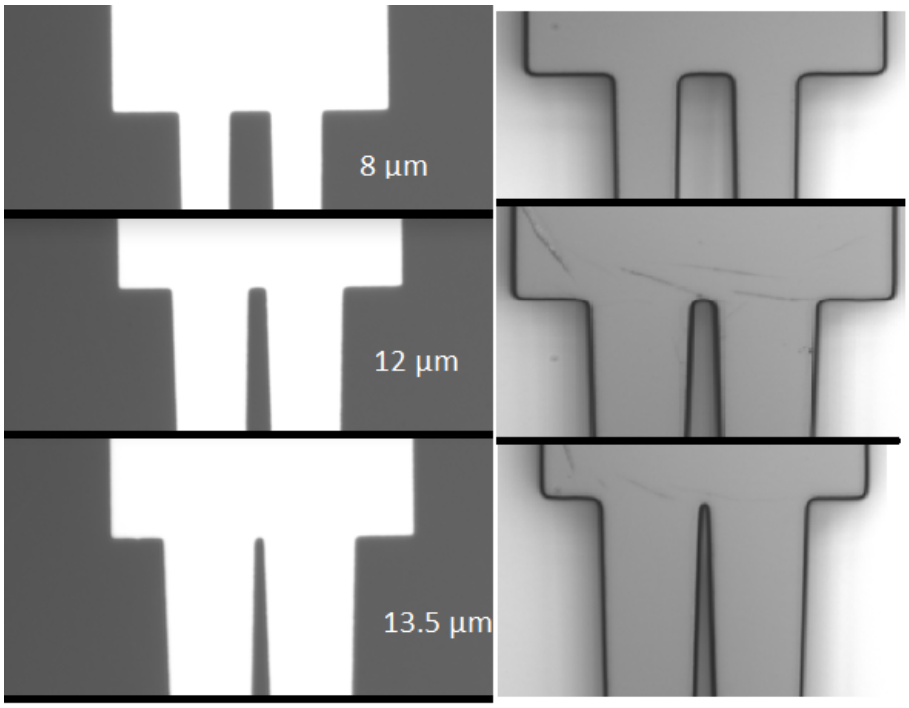

Figure 5.11: Microscope images of the photomask (left) and fabricated MMI (right), displaying the three $W_a = 8$ (top), 12 (middle) and 13.5 µm (bottom).

From Fig. 5.13 the parasitic mode looks to be a combination of guided light convolved with an over-cladding mode. The basis for this hypothesis is the idea that the over-cladding modes are guided in the top cladding material which is effectively a rib waveguide with rough edges, SiO_2 bottom cladding and an air top cladding. This top layer would have a higher roughness and significant loss, more so than the light guided in the core material and requires suppression of some kind.

To remove the cladding mode, the "standard" procedure of introducing a higher index overlay material was adopted. A layer of $As_{24}Se_{38}S_{38}$ was deposited over the clad waveguides. This material had a refractive index of 2.46 [236] making it higher than the cladding material (~ 2.2) and lower than the core material (~ 2.5) and hence would strip light only from the cladding.

$As_{24}Se_{38}S_{38}$ was chosen not just for it's refractive index but also its Tg of 135±2°C [236] which is much lower than the ~ 200°C [237] for the other glasses. This is so the glass can be heated to a plainer surface without reflowing the etched waveguides. $As_{24}Se_{38}S_{38}$ was deposited using the same method as discussed previously for the other two ChGs atop a clad wafer. This occurred after the angled deposition of $Ge_{11.5}As_{24}S_{64.5}$ and before heating the wafer to 160°C using a conventional vacuum oven that was purged with nitrogen to avoid evaporating the glass. Reflowing the glass to planarize it is key here as it means any stripped cladding light from the $Ge_{11.5}As_{24}S_{64.5}$ layer is then confined in the $As_{24}Se_{38}S_{38}$ and able to diffract laterally out of the field of view of the $Ge_{11.5}As_{24}Se_{64.5}$ core waveguide and so cannot coherently interfere with the core light. Figure 5.14 shows microscope images of the cross-section before and after heating.

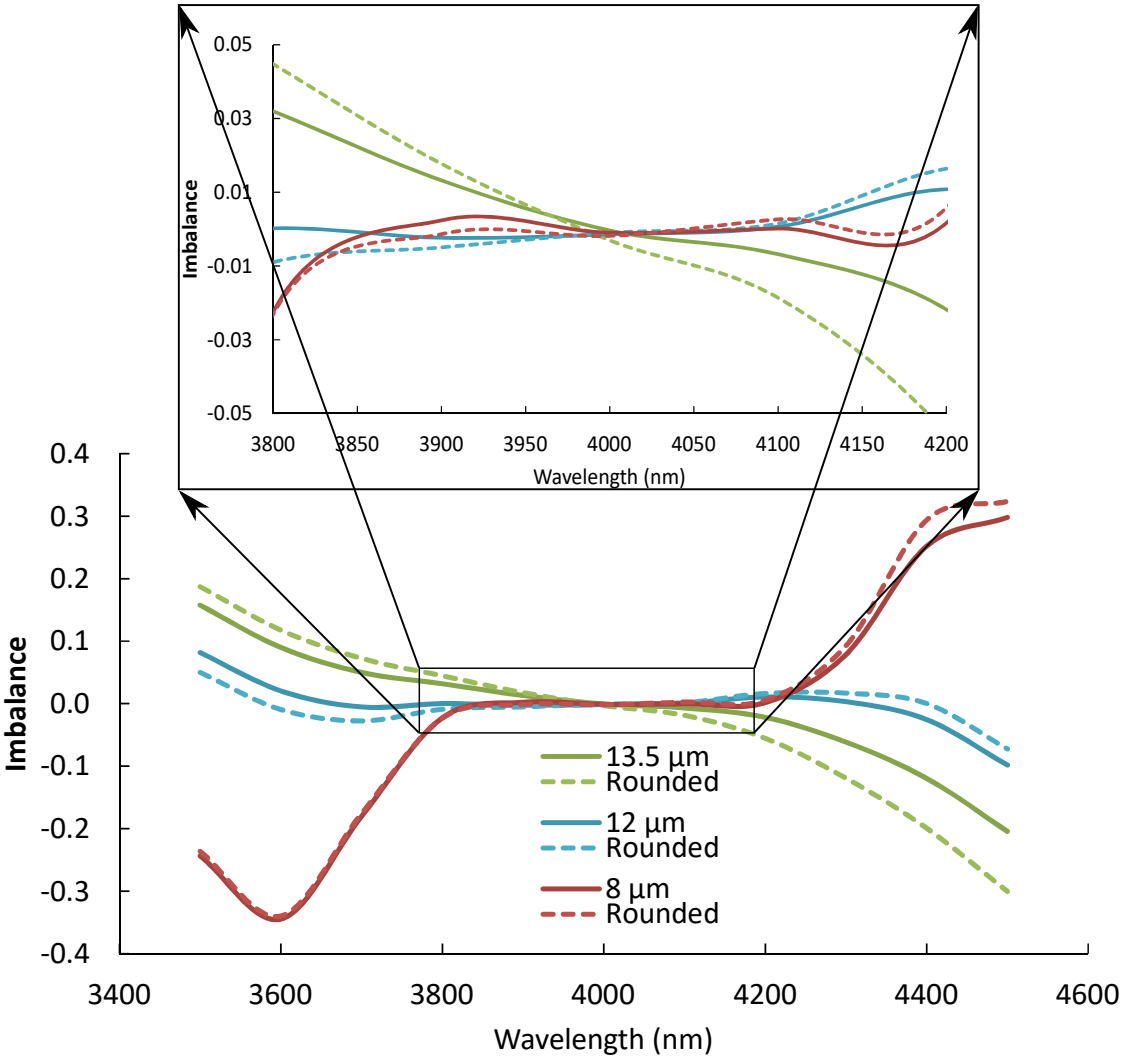

Figure 5.12: The simulated imbalance spectra for $W_a = 13.5$ (green), 12 (blue), 8 µm (red) for the nominal design (solid line) and with rounded edges (dashed line). Included is a magnified section between 3800 and 4200 nm.

Comparing Figs. 5.14a and 5.14b the reflow was a success with minimal structure in the $As_{24}Se_{38}S_{38}$ layer after reflow. What is not shown is the cracking due to a mismatch between the coefficient of thermal expansion (CTE) in the ChG and the Si-on-SiO_2 substrate. A magnesium fluoride (MgF_2) substrate was substituted to correct this mismatch and solved the cracking issue, though at the expense of producing a very delicate substrate prone to cleaving along its many cleavage planes during normal wafer handling and processing.

Although the initial purpose of the $As_{24}Se_{38}S_{38}$ was to strip the light from the waveguide formed in the over-cladding bump, the reflowing procedure highlighted the importance of heat stress on the photonic system. This is especially important if the photonic chips are to be placed in a cryostat to remove background, environmental light.

During the experiments with $As_{24}Se_{38}S_{38}$ the parasitic mode was removed by changing the angle of the wafer during over-cladding and was no longer required in the photonic chip

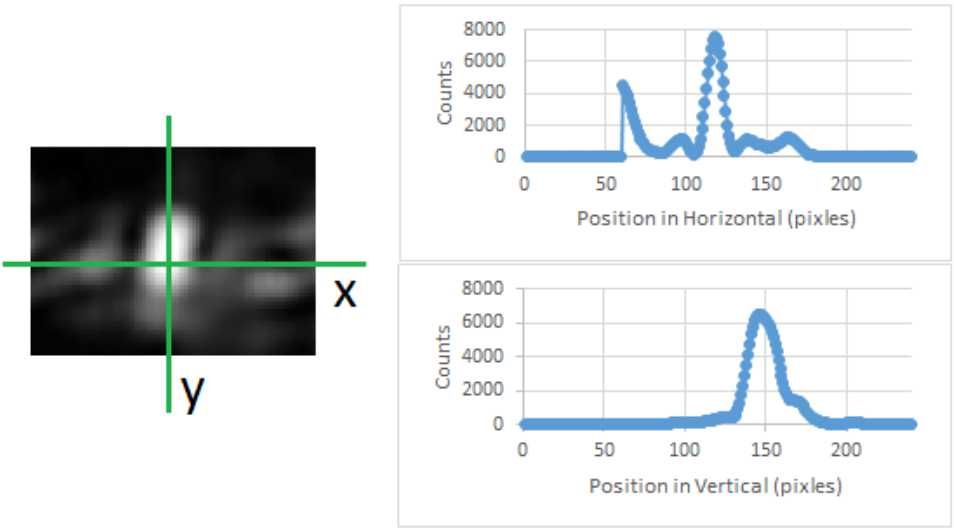

Figure 5.13: Images taken with a Xenics Onca camera for TM light through a single mode fully etched waveguide, focused using a 36x reflective objective, with horizontal (x) and vertical (y) line profiles.

design. An SEM of an $As_{24}Se_{38}S_{38}$ over the clad waveguide is included in Fig. 5.15 as a better comparison between the geometry with parasitic mode and the waveguide geometry without - included in Fig. 5.7.

Comparing the SEM in Fig. 5.7 (no cladding mode) and 5.15 (cladding mode) and the microscope images in Fig. 5.14, there are significant differences in the two geometries. Anecdotally the difference was caused by the angle of deposition being changed from $> 60°$ to $57°$. Future work will need to investigate the effect of this angle and if a small change can cause a change in mode propagation (this being an extension of work from Yu [235]) as was observed earlier, but for this work, it was enough that the mode was removed.

In regards to the reflow experiment of $As_{24}Se_{38}S_{38}$, heating the material to 160°C is enough to cause the material to flow without risk of the glass cracking. Delamination was also an issue at higher temperatures. In Sec. 5.3 it will be explained that an ion gun is used to clean the substrate surface before the ChG deposition. This cannot happen in the over-cladding procedure in fear of metal contamination (predominately tungsten) and so over-cladding is prone to delamination when heated or cleaved or diced. This is not fully addressed in this work but keeping the temperature low reduced delamination of the $As_{24}Se_{38}S_{38}$ over the clad waveguide. This is vital information for future experiments that may need a reflowable ChG glass: if future experiments use components like X- or y-couplers that require an infinitely thin point, like the triangle in Fig. 5.10, to be filled with ChG then reflow may be the only way.

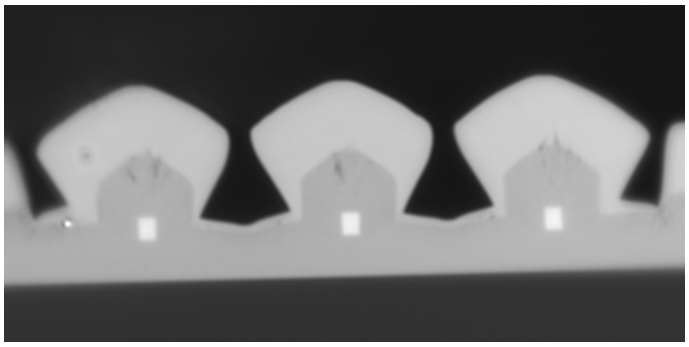

(a) Cross section of three waveguides without heating.

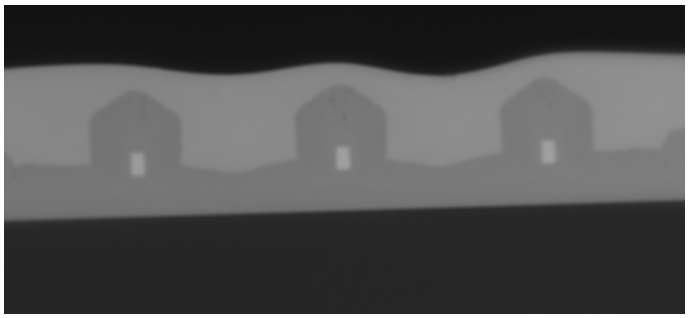

(b) Cross section of three waveguides after six hours at 160°C.

Figure 5.14: $As_{24}Se_{38}S_{38}$ over a fully etched waveguide before and after the reflow procedure.

5.4 Experimental setup

A CAD representation of the experimental setup is shown in Fig. 5.16. The purpose of this experimental setup was to measure waveguide transmission from 3000 to 5000 nm. Additional features of this setup include two microscope setups (imaging rails in Fig. 5.16) that enable rapid measurement of waveguides and MMIs on various lengths of photonic chips. This is achieved by using reflective objectives to focus and image the light into and out of the photonic chip, which enables the two microscope setups to align the selected waveguide with the laser path. This setup was used for the waveguide data included in this chapter and the experiments on the MMI in Chap. 6 and 7.

Figure 5.16 shows the path of the infrared light generated by passing a laser seeded optical parametric amplifier system (OPA) through a Periodically Poled Lithium Niobate (PPLN) crystal [165]. This provided a tuning range from 3100 nm to 4900 nm with a gap between 4200 nm to 4600 nm that fell in a region of efficient parasitic second harmonic effects that would if illuminated, damage the PPLN crystal. The infrared light was generated using a $\sim$ 1 MHz repetition rate 10 ps transform-limited Nd:YVO_4 1064 nm laser developed at the Laser Physics Centre of the Australian National University [238], directed into a periodically poled "fan out" (spatially variant polling period) $LiNbO_3$ crystal to be mixed with a selected continuous-wave (CW) seed laser with the seed wavelength chosen to produce the desired infrared wavelength. This PPLN crystal was translated laterally to select the polling period that then provided the highest conversion efficiency. The parametric process was seeded with a set of external cavity tunable lasers from Santec [239] to

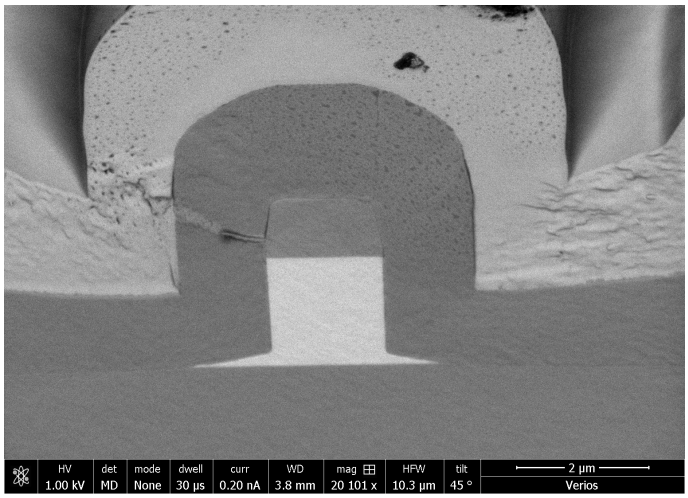

Figure 5.15: A scanning electron micrograph of a 2 µm by 2 µm fully etched waveguide with 2 µm of $Ge_{11.5}As_{24}S_{64.5}$ cladding and 2 µm of $As_{24}Se_{38}S_{38}$ cladding.

generate tunable MIR light from 3000 nm to 5000 nm with up to 200 mW average power. This is not supercontinuum light but single wavelengths that are of transform-limited bandwidth between 1 and 2.6 nm wide respectively using

$$\frac{\tau}{\chi} \times \frac{\lambda^2}{c},$$

using the time-bandwidth product (τ) which is determined by the shape of the beam (0.44 for a Gaussian pulse) and the laser pulse duration (χ), the latter measured to be 10 ps long. The whole system was calibrated and computer-controlled such that it behaved as if it were a tunable MIR laser.

The three irises in Fig. 5.16 were used to align the beam to a precisely known path and maintain the path over time by providing a mechanical reference axis. They also enabled co-linear alignment of a 633 nm Helium-Neon (HeNe) laser that was used to align the reflective objectives to the MIR beam. These apertures were approximately 3 m apart (the distance from the first to the last) to ensure accurate beam alignment and overlap.

Starting from the top left of Fig. 5.16 the light passes through two ZnSe Holographic Wire Grid Polarisers [240]. These control the light's polarization and intensity into the photonic device. Not shown is a half waveplate that shifts the polarization of the initial beam from TE to TM if required. The laser was mechanically chopped, with the chop frequency along with the detected signal fed into a 16 bit National Instruments ADC card for detection with Labview based lock-in amplifier software.

A beam splitter past the polarisers was used to tap off a small portion of the incoming laser light to a "reference" detector. This was used during the measurement of single waveguides as a real-time monitor of the laser's intensity fluctuations. For simultaneous multi-output port measurements using the InSb camera e.g. MMI coupling ratios or MZI extinction, the reference detector is not needed as any fluctuation appears in both ports, as these are ratiometric measurements themselves.

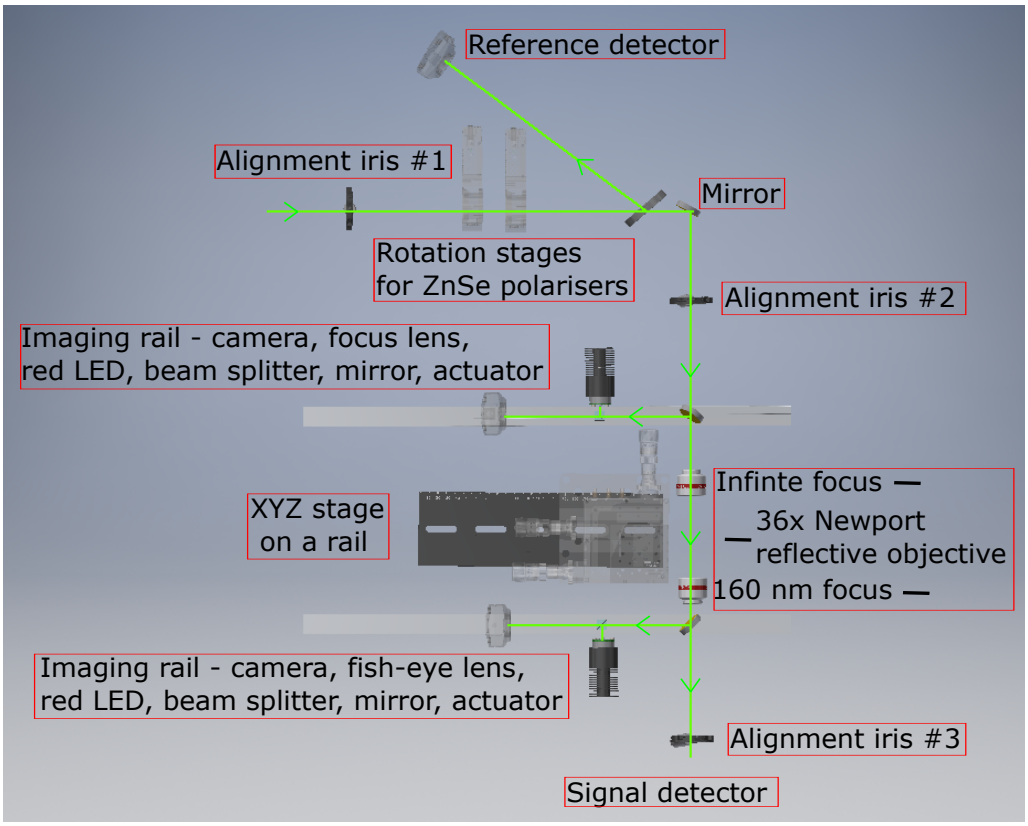

Figure 5.16: The CAD representation of the experimental setup for waveguide testing.

To achromatically focus the laser into a waveguide a 0.5 NA 36x Newport Schwartzchild type reflective objective [241] with an infinite back focal length was used. The computed Point Spread Function (PSF) of this objective is shown in Fig. 5.17, calculated as the Fourier image of a circular aperture with a central obscuration and four arms that support the rear mirror, commonly known as "spiders".

The input objective was inserted into a lockable, vertical, XY stage mount such that it could be aligned into the beam using the HeNe alignment laser. The objective position was then locked with the mount's locking collars in the plane transverse to the beam. The mount itself was attached to a single linear axis slide with a restricted travel range ($< 100\,\mu m$) to provide fine focusing without moving the photonic chip. This was important as the focus of the second objective is dependent on the photonic chip's position.

The photonic chips were mounted on a vacuum chuck positioned on a Melles-Griot 3-axis flexure stage with differential micrometres and hands-off piezo adjustment. This was used to position the chip in the focus of the input lens and close to the correct focus position.

A photo of the actual setup is included as Fig. 5.18.

For alignment of the chip, the achromaticity of the reflective objective was exploited by using it as a microscope. This consisted of a beam splitter, LED illuminator, and a 200 mm focal length achromatic tube lens with a silicon CCD camera mounted at the focal plane. They were positioned on an optical rail perpendicular to the main optical

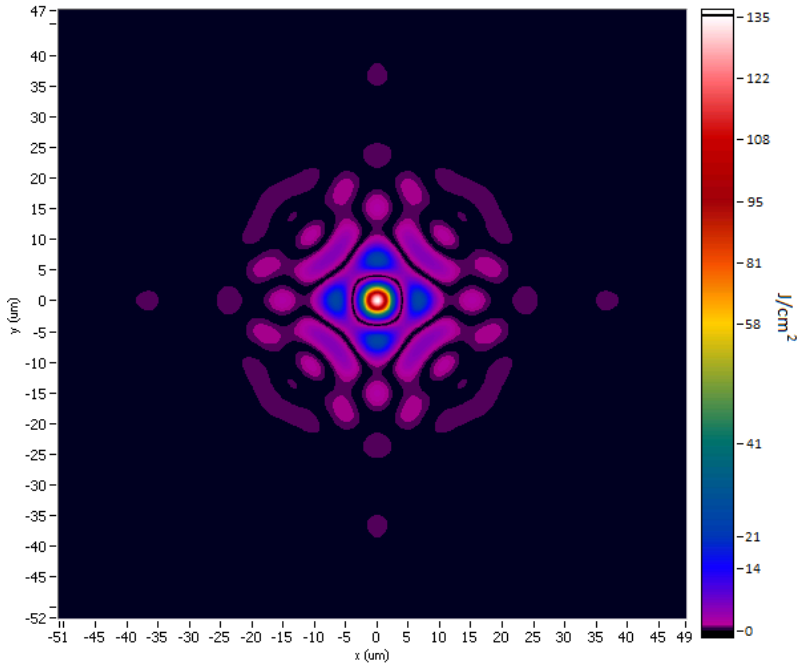

Figure 5.17: PSF calculation of the 36x Newport reflective objective.

axis before the input objective as shown in Fig. 5.18 (with a top-down view shown in the Cad drawing of Fig. 5.16). A mirror was mounted on a precision-guided pneumatic actuator which terminated on a mechanical stop, providing a repeatable position in and out of the input objective's field of view. Thus the objective could be switched between "view" mode where the waveguide cross-section could be focused and viewed in the visible regime, and "launch" mode where the MIR light was coupled into the chip. Labview code was again used to align cross hair's to the MIR spot's centre. This was found by aligning a waveguide for maximum MIR throughput and then switching to view mode and setting the cursors to the centre of the waveguide and storing the position.

A top-down Point Grey CMOS camera [242], shown in Fig. 5.18 above the photonic chip, with a beam tube and hand made LED ring light was also used to aid in waveguide alignment. Once the photonic chip was aligned, using the 3-axis stage and microscope (described above), the top-down camera was set to image the incoming waveguide. Images from the camera were displayed in Labview code where a cross-hair cursor was positioned to the focused beam position, this was after aligning the chip for maximum throughput and identifying the corresponding waveguide. This allowed for a rapid turnaround between chips and movement between waveguides on the same chip.

The output light intensity from the waveguides was measured either through an aperture onto the pyroelectric sensor, or the Xenics Onca InSb camera using another Newport reflective objective but with a 160 mm back focal length. The light from this objective would be a convolution of the PSF shown in Fig. 5.17 and the mode from the waveguide. Since the latter is small in comparison to the former the PSF will be used as an approximation of the output objective's profile. A second microscope setup was used on this

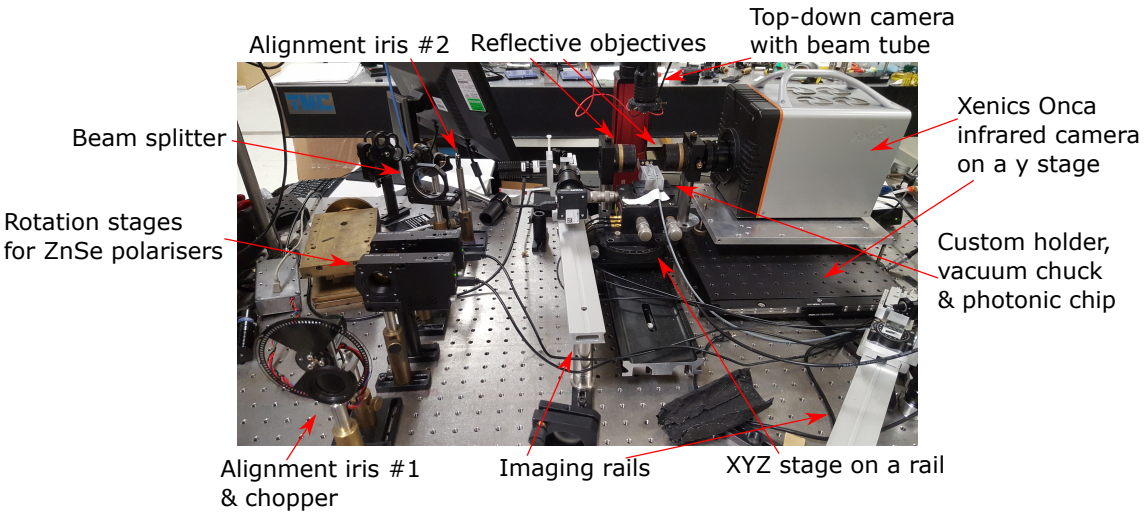

Figure 5.18: Photo of the lab bench equivalent of the CAD representation in Fig. 5.16.

objective, this time with a 1x microscope eyepiece to enable alignment and focusing of the output objective.

Pyroelectric sensors with the analogue power module attachment [243] were used because of their 40 dB dynamic range and high linearity response. The sensors however respond to all wavelengths up to 25 µm incident into their aperture. The stray signal light and background light were blocked using beam tubes that significantly restricted the sensor's field of view. Additionally; the acoustic sensitivity, inherent in pyroelectric materials due to the piezoelectric response, was addressed by chopping the signal. The sensor's slow response time meant that chopping at above 40 Hz was not practical, and the lab had significant air conditioning rumble that the sensors detected. To combat this the chopper was tuned to a narrow frequency band where the rumble was at a minimum at about 22 Hz where lock-in detection could remove the rumble and other light and environmental interference.

From ratiometric measurements of the laser source along with the signal and reference detectors, it was determined that the chopper frequency had to be more stable than an analogue chopper could attain. Therefore a chopper was built in house based on a stepper motor and driver card that had essentially the frequency stability of the 100 MHz quartz master clock on the stepper card. This proved sufficiently stable and accurate frequency tunable to minimise the acoustic effects of the air conditioning.

5.5 Loss measurement of fully etched waveguides

To measure the loss of a waveguide, fabricated using the method outlined in Sec. 5.3, the setup described above was used. The total loss (in dB) of these waveguides, at a wavelength of 4000 nm, is shown in Fig 5.19. This figure is an amalgamation of three measurements: two using the spirals (shown graphically in Fig. 5.5) and one using the standard cutback method. The two spiral chips were cleaved from the same wafer but

were of different lengths (hence a slight shift in data points). The reason for using two sets of spiral waveguides from the same wafer is so that any wafer wide error (from lithography for example) would be transferred to both sets of devices. The cutback chip used in these measurements was from a separate wafer but the same batch of four wafers. These measurements used the pyroelectric reference and signal detector configuration to calculate the total loss: insertion loss, propagation loss and (in the spirals) bend loss. The latter was expected to be negligible due to the bend radius of the spiral waveguides being 200 µm (see Sec. 5.2.2 for more details).

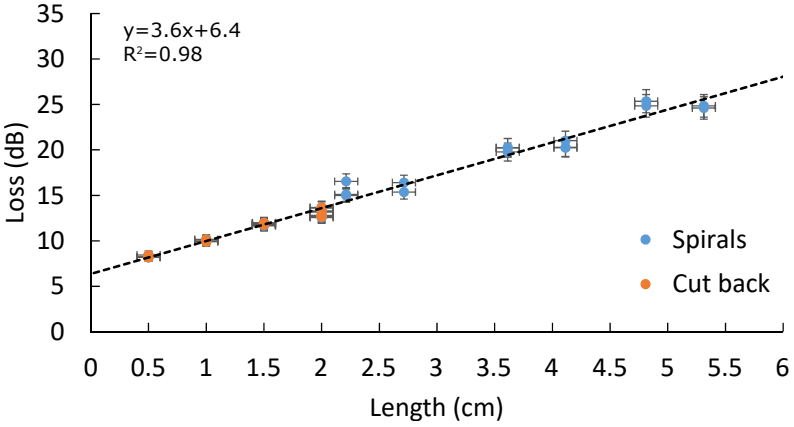

Figure 5.19: Measured loss at various waveguide lengths from three different photonic chips. The cutback measurement (orange) used chips of length 0.5, 1 and 2 cm and the spirals measurements (blue) are from two separate chips of lengths 1.5 and 2 cm.

The results from all three measurements are well fitted by a linear relationship (regression coefficient being close to 1) indicating that the measurement methodology works well and that the bends have comparatively negligible losses. The results however show an unexpectedly high, compared to the estimated minimum loss of 0.3dB/cm in Sec. 5.2.3, the propagation loss of 3.6 ± 0.7 dB/cm, the error generated from the maximum and minimum gradient of the error bars displayed in Fig. 5.19. This requires a chip length of 0.27 cm to maintain a loss of 1 dB in the chip (ignoring insertion loss) as stated in Sec. 5.2.3. Although a chip of this size is not impossible it is impractical and so the loss must be decreased.

The insertion loss in and out of the waveguides from Fig. 5.19 is 6 ± 1 dB. Using an overlap calculation between the PSF generated by the 36x Newport reflective objectives (see Sec. 5.2.1 for more detail) and the fundamental mode of a 2 by 2 µm waveguide; an insertion loss of 6 dB is expected for each face (12 dB in total). A high insertion loss is expected as the index of the material and the NA of the objectives have not been matched, however, it is double the measured loss. This error is likely caused by a simplification of the waveguide model (generated by RSoft FemSIM): the top cladding being smoother in the model than real life and causing a smaller mode; and inaccuracy in the generation of the reflective objective's PSF. Regardless, this discrepancy is insignificant when the loss through the material is 3.6 dB/cm because, as discussed in Sec. 5.2.1, the waveguides and

objectives can be tailored to match and thus reduce a high insertion loss. The propagation loss, however, is much harder to correct - as demonstrated here.

Given the unexpectedly high propagation loss, a spectral scan measurement was undertaken to identify the cause of the loss. A tuning bandwidth of 3000 to 5000 nm was available from the OPA. A "back to back" reference scan without a chip is presented in Fig. 5.20 for reference purposes and to highlight the signal level variation during the scan.

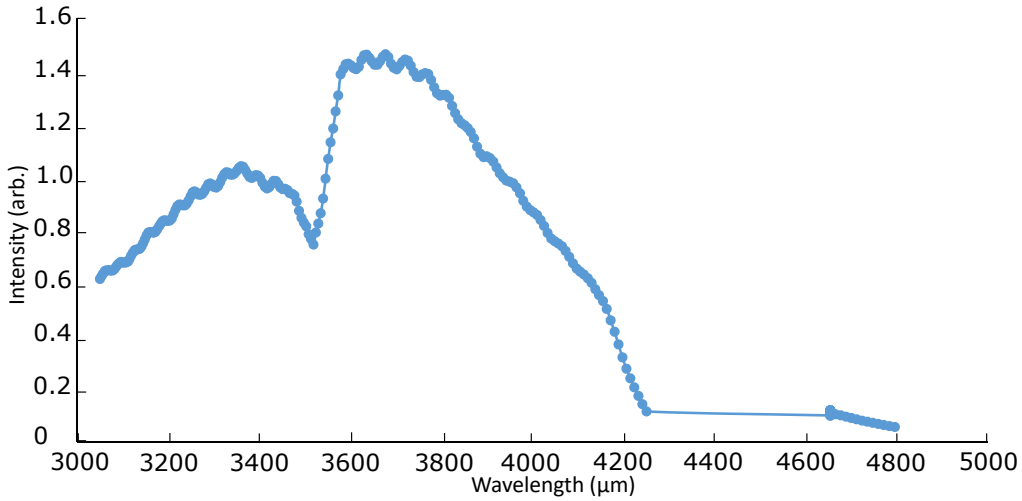

Figure 5.20: A lens to lens measurement with no chip present normalised to the reference detector.

From Fig. 5.20 the rapid onset of CO_2 absorption is observed, from 4200 nm, as is the dead zone that the OPA could not access due to parasitic nonlinear effects in the PPLN crystal, from 4250 to 4650 nm. The change between seed lasers is shown in Fig. 5.20 at 3500 nm with a dip due to laser power, and again at 4250 nm with a less noticeable lack of laser power due to the CO_2 absorption.

Figure 5.21 shows the full wavelength response, from 3000 to 5000 nm, for a cutback measurement using two photonic chips of length 2 and 4 cm. A 2 by 2 µm waveguide was measured, as a direct comparison to the 4000 nm measurement in Fig. 5.19, as well as a 5 by 2 µm waveguide, to show the relationship between the waveguide width and measured transmission.

The high loss in Fig. 5.21 illustrates the difficulty in fabricating waveguides of width and height that are the same order of magnitude as the wavelength. From Fig. 5.21 the wider waveguide has the higher transmission, with an average loss of 2 dB/cm compared to 7 dB/cm in the 2 by 2 µm waveguide. To understand why the cause of waveguide loss must be understood.

Two forms of waveguide loss are investigated in this chapter: sidewall roughness, detailed in Sec. 5.5.1, and chemical absorption, in Sec 5.5.2. The latter investigates the various chemicals that absorb IR light: specifically S-H (absorbing 4000 nm light) in the cladding layer and OH contamination which may be indicative of high water contamination - that would increase the waveguide loss significantly over a wide bandwidth [244].

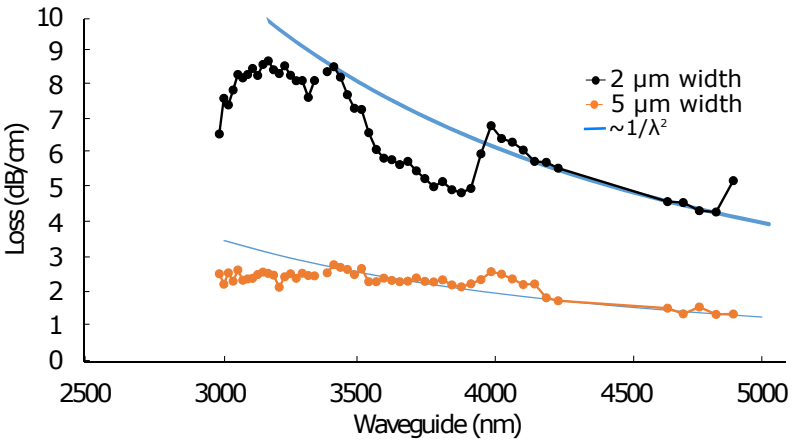

Figure 5.21: A cutback measurement using a 2 and 4 cm long chip for a 2 µm wide waveguide (black) and 5 µm wide waveguide (orange) and an overlay of light loss due to sidewall roughness as a $1/\lambda^2$ (blue) approximation.

Waveguide roughness is typically the dominant form of transmission loss. As an approximation, the loss diminishes at a rate of $1/\lambda^2$ [245] and from Fig. 5.21 both waveguides follow this trend.

The difference in transmission between the two widths of the waveguide can be explained using the overlap of the waveguide mode with the areas of top and side overcladding - where both roughness and chemical absorption in the cladding can occur. The smaller waveguide has an overlap of 16% (calculated using the finite-difference model from Ref. [246]) and the larger has a 6.5% overlap - indicating a 2.5 fold increase in loss due to this overlap. It is this discrepancy that may account for the higher transmission of the wider waveguide but it is certainly not the only variable, as discussed below.

5.5.1 Surface Roughness

Sidewall roughness is one key part of the loss discussion. There are several checks to make to establish whether surface roughness is the main contribution to the high loss shown in the MIR measurements.

Roughness occurs from the lithography fabrication step and subsequent etching. With lithography the limitation is from the resolution of the tool used, sometimes causing a large edge roughness, or from the photomask - that is itself limited by its manufacturing tolerances. For etching with plasma; the profile of the waveguide (whether the waveguide cross-section is a square or a trapezium) is dependent on the etching conditions. Many other surface artefacts can be created during the etching step. For example; cooling of the plasma at the surface of the wafer has previously caused the growth of pillars by micro-masking the surface that resulted in roughness over the entire wafer surface. This effect was identified by noticing the micro-masking pattern deviated away from structures (like waveguides) as if a fluid. Removing the cooling removed the effect.

As an example of a fully etched waveguide, one is included as Fig. 5.22. This is an SEM

micrograph of a bare waveguide. It is included here as it appears to be pitting over the top causing further roughness. This is either from deposition or etching. The edge roughens, however, does not look to be large and the loss from this level of sidewall roughness can be modelled to determine whether this is the cause of the large waveguide loss.

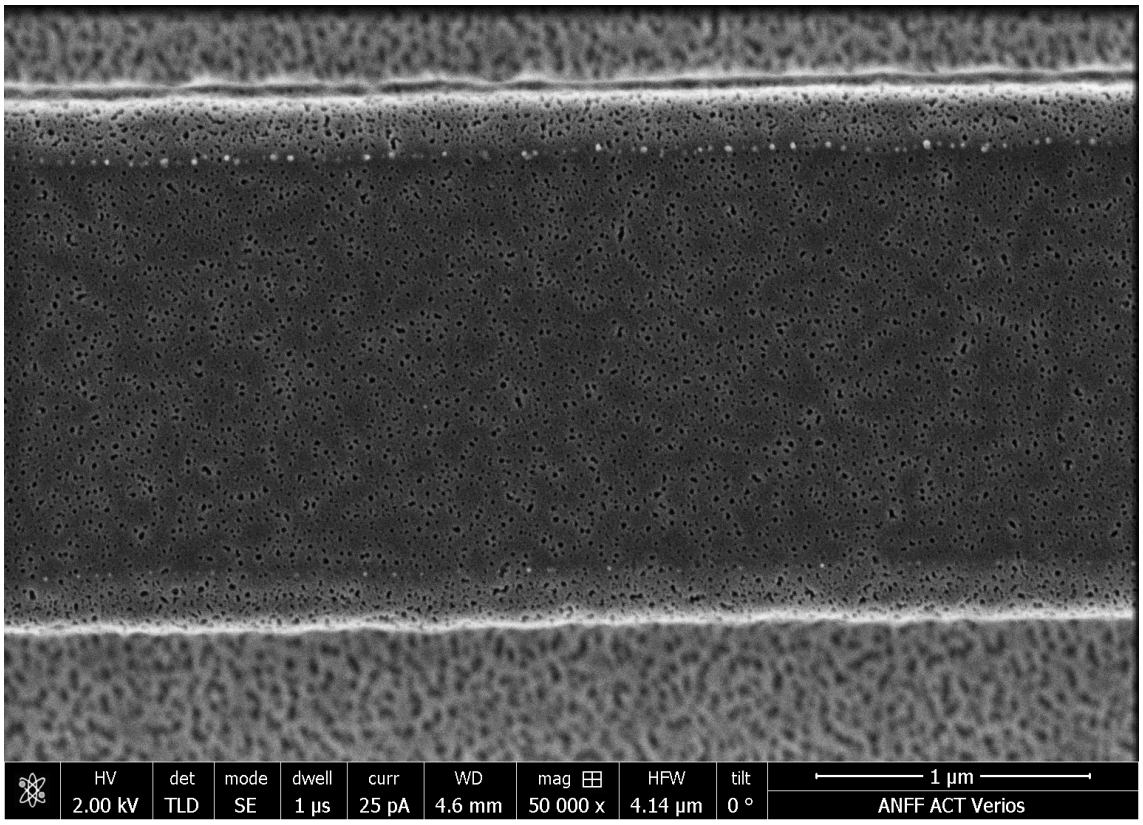

Figure 5.22: Fully etched 2 by 2 µm waveguide imaged by the SEM. All material shown is the same - $Ge_{11.5}As_{24}S_{64.5}$ - with the background as the unfocused bottom layer and the top layer in focus.

A model describing the loss from varying levels of roughness was developed by Payne & Lacey [245]. Using this model the loss at 4000 nm from Fig. 5.21 would require a root mean squared (rms) roughness of 50 nm. Comparatively the previous measurement, shown in Fig. 5.19, would require an rms roughness of 35 nm corresponding to a 210 nm deviation (peak to peak). On a 2 µm wide waveguide this is a roughness of $\sim$ 10%, indicating a roughness that should be visible to an optical microscope (not requiring an SEM to view). Note that due to the over-cladding deposition this sidewall roughness was often hidden from view in most wafers. The bare waveguide in Fig. 5.22 has a flat response compared to a 210 nm deviation indicating that the large loss measurement cannot be sidewall roughness.

To further verify that roughness is not the leading cause of loss, the transmission of the waveguides was measured at a wavelength of 1550 nm. The wavelength dependence of the scattering loss, modelled using the well known Payne-Lacy model [245], links the loss at 1550 nm and that of 4000 nm. Note that this model requires the waveguide to be

reduced to a 1-D equivalent slab waveguide via the effective index method [247] making this only an approximate model.

For this model's roughness parameters, correlation length (Lc) and rms, are from the previous waveguide that was studied at the LPC. It was established that the optical lithography of these waveguides typically exhibited an Lc in the etched waveguide of about 200 nm, with the rms roughness varying in the range $3-20$ nm depending on the material, etch chemistry and etch depth (much less than the 35 nm required for the loss in Fig. 5.19).

Figure 5.23 shows a simulation of the sidewall induced scattering loss for the TE mode for a sidewall roughness of 10 nm rms at both the expected 200 nm roughness Lc, and also at the Lc giving maximum loss. It shows a reduction in propagation loss due to

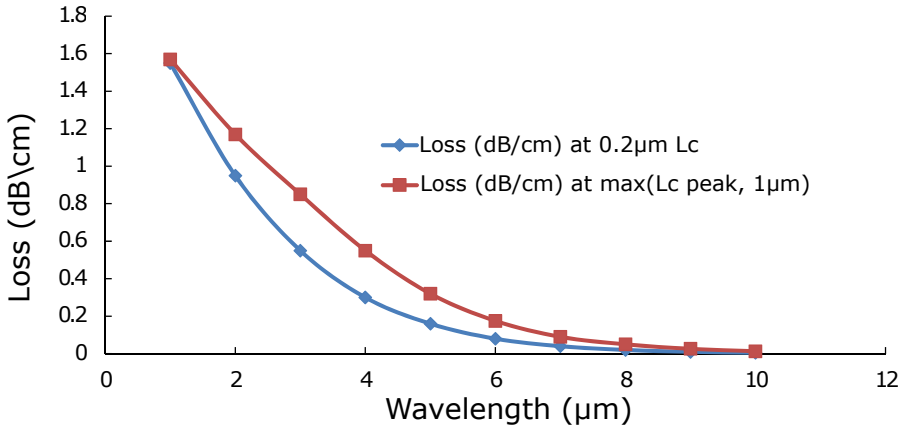

Figure 5.23: Calculated using Payne & Lacey [245], where Lc is the correlation length set to 0.2 µm (root mean squared) in blue and calculated to the beat length between guided and radiation modes (1 µm in this case).

scattering at larger wavelengths, but less than the "generally accepted" $1/\lambda^2$ functional dependence (that was used as a comparison in Fig. 5.21). For example, from 1000 to 4000 nm a 16 times reduction would be expected on this basis whereas only a fives times reduction is predicted at Lc = 200 nm and only a three times reduction at the worst-case Lc. The data also indicates that going from 3000 to 5000 nm results in a drop of the loss by three and a half which should be visible in the experimental results if the loss is indeed sidewall scattering related. This is however not typically observed in the experimental data. The propagation loss from sidewall scattering also scales quadratically with the sidewall roughness in the Payne-Lacey model, and to achieve the observed several dB/cm losses would need a rms roughness exceeding 20 nm. This equates roughly to a peak to peak deviation of 120 nm (six standard deviations) which is easily visible in an optical microscope and was not seen in samples examined this way.

Figure 5.24 is an on-chip measurement of light (around the 1550 nm wavelength) only using the spirals on the chip. The loss gradient in Fig. 5.24 shows the propagation loss is as low as 0.6 dB/cm at 1550 nm. The measurement in Fig. 5.24 used a tunable external cavity laser to measure the loss across an 8 nm bandwidth centred at 1550 nm. Aside from the expected Fabry-Perot fringes from the chip end faces, ripples in the transmission of

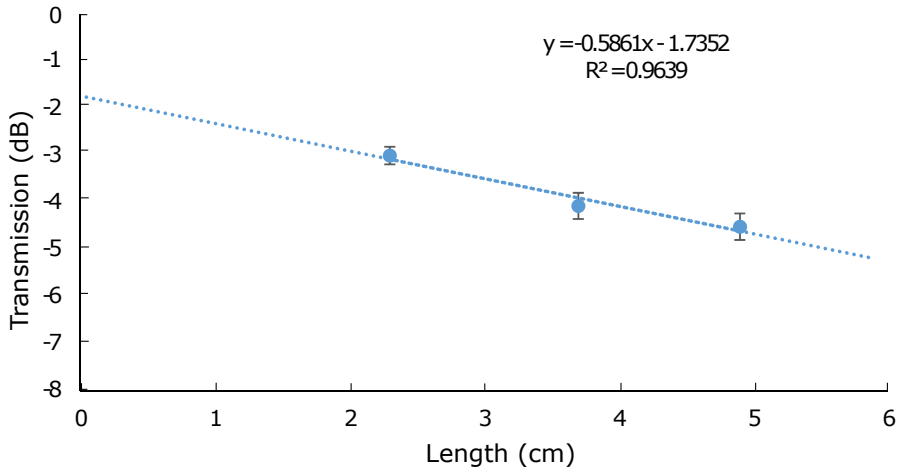

Figure 5.24: On chip loss measurement at 1550 nm using spirals of 2.3 cm, 3.7 cm and 4.9 cm. The loss is approximately 0.6 dB/cm.

$>$ 1 dB were observed as the laser was scanned particularly in the spiral waveguides due to multiple modes being excited in the waveguides. Excitation of, and interference with, higher-order modes produced a wavelength-dependent amplitude modulation. Therefore the minimum loss value observed across a 10 nm wavelength scan was used to generate each data point.

The 0.6 dB/cm propagation loss shown in Fig. 5.24 at 1550 nm and the results of the Payne-Lacey modelling suggest the sidewall scattering induced losses at 4000 nm should be $<$ 0.1 dB/cm. This is much lower than the 3.6 dB/cm measured at 4000 nm with the same waveguides (and spirals), shown in Fig. 5.19. Hence, roughness form the sidewalls is not the main contributing factor to the waveguide loss.

5.5.2 Chemical absorption

Loss in the material is not limited to sidewall roughness and chemical absorption: an oxidised metal, like Aluminium oxide for example, that has contaminated the substrates, or crystallisation (which is common for ChG like AsS_3) of the material, will increase the loss. The difficulty is identifying what is causing the loss. Testing the glass at different points in the lithography and deposition steps helps with this: testing the glass before the deposition to see the base chemical absorption features. For example, etching rib waveguides in individual glass wafers tests defects produced by the etching procedure; optical observation, and using the SEM to image the surface layer, will test crystallisation and surface roughness at any point in the lithography steps. These examples were steps taken in this work in an attempt to rationalise the loss of these waveguides. The focus of these sections is chemical absorption, which limits the focus of the work but encompasses what was predicted to be the main cause of the high waveguide losses.

What has been shown in this thesis is that sidewall roughness is not the main factor in waveguide loss: providing up to 0.1 dB/cm of loss based on experiments at a wavelength

of 1550 nm. Chemical absorption was the other indication of loss based on Fig. 5.21, specifically the additional loss at 4000 nm and between 3000 nm and 3500 nm.

The loss peak at 4000 nm for example fits the profile of an absorption feature in the cladding material, not only based on experiments shown in this work (that of Fig. 5.21) but also by common chemical absorption features recorded for S-based ChG [151, 248, 249, 250]. Table 5.2 details common chemical combinations for both the cladding and the core glass, focusing on combinations of the individual elements in the glasses: Ge, As, S and Se, with basic elements used in the fabrication: H, O and F. This includes the base S-H and Se-H pairs as well as other that may occur due to to the plasma etching of CHF_3: C-H and C-F.

Table 5.2: Applicable infrared absorption [164, 249, 250, 251, 252, 253] on the surface or in the ChG itself.

Chemical	Absorption peak (nm)	Intensity
=C-H	3033	Strong, Sharp
C-H	3125-3500	Strong
C-F	7100-10000	Strong
O-H	2920	Strong, Sharp
−O-H	2770-3120	Strong, Broad
H_2O	2760	Molecular
As-O	4329	Fundamental
Ge-O	3949	Fundamental
S-H	4032	Weak, Fundamental
	3690	Combination
	3110	Combination
Se-H	7800	Fundamental
	4570	Combination
	4150	Combination
	3550	Combination

Absorption candidates, from Tab. 5.2, for the 4000 nm absorption are Ge-O and S-H. Testing the two deposited materials individually (see below) would determine which it is, due to both having Ge but only one having S.

The absorption from 3000 to 3500 nm is less clear. With an abundance of water present in the glass it could be the result of a long "tail" of O-H but it could also be C-H combinations (CH_2, CH_3 etc.) that may remain from photoresist left on the wafer after etching. From the SEM image of a fully etched waveguide in Fig. 5.22 there does not appear to be any visible photoresist left on the waveguide but a previous study [156] found that after a CHF_3 etch (and subsequent wet etch to remove the photoresist) there are multiple absorption features at 3390, 3440 and 3515 nm present in the waveguide regardless of the presence of photoresist remaining on the waveguide surface. These were designated as C-H absorption features.

To check the quality of the materials used, the MIR transmission of $Ge_{11.5}As_{24}S_{64.5}$ and $Ge_{11.5}As_{24}Se_{64.5}$ rib, air clad, waveguides were measured and are shown in Fig. 5.25.

The waveguides in Fig. 5.25, were deposited on an oxidised Si substrate (a 5 µm thick

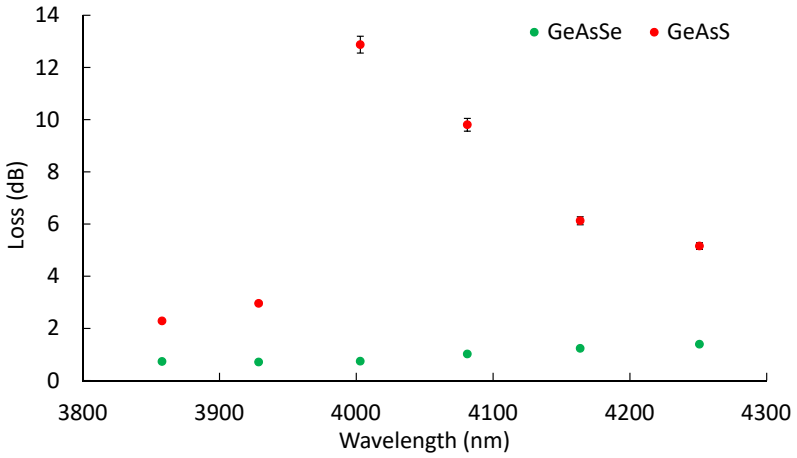

Figure 5.25: Measured transmission spectra of a 2 µm $Ge_{11.5}As_{24}S_{64.5}$ rib waveguide (red) and $Ge_{11.5}As_{24}Se_{64.5}$ (green), on a SiO_2 substrate, normalised to a measurement with only the two 36x Newport reflective objectives.

SiO_2 layer) and etched as before, to produce a 2 µm deep rib waveguide. The S glass rib waveguide had 6 µm of material deposited whereas Se had 4 µm. The reason for using rib waveguides was to replicate the etch conditions for the previous waveguides and to limit the significance of sidewall loss and light in the SiO_2 layer. In addition, thicker films were used to contain the field almost entirely in the glass so that there were minimal surface contamination effects.

The resulting transmission spectra, in Fig. 5.25, show that the S glass has an additional absorption from 3900 nm to 4200 nm, centred at 4000 nm - indicating S-H contamination. S-H contamination has been measured in ChG before, in As_2S_3, by passing hydrogen sulphide (H_2S) through the material during fabricating bulk glass a deep S-H absorption was achieved [151]. Heating the glass past its boiling point removed the contamination. The Se waveguide has a flat loss with no apparent tail from a Se-H absorption feature at 4570 nm. The wavelength itself could not be measured as it corresponded to the dead zone of the OPA. The glasses in Fig. 5.25 does not address the absorption between 3000 and 3500 nm, for this consider the spectra of the ChG rib waveguides made by Ma et al. [156] and Yu et al. [217] in Fig. 5.26.

Figure 5.26 takes data from Ref. [156] and Ref. [217] for two rib waveguides (using $Ge_{11.5}As_{24}S_{64.5}$ as undercladding and $Ge_{11.5}As_{24}Se_{64.5}$ for the core layer), one 2.5 µm high with air cladding and the other 4.4 µm high with overclad of $Ge_{11.5}As_{24}S_{64.5}$, both etched 50% through. Neither shows any particularly high loss at 4000 nm but both show a C-H loss [156] at 3450 nm.

From Fig. 5.25 and Fig. 5.26 the absorption of the waveguide shown in Fig. 5.21 have been identified as S-H and C-H respectively but this does not explain why the loss is high, especially when compared to the waveguides in Fig. 5.26. This may not be a good comparison as the waveguides in Fig. 5.26 are rib waveguides and the waveguide in Fig. 5.21 is a fully etched waveguide. Instead, the additional loss from absorption of S-H should be

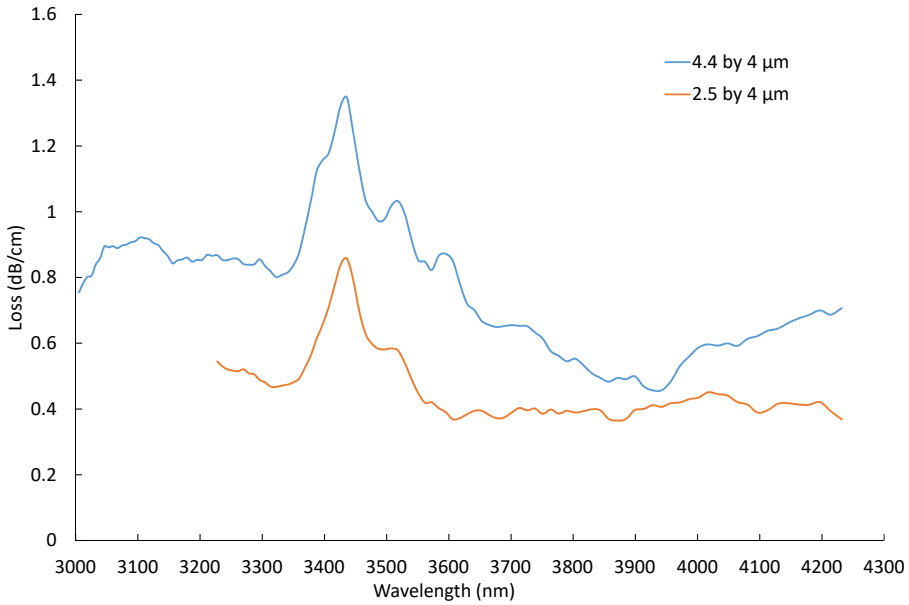

Figure 5.26: Previous results from Ma et al. [156], a 2.5 by 4 µm air clad rib waveguide, and Yu et al. [217], a 4.4 by 4 µm $Ge_{11.5}As_{24}S_{64.5}$ clad rib waveguide, both etched 50% through.

directly compared to the overlap between the electromagnetic field of the waveguide and the cladding material.

Simulation of the fundamental modes for a fully etched and rib waveguide shows that there is significantly more power in the cladding for a fully etched waveguide. These were calculated using the full-vector finite-difference method described in Fallahkhair et al. [246] using the publicly downloadable MATLAB code, which calculates the modal magnetic fields Hx and Hy, assuming that the permittivity tensor was of the form

$$\boldsymbol{\epsilon} = \epsilon_0 \begin{bmatrix} \epsilon_{xx} & \epsilon_{xy} & 0 \\ \epsilon_{yx} & \epsilon_{yy} & 0 \\ 0 & 0 & \epsilon_{zz} \end{bmatrix}, \tag{5.3}$$

where the values of ϵ_{ij} are supplied by combining both of Maxwell's curl equations (the bold text in this section meaning the tensors of permittivity ($\boldsymbol{\epsilon}$), magnetic field ($\mathbf{H}$) and electric field ($\mathbf{E}$)).

The magnetic modes in this mesh are then calculated using

$$\nabla \times (\boldsymbol{\epsilon}^{-1} \nabla \times \mathbf{H}) - \omega^2 \mu_0 \mathbf{H} = 0 \tag{5.4}$$

where μ_0 is used as the magnetic permeability since this is a nonmagnetic material and ω is from the time dependence $e^{i\omega t}$, leading to the calculation of the electric fields Ex and Ey by using

$$\nabla \times \mathbf{H} = i\omega\epsilon\mathbf{E}. \tag{5.5}$$

As an example the modal intensities for a 2 µm wide by 4 µm high half etched rib and

fully etched 2 by 2 µm calculated by this method, are shown in Fig. 5.27.

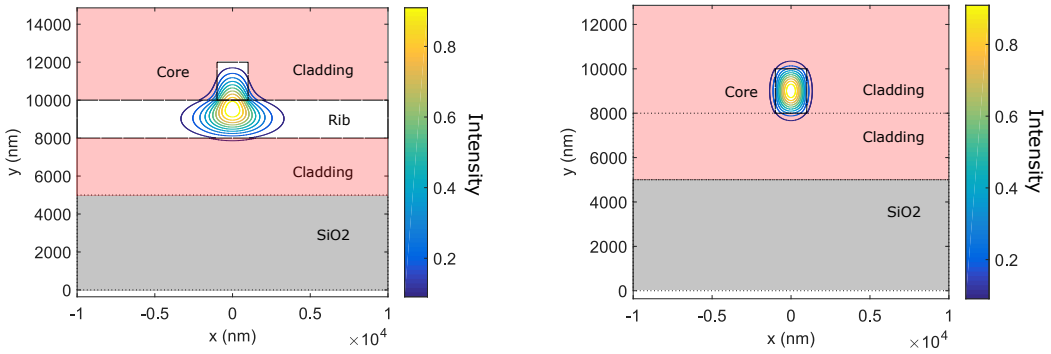

(a) Rib waveguide, 2 µm wide and 4 µm thick etched 2 µm deep.

(b) Fully etched waveguide 2 µm wide by 2 µm high.

Figure 5.27: Simulations of fundamental modes. The cladding area (in pink) surrounds the core material (in white) on a SiO_2 substrate (in grey). The intensity bar is for the contour lines.

Using the modes from Fig. 5.27 the Pointing vector (P) was calculated using the standard method:

$$\mathrm{P} = \mathbf{E} \times \mathbf{H} = \mathrm{E_x} \cdot \mathrm{H_y^*} - \mathrm{E_y} \cdot \mathrm{H_x^*} + \mathrm{E_x^*} \cdot \mathrm{H_y} - \mathrm{E_y}* \cdot \mathrm{H_x}. \tag{5.6}$$

Using the single-mode Pointing vectors, the overlap of the field with the cladding material was calculated using eq. 5.7.

$$\mathrm{Overlap_{cladding}} = \frac{\int\int \mathrm{P} \times \mathrm{Area} \cdot \mathrm{dxdy}}{\int\int \mathrm{P} \cdot \mathrm{dxdy}} \tag{5.7}$$

where the Area is a two dimensional function such that the region of the cladding has a value of one and otherwise has the value zero.

Results from this simulation are contained in Tab. 5.3 for the waveguides used for Fig. 5.26, Fig. 5.21 and an additional full etched waveguide with air cladding, for latter use.

Table 5.3: TE modal intensity percentage overlap with cladding for several prior and current waveguide designs computed using the MATLAB finite-difference model [246]. Each geometry used an undercladding material of $Ge_{11.5}As_{24}S_{64.5}$ (index 2.279 at 4 µm) and a substrate of SiO_2.

Geometry	Width (µm)	Core (µm)	Etched (µm)	Undercladding (µm)	Overclading index	Overlap (%)	Reference
Rib	4	2.5	1.25	2	1	5	[156]
Rib	4	4.4	2.2	6.1	2.279	3.4	[217]
Full etch	2	2	2	3	2.279	15	This work
Full etch	3	2	2	3	1	8.5	This work

The rib waveguides used for Fig. 5.26 have a 3.4% and 5% overlap to the $Ge_{11.5}As_{24}S_{64.5}$ cladding for the 4.4 µm waveguide from Yu et al. [217] and the 2.5 µm wide waveguide from Ma et al. [156] respectevely. Similarly, the 2 by 2 µm waveguide has a 15% overlap with the

S-glass. From these simulation the loss at 4000 nm can be calculated, the results shown in Fig. 5.28.

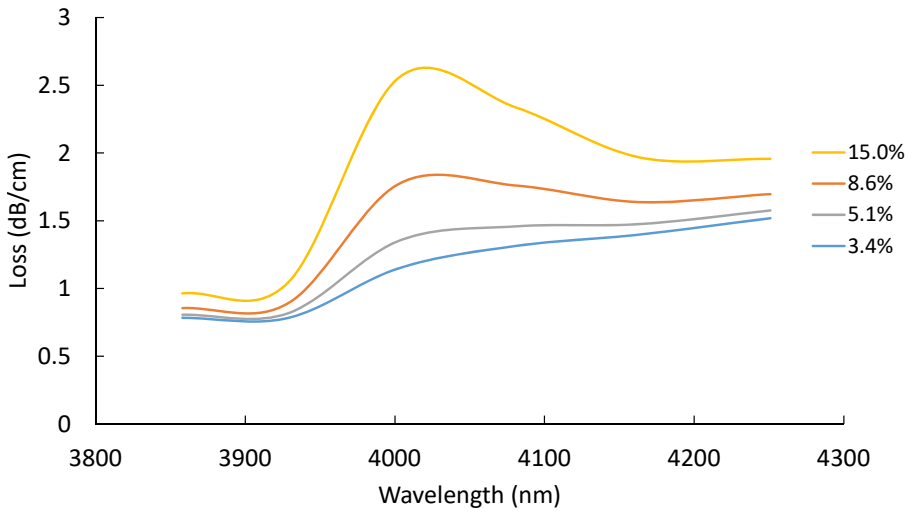

Figure 5.28: Predicted shape of the 4000 nm peak based on the measured absorption in Fig. 5.25 and the calculated overlap for the waveguides featured in Yu et al. [217] (blue), Ma et al. [156] (grey) and this work with air cladding (red) and ChG cladding (yellow).

The calculations in Fig. 5.28 explain the low absorption of S-H in Fig. 5.26 with the waveguides used in Ma et al. [156] having the higher overlap of the two rib waveguides, and shows a larger S-H absorption, but is much lower than the two fully etched waveguides. The extra waveguide used in these simulations has an 8.5% overlap with the cladding layer and should have a two to three times higher absorption peak than the spectra shown in Fig. 5.26. The spectra for this waveguide is shown in Fig. 5.29.

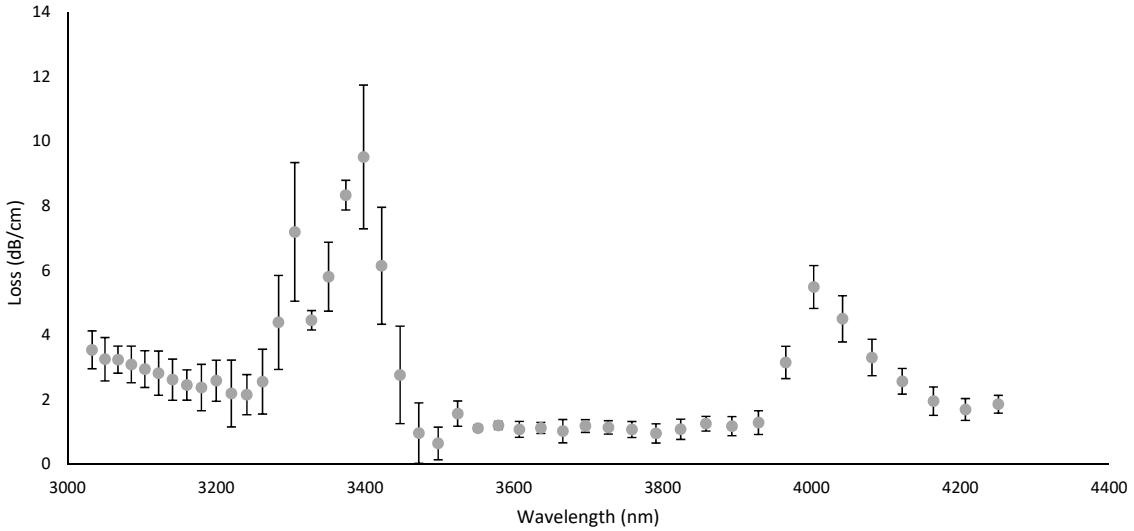

Figure 5.29: The propagation loss of a fully etched, 3 µm wide by 2 µm high, waveguide with no overcladding.

The waveguides used in Fig. 5.29 were fully etched, 3 µm wide, 2 µm high, with an

air cladding. Two chips were used, of lengths 1 cm and 2 cm, to perform the cutback measurement from 3000 to 4250 nm. Like the spectra in Ma et al. [156], shown in Fig. 5.26, this spectra has a flat wavelength response between 3500 and 3900 nm, and like that spectra it has a noticeable absorption at 4000 nm from S-H and between 3300 and 3400 nm suspected to be C-H absorption.

From Fig. 5.29 the absorption at 4000 nm is 4 dB/cm (three times) higher than the base loss of 2 dB/cm (calculated from a linear line between the points at the base of the absorption peak). For the similar peak in Fig. 5.26 the peak is 0.1 dB/cm (1.25 times) higher. Based on the calculated peaks in Fig. 5.28 the increase was expected to be approximately 1.8 and 1.4 times higher than the base loss respectively. This indicates that there is substantially more loss in the full etched waveguide than is accounted for in these simulations - indicating further contamination has accumulated in the fully etched waveguides.

A similar argument can be made in regards to the suspected C-H absorption cluster, at 3400 nm, being four to five times larger than the base loss (an extra 8 dB/cm of loss) compared to twice the loss in the previous work shown in Fig. 5.26 (an extra 0.4 dB/cm of loss). This peak may be explained by the duration of the CHF_3 etch [156] but without knowing the exact plasma conditions of the previous work it is impossible to tell.

What has yet to be discussed is water contamination in the waveguides. From Tab. 1.2 OH molecules in the ChG was a candidate for the loss between 3000 and 3500 nm. C-H contamination, potentially from the ICP etching, has accounted for this but that does not mean OH is not present: the absorption peak being at 2800 nm and thus not in the wavelength range of the OPA. This would be a key indication that water was contaminating the material which has been shown previously to lead to an increase in loss over a broad bandwidth [244].

Previously discussed in Sec. 5.3 wet etching, using a solvent was used, before an oxygen plasma (with a trace amount of CHF_3 and Ar to remove any Ge-O buildup during this step), to remove any remaining photoresist on the fully etched wafer. This step involved water cleaning the solvent off the wafer surface before the oxygen plasma. To remove the water from the procedure a longer final oxygen clean was utilised, increased the length of this step from 1 min and 30 s to 4 min and 30 s. Whether this made a substantial change in water absorption has yet to be tested but it did not lead to a low loss waveguide. This may have been due to contamination of the bulk material itself, before evaporation.

Having a treated bulk material is important as having a high S-H presence may lead to an exceptionally high loss in the waveguides. This is illustrated in two samples of $Ge_{11.5}As_{24}S_{64.5}$, one purified and the other not. The spectra of which are included in Fig. 5.30.

The purified glass had its base components mixed with $AlCl_3$, which reacts with oxygen bound to the Ge, As and S. The material was then evaporated into a separate area leaving the impurities behind. The purified Ge, As and S were then melted together to form the glass.

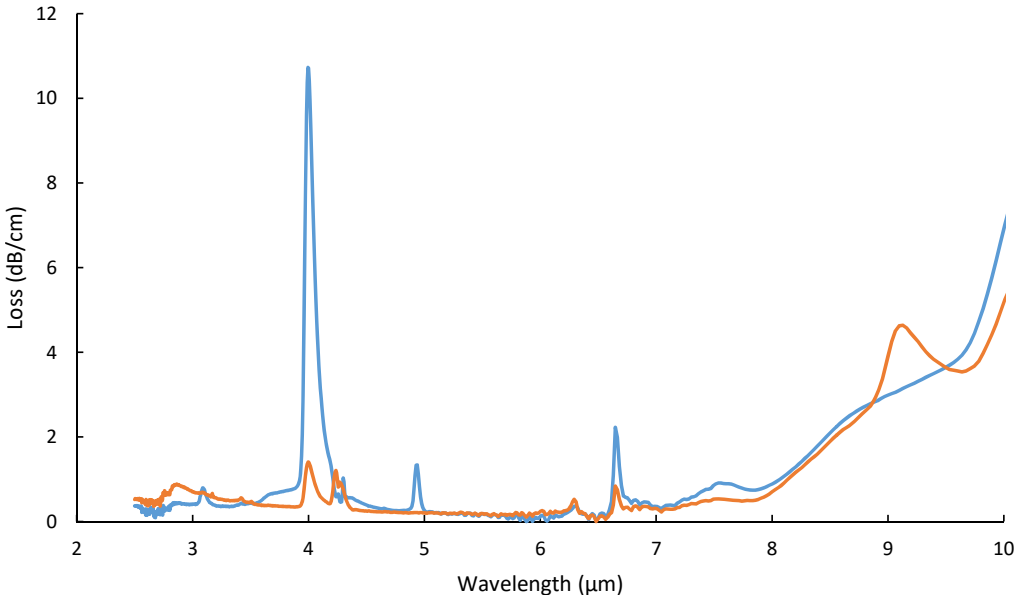

Figure 5.30: The loss of two $Ge_{11.5}As_{24}S_{64.5}$ glasses, measured using a Fourier-transform infrared (FTIR) spectrometer. The blue line is the original glass and the orange line is the treated glass, both are polished 2 mm thick windows. Corrections were made for surface reflections.

There is a significant reduction of the 4000 nm S-H absorption peak in the treated glass, shown in Fig. 5.30, from 10.5 dB/cm to 1 dB/cm. Using the treated glass should reduce the 4000 nm absorption in Fig. 5.29 from 5 dB/cm to 0.5 dB/cm assuming the S-H absorption is not worsened during the deposition in a waveguide. There is also a peak in the treated glass at 2800 nm that may be, but hopefully is not OH absorption. Regardless, the loss of the treated glass appears smaller than the non-treated glass and comparing similar waveguides will test whether water is indeed being absorbed into the material.

5.6 Summary

Chalcogenide glass is a high index material that is transparent in the mid-infrared regime. Using a combination of glasses a tailored refractive index can be made for any application, with femtosecond writing techniques used for small refractive index changes and evaporative deposition for comparatively large index changes. For this work, a glass of $Ge_{11.5}As_{24}Se_{64.5}$ and $Ge_{11.5}As_{24}S_{64.5}$ were used for the core and cladding material respectively as they have been used previously at the Laser Physics Centre at the Australian National University to create low loss waveguides. They also have the same refractive index as a thin film as the original bulk material.

Creating a single-mode waveguide in these materials requires a 2 by 2 µm waveguide. This has a large NA of 0.8. To match this to a more practical numerical aperture of 0.4 a 10 by 10 µm waveguide can be used for the input waveguide and tapered down to the single-mode waveguide. This has been shown, in theory, to add minimal total loss to the

system for waveguides 400 µm long.

The throughput of fabricated waveguides was found to be much higher than expected from the previous work at the Laser Physics Centre. The likely reason for this is due to the chemical absorption of the mid-infrared light. Future work will need to establish a fabrication technique to remove this absorption, such as ensuring the sample is heated during deposition (actively removing water during deposition), replacing the wet etching process with a dry etching process (as in this work) and failing that changing the material to ChG that do not exhibit this high -OH absorption feature (like $Ge_{11.5}As_{24}Se_{64.5}$ or As_2Se_3).

This leads to future work that extends the bandwidth past the L' astronomical band to 10 µm (where key absorption features like O_3 may exist in an exoplanet atmosphere. S-based ChG has their transmission cut-off at ∼10 µm and so moving to a Se- or Te-glass waveguide is inevitable. For this work, focusing on the 4 µm wavelength, the S-based ChG cladding material is acceptable, when treated for the -OH and S-H absorption features.

As stated in Sec. 5.2.3, for astrophysics a loss of 20% is regarded as an acceptable penalty for the benefits of using a photonic chip over bulk glass optics. A 1 dB loss, as was measured in this work, over a 400 nm bandwidth, is an acceptable loss for an on-chip nulling interferometer. The multimode interference coupler modelled in Chap. 3 does not add to this loss and is significantly robust to fabrication tolerances in respect to its transmission and imbalance. The experimental verification of the MMI has yet to be discussed. Chapter 6 explores the MMI as a 3 dB coupler and shows the longest bandwidth of a published MMI in the MIR, to the authors best knowledge. Chapter 7 then shows the null depth of these MMIs by using them as a splitter and combiner in a Mach-Zehnder interferometer configuration.

Chapter 6

Experimental Results

This chapter includes work already published in the proceedings:

Kenchington Goldsmith, H.-D., Cvetojevic, N., Ireland, M., Ma, P., Tuthill, P., Eggleton, B., Lawrence, J. S., Debbarma, S., Luther-Davies, B., and Madden, S. J., "Chalcogenide glass planar MIR couplers for future chip based Bracewell interferometers," in [*Proc. of SPIE*], **9907**, 990730 (2016).

Kenchington Goldsmith, H.-D., Ireland, M., Ma, P., Wang, R., Luther-Davies, B., Madden, S., Noris, B., and Tuthill, P., "Photonic mid-infrared nulling for exoplanet detection on a planar chalcogenide platform," in [*Optical and Infrared Interferometry and Imaging VI*], Mérand, A., Creech-Eakman, M. J., and Tuthill, P. G., eds., 33, SPIE (2018).

The purpose of nulling interferometry, for exoplanet detection, is to remove starlight and allow light from an exoplanet to be measured. This is achieved through the combination of light from multiple telescopes. For proof of principle, a two telescope system is proposed which only requires the beam combiner part to be made on-chip. The multimode interference coupler was chosen as the on-chip beam combiner due to its tolerance to fabrication errors in regards to its transmission [176]. In Chap. 3 the MMI was modelled to show the imbalance was robust to fabrication error as a 3 dB coupler. Chapter 4 then furthered the investigation into the imbalance by modelling the effect of changing the MMI's taper width - the result being an increase in bandwidth at a deep (40 to 60 dB) null. The experimental verification of the coupling characteristics is detailed in this chapter.

A note here in regards to the model used in Chap. 4: this model describes what occurs in the MMI cavity at any point in the main cavity - it does not include the tapers directly. Indirectly, the model uses the taper widths to know what modes are excited in the MMI cavity but it does not take into account the length of the tapers. Assumptions confining the wavefunction to the MMI cavity were made in this model that are not representative of what a real MMI will produce. Its purpose was to show only the effect of individual modes on the final wavefront in an attempt to understand the imbalance curve with the change in taper width and was used as such in that chapter. It does not include any potential mode coupling effects in the input or output tapers that may change the imbalance curve further. As such the simulations by RSoft BeamPROP are used as a comparison to the experimental results instead.

In this chapter the focus is on the performance of the MMI in terms of the imbalance

(eq. (3.15)):

$$\text{Imbalance } (\%) = \frac{\text{Cross} - \text{Bar}}{\text{Cross} + \text{Bar}} \times 100$$

where the Cross and Bar refer to the intensity of the PSF, measured by the pyroelectric detectors (see Sec. 5.4 for more details) in the output ports. Figure 6.1 shows the terminology for the MMI measurements in this chapter: left and right (in the direction of the beam) input ports and the cross and bar ports for each input. Note here that in all calculations and simulations displayed the cross and bar ports are normalised by the total transmitted power, that being the addition of the two output ports.

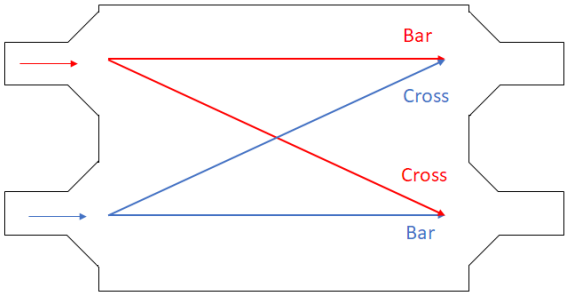

Figure 6.1: MMI schematic illustrating the cross and bar ports for input into port left (red) and port right (blue).

Light contamination from the MMI itself is a key issue in this chapter and the investigation of methods of limiting this source of error are reported here. Spurious light is generally an issue for wavelengths away from the optimum design wavelength (4000 nm), due to the mismatch between the localised intensity maxima in the MMI forming away from the output taper positions, but for estimating the null depth the scattered light is an issue everywhere. Section 6.2 and 6.3 compare the scattered light impact on the null depth with and without a topcoat treatment of carbon and amorphous silicon respectively and Sec. 6.4 uses a rotated MMI whilst offsetting the input and output waveguides to remove any light contamination.

6.1 Noise reduction techniques

6.1.1 Isolating the waveguide outputs

Background light and scattered light from the MMI (or from the waveguides) limit the certainty of the measurements and needs to be addressed. This is a particular issue for pyroelectric detectors, used for measuring waveguide loss, as they are sensitive to an extremely wide range of wavelengths and so thermal background is also an issue. To reduce the measurement uncertainty due to background light the Xenics Onca InSb camera (sensitive only in the $1.5 - 5.5\,\mu m$ window), previously just used for alignment, was instead used to image both the output arms of the MMI simultaneously. One pyroelectric detector remained to monitor the laser fluctuations as a normalisation between measurements (when required). An image produced by the camera is shown in Fig. 6.2. The experimen-

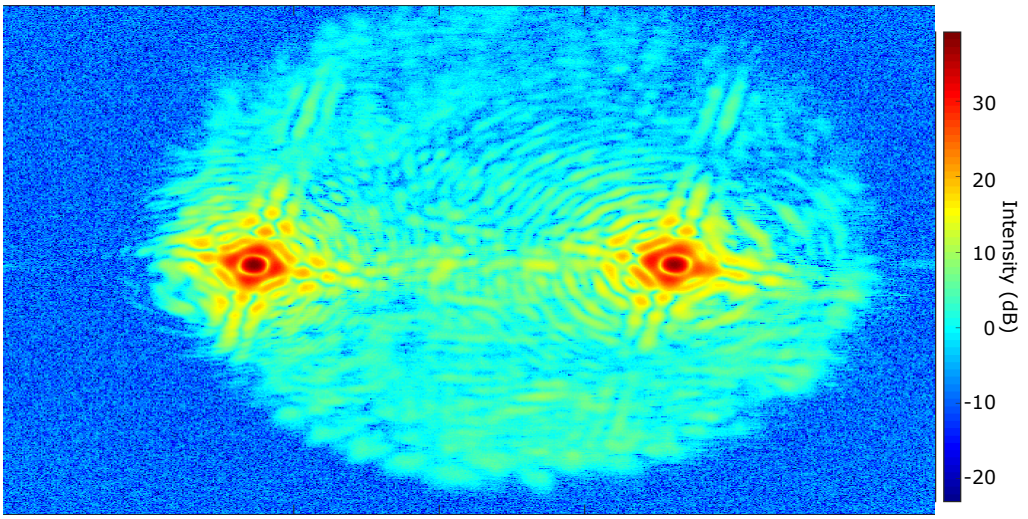

Figure 6.2: The PSF of the MMI's output ports, of an MMI with $W = 45\,\mu\text{m}$ at a wavelength of 4000 nm, taken with the Xenics Onca Camera without the imaging lens attachment. A logarithmic colour scale has been used. The circular aperture of the camera's cold shield blocks stray light from entering into the camera.

tal setup was the same as before, described in Sec. 5.4, but without the two pyroelectric detectors. An iris is not required to isolate the individual output waveguide point spread function (PSF) to reduce the scattered light as it is now spatially resolved and a software iris can be used instead. Output light was measured using integration over the area encircled by the first null of the PSF: the areas of highest intensity (the maroon circle) in Fig. 6.2.

In Fig. 6.2 the two output ports have a much higher intensity than the background and scattered light. The surrounding circle is the cold shield of the camera blocking stray thermal emissions from entering the camera. It is visible in this image because the reflective objective used to image the output face of the photonic chip does not have a pupil plane located at the cold shield position. The signal closest to the shield (left of Fig. 6.2) appears slightly vignetted, as would all light close to the cold shield, but the central lobe was unaffected. For each measurement, the two PSFs were shifted so that their central lobe, and a large proportion of their radial disks, did not experience vignetting.

The camera array non-uniformity and pixel linearity were corrected using the supplied (by the manufacturer) non-uniformity correction (NUC) that was calibrated for integration times between 0.1 and 10 ms, where lower integration times are not guaranteed to produce linear results and higher times would saturate the camera from the background light. This is only a 30 dB difference and would thus not be enough to measure the extinction depths suggested by theoretical predictions in Chap. 4 and so frame integration, of 1000 frames as standard, was applied with appropriate chopping of the signal for active background subtraction via the lock-in methodology.

Figure 6.3 shows the required degree of frame integration to measure a specified extinction by reducing the background light and camera noise by lock-in and averaging compared

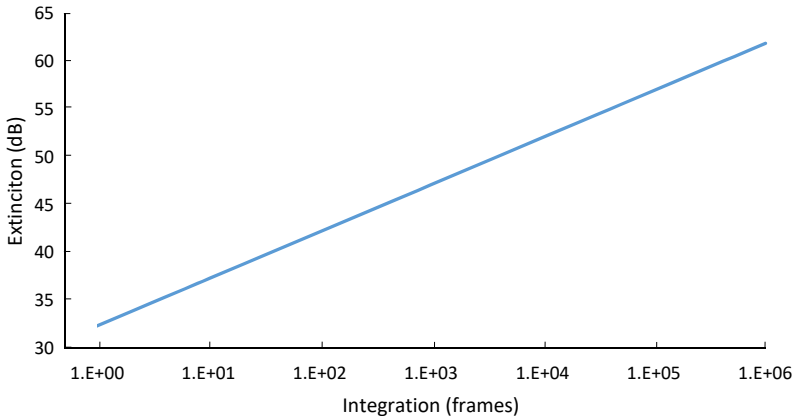

Figure 6.3: A simulated reduction of background and camera noise based on a frame integration (starting at 1 frame), lock-in detection, methodology - chopping the signal for a collection of light and dark frames. The extinction was calculated using $10 \log 10(\sigma/10000)$ where the standard deviation of the noise was calculated for each pixel of the camera compared to a nearly saturated signal of 10000 units. The exposure time is irrelevant here as the saturation of the antinull port is the critical component to having a high contrast ratio to the noise.

to a near-saturated signal. Increasing the exposure time so that the signal from the antinull port is almost saturating the camera provides the best contrast between the two ports. Using this simplified model (that compared the background light to the near-saturated signal) 10^6 frames would be required to measure a 60 dB extinction (the difference in light emitted from a star like our own and a planet like our own at a wavelength of 10 µm), and the 1000 frames as standard providing an approximate 40 dB extinction measurement capability (the difference in light to a star like our own and a Jupiter sized exoplanet at 1000 K at a wavelength of 4 um).

6.1.2 Polarisation response

Using frame integration and lock-in detection, an experiment was performed to verify the polarization response of the splitting ratio. To do this MMIs with $W = 45$ and 46 µm were measured with both TE and TM input polarisation states and their imbalance calculated. Both are displayed in Fig. 6.4a and 6.4b respectively.

The imbalance curves of these MMI with $W = 45$ and 46 µm, shown in Fig. 6.4, follow the overlaid simulated imbalance of the MMI with the same width and $W_a = 8$ µm. A loss in one arm was implemented in the simulation to maintain this match and is required due to a higher loss of one of the output waveguides. Ideally, this would not be required.

The simulation included in Fig. 6.4 was of the TE mode at each wavelength and by Fig. 6.4a the TE data appears to match the prediction better than TM at the extremities of the bandwidth. For the data in Fig. 6.4b however both the TE and TM modes fit the imbalance simulation better than the other at various points along the extremities: the TM from 4700 to 4800 nm and TE from 4850 to 5000 nm. Over the areas of importance, from 3800 to 4200 nm in Fig. 6.4a and 4000 to 4250 nm for Fig. 6.4b, the TE and TM

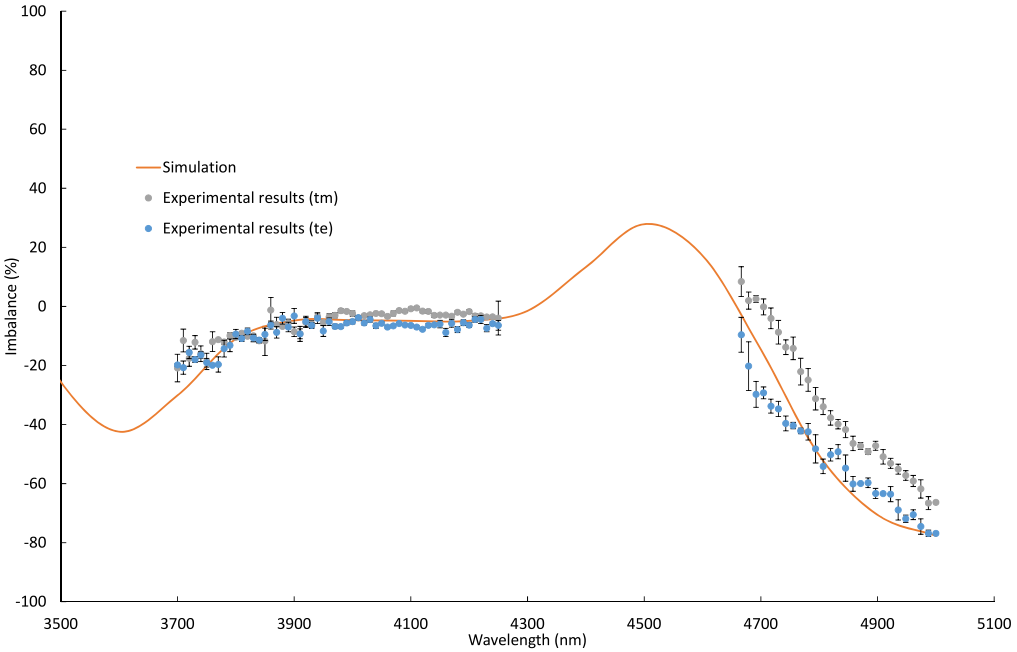

(a) An MMI with $W = 45\,\mu\text{m}$ and $W_a = 8\,\mu\text{m}$.

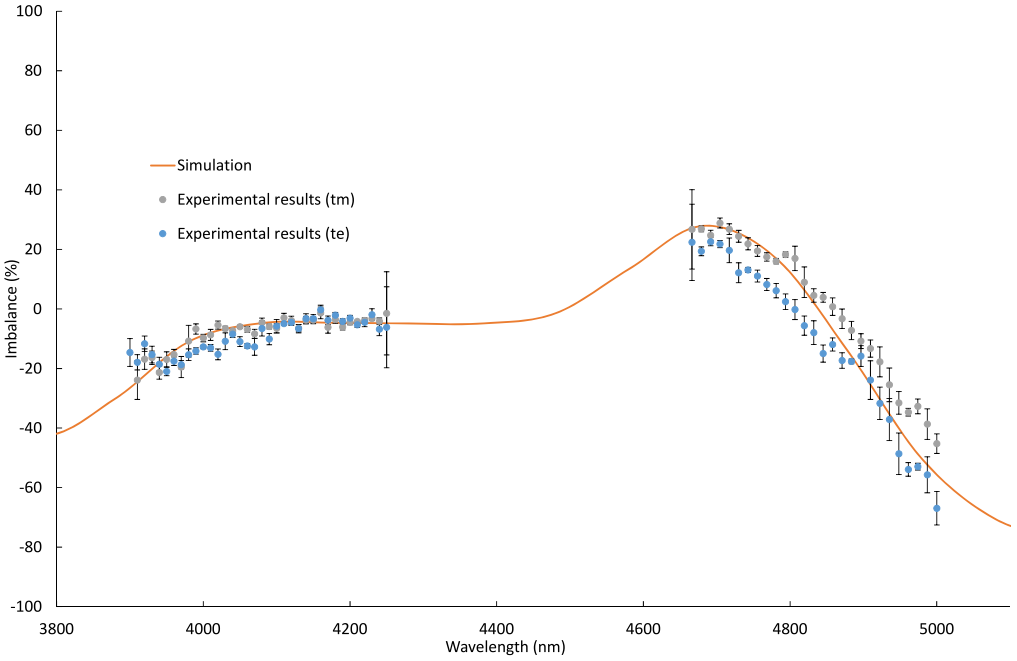

(b) An MMI with $W = 46\,\mu\text{m}$ and $W_a = 8\,\mu\text{m}$.

Figure 6.4: The imbalance between the bar and cross port, measured by the Xenics Onca camera when launching TM (grey circles) or TE (blue circles) light into the left input port of the MMI. An overlaid simulation (the orange line) of the same MMI for TE light and a 4% and 10% loss in the bar port respectively.

modes are indistinguishable for both figures. This shows that the MMI's splitting ratio is comparatively constant, for both polarisations, in a 400 nm region, compared to the extremities.

To understand why there is such a little change in one area and a significant difference

in another it is prudent to return to Sec. 3.4.3 and look to the MMI's dependence on the refractive index. For a perfectly square waveguide, the effective index is the same for TE and TM light. A slight change in waveguide dimension is expected due to a fabrication error. The MMI is however robust to this error at the designed wavelength of 4000 nm. What Fig. 6.4 shows is an extension of this: the MMI is robust to a slight change in refractive index difference at wavelengths corresponding to light entering the MMI tapers. Away from these areas, the index will change the imbalance. This is shown in Fig. 3.17 with the imbalance of the TE and TM light deviating as the core material's refractive index increases (which changes the position of where the localised intensity maxima form and thus whether the light is captured by the output tapers).

In terms of measuring the extinction, with both TE and TM mode illuminated together, the small fluctuations are shown in Fig. 6.4a (less so in Fig. 6.4b) at 4100 nm would cause a limitation. The difference in the imbalance between the TE and TM mode at 4100 nm is 6% and, assuming the imbalance is corrected to zero for the TE mode (and thus a theoretically infinite extinction), the extinction would only be measured to 30.5 dB. Hence when measuring the extinction it is advisable to use a single polarisation but future work, for astronomical purposes, both polarisations will need to have a similar imbalance, like in Fig. 6.4b (but even in this data there is an extinction limitation of 40 dB).

A key point that has been neglected in Fig. 6.4a and 6.4b are the error bars. The uncertainty in the measurement was calculated using the standard deviation of the mean intensity of both ports. What they show, as a generalisation, is that minor fluctuations occur in the bandwidth of interest, and major fluctuations occur at the extremities, with an exception at 4250 nm which is known as a weak point in the spectra (see Chap. 5 as to why). The reason for this difference in measurement uncertainty is the dependence of the scattered light from the MMI being wavelength dependent. During the bandwidth where the imbalance is approximately constant the scattered light is low as most light enters the output tapers of the MMI, but away from this region light escapes the MMI slab and interferes coherently with the signal light increasing measurement variability. At the

6.1.3 The impact of scattered light

There are several sources of scattered light present in the MMI measurements displayed so far. At the design wavelengths, the scattered light arises from particulate contamination within the MMI slab region, from uncoupled launch light trapped in the core layer by the high index cladding, and from waveguide sidewall scattering losses. An example of this was shown in Fig. 6.2 with the two evenly split PSFs displayed. Both have a 40 dB peak and regions of up to 15 dB scattered light in a (horizontal) line between them. At other wavelengths, the scattered light also includes effects from the now incorrect length MMI. At longer wavelengths, localised intensity maxima forms in front of the output ports and begins to spread out. At shorter wavelengths, the localised intensity maxima have yet to form. In both cases, the light interacts with the end of the MMI cavity and some are not coupled into the output waveguides and proceeds through the cladding material to the

end of the chip. Figure 3.28 shows the wavelength dependence of the localised intensity maxima in the MMI slab: the diffraction in the MMI at shorter wavelengths and the diffraction in the cladding at larger wavelengths.

Gating over the PSF's central peak, in post-processing, creates an integration zone that is proportionately more signal than scattered light. The light in the integration zone is not completely free of contamination and is a combination of the strongest part of the signal, portions of the scattered light that exists in the cladding material, and light from the other output port - bands of the PSF that extend out to infinity in all directions at varying intensities. Two cross-sections of a numerically computed PSF from the Newport objective [241] are displayed in Fig. 6.5. The horizontal curve is along the axes of the four equispaced "spiders" that support the secondary mirror, and the diagonal curve is 45° away from the spiders. The relative amplitude from one PSF at the position of the other was found to be approximately 37.2 dB at a 120 µm spacing and 40.5 dB for a 240 µm spacing (the two spacings of the chip used for these experiments). Turning the objectives so that the spiders are at diagonal to the chip plane reduces this to 53 dB and 55 dB respectively.

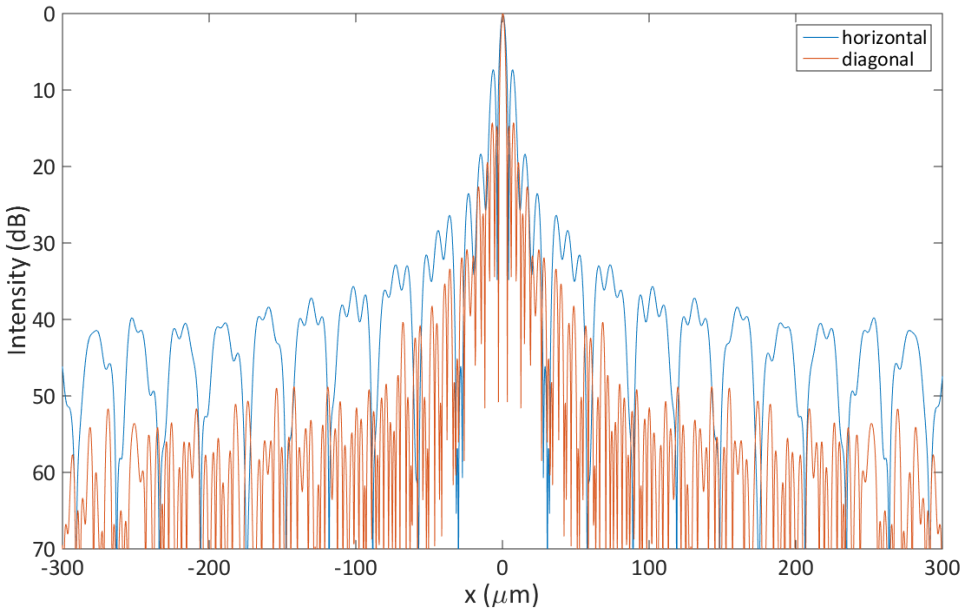

Figure 6.5: Numerical computation of the horizontal (blue) and diagonal (orange) output objective's PSF cross section.

Whilst these sound like small numbers compared to the centre lobe, it is important to note that the light is coherent and so interference effects will amplify the impact of small amounts of scattered light.

$$\begin{matrix}\text{upper}\\\text{lower}\end{matrix}\ \text{bound} = (\sqrt{\text{intensity}} \mp \sqrt{\text{scattered light}})^2 \tag{6.1}$$

for coherent light whereas incoherent light only provides an upper bound

$$\text{upper bound} = \text{intensity} \; + \; \text{scattered light}. \tag{6.2}$$

For example, if the signal is 40 dB then the calculated extinction depth from the measured imbalance could be anything from 33 to 40 dB. This is a fundamental limit to the measured null depth uncertainty as it cannot be removed from the measurement. Scattered light, however, can be reduced by using an additional top material that will absorb the guiding light in the cladding. It is noted here that conventional cladding mode stripping methods are difficult to implement with high index materials as there are no polymers with refractive index beyond 2.3 that are transparent in the IR. Experiments using an intermediate glass were reported in Sec. 5.3.2 but as was clear this method has issues of its own.

The coherent interference from scattered light has a great effect on the imbalance (and extinction) measurements compared to the background light. The interfering terms are generated on-chip and are thus expected to have a stable phase relationship over periods on the order of minutes. The implication is that coherent light cannot be reduced by frame integration in this setup.

This uncertainty affects the accuracy of the imbalance and the corresponding predicted extinction of the MMI when used as a two-beam combiner for nulling interferometry. The impact of coherent and incoherent scattered light on the inference of extinction from measured imbalance can be illustrated with an example calculation. Figure 6.6 shows the upper and lower bound uncertainties of a hypothetical inferred extinction of 46 dB - corresponding to an actual MMI imbalance of:

$$\frac{(10100 - 9900)}{(10100 + 9900)} \times 100 = 1\%.$$

.

The calculation of the uncertainty is:

$$\sigma_{\text{Imbalance (\%)}} = \frac{(10100 - 9900) + 2 \times \text{Scattered light}}{(10100 + 9900)} \times 100$$

for incoherent light and

$$\sigma_{\text{Imbalance}} = \frac{((\sqrt{(}10100) + \sqrt{(}\text{Scattered Light}))^2 - (\sqrt{(}9900) - \sqrt{(}\text{Scattered Light}))^2)}{((\sqrt{(}10100) + \sqrt{(}\text{Scattered Light}))^2 + (\sqrt{(}9900) - \sqrt{(}\text{Scattered Light}))^2)}$$

for coherent light.

The equations here, along with Fig. 6.6, are meant to convey the effect of coherent and incoherent light on the output power readings (near the saturated limit of the camera). This effects the confidence of the imbalance calculation, that then influence the extinction prediction, via the equation computed from Fig. 3.6:

$$\text{Extinction (dB)} = 46 \times |\text{Imbalance (\%)}|^{-0.2}. \tag{6.3}$$

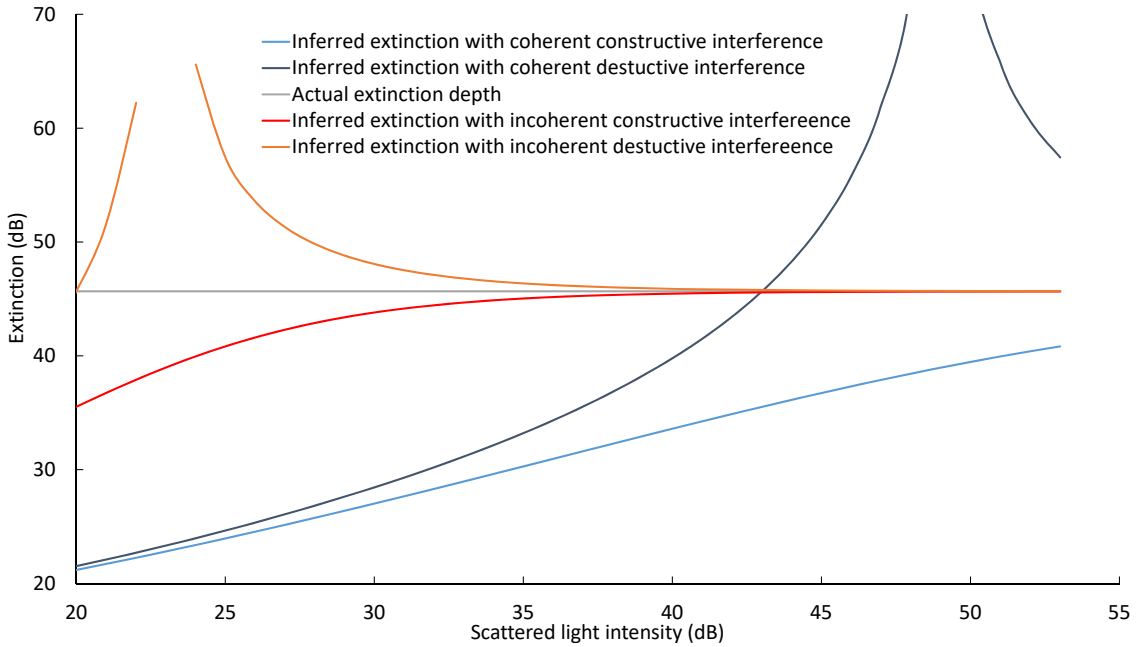

Figure 6.6: Simulating the upper and lower bound uncertainties of a 46 dB extinction (grey), corresponding to a 1% imbalance in MMI coupling, due to coherent scattered light (dark and light blue for destructive and constructive interference respectively) and an overlap with incoherent scattered light (red).

Figure 6.6 represents the worst-case inferred extinctions from the imbalance measurement contaminated with differing levels of scattered light. For incoherent light an inferred extinction of 46.4 dB (for an actual extinction of 46 dB) requires the incoherent scattered light intensity to be reduced to 35 dB lower than the total light exiting the MMI. Suppressing the incoherent light to 35 dB of the MMI light is not trivial but not unreasonable to attain. Measuring the extinction directly, shown later, is limited far more by incoherent light in this respect.

Coherent scattered light requires a greater suppression, as shown in Fig. 6.6. At a suppression of 35 dB the calculated extinction is so great that both the constructive and destructive interference calculations provide extinctions of 30 dB. What this indicates is a limitation of the graph, not the calculation, and what it shows is that the inferred extinction would be anywhere from 35 dB to infinity (of an actual extinction of 46 dB). The wide variation and upper bound of infinity is a result of the uncertainty in the imbalance passing through zero in eq. (6.3) - a zero imbalance corresponding to an infinitely deep extinction. Only when the scattered light is reduced to below the actual extinction depth does the inferred extinction have an upper bound. Hence, measuring the extinction directly would be more accurate if the light is coherent.

As mentioned above, the scattered light from the MMI cannot be reduced through the lock-in already in place or a higher frame integration. Instead, the light must be removed through an absorption layer, such as carbon, silicon, or through altering the geometry of the photonic chip such that scattered light from the MMI can never reach the same position as the output ports.

6.2 Reducing light contamination with a layer of carbon

The purpose of this section is to show that a measurement of the imbalance, to infer an extinction depth and bandwidth when used as a beam combiner, will have a significant uncertainty if the measured scattered light is coherent. As to not misrepresent the data the light scattered in the glass must be assumed coherent. Future work will require some way to ensure scattered light is incoherent and some methods are explored here. One method uses an offset between the light cone from the MMI and the measured waveguides. Another is to absorb the scattered light using an additional over-cladding material - amorphous silicon (α-Si) and carbon were two materials trialled in attempts to do so.

A carbon layer was used as the first method to remove scattered light from the endpoint of the photonic chip. It was deposited over the fully fabricated wafer as an additional fabrication step. Beginning as a fine powder, the carbon was mixed with a one-part SU-8 [254] and three parts SU-8 developer and deposited over the wafer surface via a syringe. The solution formed pools of opaque carbon on the surface that solidified on the top of the wafer as the solvent evaporated. The distance between the deposited carbon and the waveguide varied based on the deposited angled over-cladding, approximately 3 µm thick.

Carbon was used to take advantage of its high absorption in the IR. Any light that interacted with the layer would be absorbed (by the carbon and the SU-8 solution that had not evaporated) leaving only light guided by the waveguides at the output facet. Leaving the guided light unaffected would of course depend on the ChG upper cladding being sufficiently thick to contain the guided light such that it did not interact with the carbon and cause excess propagation loss. This was, however, not the focus of this section and the reduction in scattered light as compared to any additional propagation loss was not explored. If the use of carbon is to continue in future work "trenching" the ChG and back-filling with carbon would produce absorptive "fences" to the sides of the waveguides that would significantly attenuate scattered light without affecting the waveguide's transmission.

The reduction of scattered light due to the layer of carbon is shown in Fig. 6.7. This shows the comparison of the same MMI before and after carbon deposition. The wavelength selected for these images was 3600 nm to illustrate a case where significant light would be scattered from the MMI slab.

As shown in Fig. 6.7 the addition of the carbon top cladding has removed the majority of scattered light without diminishing the two signals. The two images presented are from the same MMI to limit any inter-wafer effects that may occur during fabrication.

The reduction of light between the two PSFs intensity from the MMI output ports is approximately 20 dB on average but there are still large intensity regions between the two PSFs which limits the reduction to approximately 10 dB. The rings around the PSFs are marginally more visible with the carbon overlaid. The areas of high intensity radially outward from the PSFs dominate in this image and show that without the carbon cladding the scattered light is the dominant source of noise, but with the carbon, it is these lateral lobes of the PSF (as was shown in Fig. 6.5). Separation of the output waveguides in this

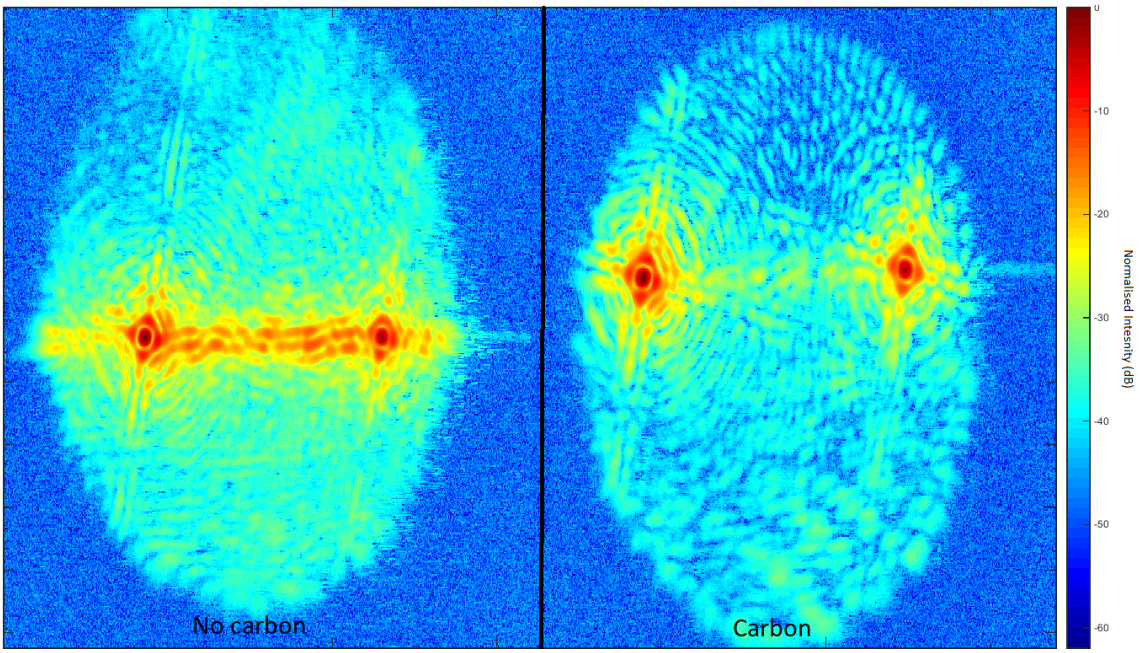

Figure 6.7: The two PSFs from an MMI with $W = 45\,\mu m$ at a wavelength of 3600 nm with (right) and without (left) a carbon overcladding. Both images were taken with the Xenics Onca Infrared Camera and normalised to the maximum value of the measurement without carbon in post processing. A logarithmic scale is used for this figure.

configuration is 240 µm and by Fig. 6.5 this means the overlap between the two PSFs is approximately 60 dB (due to the PSF's side lobes being at a slight angle from each other). On that note, Fig. 6.7 shows the large peaks in the PSFs (following the lines that come from the large lobes both horizontally and vertically) that are approximately 40 dB in intensity 240 µm away from their origin (as expected from Fig. 6.5).

The measured imbalance curves of this MMI with and without a carbon layer are shown in Fig. 6.8 with the error bars indicating the confidence of the measurement due to interference with coherent scattered light, calculated using eq. (6.1). The scattered light intensity selected was the maximum value between the two PSFs and the imbalance calculation used the maximum value of the PSFs.

Figure 6.8 compares the imbalance for MMI with and without carbon over-cladding with both following the simulation imbalance curve of an MMI with $W = 45\,\mu m$, $W_a = 8\,\mu m$ and 10% loss in the bar port. The loss in one arm implies the expected trend of 40 dB over the 400 nm bandwidth, predicted in Chap. 4, could not be realised when combining the light of equal intensities and so when used as a combiner this MMI would require unbalanced input intensities.

The decreases in the error bars between the data with and without carbon highlight the effect, visualised in Fig. 6.7, of the scattered light on the imbalance. The data without carbon have larger error bars and encompass the simulation at every point whereas the data with a carbon layer does not. In the area of interest, however, it is accurate enough. As explained in Chap. 3, the MMI's imbalance is robust to fabrication errors but that

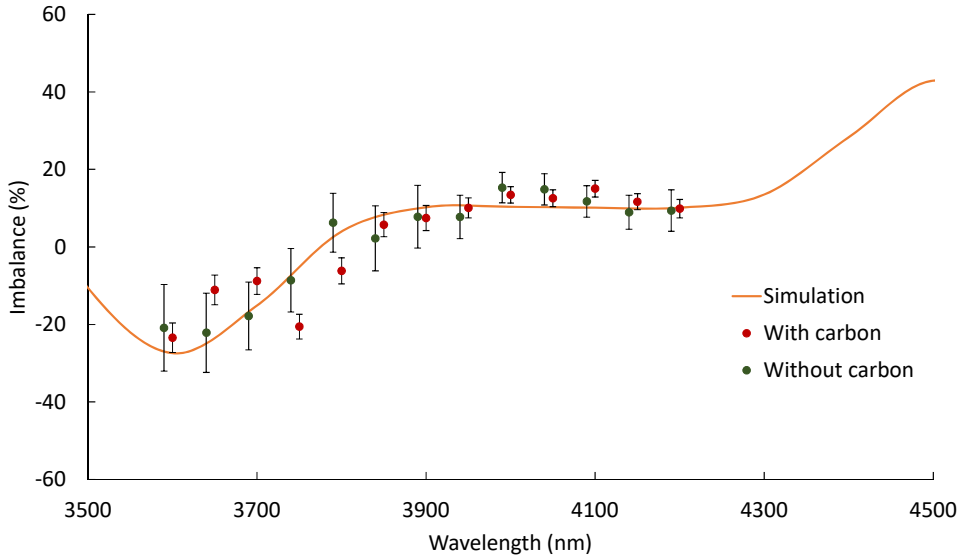

Figure 6.8: The calculated imbalance after measuring the cross and bar port of a 45 µm MMI simultaneously using the Xenics Onca camera, with carbon (red) and without carbon (green) overcladding. A 10 nm offset was applied to one data set in order to better show the error bars. The simulated imbalance (orange) is of a 45 µmW MMI with a $W_a = 8$ µm and a 10% loss in the bar output port.

is only at the designed wavelength of 4000 nm. Figure 6.8 indicates that the imbalance is also robust to fabrication error over the region of interest - in this case between 3700 and 4200 nm. The data points from Fig. 6.7 with carbon shows additional structure in the imbalance curve that does not match the simulation. This could be due to the taper width being smaller than the intended 8 µm width. In particular the point at 3750 nm shows a far deeper dip than was expected when comparing to the data point without carbon. The extra dip could be an issue with the previous measurement mistaking scattered light for output signal and artificially increasing the "measured" intensity from the output port with the weaker signal. This shows that a large amount of scattered light hides structure in the data.

Extreme cases of scattered light reduction have also been seen. Figure 6.9 shows two MMIs that have a large uncertainty due to scattered light, from a wafer wide phenomenon - in this case, a chemical spill of AZ MIF 312, that removed portions of some waveguides. Coating the MMI in carbon reduces the uncertainty considerably as Fig. 6.9 (in the right panels) shows a $> 10\times$ reduction in the uncertainty.

Reducing the scattered light in Fig. 6.9 indicates that the fabricated MMI has the same shape as the simulated MMI, which is dependent on the taper width (as shown in Chap. 4). From Fig. 6.9 the flat bandwidth response of the $W_a = 8$ µm is also shown and, as a result, the predictions of extinction depth should be measurable over the entire bandwidth of interest (between 3700 to 4200 nm), shown in Sec. 6.5.

Rather than using an opaque material to absorb the scattered light, transparent material with a higher index than the cladding could also be used such that light would

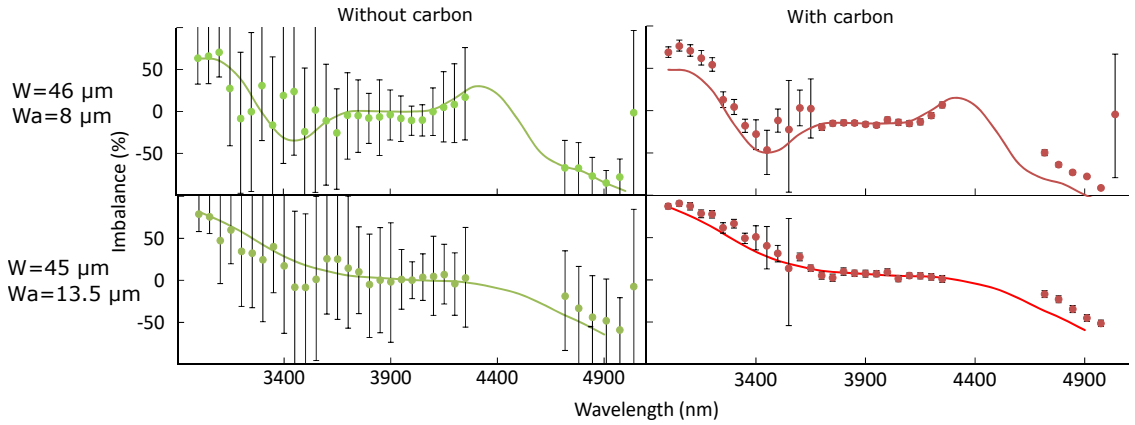

Figure 6.9: Two MMI with large scattered light, reduced with a carbon layer. The experimental data (circles) and equivalent simulation (solid line) with appropriate loss in one arm to fit the data between 3700 to 4300 nm.

be preferentially trapped in that material and potentially absorbed. Amorphous silicon (α-Si) was therefore trialled similarly to carbon to try and achieve the same effect.

6.3 Removing scattered light using amorphous silicon

Depositing a layer of unordered (hence amorphous) silicon (α-Si) onto the wafer, over the ChG over-cladding, was proposed as another way to remove scattered light. Having a higher refractive index (3.4 at 4000 nm) than the ChG, the light should then be guided or stripped by the α-Si layer. At 4000 nm α-Si is transparent [255] and so will guide light through to the end of the chip. Unlike guiding in the cladding material, however, this scattered light will be spatially offset from the PSF coming from the output ports of the MMI and will thus not overlap with the measured signal.

As an aside, $As_{24}Se_{38}S_{38}$, from Sec. 5.3.2, should also fulfil this purpose. With a refractive index of ~2.4 it is lower than the core material but higher than the cladding. However, as mentioned in Sec. 5.3.2, reflowing this glass (so that it does not form a waveguide) is arduous and requires an MgF_2 substrate to prevent the glass cracking (that is caused by the thermal expansion contrast between Si and ChG). Depositing α-Si is much easier.

An initial test was undertaken to ascertain whether the α-Si would successfully remove the scattered light. 100 nm was deposited over a full wafer using plasma-enhanced chemical vapour deposition (PECVD). The wafer was cleaved after the deposition so that the edges would be clear, equivalent to the carbon cladding previously.

Figure 6.10 shows an MMI with $W = 45\,\mu$m at 3600 nm and 100 nm of α-Si deposited over the ChG overclading layer.

The light between the MMI ports in Fig. 6.10 is approximately 20 dB less than the intensity from the MMI output ports. This is much worse than the carbon cladding. The limit to a measurable extinction is the amount of scattered light compared to the intensity

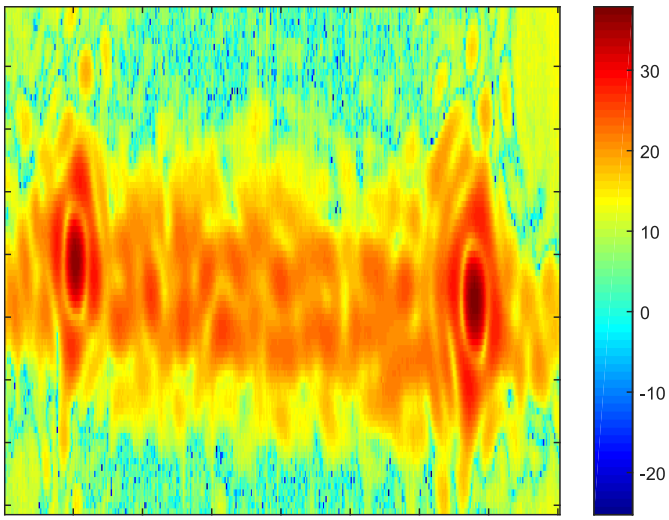

Figure 6.10: The measured PSFs of an MMI with $W = 45\,\mu m$ covered in α-Si at a wavelength of 3600 nm. The intensity was converted to a logarithmic scale to highlight the light between the PSFs.

through the output ports. Figure 6.11 shows the scattered light normalised to the average intensity between the two output ports of the MMI.

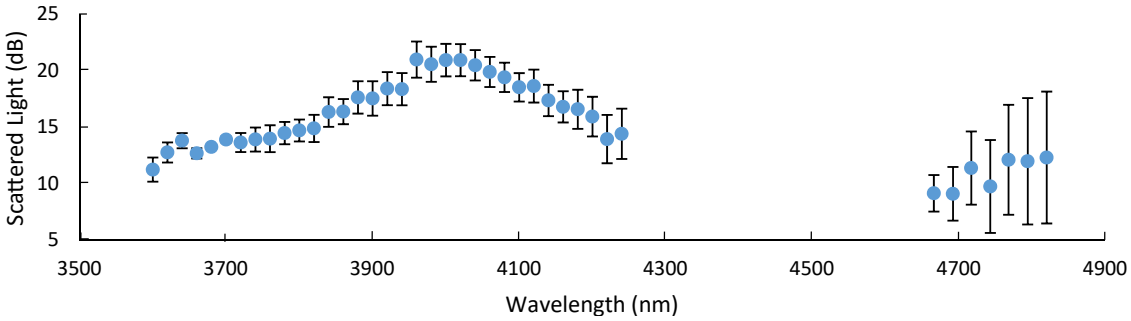

Figure 6.11: The measured scattered light, as compared to the average intensity, of an MMI with $W = 45\,\mu m$ and a 100 nm layer of α-Si.

Figure 6.11 indicates that an extinction measurement of 20 dB is possible using the MMI presented, with an over-cladding of α-Si, but no more. This is significantly worse than the carbon over-cladding and hence not a viable alternative.

The reason for the failure of this material may be due to the large index difference between the α-Si and the ChG over-cladding meaning there is a significant reflection at the boundary. Further research is required to identify whether, with careful modification, the α-Si layer could work, increasing the height of the α-Si layer at a potential cost of transmission for instance, but due to the previous success of the carbon layer, this was not investigated in this thesis. There are also however geometrical approaches to reducing scattered light that is now discussed.

6.4 Offset on the MMI

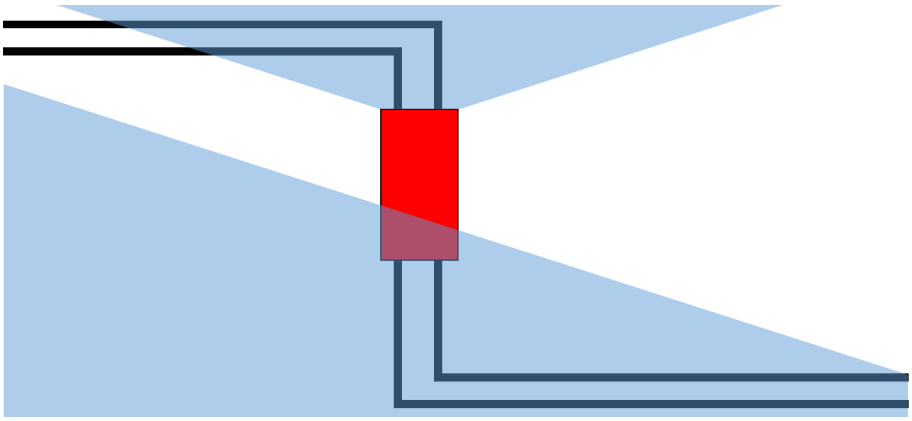

Figure 6.12: A schematic for the new MMI design that stops light from the MMI reaching the wafer output ports. The blue colour indicates where scattered light could appear, either from the MMI or the input waveguide.

Rather than, or in addition to, over-cladding the MMI and subsequent waveguides with carbon or α-Si, a new geometry was proposed. Figure 6.12 shows a schematic of this new geometry with the MMI at a 90° angle to the input and output waveguides of the wafer. The schematic contains a visual representation of the scattered light from the MMI and light inserted into the cladding at the interface into the photonic chip. Using Snell's law the injected light angle (θ) is calculated as

$$\frac{\sin(\theta)}{0.52} = \frac{n_{\text{air}}}{n_{\text{cladding}}}$$
$$\theta = 13.2^{\circ},$$

where the angle incident into the cladding material is calculated from the Newport objective's NA = 0.52. Light from the MMI is also assumed to spread from the MMI cavity's end face at the same angle as the launch light (simulation in RSoft BeamPROP confirms this). Hence the output waveguides were positioned such that there was no overlap with the potential scattered light from the launch field or from the MMI slab light itself. As a minimum, this should lead to a reduction in the scattered light at the wavelength extremities where localised intensity maxima are not formed at the endpoint of the MMI. If scarred light is still an issue with the offset geometry, if there is no room to bend the waveguides, as is the case for femtosecond written MIR optics, for example, then filling the scattered light pathways, that contain no waveguides, with carbon will remove any scattered light from the system.

The optical path length difference between the light that is guided to the end of the waveguide and uncoupled input light is between 3.2 and 3.9 mm depending on where the photonic chip is cleaved. With a laser pulse length of 10 ps the uncoupled input light cannot be coherent with the light that guided through the chip.

The first MMI with $W_a = 12\,\mu\text{m}$ was fabricated in such a geometry with the imbalance

curve included in Fig. 6.13.

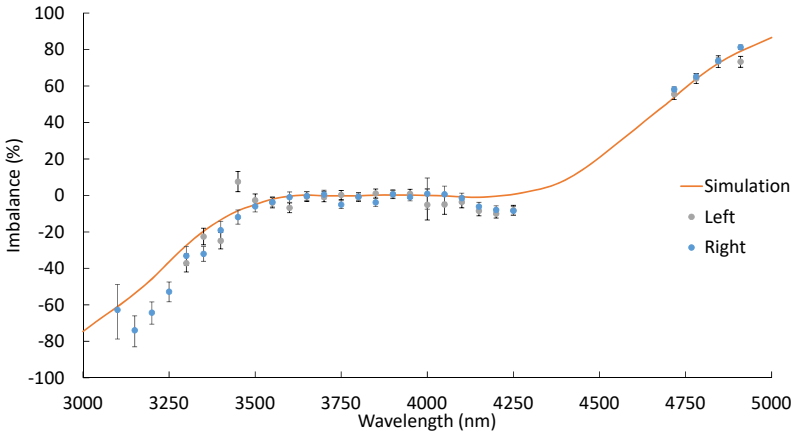

Figure 6.13: The calculated imbalance curve, measured from the output ports of an MMI with $W_a = 12\,\mu m$ for light launched into the right (blue circles) and left (grey circles) input ports. A 21% and 19% correction respectively has been used to zero the imbalance curve from loss in one arm. The simulation (orange) is also included here. Uncertainty bands are calculated from the maximum light between the output intensities (scattered light) using eq. (6.1) assuming coherent light.

Figure 6.13 only used the geometry of Fig. 6.12 to remove scattered light: there are no additional layers to absorb scattered, spurious light in the cladding layer. The uncertainty levels in Fig. 6.13 are calculated using the assumption that the light between the output PSFs of the MMI is coherent, this means the light is not coming from the MMI itself or uncoupled input light but from the output waveguides. Future work may remove this light by deposition carbon in a trench etched between the waveguides but as will be shown below this light is not the limiting factor in these measurements.

The slight mismatch between the calculated imbalance from the measured intensities and the simulation is likely due to the simulation assumption of a perfect 12 µm W_a. As stated before the fabrication error in the taper width can cause a slight deviation in the imbalance curve, as is shown here.

At three wavelengths (3550, 3950 and 4900 nm) the PSFs were imaged with the camera to illustrate the intensity of the noise compared to the PSF observation. These are included as Fig. 6.14.

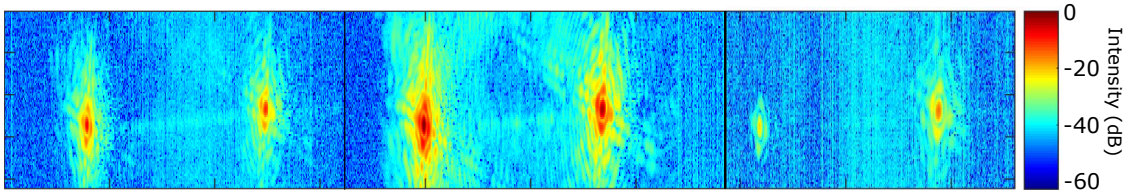

Figure 6.14: Three sets of PSFs, taken with the Xenics Onca Camera, from an offset geometry MMI with $W = 45\,\mu m$ and $W_a = 12\,\mu m$ at wavelengths 3550, 3950 and 4900 nm (from left to right).

The scattered light intensity in Fig. 6.14 is much lower when carbon is used to reduce

the scattered light (see Fig. 6.8). Between the PSFs the scattered light intensity is at the same level as the background light (approximately 40 dB lower than the PSFs) at all three wavelengths. The scattered light would then limit the inferred extinction depth (of an actual extinction of say 45 dB) to 35 dB, assuming the scattered light is scattered from the output waveguides and thus coherent.

Figure 6.15 shows the average intensity of the PSFs compared to the scattered light intensity, using 1000 frames for each wavelength. Note here that this figure used the average of three different MMIs, with $W_a = 8$, 12, 13.5 µm, to avoid any taper width dependence that may create inaccuracies in the scattered light comparison.

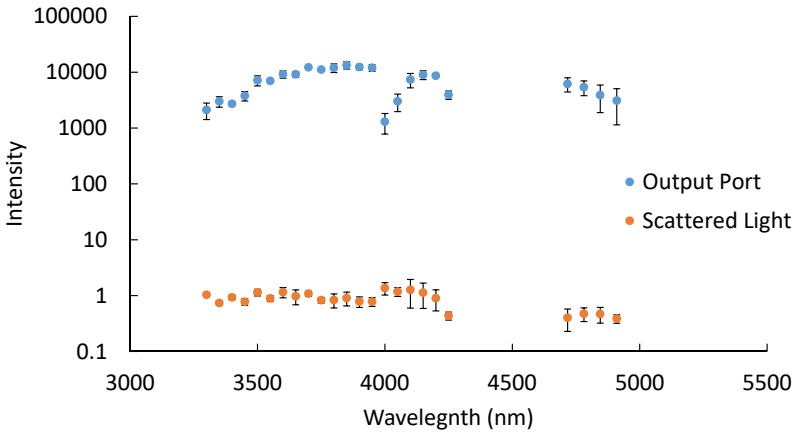

Figure 6.15: The measured cladding light intensity and the MMI output port intensity taken with the Xenics Onca camera against wavelength, in the offset geometry configuration. Both were averaged over three MMI measurements with uncertainty based on the standard deviation of the three measurements.

Figure 6.15 shows that the cladding light is constant compared to the variation in the intensity from the two MMI PSFs. The figure also shows the S-H absorption dip at 4000 nm identified in Chap. 5. At this wavelength, as with all wavelengths, the integration time was increased to have a signal near the saturation threshold of the camera. Even so, the increase in the background was minimal and indicates that the scattered light was uncoupled from the MMI transmission.

From the results provided, the offset and rotated geometry provide greater suppression of scattered light than using an absorbing layer. The inferred extinction is yet to be calculated, this will show whether the reduction is enough to reproduce the expected extinction curves and provide an insight into whether the MMI can be used as a two telescope beam combiner.

6.5 Extinction calculation

How deep the null depth will be can be predicted using the imbalance curves, this has been shown in Sec. 3.3.2 with simulations shown in Sec. 4.5.1, however, the scattered light causes significant uncertainty in the prediction. For the MMI coated in carbon the data

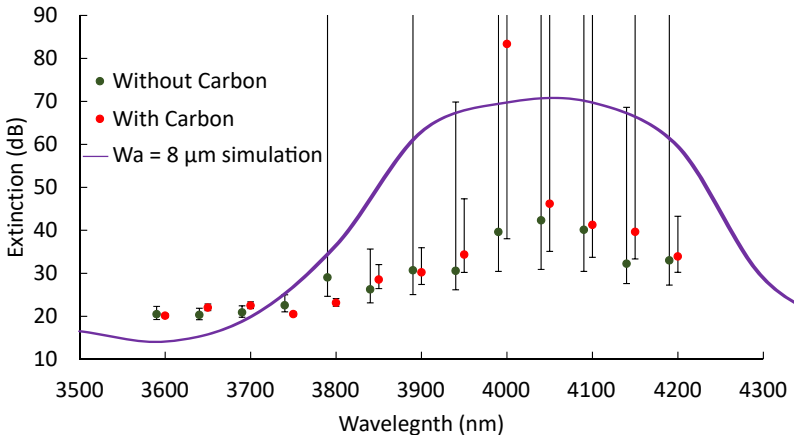

Figure 6.16: The deepest extinction based on the results shown in Fig. 6.8, with a carbon layer (red) and without (green) compared to the simulated extinction (purple) from Fig 4.25. The 13% loss in the bar port has been corrected for this calculation, a loss that was found to optimise for the maximum bandwidth at a 30 dB null depth. The error bars were maintained from Fig. 6.8 providing an upper and lower bound of extinction depth. Since a zero imbalance occurred between 3700 nm and 4200 nm the upper limit may have no bound.

from Fig. 6.7 was used to predict the MMI performance as a two telescope beam combiner, shown in Fig. 6.16. Equation (6.3) was used to convert the imbalance to extinction. Note that the imbalance data was optimised to have the widest bandwidth at the deepest null, by setting a 13% loss in the bar port - a similar correction in intensity that would be required in a real device.

Figure 6.16 highlights the reduction in the uncertainty due to the reduction of scattered light. These error bars were calculated using the upper and lower bounds from Fig. 6.8 unless the uncertainty of the imbalance passed zero in which case there is no upper bound uncertainty in Fig. 6.16. In general, the experimental data matches the shape of the simulation but with the reduction in error bars, it is clear that the depth is lacking. This is likely a fabrication issue with the MMI and must be corrected when measuring the extinction directly, to achieve low extinction depths.

The data points in Fig. 6.16 with the carbon layer have a worst-case inferred extinction of ~30 dB over 250 nm. The null of 40 dB over 400 nm, predicted in Chap. 4, could not be realised with this data due to such a high error even with a reduction of scattered light.

This leads to the question of whether the extinction of 40 dB could be measured had this been an extinction measurement rather than an extinction inference. Figure 6.17 shows the maximum intensity of the scattered light, between the PSFs, compared to the minimum intensity from the two MMI PSFs. The minimum intensity is used here as to not inflate the scattered light depth.

The light reduction due to the carbon over-cladding is shown in Fig. 6.17. It shows that the carbon reduces the light by, on average, 7 dB. It also shows that with only 1000 frames the background is the limiting factor in this experiment at 4000 nm, as 40 dB is the calculated limit, as per Fig. 6.3. At wavelengths away from 4000 nm scattered

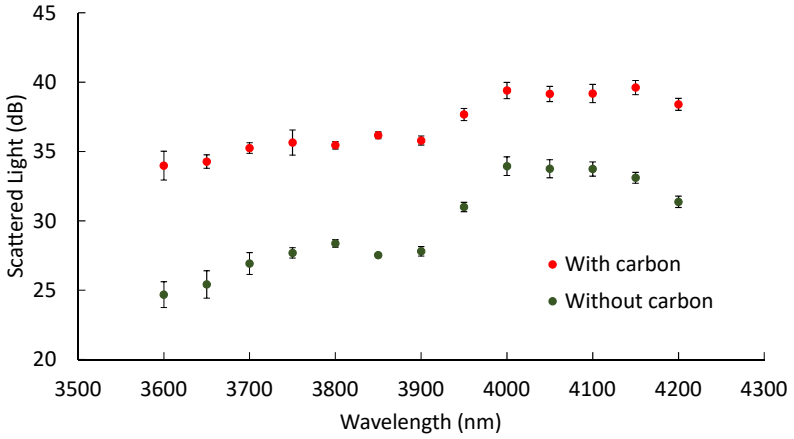

Figure 6.17: The measured scattered light depth, with background light and light from the smaller radial bands of the airy disks included, as compared to the minimum output intensity, with carbon overcladding (red) and without (green).

light from the MMI cavity may be further limiting the detectable extinction, with 35 dB extinction being the detection limit from 3600 nm to 3900 nm. Note here that if the scattered light is coherent it cannot be reduced by frame integration, chopping the signal or other methods of random noise reduction. Based on Fig. 6.16 a 35 dB null over 300 nm could have been measured if this was an extinction measurement, which does not replicate the extinction depth or bandwidth predicted in Chap. 4.

Rather than using a layer of material to absorb the scattered light, an offset geometry can be used, as was shown in Sec. 6.4. To properly compare how this geometry reduces scattered light in the signal to the previous method the inferred extinction needs to be calculated. Using the imbalance measurement displayed in Fig.6.13, the extinction for both input arms is displayed in Fig. 6.18.

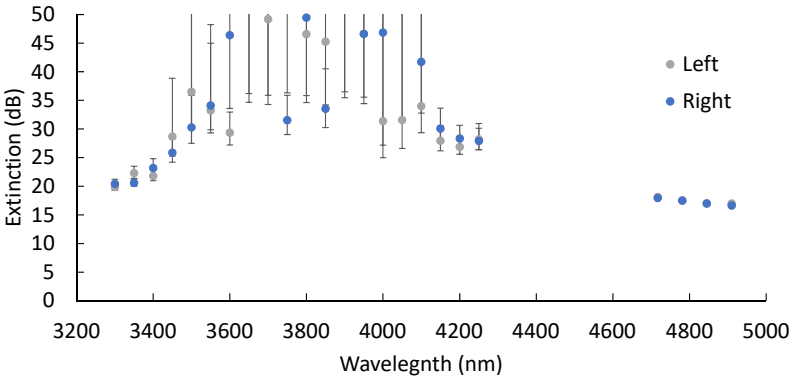

Figure 6.18: The extinction inferred by the measured results of Fig. 6.13 for light launched into the left (grey) and right (blue) ports.

The implication of Fig. 6.18 is that using the offset geometry (and rotation of the MMI) is an effective alternative, if not a better option, than using a carbon cladding to remove scattered, coherent light. That is not to say that using both an absorption layer and an

offset geometry would not improve the extinction uncertainty but, to limit production steps, the carbon cladding is not required for an initial test of imbalance when using an offset geometry. Note too that the 1000 frames used as standard limits the extinction measurement to 40 dB. More frames will increase this but the limiting factor here is not that a 40 dB extinction cannot be measured but because the measured PSFs intensities do not indicate a high extinction. The analysis below explains this further.

An analysis of Fig. 6.18 revealed that for light launched into the left input port the upper bound restricts the inferred extinction to 35 dB over 300 nm. For the right input port however there are two outliers at 3750 and 3850 nm that restricts the 35 dB bandwidth, but removing them provides an even wider bandwidth of 450 nm at the same extinction depth. Note that these are the upper bounds calculated based on the light remaining between the PSFs. If this was found to be incoherent scattered light then the error bars would be inside the data points and the depth would be 45 dB over the 300 nm bandwidth and 40 dB over a 500 nm bandwidth (neglecting the outliers again), for launching light into the left and right input ports respectively. Hence an offset geometry can be effective in reducing the scattered light overlap to the output port's PSF.

This is not yet comparable to the RSoft simulations from Chap. 4 that predict a 50 dB null depth over 400 nm. This is despite the imbalance curve following the RSoft simulation in Fig. 6.9 and 6.13. The slight mismatch in the simulated imbalance curve to the calculated imbalance curve is enough to reduce the predicted extinction depth by up to 20 dB as shown Fig. 6.16. This may relate to the fabricated MMI not being identical to the simulation, specifically the taper width being slightly smaller due to fabrication errors. The prediction of the extinction depth, however, is limited if the error in the imbalance curve overlaps zero imbalance - equivalent to an infinite extinction - and only the lower bound of the extinction depth can be predicted. Measuring the extinction directly is required to find the upper bound of the extinction depth.

6.6 MMI transmission

Using the offset geometry the transmission of the MMI can be checked against the theoretical prediction. For this measurement, the combined light through the MMI was compared to a waveguide of the same length. For consistency, the waveguide and path into (and out of) the MMI had the same number of bends and the same bend radius.

When measuring a waveguide solely with the Xenics Onca camera there is no way to rectify any laser power fluctuations occurring during the measurement and so the "reference" detector (used previously to measure waveguides and when measuring the output ports of the MMI individually with the "signal" detector) was used. The reference detector was also used for the MMI transmission measurements to have a direct reference to the laser intensity input into the photonic chip. These measurements all occurred on the same day, with no change to the lab bench (described in Sec. 5.4), so that there could be no question that these measurements are comparable.

The two simulations in Fig. 6.19 show the MMI transmission for an MMI with $W_a = 8$ and 12 µm. There is little difference between the simulation and experimental data in these figures in the band of interest (3700 to 4200 nm) with the only apparent substantial deviation at the extremities, presumably due to a mismatch in simulated and fabricated taper width. An MMI with $W_a = 13.5$ µm is not shown here due to the difficulty to fabricate one without truncated taper widths.

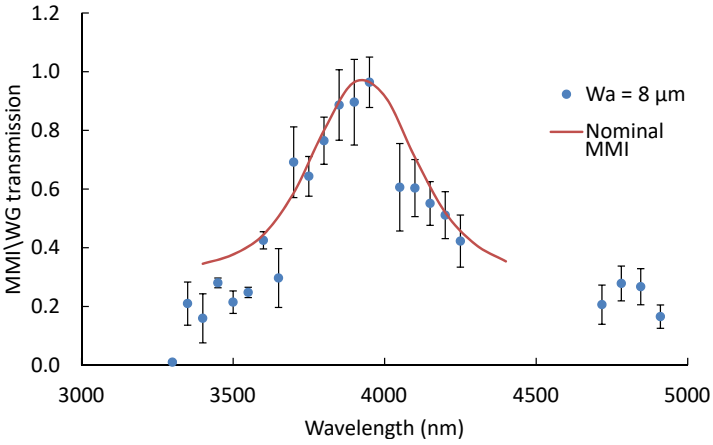

(a) MMI with $W_a = 8$ µm.

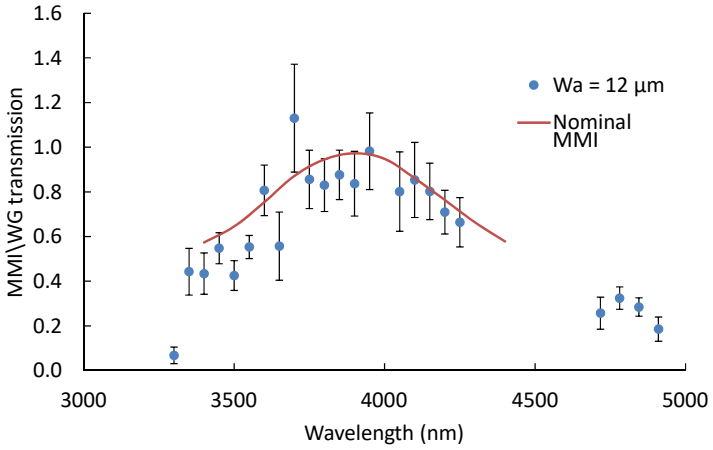

(b) MMI with $W_a = 12$ µm.

Figure 6.19: The measured transmission of the three MMI using the Xenics Onca camera (blue circles), normalised with a waveguide measurement, with simulation (in red and green lines) preformed by RSoft BeamPROP for the nominal MMI.

The experimental data displayed in Fig. 6.19 is a combination of two different MMIs (for each W_a) for light launched into the two input ports individually (first left and then right) for a total of four data sets. The error bars were calculated as the standard deviation of these four measurements.

The devices with the narrower tapers behave essentially as predicted (Fig 6.19a and Fig. 6.19b). The latter appears to have additional loss compared to that in the simulation, even with such a large uncertainty. These serve to illustrate that no, substantial, additional loss occurs in the wide extinction bandwidth MMIs.

6.7 Summary

The focus of this chapter was the MMI imbalance and the challenges of measuring that imbalance with high accuracy. The main issue that was dealt with, in two ways, was coherent scattered light. By over-cladding the MMI and surrounding areas with carbon, over the ChG over-cladding deposited via angled deposition, the scattered light intensity was shown to drop by approximately 7 dB in the bandwidth of interest (the bandwidth where the deep extinction would occur in a beam combiner configuration) and 10 dB at the extremities. With a geometry that offset the input and output waveguides and rotated the MMI to be perpendicular to the waveguides, the scattered light was reduced 30 to 40 dB below the desired signal. Whilst this is a significant improvement, more still is required to be able to obtain imbalance measurements with low enough uncertainty to infer extinction of beyond 40 dB. This will likely be accomplished by adding customised carbon light-trapping structures to the offset and rotated geometry. Once the low noise level has been achieved and a deep null can be inferred from an imbalance, or measured from an extinction measurement (as will be attempted in Chap. 7), then there will be enough evidence to suggest that an MMI can be used as a nulling interferometer for exoplanet detection.

In this chapter it has been shown that the MMIs discussed in Chap. 4 do indeed provide a flattened imbalance curve at the zero imbalance point. An extended discussion regarding taper variables is still required to potentially increase this further, and detail the cost involved in terms of transmission, but what has been shown here is that the MMIs fabricated fit the imbalance curves.

The transmission of the MMI may require further work as the transmission curve simulations fit the experimental data only at the bandwidth of interest and only for $W_a = 8$ and 12 µm. This may be due to a fabrication tolerance underestimated in Chap. 3 in terms of the rounding at the taper edges at the interface of the MMI cavity.

Throughout the chapter the inferred extinction was computed from the measured imbalance curves, using the conversion equation included in Fig. 3.6, with the best extinction depth of 30 dB over 300 nm for the offset geometry photonic chip. With this measurement, the remaining scattered light was assumed coherent and future work will need to justify this assumption. This measurement limitation highlights the difficulty in inferring an extinction measurement using an imbalance curve. The next best extinction bandwidth (30 dB over 250 nm) was achieved using a carbon over-cladding. Whilst these results are not as broad as predicted by theory and the reasons for this are not currently understood despite extensive modelling of all effects conceived to date, they nevertheless are of utility to future interferometry systems on ground-based and space telescopes.

How the MMI acts as a two-beam combiner is explored in Chap 7. Although this chapter is also not successful in reproducing the extinction predicted by Chap. 7 it contains vital information for future nulling interferometers and highlights potential fundamental issues with the lithography used in this work.

Chapter 7

Nulling interferometer

This chapter contains work already published:

Kenchington Goldsmith, H.-D., Ireland, M., Ma, P., Wang, R., Luther-Davies, B., Madden, S., Noris, B., and Tuthill, P., "Photonic mid-infrared nulling for exoplanet detection on a planar chalcogenide platform," in [*Optical and Infrared Interferometry and Imaging VI*], Mérand, A., Creech-Eakman, M. J., and Tuthill, P. G., eds., 33, SPIE (2018).

Measuring the coupling ratio of a multimode interference coupler (MMI), in Chap. 6, was used to infer the extinction of an MMI when used as a two-beam combiner. This can be measured directly if two beams of equal intensity are launched into the MMI at a matching phase difference to the MMI phase (described in eq. (3.18)). If the light does not have this phase difference the wide bandwidth extinction will not occur and is thus vital to control either before launching into the photonic chip or in the chip itself. Phase modulators will be required for future iterations of the beam combiner (the Kernel-Nuller for example [85]) and it was decided that phase modulation would be used to control the light in the input waveguides to tune the MMI's extinction and bandwidth response.

To produce an extinction in an MMI the single beam that was used for the imbalance measurements in Chap. 6 must be split. To do so in a bulk optic configuration a precision achromatic beam splitter, in a Michelson configuration, can be used. Having one of the mirrors slightly tilted provides a second beam at an arbitrary spatial offset and having that mirror on a linear stage provides phase control between the two chip inputs. This method was utilised by Tepper et al. [162] to provide an interferogram of a directional coupler.

Another bulk optic solution is to overfill a micro-electromechanical system (MEMS) array of mirrors and mask out all but two (that are not adjacent). This is similar to a typical "on-sky" setup that uses a MEMS to account for atmospheric disturbances [256]. A simplistic version of this is to have the beam incident on two-segmented mirrors, one of which is tilted and on a transition stage. This was the method used by Martin et al. [257] to input two equal intensity beams into a Ti:$LiNbO_3$ photonic chip.

Using only photonic solutions a 3 dB coupler (like an MMI) splits the light on the chip itself, with artificial phase shifters used to arbitrarily tune the MZI. An example simulation is included as Fig. 7.1 with two MMI in series, generated using RSoft BeamPROP, used as the 3 dB coupler and then the two beam combiner - the phase shifters are omitted.

Highlighted in Martin et al. [257] is an on-chip Mach-Zehnder interferometer (MZI)

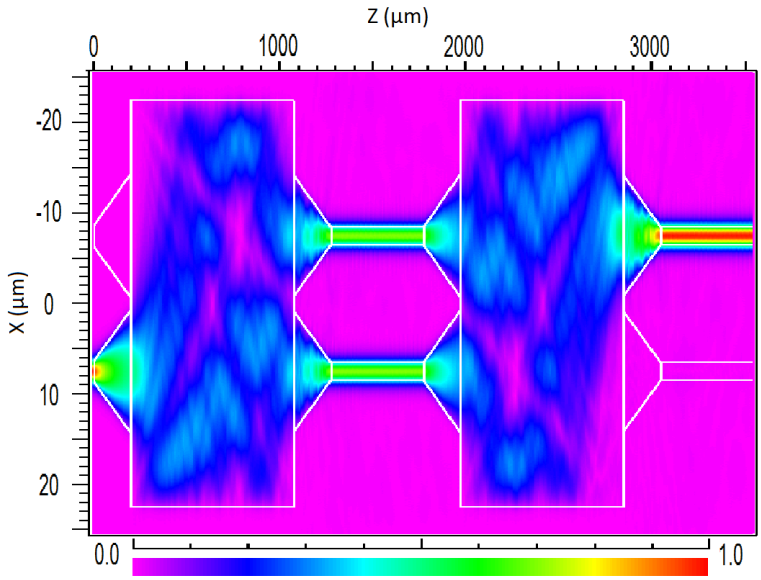

Figure 7.1: Mach-Zehnder interferometer simulation in RSoft BeamPROP, using two MMIs as a 3 dB coupler and beam combiner respectively. Artificial phase shifters placed over the interlinking waveguides are omitted in this simulation. A light intensity of 1 unit is input in the left and measurement of 0.98 units in the topmost output port, with an approximate 46 dB extinction in the bottom-most port.

that was used to actively control phase and intensity through constructive and destructive interference. Two MMIs were used to match the input intensities before injecting light into a beam combiner. A segmented mirror was used as a global phase control before the light was launched into the phonic chip itself. These MZIs were two y-junctions, used for their achromatic response. This highlights how an MZI might be used in the future for a nulling interferometer for an on-chip intensity control but for this chapter it is the MZI itself, with a controllable phase delay in the arms, to modulate the extinction curve. The MMI, unlike the y-junctions, are not achromatic and their response to wavelength and various phase differences is what is measured in this thesis.

The MZI configuration, included as Fig. 7.1, is shown with an electric field incident into the left side of the system. A schematic diagram of this is shown in Fig. 7.2. The two MMI coupling ratios have been designated as α and β.

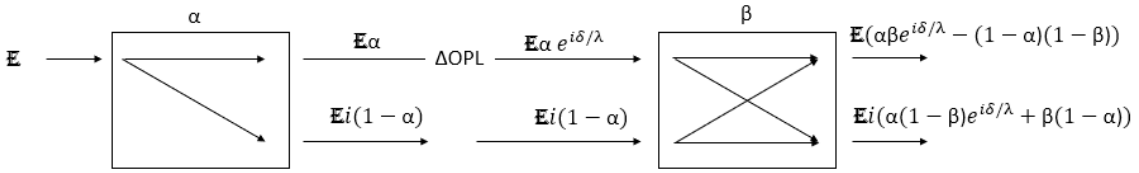

Figure 7.2: Schematic of a Mach-Zehnder interferometer. The lines indicate the movement of the electric field (E): first, the field is split by an MMI, with coupling ratio α, a change in the optical pathlength (ΔOPL) shifts the phase of the light in one arm (as compared to the other arm) before the second MMI combines the field in the two input ports with a coupling ratio of β. 'i' denotes the imaginary terms of the electric fields as they travel through the waveguides.

The schematic in Fig. 7.2 shows that for a single input the electric field is split by the coupling ratio - a term dependent on the wavelength (λ), MMI width (W) and taper width (W_a) and calculated by RSoft BeamPROP for this chapter - followed by a long path to the second (beam combiner) MMI. An OPL difference in one arm was added in the model as a pseudo-pathlength controller for the MZI: If the fabrication of the waveguides was perfect this term would be zero. The expected extinction in the second MMI is explored in Sec. 7.1 and compares this theory and that of launching two fields directly into the MMI.

This chapter follows from the last with an overlap in terms of scattered light and how to reduce it: using the scattered light level to set the limits on what can be measured in Sec. 7.2, the use of an overlaid carbon in Sec. 7.3.1, and using the new offset geometry that rotates the MMI (both MMIs in this case) by 90° in Sec. 7.3.2, to reduce the scattered light. However, this is not the focus of this chapter. Using the offset geometry and overlaying carbon will be needed in future work to be able to measure a deep extinction, but they do not aid in producing a deep extinction. Instead, the focus is on phase manipulation and the chromium heaters that are used in an attempt to optimise the extinction over the large bandwidth predicted in Chap. 4 and hinted at with the MMI measurements in Chap. 6. Section 7.5 shows the progress around controlling the OPL in the connecting waveguides between two MMIs. Before this can be studied, however, the fabrication tolerances in the MZI's connecting waveguides and the impact on the extinction must be explored, in Sec. 7.4, to know how much manipulation is required to return the OPL to zero.

7.1 Mach-Zehnder interferometer model

A model was constructed to replicate two MMIs in series (to form an MZI as per Fig. 7.2). This was to have a robust analysis tool that would show how fabrication errors in the connecting waveguides affect the extinction produced by the MZI. The new model differs slightly from the previous model that used a single MMI to form an extinction. Figure 7.2 details how light travels through the two MMIs (and the connection waveguides), expressed in terms of the electric field (E). The output fields after the beam combiner MMI are converted to intensity using $I_{1\text{ or }2}/I = |EE^*|_{1\text{ or }2}$ where I is the input intensity and $I_{1\text{ or }2}$ is the power from either output port. Note here that the transmission of the two arms are also included in this calculation, as T_1 and T_2, but are not included in Fig. 7.2.

$$\begin{aligned} I_1/I &= T_1\alpha\beta + T_2(1-\alpha)(1-\beta) - 2T_1T_2\sqrt{\alpha}\sqrt{\beta}\sqrt{1-\alpha}\sqrt{1-\beta}\cos(2Z_+ - 2\pi\delta/\lambda) \\ I_2/I &= T_1(1-\alpha)\beta + T_2\alpha(1-\beta) + 2T_1T_2\sqrt{\alpha}\sqrt{\beta}\sqrt{1-\alpha}\sqrt{1-\beta}\cos(2Z_+ - 2\pi\delta/\lambda) \end{aligned} \tag{7.1}$$

where δ/λ is the pathlength difference term and Z_+ is the phase of the MMI as defined in eq. (3.18). Note that a simplification has occurred here where the phases from eq. (3.18) are the same for both MMIs, despite the coupling coefficients potentially not the same. By design the two MMIs should be exactly the same and so this simplification is fine, as is setting $\alpha = \beta$. For this chapter the Z_+ is simplified to a constant 90°, which changes the

ΔOPL term to $\cos(+2\pi\delta/\lambda)$. This simplification of eq. (7.1), allows for rapid comparisons to the measured MZIs below without the need to account for the potentially different phases of both MMI at each wavelength. The full model of the MZI with accurate MMI phase is beyond the scope of this work but as we are using this model to simply look for the ΔOPL it is accurate in this regard.

$$\begin{aligned} I_1/I &= T_1\alpha^2 + T_2(1-\alpha)^2 - 2T_1T_2\alpha(1-\alpha)\cos(2\pi\delta/\lambda) \\ I_2/I &= \alpha(1-\alpha)(T_1 + T_2 + 2T_1T_2\cos(2\pi\delta/\lambda)) \end{aligned} \tag{7.2}$$

Equation (7.2) is used to calculate the extinction (in dB) using

$$\text{Extinction} = -10\log_{10}\left(\frac{\mathrm{I}_1}{\mathrm{I}_2}\right). \tag{7.3}$$

This is similar to the inference of extinction by the MMI coupling results in eq. (4.1). Figure 7.3 compares the calculated extinctions using eq. (4.1) and (7.2) for the same MMI and same coupling ratio (with $\alpha = \beta$) for $W_a = 13.5$, 12 and 8 µm.

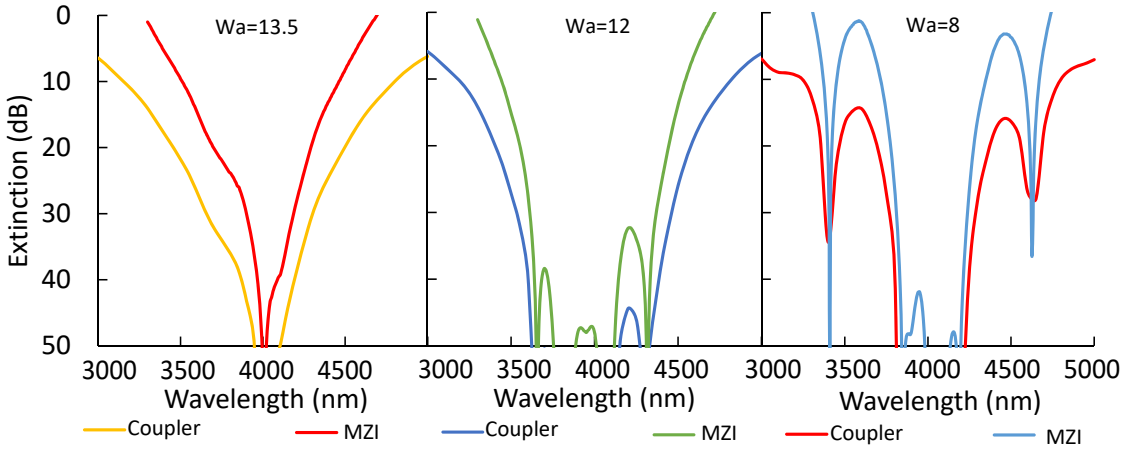

Figure 7.3: The extinction expression provided by eq. (7.3) with $\delta = 0$ as compared to the coupling ratio from the MMI as a beam combiner, using eq. (3.18). The MMIs included have $W = 45$ µm and $W_a = 13.5$ (left), 12 (middle) and 8 µm (right).

Figure 7.3 shows that the two equations for the MMI and MZI extinction are similar in shape but not necessarily the same in extinction bandwidth.

For each comparison in Fig. 7.3, the extinction curves are similar. The single MMI consistently has a wider extinction bandwidth, especially at smaller extinctions, but none of the curves differs drastically. The distinction is highlighted here to show that eq. (7.2) is an accurate model for an MZI but does not necessarily represent an MMI used as a beam combiner. It is different than using two equal intensity launch fields (with a phase shift matched to the MMI, as per eq. (3.18)) and should be used when testing whether the MZI is behaving as expected by the simulation. However, when using the MMI on a telescope as a two-beam combiner the simulation provided by eq. (3.18) is applicable (assuming the intensities are equal at every wavelength). Future work will need to look

into the MMI behaviour with two launch fields but for now, the MZI theory will be used to determine whether the two MMIs in the series behave as expected.

The impact of shifting the OPL away from zero on the MZI extinction also has to be considered. Figure 7.4 uses the same parameters as Fig. 7.3 but for $\delta = 0$ (refereed to as OPL in the image) and a shift to 0.1 µm.

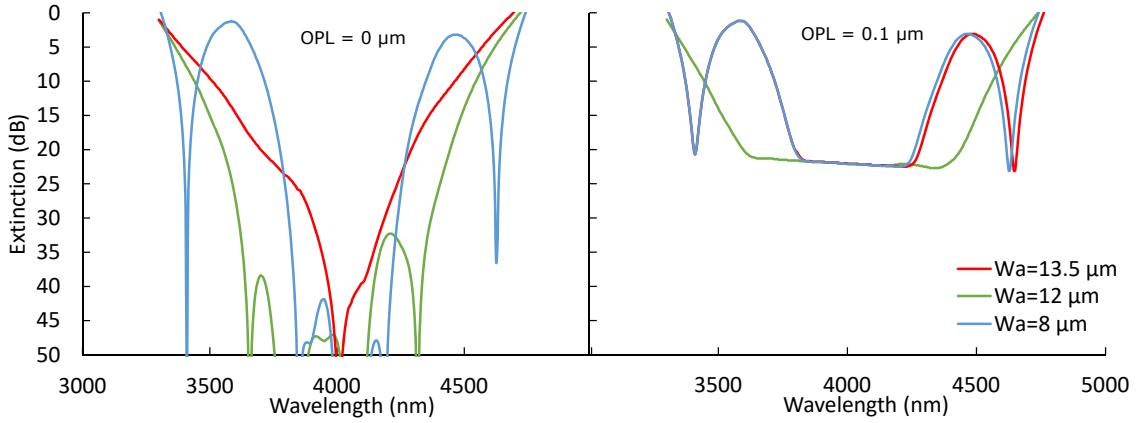

Figure 7.4: MZI performance from eq. (7.3) with $\delta = 0$ (left) as compared to $\delta = 0.1$ µm (right).

Figure 7.4 shows the drastic effect of the OPL away from zero. It shows that for a $\delta = 0.1$ µm the extinction is limited to 20 dB. It also shows that the $W_a = 13.5$ µm and 8 µm will provide the same extinction over the entire bandwidth (with a slight variation but the same shape at longer wavelength) with the $W_a = 12$ µm providing a wider extinction bandwidth of 800 nm compared to 400 nm. This change in OPL is highly detrimental in determining whether an MMI can produce a deep null as this change in OPL means the measured results will no longer represent what the MMI can achieve with external path matching.

Equation 7.2 has a term for a loss in one arm so the impact of this on the extinction can be simulated. This is vital as the additional loss was observed in one arm of the MMI, see Chap. 6 for further details. Not only that but there is a 14 cm interconnect between the two MMIs. From particulates in the film, there is a non-zero chance that these two waveguides will not have the same transmission and this difference in loss will change the extinction measurement.

Figure 7.5 has the simulated MMI response (over the same bandwidth) with a 10% loss in one arm.

Figure 7.5 shows that a 10% loss in one arm is enough to restrict the extinction depth to 25 dB, in the normal operating window suggested in Fig. 7.4, for MMI with $W_a = 12$ and 8 µm. The only MMI to not have their extinction bandwidth significantly reduced is one with $W_a = 13.5$ µm which instead had its high extinction zone shifted away from 4000 nm to 3800 nm. Comparing Fig. 7.4 and 7.5, the extinction bandwidths are the same as for each MMIs with $\delta = 0.1$ µm whereas each extinction curve in Fig. 7.5 retains at least one deep null point and this can be a discriminating factor between loss in one arm and a minor OPL difference when comparing experimental data to the theoretical prediction.

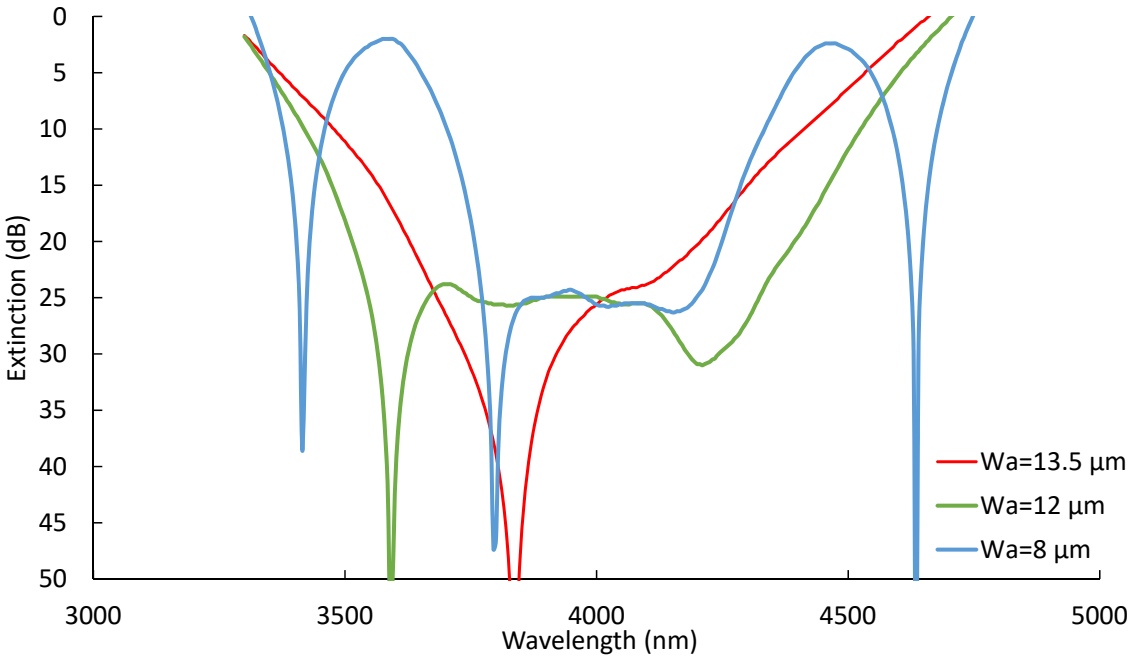

Figure 7.5: The extinction theory provided by eq. (7.3) with $\delta = 0$ but with 10% loss in one arm (right arm from Fig. 7.2 and the equivalent for the left arm would provide a symmetric response).

The limitation due to an OPL difference or loss in one arm is highlighted here and shows that a slight change is catastrophic to the null depth. For the fabrication of the waveguides between the MMIs it is important to know how much the OPL will change so that future work may attempt to rectify this OPL change.

Before delving into phase control and how to generate a wide bandwidth extinction it is pertinent to analyse the uncertainty of an extinction measurement due to the scattered light observed in Chap 6. This is to understand the limitations of coherent light on any extinction measurement.

7.2 Restriction due to scattered light

An analysis into the effects of scattered light was conducted in Chap. 6. The focus of that chapter was to understand the limitation, due to scattered light, of inferring a measurable extinction from an MMI imbalance measurement. For an MZI measurement, the limitation is to the observable extinction due to the scattered light. A similar simulation, shown in Fig. 7.6, was conducted for the case where the interfering light is coherent and where it is not. Note that this simulation uses base parameters of a 40 dB extinction then recalculates the intensity of the two output ports to determine an upper bound due to scattered light.

Note here that when the scattered light is brighter than the null port the calculated extinction bounds are much higher than the actual extinction (providing only a lower limit on what can be measured rather than uncertainty in the measurement).

Figure 7.6 shows that if the scattered light is incoherent then an almost 40 ± 1 dB extinction can be measured with a scattered light depth of about 46 dB relative to the

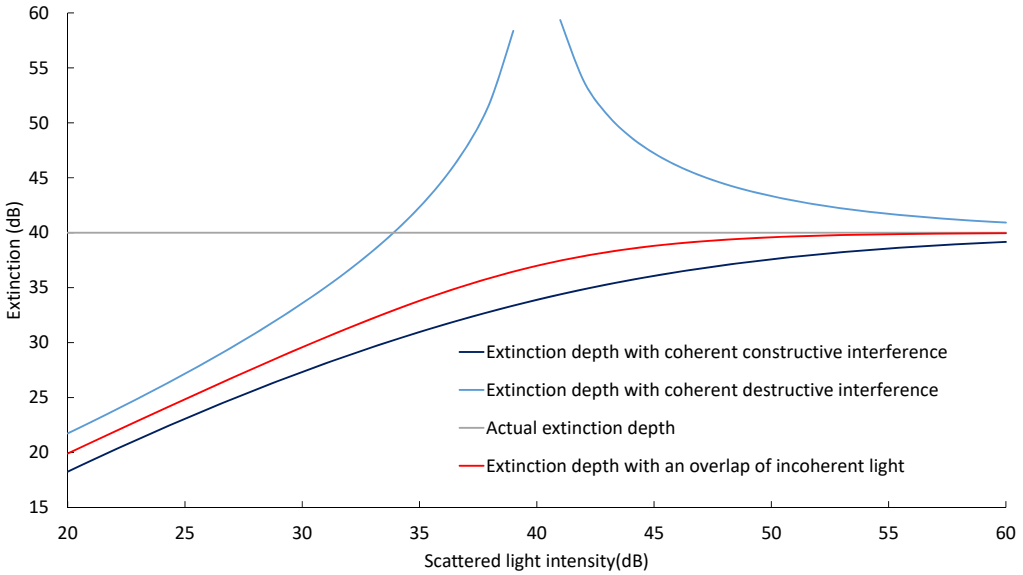

Figure 7.6: A simulated extinction of 40 dB (grey), with uncertainty in the potential measurement calculated using coherent scattered light (orange and red) or the upper limit on what can be measured with incoherent scattered light overlapping with the null signal (blue).

constructive interference port of the MZI. If the light is coherent then a scattered light 60 dB is required to achieve the same uncertainty. This uncertainty is much better than if the imbalance had been measured and the extinction inferred (from Fig. 6.6). Incoherent light limits the direct extinction measurement more than it did for the inferred extinction from Chap. 6. This is because the nulled light in an extinction measurement is similar to, if not at the same level as, the background noise or scattered light, whereas an imbalance measurement has two measured signals well above the noise or scattered light level.

The destructive interference of the light, for coherent light, provide the limits to the extinction (once sufficiently limited in intensity). The discontinuity of the lower limit (the high extinction area at 40 dB in Fig. 6.6) curves is due to a mathematical infinity when calculating for a scattering light level of 40 dB. This is not a physical occurrence but shows that in some cases the measured extinction may be significantly lower than it should be due to interference.

Thus reducing the scattered light, as for measuring the imbalance of the MMI, was a priority in this work. Two methods of scattered light reduction were included here: using a layer of carbon to absorb the scattered light, and using offset waveguides with a rotated MMI geometry - designed so that scattered light cannot possibly overlap with the output ports.

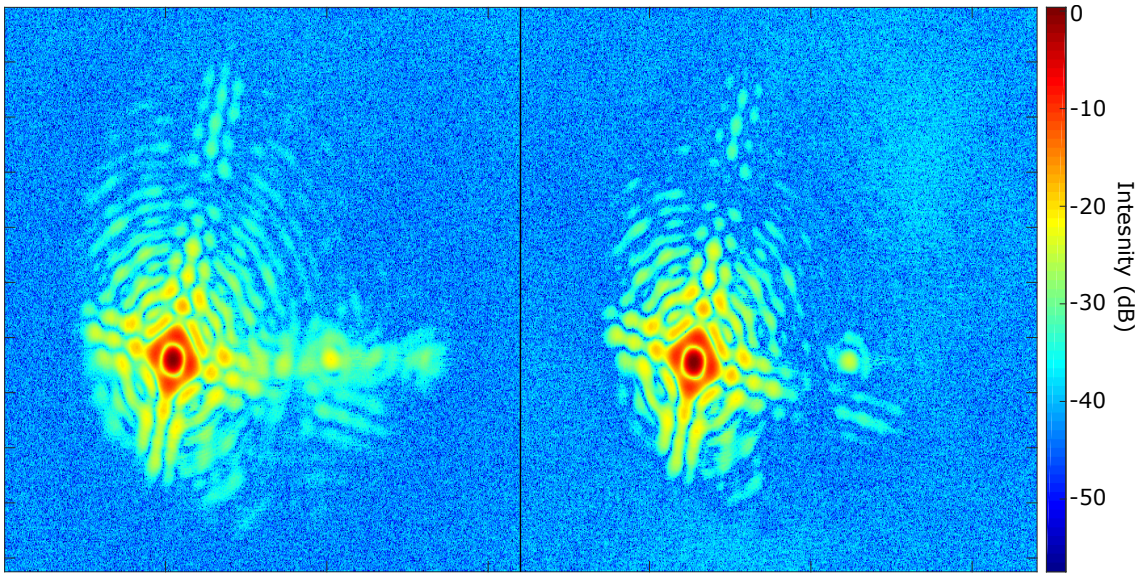

Figure 7.7: The MZI PSF measurements for the same chip, once with carbon overcladding (right) and the other without (left) at the wavelength 4250 nm.

7.3 Scattered light reduction techniques

7.3.1 Carbon layer

A thick (>1 mm) layer of carbon was deposited over the cleaved chip in the same manner as Sec. 6.2. Both the MMIs, the waveguides going into and out of both MMIs, and the MZI arms were covered with carbon, without covering the chip faucets (so that insertion loss was not increased).

Figure 7.7 shows the diffraction-limited PSFs in an extinction measurement, using the Xenics Onca camera, of the same MZI with and without carbon at a wavelength of 4250 nm. The figure shows that using an over-cladding of carbon the scattered light in the plane of the null and antinull ports is reduced. Using the given scale the scattered light level falls from −25 dB (as compared to the maximum intensity) to the noise floor of approximately −40 dB.

The camera image highlights a previously discussed point regarding the separation of the two PSFs and their overlap. So that the high-intensity PSF bands do not overlap with the other PSF central lobe; the output objective, between the photonic chip and the camera, was rotated 30°. This provides the angle shown in Fig. 7.7 of the antinull PSF. At the extreme end of the PSF arm light with an intensity of −30 dB is visible whereas the side lobes fall to −40 dB (on the carbon over-cladding side). This indicates that at these distances, with this rotation of the output objective, the PSF of the antinull port could now be the limiting factor in determining the actual extinction depth.

For a direct comparison of measured extinction between the MZI with a carbon layer and without, over the bandwidth of 3000 nm to 5000 nm, see Fig. 7.8. This shows MZIs comprising two MMIs with $W = 44\,\mu\text{m}$, $W_a = 8\,\mu\text{m}$ and an OPL difference of 4.3 µm. As was standard for the measurements in Chap. 6 the 1000 frame lock-in detection was used

(1000 light frames and 1000 dark frames were taken from a chopped signal, see Sec. 5.4 for more information), providing a noise floor of 40 dB.

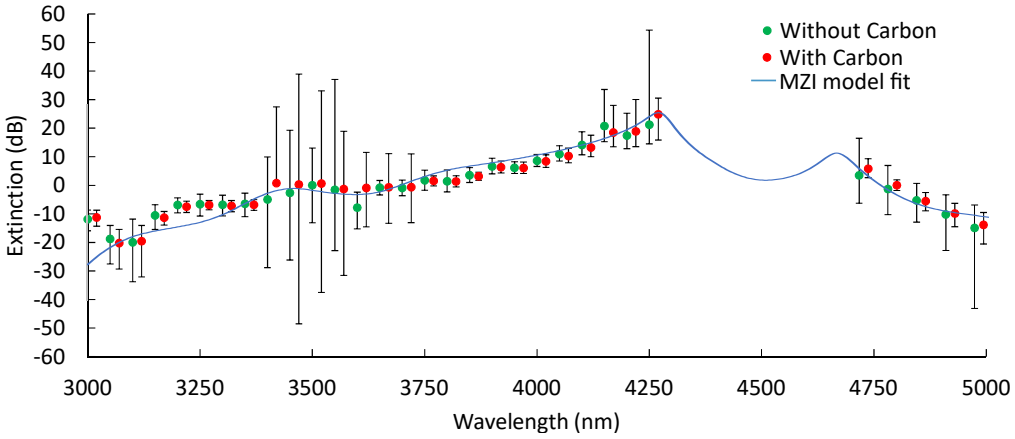

(a) Using the left input port.

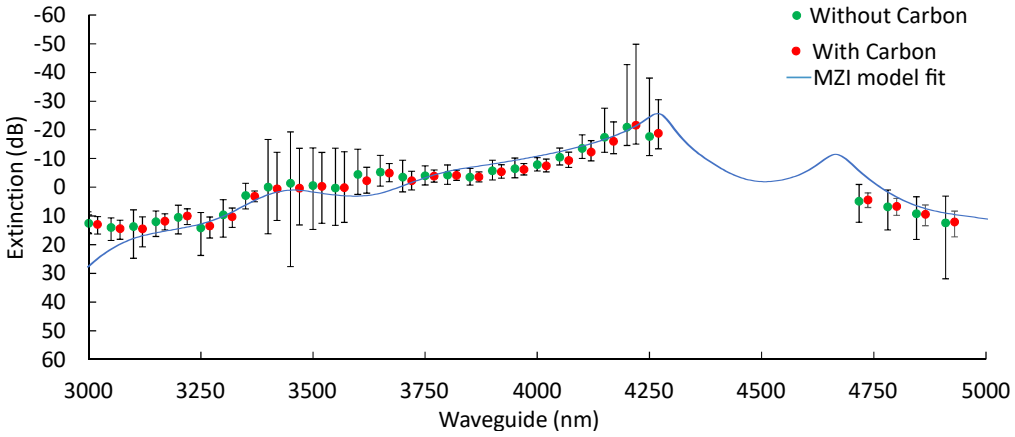

(b) Using the right input port.

Figure 7.8: The extinction measurement of the MZI in Fig. 7.7 with and without a carbon layer, the prior having an offset of 20 nm so that the points are distinguishable. The MMI have $W = 44\,\mu\text{m}$ and $W_a = 8\,\mu\text{m}$. The error bars are calculated as the upper and lower limit due to coherent scattered light between the signals. The MZI model (blue) shows an OPL difference of 4.3 µm.

These figures show that the scattered light is less with a carbon layer than without but whether this is a significant reduction is still questionable. In the area where the MMIs would have little scattered light (between 3700 and 4200 nm) the scattered light is already minimal with the carbon layer providing a reduction of up to 0.5 dB in the extinction uncertainty. At 4250 nm the deepest extinction is 21^{+33}_{-6} dB and -21^{-29}_{+6} dB, for light launched into the left and right input port respectively, which is shallower than predicted in Chap. 4. As mentioned before, this is likely because the OPL has changed the phase of the combined light (in the MMI) and reducing the OPL to zero may be a requirement to directly measuring a deep null.

Away from the null the carbon provides an 8 to 10 dB reduction in scattered light (this ignores the area between 3400 and 3600 nm that has a high uncertainty due to the

PPLN:$LiNbO_3$ crystal being damaged and thus providing a low transmission compared to the background light). These areas help fit the MZI theory curves to the data with higher accuracy. An OPL difference of 4.3 µm in the MZI arms was used to fit the MZI theory to the experimental data (with a sign flip to fit the right input port data). Note that an OPL of zero would provide a 40 dB null between 3500 and 4050 nm. For this data however, the deepest extinctions occur at $\lambda = 4250$ nm at a depth of 21^{+33}_{-6} dB and -21^{-29}_{+6} dB for light launched into the left and right input port respectively. This shows that even with limited scattered light, due to the carbon cladding, the uncertainty in a deep extinction can be great. This was compounded by the lack of laser light at 4250 nm and with less light comes more uncertainty due to the noise floor being higher through a higher integration time.

To increase the theoretically measurable null depth a redesign of the chip layout is required, so that light from the output ports does not overlap with the scattered light.

7.3.2 Offset geometry

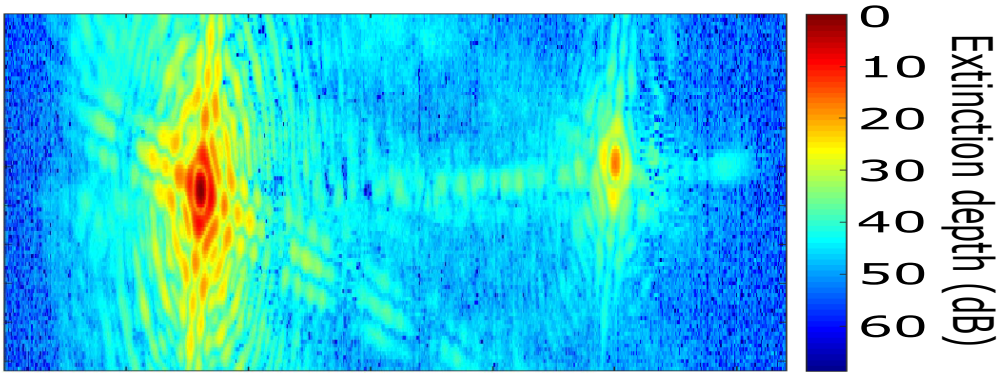

Figure 7.9: The PSFs from the two outports of an MZI for a wavelength of 3900 nm. A log (dB) scale has been used for this image, with the maximum intensity value set to zero.

In Sec. 6.4 the input and output waveguides were offset and the MMI rotated 90° in a geometry intended to reduce the intensity of scattered light overlapping with the two PSFs. Figure 7.9 is an image taken with the Xencis Onca camera of the MZI's output facet for a photonic chip using this geometry, at $\lambda = 3900$ nm. There is approximately 35 dB of scattered light between the null and antinull PSFs. Whether this light is still coherent is unclear. In the case of the $\sim$ 10 ps measurement pulses used in this thesis, however, the light has been assumed coherent as to not misrepresent the confidence in the data. The scattered light level as compared to the combined PSF intensities for a broad bandwidth is included as Fig. 7.10 to illustrate the lack of wavelength dependence.

The scattered light's comparative intensity was calculated using:

$$\pm \text{Scattered light depth} = 10\log_{10}\left(\frac{\text{SL}}{(\sqrt{\text{Null}} \pm \sqrt{\text{SL}})^2 + (\sqrt{\text{Antinull}} \mp \sqrt{\text{SL}})^2}\right) \quad (7.4)$$

with the measured scattered light (SL). The flat wavelength response indicates that the scattered light is not from the MMI as seen previously but likely the light leaking from

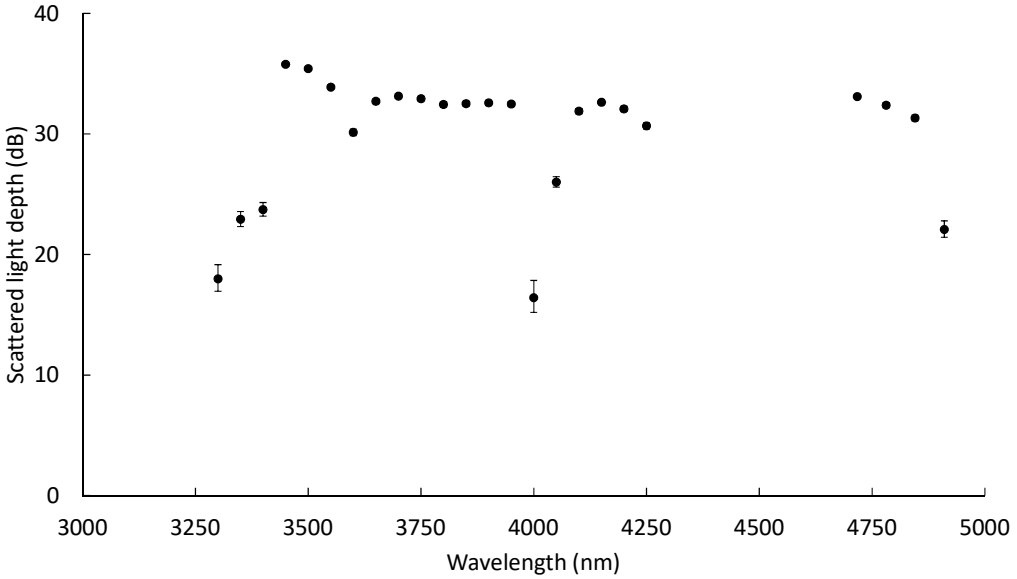

Figure 7.10: The measured scattered light intensity depth, between the two PSFs from the MZI, normalised to the the combined PSF intensity.

the output waveguides.

On average scattered light intensity from Fig. 7.10 is approximately 35 dB lower than the MZI PSFs, with outliers occurring when the throughput is reduced either through light absorption by the cladding material at 4000 nm or simply a lack of light (due to low laser output at 3300 nm and 4900 nm). This is the same as for the equivalent spectra shown in Sec 6.4 for the scattered light from a single MMI.

Based on the scattered light model in Fig. 7.6 a 40 dB null (the level of background light by the frame integration) would be limited to 25 dB for this level of coherent light. This implies that a carbon cladding is still required to absorb the remaining scattered light even in the offset geometry. The precise sources of this light are yet to be elucidated: whether it is sidewall scattering from the output waveguides or uncoupled input light scattered off the waveguide structures, but additional baffling structures etched through the Chalcogenide (ChG) layers, filled with carbon, seems to be necessary to absolutely minimise background light - coherent or not.

As an initial test of the offset MZI geometry, two MMIs were placed in series with a 200 µm connecting waveguide. The width of this waveguide was the same as the MMI's W_a. A measurement of an MZI using two MMIs with $W = 45\,\mu\text{m}$ and $W_a = 12\,\mu\text{m}$ is shown in Fig. 7.11.

The extinction-level in Fig. 7.11 is much lower than expected, indicated by the two simulations included in the figure. These simulations, conducted in RSoft BeamPROP, represent the ideal MZI response and one that has the input and output waveguides (and tapers) offset by 1 µm. RSoft BeamPROP was used because the MZI model, used before, has no variables for taper offset. The reason for the second simulation was because an optical microscope measurement indicated that the real devices have this offset (due to a

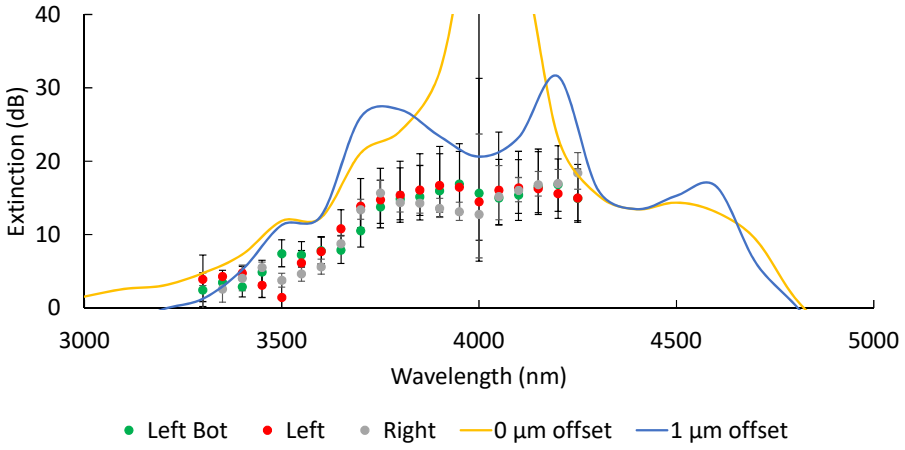

Figure 7.11: Measurements of two MZI $W = 45\,\mu m$ and $W_a = 12\,\mu m$ MMI, one with both input ports individually illuminated (red and grey for launching light into the left and right input port respectively) and one with only the left port illuminated (green). A simulations of the equivalent MZI is overlaid (yellow line) and another with a 1 µm offset (in the width direction) for every waveguide (blue line).

mask design error). The uncertainty, due to the scattered light, shows that this offset does not wholly account for the low extinction value but shows that it is certainly a factor.

7.4 Fabrication tolerance in a on-chip Mach-Zehnder interferometer

The two MMIs in an MZI are connected by lengths of the nominally identical waveguide. In practice photomask, critical dimension control dictates the level at which they are the same. Thus the question arises as to how much width difference is tolerable in the MZI interconnecting waveguides. This discussion is of course equally applicable to a beam combiner but if a MEMS is used then the 90° offset is tuneable as is the intensity in the event of additional loss in one input waveguide.

Figure 7.12 shows the calculated OPL as a function of the width difference between the interconnecting waveguides for different nominal widths, assuming the interconnecting waveguides are 14 mm long (the interconnect distance for the remaining MZIs in this work). It shows that even for a waveguide width difference of 1 nm, between two 2 µm wide waveguides over 14 mm, the change in OPL is significant - reaching 1 µm. This explains how it is possible for the results shown in Fig. 7.8 to have a high OPL difference (4.3 µm) - the width difference between the connecting waveguides was $\sim$ 5 nm, which is below the control limits of commercially available 1x photo lithography masks. For a waveguide width of 6 µm the tolerance to this waveguide fabrication error is increased. Shown in Fig. 7.4 an OPL difference of 0.1 µm reduces the extinction depth to 20 dB. Currently, the most advanced processing in the semiconductor industry has approximately 1 nm dimensional control though on much smaller feature sizes than considered here. Thus it is clear that passive matched interconnects of centimetre plus lengths are going to present

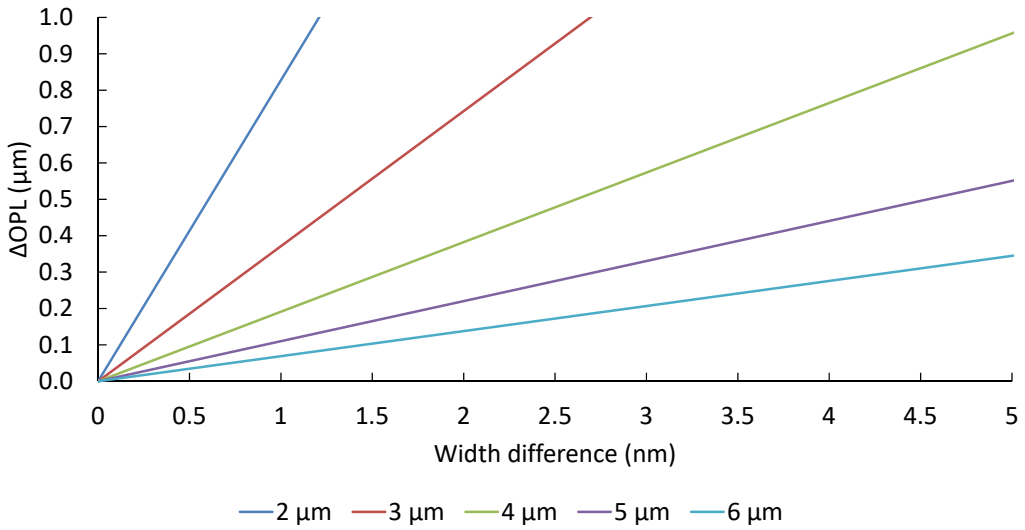

Figure 7.12: Simulations of the OPL difference for an original width of 2 (blue), 3 (red), 4 (green), 5 (purple) and 6 µm (teal) waveguide and one with a slight increase in width.

significant issues in on-chip interferometers.

Sidewall roughness is another source of error to consider when deciding how to control errors in the waveguide - discussed in Chap. 5. A waveguide with high sidewall roughness will produce a random phase shift between two identical waveguides. If the error was a static length difference then the issue may be resolved when designing the mask but a random error requires active control.

The fabricated MZI arms in this work were constrained to a width of 2 µm (keeping them single mode). Even if they were increased to width to 6 µm, with periodic up and down tapers to preserve single-mode operation through mode filtering, it is not enough to avoid the OPL difference intolerance in the fabricated devices. This leads to two options: changing the geometry of the MZI design, included in Sec. 7.3.2, and developing heaters to actively rectify the high OPL difference intolerance. These heaters were made by depositing chromium (Cr) over the MZI arms. When a current is passed through these heaters they actively change the refractive index of the waveguides via the thermo-optic effect. Chromium was a quick and easy method to achieve this and future work may choose to spend additional time to fabricate higher quality heaters.

7.5 Chromium Heaters

As noted previously, very small width errors in the interconnecting waveguides can produce a significant change in OPL to the extent that even a quarter wavelength difference (a 1 nm difference in some cases) causes the performance to be significantly reduced. It is not practical to make waveguides that are of such high quality, hence a method of pathlength compensation is required.

Heaters made of Cr were utilised in this work as an OPL control. They were deposited over interconnecting waveguides (shown in the MZI schematic Fig. 7.2) of the MZI with

probe pads used to connect the electrical circuit. When current flows through the Cr circuit, it undergoes restive heating, via the Joule-Lenz law,

$$P = I^2 R \tag{7.5}$$

for power (P), current (I) and resistance (R). The heat produced by the Cr affects the material via its thermo-optic coefficient.

The thermo-optic coefficient of a material is the rate at which that material's refractive index changes with temperature change (dn/dT). For ChG the coefficient varies with composition, but for the materials used in this work an approximation of dn/dT = 21 ppm/°C [258] was made. Utilising the thermo-optic coefficient the effective index can be altered through heating and, due to the OPL= $n \cdot L$ where L is the physical length, the pathlength can be corrected.

7.5.1 Heater placement model

The optimal position of the Cr heater was determined using RSoft Multi-Physics Utility [259]. The initial idea was to use a duel heating system of two heaters around the waveguide. Two options were available: before or after angled deposition of the over-cladding material. For the latter, a trench would have to be etched into the over-cladding to access the heater's probes. It would also require the heater's connection to the probes to be completely separate from the waveguide as an overlap would absorb all of the light from the waveguide. The index profile for the Multi-Physics simulations is shown in Fig. 7.13 for the case where the heaters are above the over-cladding and at the same level as the under-cladding.

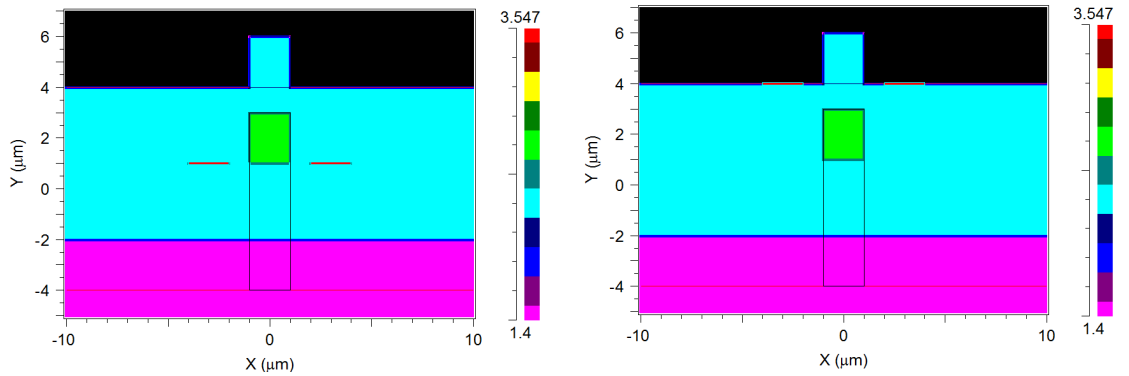

(a) Cr deposited on the undercladding after core etching step.

(b) Cr deposited on the overcladding (3 µm above the waveguide's base) after angled deposition.

Figure 7.13: Refractive index profile of a dual heater system (red) where heaters are placed 2 µm away from the waveguide (green) and either embedded in the cladding (blue) or on top for figures (a) and (b) respectively. The simulation is for a SiO_2 (pink) substrate. The black line around and below the waveguide is for simulation purposes only and not a physical feature, nor are the lines between under-cladding and air (black) and the SiO_2 substrate.

The simulations using these index profiles showed that placing the heaters on the

bottom would require a 6 µm displacement from the waveguide to have a loss, from the Cr absorption, < 1 dB/cm whereas the heaters on the top only required a 4 µm horizontal displacement (5 µm diagonal displacement) from the waveguide.

At $\Delta T = 180$ K the heaters on the surface (4 µm away) produced an OPL shift of 6 µm and the equivalent heat for the bottom layer heaters (6 µm away) produced an OPL shift of 3 µm.

A single heater, on the top layer, was also investigated to see if the losses (and OPL change) were acceptable as it would be easier to create a single heater system using the proposed lift-off technique (described below) and Cr deposition. Figure 7.13 has approximated the cladding bump above the waveguide as 2 µm high by 2 µm wide. This provides the model with a 3 µm displacement for a single heater over the top of the waveguide. As such the loss was 0.01 dB/cm for an OPL change of 4 µm, making it a much better choice than both duel heater scenarios. Thus, using a single heater above the waveguide was chosen for this work.

Note here that future work may require these heaters to perform real-time phase-matching or even fast phase flipping. This may not be possible, depending on the required speed. Future experiments will need to measure the relaxation time of the ChG to test what speeds can be achieved using this method of index change.

The fabricated MZI has 14 mm long arm lengths. Heaters of 8 mm (used for the OPL calculations above) were deposited over the waveguides connecting the two MMIs. These heaters were set sufficiently far away from the MMI (3 mm) that the heat would dissipate before reaching them and only change the refractive index of the waveguides.

7.5.2 Deposition

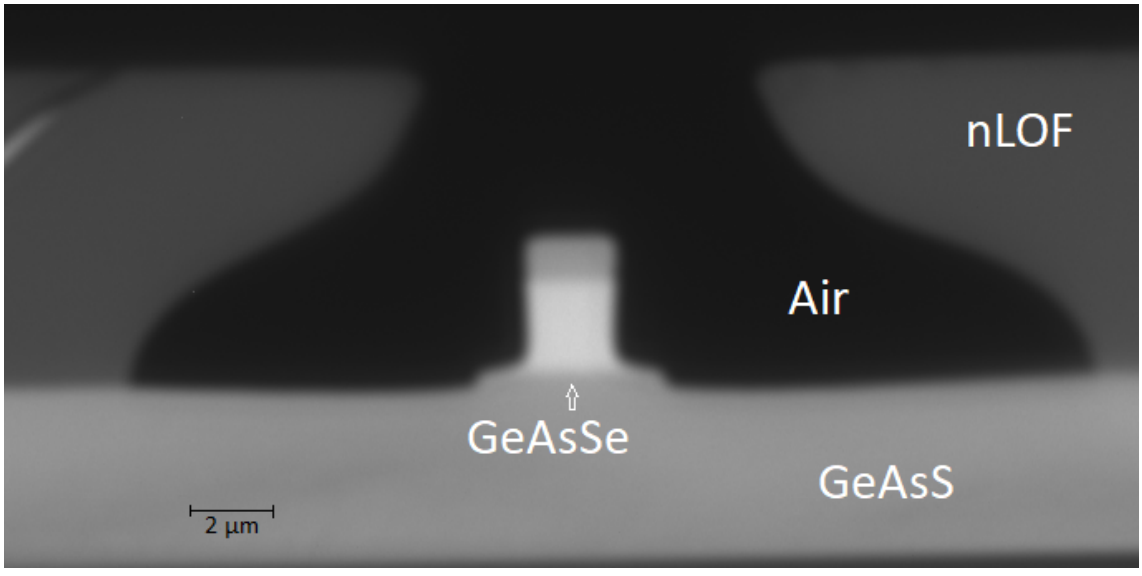

Figure 7.14: Fully etched 2 µm wide waveguide without ChG overcladding. The nLOF has been spun onto the wafer and undergone photo-lithography, using a mask with a 6 µm wide space over the waveguide.

To fabricate the heaters a lift-off process was undertaken, using the negative photoresist nLOF 2070 (hereby referred to as nLOF) [260]. After the photoresist was developed (using the standard developing process), which produced trenches in the nLOF for the Cr heaters to be placed, and Cr deposited the remaining resist was chemically removed using TechniStrip. This removal step did not affect the Cr in any way. The nLOF was used because it was able to create a thick resist (the target being 7 µm) that, when spun onto the wafer's surface, provided a flat profile over the waveguide ridges, for the Cr lithography step.

To illustrate the final resist profile over topography, Fig. 7.14 shows a waveguide without over-cladding and a 7 µm layer of nLOF deposited. The resist was printed using the previously described photo-lithography and development steps in Sec. 5.3. It shows that the resist profile will not impede the Cr deposition and will allow for the sidewalls to be exposed to the Cr.

Chromium was deposited using an ATC 2400 V sputter machine by AJA International [261]. An electron beam evaporation tool (E-beam) (commonly used for thin metallic film deposition) was not used because sputtering is omnidirectional and the E-beam is not. This ensures that the waveguide's sidewalls will be covered rather than just the top surface (as well as the exposed, horizontal, areas shown in Fig. 7.14, directly adjacent to the waveguide). These wafers having a 3 µm layer of cladding over the waveguide, unlike the test sample shown in Fig. 7.14, and so sputtering provides more uniform coverage over the entire topology of the cladding bump compared to other methods.

The sputtering chamber was set to a pressure of 4×10^{-3} Torr and the Cr were sputtered with 20 sccm of Ar at a power of 195 W over a 2 h duration. This deposited approximately 200 nm of Cr but only 40 nm over the waveguides due to the shadowing effect of the nLOF.

7.5.3 Thin film resistance

An initial test of resistivity was undertaken by depositing 100 nm (20 nm due to shadowing and measured by an optical profiler) of Cr onto a blank, insulator - a SiO_2 wafer. The mask used is displayed in Fig. 7.15 and was used to mask the areas where the photoresist (nLOF) would be etched away by the developer. The resist profile was the same as in Fig. 7.14 but without the waveguide so that the heater would be smooth and uniform against the SiO_2. A full wafer of heater probe pairs (connected by one or two heaters) was tested with the results shown in Fig. 7.16. Note that the heaters connecting the probes were measured to be 28 µm wide compared to a mask opening intended to be 6 µm wide. This is a result of the more omnidirectional nature of sputtering leading to leakage under the mask edges, and the extended nature of the bottom part of the removed nLOF (which is seen in Fig. 7.14).

Figure 7.16 shows that there is a spatial dependence of the resistance in the heaters, both in the horizontal and vertical directions of the wafer. Also note that columns 2, 7, 12, 17 and 22 are two heater tracks in parallel. The maximum resistance of 800 $k\Omega$ is in the centre of the wafer and corresponds to the thinnest heaters. The smallest resistance is

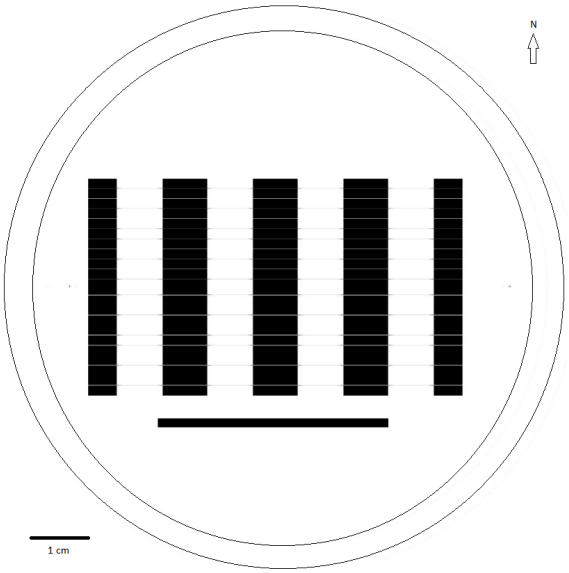

Figure 7.15: The mask design for the Cr heaters. The large areas are probe contact points and the lines between them are the heaters. This mask used the alignment markers on the side to align the heaters with the MZI arms. The bar in the south position of the mask is used for directional purposes.

300 $k\Omega$ (excluding the parallel heaters where the lowest is 180 $k\Omega$) for the heaters on the wafer edges.

These resistance (R) variations are due to the wafer being centred and the Cr source offset from the centre. The wafer spins inside the chamber so that deposition should be uniform but the thick nLOF provides a shadowing effect that blocks material at steep angles that cannot be compensated through a full rotation.

Using the calculation of the R in a wire:

$$R = \rho L/A \tag{7.6}$$

as an approximation, for a heater length (L) of 8000 µm, a measured height and width of 18 ± 1 nm and 22 ± 1 µm respectively (multiplied together for the cross sectional area A) with the resistivity (ρ) of Cr ($= 2.7 \pm 0.5 \times 10^{-3}\,\Omega$·cm [262]), R should be approximately 550 $k\Omega$. The fluctuation between 750 and 325 $k\Omega$ is indicative of the error in the height and the ρ due to the change in height. For example an increase to 22 nm would provide a $\rho = 2.33 \times 10^{-4}\,\Omega$·cm and decreasing down to 10 nm would provide a $\rho = 2.25 \times 10^{-3}\,\Omega$·cm [262] changing R to 40 $k\Omega$ and 818 $k\Omega$ respectively. From these resistances RSoft Multi-Physics Utility can be used to determine the maximum current to be put through the system without increasing the temperature of the ChG above its transition temperature (T_g) where the chalcogenide becomes malleable and may reflow.

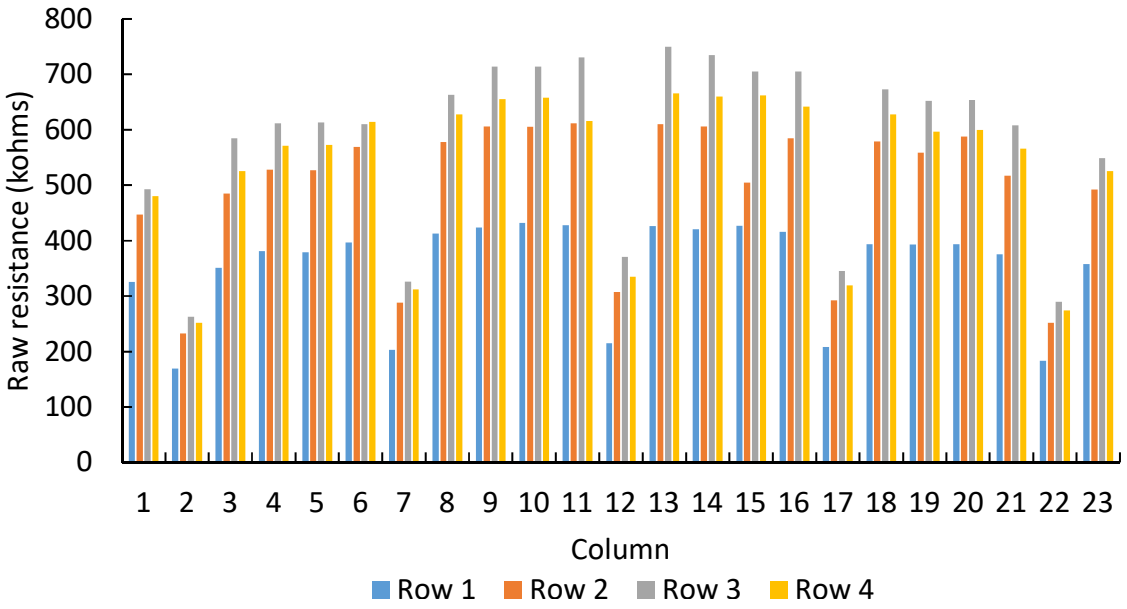

Figure 7.16: The measured resistance between 92 probes split into 23 columns (north to south in Fig. 7.15) and 4 rows (left to right).

7.5.4 Heater model

RSoft Multi-Physics Utility can model the refractive index difference of a waveguide from the heaters. An example is included as Fig. 7.17 for a single heater 3 µm above the waveguide. It shows an index change between 0.0008 and 0.0005 for a constant temperature of 150°C - providing an OPL change of 6.4 to 4 µm. Note here that this model is slightly different from before. From the nLOF profile shown in Fig. 7.14 the Cr will cover more area than the 2 µm used in the heater placement model (Sec. 7.5.1). A new RSoft model (shown in Fig. 7.18), where the Cr covers the waveguide cladding bump and extends to the sides of the cladding bump, indicates a loss of 6 dB/cm due to the Cr heater.

Figure 7.18 is the CAD model used to simulate the absorption due to the Cr heater. Using the model the relation between Cr absorption, for 20 nm of deposited Cr, and the SiO_2 buffer layer was found.

From Fig. 7.19 the loss is reduced to < 1 dB/cm (the requirement used when modelling the duel heater system) when the buffer layer is 100 nm thick. These experiments doubled that layer, using a 200 nm buffer layer of SiO_2 deposited using plasma-enhanced chemical vapour deposition (PECVD) tool so that the loss was approximately 0.25 dB/cm. The parameters of the plasma were 9 sccm of SiH_4, 710 sccm of N_20 and 161 sccm of N_2, at a pressure of 0.65 Torr, a radio frequency (RF) power of 20 W at 80°C. The low temperature was used so that the film did not crack (due to the coefficient of thermal expansion mismatch between the Si, SiO_2 and ChG) during deposition. This was a wafer wide process that occurred before the nLOF step. This had the dual purpose as a buffer layer between the solvent, used to make the nLOF removal easier, and the ChG. It was, however, found that the ChG did not require protection from the solvent and the nLOF could be

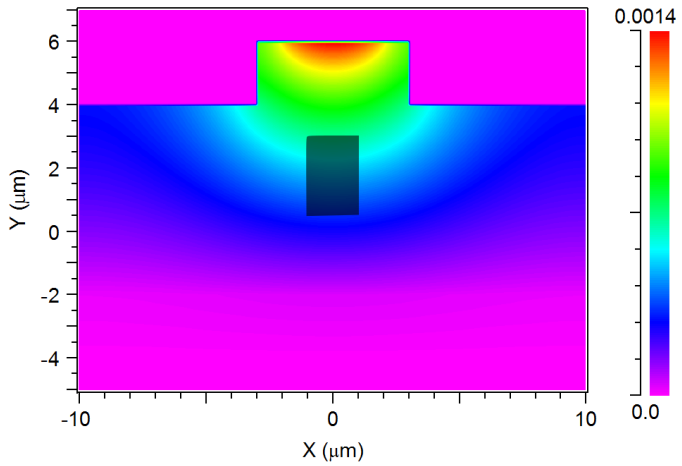

Figure 7.17: Simulated refractive index change of a Cr heater at 150° (waveguide is the overlaid black square).

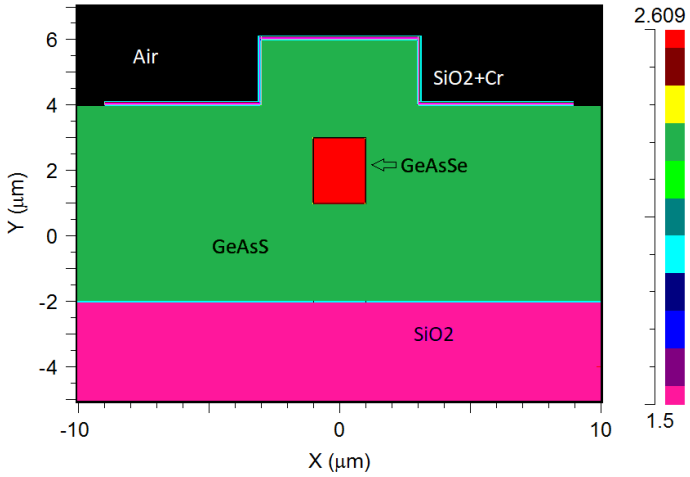

Figure 7.18: RSoft CAD model of a deposited Cr heater (20 nm thick) and SiO_2 buffer layer (100 nm thick) covering the waveguide cladding bump and extending 6 µm in both directions.

removed cleanly without a layer of SiO_2 meaning the SiO_2 can be deposited after the nLOF step, which better represents the model in Fig. 7.18. The preference before the nLOF step stems from the timing of PECVD, Cannon MPA-500 FAB and Sputter tool availability.

The model in Fig. 7.18 could not be used for RSoft Multi-Physics Utility accurately as it used unconnected segments of Cr instead of a single segment that generated heat. As such the model used for Fig. 7.17 had a single heater above the waveguide, on the waveguide cladding bump, to simulate the OPL vs. heat relation.

For the ChG used in these experiments, an upper limit of temperature was set as 200°C as to not exceed the material's T_g. If the temperature did reach above the 200°C then any pressure on the surface (like probes pressing on prob pads) could cause the glass to flow.

The power limit for the heaters measured in Sec. 7.5.3 was then found to be 8 µW (to keep the temperature below 200°). By the measured R, the current (I) and potential (U)

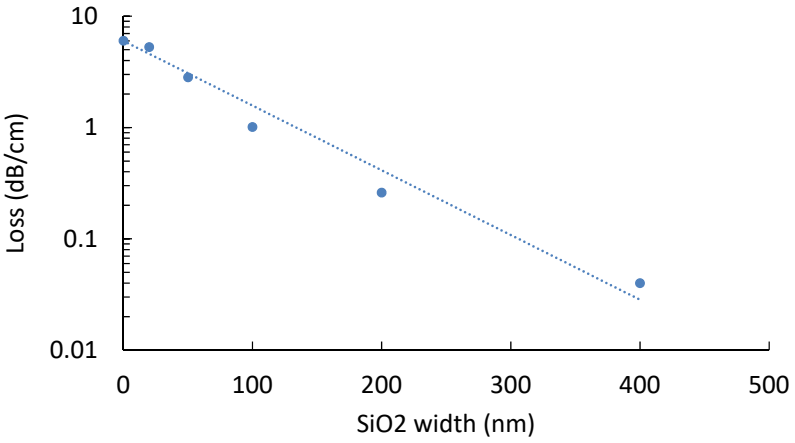

Figure 7.19: The simulated relation between the SiO_2 buffer layer and the absorption of a 20 nm layer of Cr.

upper limits are calculated to be $4 \pm 1\,\mu A$ and $2 \pm 0.5\,V$ respectively.

During experimentation the Cr layer oxidised, causing a short in the heater. Figure 7.20 shows the aftermath of the oxidised Cr. There is a tendency, when viewing this image, to assume that the lithography could be a reason for what is shown in Fig. 7.20: that the nLOF was not removed completely before the Cr deposition. From previous experiments, when nLOF was not removed correctly before the Cr deposition large chips of the probe area was removed during the lift-off process, as was the layer over the MZI interconnecting waveguides - no heaters surviving the final nLOF removal. Being a photoresist that is used for lift-off lithography, nLOF would not remain on the wafer after being immersed in TechniStrip. Oxidisation is much more likely to produce the dark areas highlighted in Fig. 7.20.

To make the Cr more robust to oxidisation a thicker layer was used in the final experiments, with a thickness of up to 100 nm. From RSoft FemSIM this decreased the loss to 0.18 dB/cm and from RSoft Multi-Physics Utility this changed the heat limitation to 25 µW with the other electrical changes calculated to be $R = 10.3\,\Omega$, $U = 0.5\,V$ and $I = 0.5\,\mu A$. Using this power a refractive index change of 7×10^{-4} was simulated, with a maximum OPL change of 5.8 µm.

7.5.5 Experimental verification

With the heaters deposited over the MZI the OPL change (δ from eq.(7.2)), could be changed arbitrarily but within the tolerances of the heater material due to oxidisation, the glass by its T_g and the range of the power supply (300 V, 0.1 A). To this end, an MZI constructed using two MMIs, of $W = 46\,\mu m$ and $W_a = 13.5\,\mu m$, was measured over the bandwidth 3300 nm and 5000 nm. The choice of $W_a = 13.5\,\mu m$ is not ideal but opportunistic as this experiment relied on a photonic mask design for a different experiment and only had MZIs with $W_a = 8$ and 13.5 µm. Future masks will include MZIs with $W_a = 12\,\mu m$.

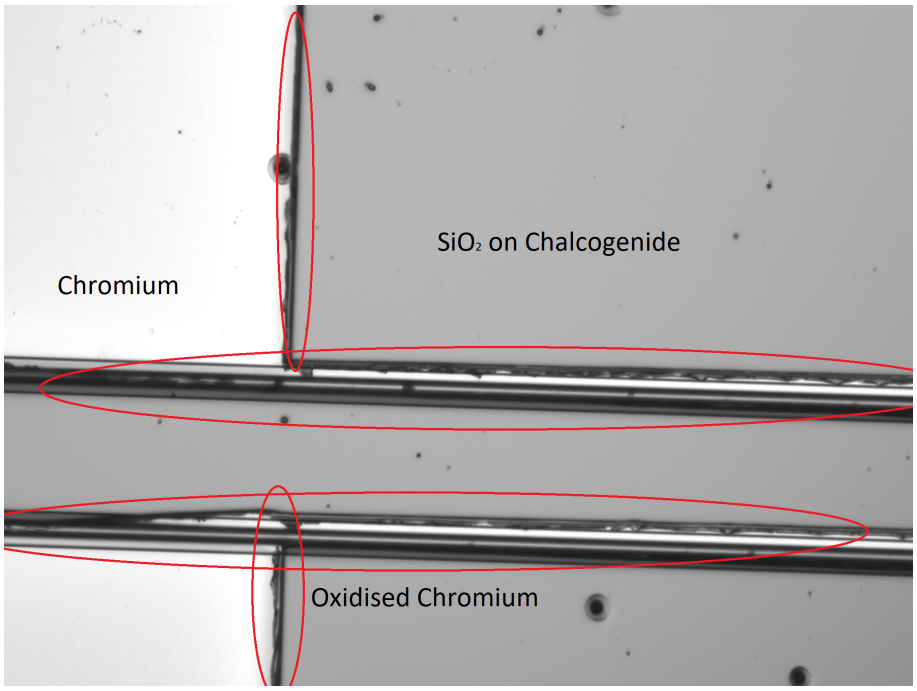

Figure 7.20: Top down view of the Cr probe pads connecting to the Cr heaters. The oxidised areas are circled in red.

The MZI measured in Fig. 7.21 was fit, such that the model aligned with the measured points (i.e. by eye), to eq. (7.3). It shows an MZI simulation with $\delta = 13.7\,\mu\text{m}$. This is higher than the 6 µm change limit simulated in Sec. 7.5.4 but the change due to the heater can still be measured. The simulation used in Fig. 7.21 does not include the loss difference in the MZI arms and shows that the extinction at 3900 nm should have reached 30 dB if it hadn't been for the additional loss in one arm. In addition, it shows the extinction curve reversing to cause a second extinction at 4550 nm. This is normal to see with a high δ especially if, rather than looking at the curve in terms of OPL, the perspective is of the free spectral range (FSR):

$$\text{FSR} = \frac{\lambda^2}{n\delta}.$$

As the OPL gets bigger the FSR gets smaller and the osculations between the positive and negative extinction increase. By heating the waveguide these osculations indicate whether the δ is going towards or away from zero.

The effect on the OPL by heating the waveguide is shown in Fig. 7.22, with power put through the heater such that a null (positive or negative) appeared at a wavelength of 3800 nm (any wavelength could have been selected but 3800 nm has the highest transmission). It shows the change in OPL with power through the heater using only one side of the heater.

Figure 7.22 was calculated by measuring the spectra of two MZIs, one with MMIs of $W = 44$ and $W_a = 13.5\,\mu\text{m}$ and the other using the same MZI from Fig. 7.21 ($W = 46$ and $W_a = 13.5\,\mu\text{m}$) and using the model in eq. (7.2) to fit δ. The large error bars in the $W = 46\,\mu\text{m}$ data are from repeat measurements that are from a decreasing power from the higher

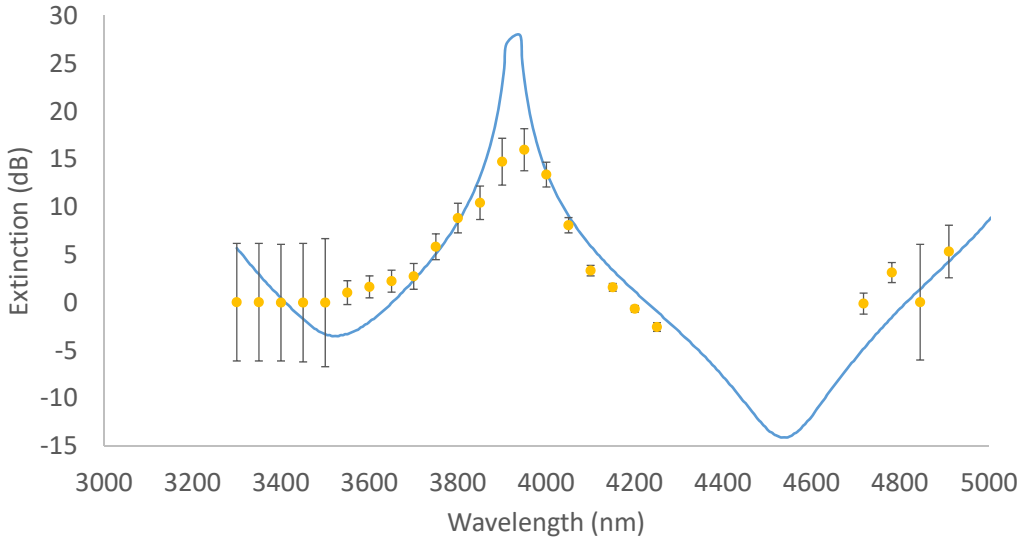

Figure 7.21: The extinction measurement of two MMI in series, both with $W = 46\,\mu m$ and $W_a = 13.5\,\mu m$. The simulated line (blue) uses $\delta = 13.7\,\mu m$ and has no loss between the MMIs.

power measurements rather than increasing from zero. The difference in measurement may be due to a change in the heaters (possibly oxidisation) at higher temperatures. The MZI with $W = 44\,\mu m$ did not change significantly for similar experiments.

The positive power region in Fig. 7.22 corresponds to the power applied to the MZI arm whereas the negative power region (the greyed area) corresponds to the theoretical power if the other MZI arm had been heated instead. The linear trend lines for both MZIs point to a $\delta = 0$ when the heater covering the other MZI arm is powered appropriately. However, the heater on the other arm exhibited a systemic failure (see Fig. 7.20 for an image of a failed heater) across all devices tested where it would become an open circuit at quite low applied currents (compared to the side that did not exhibit this failure). This is likely due to a nonuniform Cr covering of the waveguide sidewalls, specifically at the interface between the heater and the probe pads. This arises due to the deposition method (sputtering) having the material source positioned at an angle.

7.5.6 Deep nulls

Even without a zero OPL an extinction of 40 dB should be tuneable, by varying the OPL difference, according to the model in eq. (7.2) - assuming the light is of equal intensity when entering the second MMI. Figure 7.23 shows a cross-section of the two output ports of an MZI, comprised of two 45 µm wide MMI with taper widths 13.5 µm at a wavelength of 4000 nm.

Figure 7.23 shows the 30±5 dB deep extinction of an MZI. To achieve this result the light was held constant at 4000 nm and the current through the Cr heater was increased until a null formed. That null was tuned slightly so that the deepest null was found. This is similar to how Fig. 7.22 was produced: the OPL was varied until the deepest null was obtained in either output port. This null is deeper than the 40 dB noise floor and thus

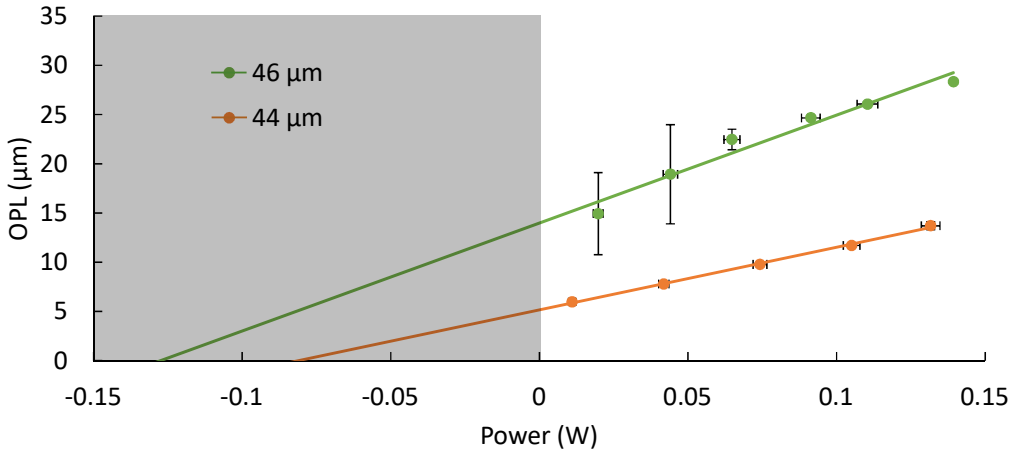

Figure 7.22: The comparison between the measured OPL (δ in eq. (7.2)) and the electrical power sent through the heater for two MMI in series with $W = 44$ (orange), 46 µm (green) and $W_a = 13.5$ µm. The grey area is the nonphysical area for the heater but the theoretical area for manipulating the other MZI arm.

this particular measurement of extinction is not limited by scattered light or background noise. Looking at the scattered light level it appears, from Fig. 7.23, to drop down to 40 dB below the peak output. Using constructive interference calculations limits the measurable extinction depth to 32 dB - within the error of what was measured here.

The PSF rings (like those around an Airy disk) are also a contaminating light source of the antinull port. The larger of which (the peak at 110 pixels) is of the same magnitude as the null signal. Subsequent peaks appear to taper below 40 dB before reaching the position of the null signal (extrapolations indicate that they would be approximately 50 dB down from the antinull peak). This shows that the airy disk rings are not causing this peak at the null. Realistically the OPL difference, in the MZI arms, is the limiting factor in producing a large extinction depth. Specifically the additional loss it would cause in the arm.

The example of a null measurement in Fig. 7.23 is typical of the MZI extinction measurements. From the MZI intensity equation (eq. (7.2)), additional loss in one MZI arm would increase light in the null port. For example, a 10% loss in one arm reduces a 40 dB extinction to 22 dB. This together with the OPL issue, is to be addressed in future work.

7.6 Summary

In this chapter, it has been shown that the MMI, designed in previous chapters, splits and then recombines light in an MZI configuration as expected (with accordance to an OPL difference between the two MZI arms). The deepest recorded null was 30 dB at the single wavelength of 4000 nm. A deep null at a broad bandwidth has not been measured due to the OPL difference between the MZI's connector waveguides.

In every measured MZI, there was an OPL difference, likely caused by the critical dimension of the photomask randomly increasing the difference in width between the

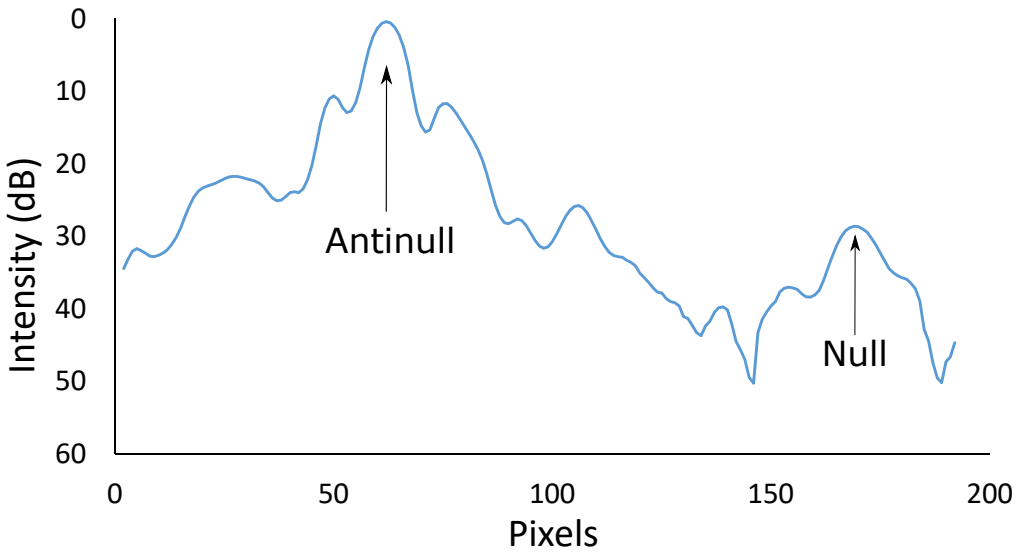

Figure 7.23: Normalised cross-section of a measured extinction (null) port and antinull output port. The MZI consisted of two 45 µm wide MMI, with taper width of 13.5 µm, in series. The wavelength was set to 4000 nm. The calculated δ for this MZI was 6 µm.

interconnecting waveguides. This prevented the MZI from producing the predicted broad bandwidth that was expected from Chap. 4 and 6. Even with heaters used to alter the OPL difference the critical zero OPL difference was not achieved. The MZI model (see eq. (7.2)) predicts that at specific wavelengths, at set OPL differences, a deep null should still be achievable. The model also shows that when there is more loss in one arm (even 10%) the null depth is significantly diminished. This prevented a deeper null than 30 dB to be measured. Both these factors will need to be addressed to achieve a large null depth for a broad bandwidth in future work.

The over-cladding of carbon aids in the measurement of the two output port intensities thereby reducing uncertainty in measuring the MZIs. The offset geometry, with MMIs, rotated 90° to the input and output ports, further reduces scattered light and the improvement is of the order that, with additional frame integration and a combination of a carbon layer, the measurable extinction depths will be approaching 50 to 60 dB.

Time constraints restricted the addition of the carbon layer in trenches around the waveguides. Table 7.1 details the process steps required to fabricate a single MZI photonic chip with Cr heaters. It also shows the time frame for fabrication. This does not include the waiting time when the Cothermal Angstrom Engineering Inc. EvoVac chamber (Cothermal) was in use or if it was under repair.

Table 7.1 shows that if the masks are already designed and made (two being required for this procedure) it takes eight days, in a best-case scenario, to fabricate an MZI with Cr heaters. This is assuming that the Cothermal chamber, the Cannon MPA-500 FAB (that has a lead time of one day), ICP reactive ion etching tool, PECVD for the SiO_2 top layer deposition, Sputter tool and the lithography track (that has the spin coater for resist and developer) at the Laser Physics Centre and Australian National Fabrication Facility are

Table 7.1: The list of steps to fabricate the MZI with Cr heaters. *The lead times for the PECVD and Sputter system is approximately three days and three weeks respectively. See Chap. 5 for further details on fabrication. †Preparation of the wafer includes lifting off the nLOF with the nominated solvent [260] and cleaving the wafer.

Event	Machine	Time	Product
Mask Delivery	-	Three months	Mask
Initial Dep.	Cothermal	Three days	Four wafers ready for Fab.
Fab.	Cannon/ICP	One day	Four wafers ready for Dep.
Overclad	Cothermal	One day	One wafer
Second Fab.	PECVD*/Cannon	One day	One wafer ready for Cr Dep.
Cr Dep.	Sputter*	One day	One wafer
Prep.†	-	One day	Multiple MZI ready for testing

all in working order.

If a new mask is required, for etching of trenches to be filled with carbon for example, then the turnaround is on the order of three months for a sidewall roughness optimised version and thus rapid testing of new geometries, new masks and new ideas, that may reduce scattered light, takes months of planning[i].

Using a direct-write style of lithography that patterns directly onto the photoresist, will limit the need for a photomask during each design iteration. Using a direct laser writing lithography tool a quick turnaround process can be enabled. Initial tests using a Heidelberg DWL-66 laser writer however indicated considerable care is required as the high laser power (approaching 100 mW of 405 nm light focused into a small spot) proved capable of damaging the glass as it is above the bandgap. This however is an approach that warrants further investigation to enable much faster iterative design cycles.

A reimagining of the experimental procedure may also provide an increase in measurable null depth, specifically a measurable null. Using a knife-edge the antinull port can be blocked, allowing for the null port to be measured without saturating the camera. This is inspired by coronagraphy - the star is blocked to allow for an exoplanet to be imaged. By doing this the full range of the camera's integration should be available, adding 40 dB contrast to the current limit. This idea needs to be explored in future work to test the accuracy of such a null.

This last point relies on the MZI producing a null that is so deep that it cannot be seen when the antinull port is being viewed simultaneously. Presently this is not the case due to the OPL difference and the additional loss in one interconnecting arm as compared to the other. To overcome this issue it may be pertinent to use a MEMS device, as discussed in Chap. 2, to direct multiple beams into the photonic chip instead of using an MMI to split the light on the chip. This provides phase control and intensity control - through misaligning the beam. These ideas and more will be explored in the future and are not in the scope of this thesis.

[i]Using local suppliers a lower-quality mask for test purposes can be manufactured and sent back in 11 days but that does not encompass the design time of a mask that may stretch to months (depending on complexity).

Chapter 8

Conclusions and future work

The main focus of this work was the simulation, fabrication and experimental verification of a multimode interference coupler (MMI) as a broadband 3 dB coupler for use as a two-beam combining nulling interferometer. Work to test the null depth of the MMI, as a two telescope beam combiner, was fraught with difficulties - emphasising the challenge in fabrication and measurement for such a task. Regardless, a deep null of 30 dB was achieved - if only at a single wavelength - which is close to but not as deep as the contrast ratio for the first exoplanet detection using interferometry (recorded earlier in 2019) of 40 dB [5], keeping in mind that 40 dB was the preliminary goal of the nulling interferometer based on limitations due to the glow of the atmosphere at 4000 nm in wavelength.

At the outset, this work endeavoured to add to the previous work in exoplanet discovery, photonic chips and interferometry. Directly imaging exoplanets using interferometry has the potential to image exoplanets at any distance from their host star (dependent only on the largest distance between two telescopes - the baseline of the system). The novelty of this work was that future interferometry space missions, and even ground-based telescopes will need mid-infrared optics to overcome the overwhelming glare of a star to observe surrounding exoplanets, and far-infrared optics if the Earth's glare was not an issue. Taking a simplistic standpoint of reducing the starlight to be the same intensity as an orbiting exoplanet (that has all the properties of Earth) only 60 dB of contrast need be overcome at a wavelength of 10 µm. At 4 µm this increases to 80 dB and with current technology working in the visible (and 1550 nm) wavelengths a 100 dB null over the star is required. For a young Jupiter sized exoplanet (with a temperature of approximately 1000 K) the reduction requirements are much less: only a 40 dB null is required at 4 µm for the exoplanet and star (with the same brightness as our sun) to have equal intensities. If, however, the camera system is limited only by shot noise then a 40 dB reduction in starlight is all that is needed for an Earth-like exoplanet, at a wavelength of 10 µm, to be detected - using a space telescope.

For a photonic chip, the choice of material is restricted by the choice of wavelength. Chalcogenide glass (ChG) is transparent up to a wavelength of 15 µm (or even 20 µm for telluride glasses) and hence suitable for both mid- and far-infrared light. This work focused on wavelengths in the astronomical L'-band (around 4 µm) which takes advantage of the absorption gap in the atmosphere (specifically the CO_2 in the atmosphere). Due to the wide transparency of ChG this work can be redesigned to one able to operate at 10 µm where exoplanets are easier to image and where absorption features of O_3 in exoplanet atmospheres can be detected. This would utilise the real strength of ChG: which is the

depth of work in this field that dates as far back as the 1870s [152], resulting in a vast selection of materials to choose from and thus the ability to tailor a required refractive index, and index difference when using a cladding, to any project. To start working at 10 µm, however, was not elected here due to the technological leap it would require and as such requires this work as a "stepping stone".

The two selected ChGs for this work were $Ge_{11.5}As_{24}Se_{64.5}$ and $Ge_{11.5}As_{24}S_{64.5}$ as the core and cladding materials respectively. These were chosen because they have similar properties, have the same refractive index whether as a thin film or as a bulk glass, and previous work at the Australian National University showed that they create low loss rib waveguides [156, 165]. The fully etched waveguide loss measured in this work was higher than expected, with the previous success with rib waveguides not replicated. The minimum loss was measured as 1 dB/cm but on average the loss was much higher. Progress was made in determining the origin of the high loss so that future work can generate low loss waveguides: water contamination was discussed as a possibility for the high loss. The source of the contamination is not known but as was discussed in Chap. 5 the contamination is likely in the cladding material. Regardless, with the current loss, and the calculated bend radius (of approximately 200 µm), it was shown that a compact circuit is indeed possible with this material. The bend radius is a key factor in determining the entire length of a photonic chip due to the offset requirements of the input and output waveguides of the chip to prevent scattered light from the input overlapping with the output waveguide.

The chosen photonic device to be the 2-beam combiner for this work was an MMI due to the basic MMI design being robust to typical fabrication errors in terms of its transmission (as expected from previous publications [263]). This work initially focused on a detailed analysis of how the splitting ratio (calculated as imbalance) is affected by the MMI design and the errors in the fabrication. This parameter space is unique, to the author's best knowledge, with the main variable of concern was the MMI width (W) and by extension a full, wafer wide, outline deviation - including a simultaneous change in W, MMI length and taper width (W_a). The most significant find in this work was that a change in W_a increased the even splitting ratio to an almost constant value over a broad bandwidth with a small reduction in its transmission. For the other variables it was found that even with large (in terms of realistic fabrication constraints) variations, they would not affect the optimised extinction depth significantly.

The ratio of $W/W_a = 0.3$ was already established to have the highest transmission for any 2x2 MMI [196] but as a result the imbalance of the MMI is zero at a single wavelength. With the goal to extend the bandwidth at which the imbalance is zero (and as a result the extinction bandwidth when used as a beam combiner) with as little cost to transmission as possible, the MMI was fabricated with a $W_a = 12$ µm instead as simulations pointed to this MMI have the widest extinction bandwidth at a 40 dB null. Originally a $W_a = 8$ µm was tested in the initial set of fabricated MMIs for purposes explained below, but $W_a = 12$ µm has a higher transmission and longer extinction bandwidth and thus is the optimal MMI

for astronomy.

In the initial experiments, MMIs with $W_a = 13.5$ and 8 µm, and lengths of 200 µm, were used. The optimal transmission MMI was fabricated to test the simulations regarding its fabrication tolerances and the $W_a = 8$ µm MMI was fabricated if the lithography could not resolve the gap between the two 13.5 µm wide tapers in the optimal transmission MMI. From these initial results it was shown that fabricating the MMI with $W_a = 8$ µm was fortunate as the 13.5 µm MMI did not have the expected transmission nor the exact imbalance as predicted whereas the $W_a = 8$ µm did (in both respects). The error in the fabrication appears to come from the lithography step as the photomask shows a clear gap between the tapers whereas the etched MMI has the inner edges of the tapers connecting.

The taper length is one aspect of the MMI that has yet to have a full investigation and the subject of future analysis. Basic simulations show that there is a relationship between the taper length and an increased extinction bandwidth, without sacrificing transmission. The mechanism for how a change in taper length achieves this has not been studied (to the author's best knowledge). Further work, and experimental verification, is recommended once the gap between the tapers (for an MMI with $W_a = 13.5$ µm) is resolved, otherwise the loss in transmission will not be representative of what the MMI can achieve, as was shown in Chap. 6.

The expected null, with the expected broad bandwidth, of an MMI was not confirmed experimentally in this work. Broadly speaking the MMI imbalance measurements fit the simulations, especially over the wavelength range from 3.8 to 4.2 µm, but not to the extent where a deep null would be expected. One reason for this discrepancy is coherent scattered light from either the MMI or the input waveguide interfering with the light in the output waveguides. From experiments, it was found that the main source of scattered light comes from the MMI. This was inferred from an increase in the scattered light at wavelengths away from the optimum transmission design such that the wavefront in the MMI is either pre- or post-formation into the two localised intensity maxima coupled into the output waveguides. This scattered light is coherent with the light contained in the waveguides and as such provides a large uncertainty in the measurement.

To reduce the scattered light, carbon was deposited indiscriminately over the entire design, without covering the input and output waveguide faces. This led to −25 dB of scattered light being reduced down to −35 dB as compared to the flux intensity output from the MMI. A second method used an offset of the input and output waveguides, and a 90° MMI rotation, rather than using a cladding of any kind, so that any scattered light would never overlap with the light inside the output waveguides. This offset with a rotation approach provided a reduction of the scattered light to −40 dB. A 40 dB null over a broad bandwidth, however, was still not measured with either of these solutions in scattered light reduction.

The reason for not being able to measure a broad bandwidth null (of at least 40 dB) may be due to the methodology used in this work. To measure the null two MMIs were combined in series to form an MZI - the idea being that the first would split the light

equally and the second would combine it to form the null. Simulations of this showed it to be possible but the loss and phase change of the light was not accounted for. Through simulation, it was found that even a 1 nm width difference between the two interconnecting waveguides would provide a significant change in the optical path length difference (ΔOPL) leading to a severe change in wavelength response. With a typical critical dimension tolerance of a mask writer being 10 nm, it was decided that active correction on-chip was required to reduce the ΔOPL to zero. Future work may choose to split the laser light before it enters the chip, to replicate the light from two telescopes sent into the chip, however, a large phase control will still be required to rectify the phase difference in the input waveguides. In addition, phase control is necessary for more complex devices, like the Kernel-nulling interferometer [85]. Hence, an active phase controller is pertinent to future work.

To actively control the phase a thin layer (40 nm) of chromium was deposited over the waveguides to act as a heater when a current was passed through it. These heaters were successful in many regards: they had no lasting deleterious effects on the waveguide when heated, they provided a reversible change in the ΔOPL but where they failed was in reducing the ΔOPL to zero. Had the deposition taken place on a flat surface this may have worked without fault but as the surface above the waveguide was not flat (due to the over-clading not only creating an inhomogeneous surface but resulting in a "bump" over the waveguide) the thin layer of chromium on the sidewalls caused a short in the heater and prevented a zero ΔOPL.

A redesign of the chromium mask will attempt to rectify this and allow for active phase control to the point of providing a Mach-Zehnder interferometer that has a broadband null, the depth of which is theoretically 40 dB. What may still be an issue is the difference in intensity of the light in the interconnecting arms. Any difference in intensity in the interconnecting arms will reduce the null depth. If the waveguide losses become minimal (< 0.3 dB/cm) then this may not be an issue but future work may choose to address this regardless as an adaptive intensity control, on-chip, may be required in the final version.

For a full interferometry system to be redesigned to reach the 10 µm wavelength a change in a material may be required. The Sulphur glass cladding is limited to 11 µm and so should be compatible (with the Selenide core glass much further) but the index difference of 0.33 for this work may limit the waveguides to a width too small to be fabricated at the Australian National University.

Following the results of this work, waveguide loss is the most pressing issue with the current 2-D technology. The competing technologies posting losses of 0.25 dB/cm [154] for a single-mode waveguide is similar to that of the previous 2-D technology work [156] and should be achievable with the current technology once the water is removed from the cladding material. The advantage of a two-dimensional geometry: small bend radii and small components, attempt to overcome the high losses by making small circuits, but for complicated circuits, this may not be possible. Once the high losses are overcome the improvements on the 2-D technology shown in this thesis: the adaptive phase con-

trollers and the broad bandwidth MMIs, will make the 2-D platform competitive for future astronomical instruments.

The multimode interference coupler is the most robust tool in the photonics arsenal. As shown in this work it can be made to split light evenly for 400 nm with a predicted null depth of 40 dB over the same range. Utilising rotation and offsetting input and output waveguides scattered light won't limit the MMI as a nulling interferometer and placing heaters over input ports will control the phase and correct for phase errors due to waveguide fabrication errors. Integrating this onto a telescope is the next greatest challenge in this field and then adapting it into a space mission the one after that. This will require matching the input and output waveguides to the chip single-mode width, testing for temperature dependences, and increasing the number of input ports to support more telescopes. What this work has shown, is that the MMI is reliable, and future works will benefit from this reliability.

his itur ad planetarum extra

Bibliography

[1] Baird, J. L., "Apparatus for transmitting views or images to a distance." https://patents.google.com/patent/US1699270 (1929). Accessed: 2019-06-26.

[2] Hansell, C. W., "Picture transmission." https://patents.google.com/patent/US1751584A/en?inventor=Clarence+W+Hansell&before=priority:19310101&after=priority:19190101 (1930). Accessed: 2019-06-26.

[3] Angel, J. R. P., Adams, M. T., Boroson, T. A., and Moore, R. L., "A very large optical telescope array linked with fused silica fibers," *The Astrophysical Journal* **218**, 776–782 (1977).

[4] Gilbert, J., Muller, R., Heijmans, J., Bennet, A., Tims, J., Goodwin, M., Saunders, W., Brzeski, J., Waller, L., and Miziarski, S., "Starbugs: all-singing, all-dancing fibre positioning robots," *Modern Technologies in Space- and Ground-based Telescopes and Instrumentation II* **8450**(September 2012), 84501A (2012).

[5] Lacour, S., Nowak, M., Wang, J., Pfuhl, O., Eisenhauer, F., Abuter, R., Amorim, A., Anugu, N., Benisty, M., Berger, J. P., Beust, H., Blind, N., Bonnefoy, M., Bonnet, H., Bourget, P., Brandner, W., Buron, A., Collin, C., Charnay, B., Chapron, F., Clénet, Y., Coudé du Foresto, V., de Zeeuw, P. T., Deen, C., Dembet, R., Dexter, J., Duvert, G., Eckart, A., Förster Schreiber, N. M., Fédou, P., Garcia, P., Garcia Lopez, R., Gao, F., Gendron, E., Genzel, R., Gillessen, S., Gordo, P., Greenbaum, A., Habibi, M., Haubois, X., Haußmann, F., Henning, T., Hippler, S., Horrobin, M., Hubert, Z., Jimenez Rosales, A., Jocou, L., Kendrew, S., Kervella, P., Kolb, J., Lagrange, A.-M., Lapeyrère, V., Le Bouquin, J.-B., Léna, P., Lippa, M., Lenzen, R., Maire, A.-L., Mollière, P., Ott, T., Paumard, T., Perraut, K., Perrin, G., Pueyo, L., Rabien, S., Ramírez, A., Rau, C., Rodríguez-Coira, G., Rousset, G., Sanchez-Bermudez, J., Scheithauer, S., Schuhler, N., Straub, O., Straubmeier, C., Sturm, E., Tacconi, L. J., Vincent, F., van Dishoeck, E. F., von Fellenberg, S., Wank, I., Waisberg, I., Widmann, F., Wieprecht, E., Wiest, M., Wiezorrek, E., Woillez, J., Yazici, S., Ziegler, D., and Zins, G., "First direct detection of an exoplanet by optical interferometry," *Astronomy & Astrophysics* **623**, L11 (2019).

[6] International Astronomy Union, "Resolution 5a." https://www.iau.org/news/pressreleases/detail/iau0603/ (2006). Accessed: 2019-06-26.

[7] Nobel Media AB 2019, "Press release: The nobel prize in physics 2019." https://www.nobelprize.org/prizes/physics/2019/press-release/ (2019). Accessed: 2019-10-18.

[8] Mayor, M. and Queloz, D., "A Jupiter-mass companion to as solar-type star," *Nature* **378**, 783–785 (1995).

[9] Perryman, M., "Resource Letter Exo-1 : Exoplanets," *American Journal of Physics* **82**(6), 552–563 (2014).

[10] Latham, D. W., Stefanik, R. P., Mazeh, T., Mayor, M., and Burki, G., "The unseen companion of HD114762 - A probable brown dwarf," *Nature* **339**, 38–40 (1989).

[11] Wolszczan, A. and Frail, D. A., "A planetary system around the millisecond pulsar PSR1257 + 12," *Nature* **355**(6356), 145–147 (1992).

[12] Charbonneau, D., Brown, T. M., Latham, D. W., and Mayor, M., "Detection of Planetary Transits Across a Sun-like Star," *The Astrophysical Journal* **529**(1), L45–L48 (2000).

[13] Han, E., Wang, S. X., Wright, J. T., Feng, Y. K., Zhao, M., Fakhouri, O., Brown, J. I., and Hancock, C., "Exoplanet Orbit Database. II. Updates to Exoplanets.org," *Publications of the Astronomical Society of the Pacific* **126**(943), 827–837 (2014).

[14] Bond, I. A., Udalski, A., Jaroszyn, M., Rattenbury, N. J., Paczyn, B., Soszyn, I., Eguchi, S., Furuta, Y., Hearnshaw, J. B., Kamiya, K., Kilmartin, P. M., Kurata, Y., Masuda, K., Sumi, T., Tristram, P. J., Yanagisawa, T., Yock, P. C. M., Collaborations, T. M., and OGLE, "OGLE 2003-BLG-235/MOA 2003-BLG-53:A Planetary Microlensing Event," *The Astronomical Journal* **606**, L155–L158 (2004).

[15] Suzuki, D., Bennett, D. P., Udalski, A., Bond, I. A., Sumi, T., Han, C., Kim, H.-i., Abe, F., Asakura, Y., Barry, R. K., Bhattacharya, A., Donachie, M., Freeman, M., Fukui, A., Hirao, Y., Itow, Y., Koshimoto, N., Li, M. C. A., Ling, C. H., Masuda, K., Matsubara, Y., Muraki, Y., Nagakane, M., Onishi, K., Oyokawa, H., Ranc, C., Rattenbury, N. J., Saito, T., Sharan, A., Sullivan, D. J., Tristram, P. J., Yonehara, A., Poleski, R., Mróz, P., Skowron, J., Szymański, M. K., Soszyński, I., Kozłowski, S., Pietrukowicz, P., Wyrzykowski, Ł., and Ulaczyk, K., "A Likely Detection of a Two-planet System in a Low-magnification Microlensing Event," *The Astronomical Journal* **155**(6), 263 (2018).

[16] Han, C., Udalski, A., Choi, J. Y., Yee, J. C., Gould, A., Christie, G., Tan, T. G., Szymański, M. K., Kubiak, M., Soszyński, I., Pietrzyński, G., Poleski, R., Ulaczyk, K., Pietrukowicz, P., Kozłowski, S., Skowron, J., Wyrzykowski, Almeida, L. A., Batista, V., Depoy, D. L., Dong, S., Drummond, J., Gaudi, B. S., Hwang, K. H., Jablonski, F., Jung, Y. K., Lee, C. U., Koo, J. R., McCormick, J., Monard, L. A., Natusch, T., Ngan, H., Park, H., Pogge, R. W., Porritt, I., and Shin, I. G., "The second multiple-planet system discovered by microlensing: Ogle-2012-BLG-0026Lb, c - A pair of jovian planets beyond the snow line," *Astrophysical Journal Letters* **762**(2), 6–11 (2013).

[17] Chauvin, G., Lagrange, A.-M., Dumas, C., Zuckerman, B., Mouillet, D., Song, I., Beuzit, J.-L., and Lowrance, P., "Astronomy & Astrophysics A giant planet candidate near a young brown dwarf Direct VLT/NACO observations using IR wavefront sensing," *a&a* **425**, 29–32 (2004).

[18] Stevens, D. J. and Gaudi, B. S., "A Posteriori Transit Probabilities," *Publications of the Astronomical Society of the Pacific* **125**(930), 933–950 (2013).

[19] Vogt, S. S., Wittenmyer, R. A., Butler, R. P., O'Toole, S., Henry, G. W., Rivera, E. J., Meschiari, S., Laughlin, G., Tinney, C. G., Jones, H. R. A., Bailey, J., Carter, B. D., and Batygin, K., "A SUPER-EARTH AND TWO NEPTUNES ORBITING THE NEARBY SUN-LIKE STAR 61 VIRGINIS," *The Astrophysical Journal* **708**(2), 1366–1375 (2010).

[20] Endl, M., Cochran, W. D., Hatzes, A. P., and Robert, A., "News From The γ Cephei Planetary System," in [*AIP Conference Proceedings 1331*], 88–94 (2011).

[21] Campbell, B., Walker, G. A. H., and Yang, S., "A search for substellar companions to solar-type stars," *The Astronomical Journal* **331**, 902–921 (1988).

[22] Cochran, W. D., Hatzes, A. P., and Hancock, T. J., "Constraints on the companion object to HD 114762," *The Astrophysical Journal* **380**, L35 (1991).

[23] Mordasini, C., Alibert, Y., Benz, W., and Naef, D., "Extrasolar planet population synthesis," *Astronomy & Astrophysics* **501**(3), 1161–1184 (2009).

[24] Pepe, F., Mayor, M., Queloz, D., Benz, W., Bonfils, X., Bouchy, F., Lo Curto, G., Lovis, C., Mégevand, D., Moutou, C., Naef, D., Rupprecht, G., Santos, N. C., Sivan, J.-P., Sosnowska, D., and Udry, S., "The HARPS search for southern extra-solar planets," *Astronomy & Astrophysics* **423**(1), 385–389 (2004).

[25] Johnson, J. A., Butler, R. P., Marcy, G. W., Fischer, D. A., Vogt, S. S., Wright, J. T., and Peek, K. M. G., "A New Planet around an M Dwarf: Revealing a Correlation between Exoplanets and Stellar Mass," *The Astrophysical Journal* **670**(1), 833–840 (2007).

[26] Gould, A. and Loeb, A., "Discovering Planetary Systems Through Gravitational Microlenses," *The Astrophysical Journal* **396**, 104–114 (1992).

[27] Einstein, A., "Lens-like action of a star by the deviation of light in the gravitational field," *Science* **84**(2188), 506–507 (1936).

[28] Chwolson, V. O., "Über eine mögliche Form fiktiver Doppelsterne," *Astronomische Nachrichten* **221**(20), 329–330 (1924).

[29] Einstein, A., "Antwort auf eine Bemerkung von W. Anderson," *Astronomische Nachrichten* **221**(20), 329–330 (1924).

[30] Mao, S. and Paczynski, B., "Gravitational microlensing by double stars and planetary systems," *The Astrophysical Journal* **374**(June), L37–L40 (1991).

[31] Perryman, M. A. C., de Boer, K. S., Gilmore, G., Høg, E., Lattanzi, M. G., Lindegren, L., Luri, X., Mignard, F., Pace, O., and de Zeeuw, P. T., "GAIA: Composition, formation and evolution of the Galaxy," *Astronomy & Astrophysics* **369**, 339–363 (apr 2001).

[32] Bell Burnell, S. J., "Petit four*," *Annals of the New York Academy of Sciences* **302**(1), 685–689 (1977).

[33] Hewish, A., Bell, S. J., Pilkington, J. D. H., Scott, P. F., and Collins, R. A., "Observation of a Rapidly Pulsating Radio Source," *Nature* **217**(5130), 709–713 (1968).

[34] Wolszczan, A., "Confirmation of Earth-Mass Planets Orbiting the Millisecond Pulsar PSR B1257 + 12," *Science* **264**(5158), 538–542 (1994).

[35] Guillemot, L., Octau, F., Cognard, I., Desvignes, G., Freire, P. C. C., Smith, D. A., Theureau, G., and Burnett, T. H., "Timing of psr j2055+3829, an eclipsing black widow pulsar discovered with the nançay radio telescope," *A&A* **629**, A92 (2019).

[36] Struve, O., "Proposal for a project of high-precision stellar radial velocity work," *The Observatory* **72**, 199–200 (1952).

[37] Konacki, M., Torres, G., Jha, S., and Sasselov, D. D., "An extrasolar planet that transits the disk of its parent star.," *Nature* **421**(January), 507–509 (2003).

[38] Udalski, A., Zebruń, K., Szymański, M., Kubiak, M., Soszyński, I., Szewczyk, O., Wyrzykowski, and Pietrzyński, G., "The optical gravitational lensing experiment. Search for planetary and low-luminosity object transits in the galactic disk. Results of 2001 campaign - Supplement," *Acta Astronomica* **52**(2), 115–128 (2002).

[39] Baglin, A., Auvergne, M., Boisnard, L., Lam-Trong, T., Barge, P., Catala, C., Deleuil, M., Michel, E., and Weiss, W., "CoRoT: a high precision photometer for stellar ecolution and exoplanet finding," in [*36th COSPAR Scientific Assembly*], (2006).

[40] Dunham, E. W., Geary, J. C., Philbrick, R. H., Stewart, C. K., and Koch, D. G., "The Kepler mission's focal plane," in [*Proc. SPIE*], Blades, J. C. and Siegmund, O. H. W., eds., (4854), 558 (2003).

[41] Ricker, G. R., Winn, J. N., Vanderspek, R., Latham, D. W., Bakos, G. Á., Bean, J. L., Berta-Thompson, Z. K., Brown, T. M., Buchhave, L., Butler, N. R., Butler, R. P., Chaplin, W. J., Charbonneau, D., Christensen-Dalsgaard, J., Clampin, M., Deming, D., Doty, J., De Lee, N., Dressing, C., Dunham, E. W., Endl, M., Fressin, F., Ge, J., Henning, T., Holman, M. J., Howard, A. W., Ida, S., Jenkins, J. M., Jernigan, G., Johnson, J. A., Kaltenegger, L., Kawai, N., Kjeldsen, H., Laughlin, G., Levine, A. M., Lin, D., Lissauer, J. J., MacQueen, P., Marcy, G., McCullough, P. R., Morton, T. D., Narita, N., Paegert, M., Palle, E., Pepe, F., Pepper, J., Quirrenbach, A., Rinehart, S. A., Sasselov, D., Sato, B., Seager, S., Sozzetti, A., Stassun, K. G., Sullivan, P., Szentgyorgyi, A., Torres, G., Udry, S., and Villasenor, J., "Transiting Exoplanet Survey Satellite," *Journal of Astronomical Telescopes, Instruments, and Systems* **1**(1), 014003 (2014).

[42] Huang, C. X., Burt, J., Vanderburg, A., Günther, M. N., Shporer, A., Dittmann, J. A., Winn, J. N., Wittenmyer, R., Sha, L., Kane, S. R., Ricker, G. R., Vanderspek, R. K., Latham, D. W., Seager, S., Jenkins, J. M., Caldwell, D. A., Collins, K. A., Guerrero, N., Smith, J. C., Quinn, S. N., Udry, S., Pepe, F., Bouchy, F., Ségransan, D., Lovis, C., Ehrenreich, D., Marmier, M., Mayor, M., Wohler, B., Haworth, K., Morgan, E. H., Fausnaugh, M., Ciardi, D. R., Christiansen, J., Charbonneau, D., Dragomir, D., Deming, D., Glidden, A., Levine, A. M., McCullough, P. R., Yu, L., Narita, N., Nguyen, T., Morton, T., Pepper, J., Pál, A., Rodriguez, J. E., and Team, t. T., "TESS Discovery of a Transiting Super-Earth in the $$ Mensae System," *The Astrophysical Journal Letters* **868**(2), L39 (2018).

[43] Hartung, M., Blanc, a., Fusco, T., Lacombe, F., Mugnier, L. M., Rousset, G., and Lenzen, R., "Calibration of NAOS and CONICA static aberrations," *Astronomy and Astrophysics* **399**, 385–394 (2003).

[44] Minowa, Y., Hayano, Y., Oya, S., Watanabe, M., Hattori, M., Guyon, O., Egner, S., Saito, Y., Ito, M., Takami, H., Garrel, V., Colley, S., Golota, T., and Iye, M., "Performance of Subaru adaptive optics system AO188," in [*Adaptive Optics Systems II*], Ellerbroek, B. L., Hart, M., Hubin, N., and Wizinowich, P. L., eds., **7736**, 77363N (2010).

[45] Oya, S., Bouvier, A., Guyon, O., Watanabe, M., Hayano, Y., Takami, H., Iye, M., Hattori, M., Saito, Y., Itoh, M., Colley, S., Dinkins, M., Eldred, M., and Golota, T., "Performance of the deformable mirror for Subaru LGSAO," in [*Advances in Adaptive Optics II*], (62724), 62724S 1–8 (2006).

[46] Jovanovic, N., Martinache, F., Guyon, O., Clergeon, C., Singh, G., Kudo, T., Garrel, V., Newman, K., Doughty, D., Lozi, J., Males, J., Minowa, Y., Hayano, Y., Takato, N., Morino, J., Kuhn, J., Serabyn, E., Norris, B., Tuthill, P., Schworer, G., Stewart, P., Close, L., Huby, E., Perrin, G., Lacour, S., Gauchet, L., Vievard, S., Murakami, N., Oshiyama, F., Baba, N., Matsuo, T., Nishikawa, J., Tamura, M., Lai, O., Marchis, F., Duchene, G., Kotani, T., and Woillez, J., "The Subaru Coronagraphic Extreme Adaptive Optics System: Enabling High-Contrast Imaging on Solar-System Scales," *Publications of the Astronomical Society of the Pacific* **127**(955), 890–910 (2015).

[47] Marois, C., Macintosh, B., Barman, T., Zuckerman, B., Song, I., Patience, J., Lafrenière, D., and Doyon, R., "Orbiting the Star HR 8799," *Science* **322**(November), 1348–1352 (2008).

[48] Marois, C., Lafreniere, D., Doyon, R., Macintosh, B., and Nadeau, D., "Angular Differential Imaging: A Powerful HighContrast Imaging Technique," *The Astrophysical Journal* **641**(1), 556–564 (2006).

[49] Lyot, B., "The study of the solar corona and prominences without eclipses (george darwin lecture, 1939)," **99**, 580 (June 1939).

[50] Guyon, O., Hinz, P. M., Cady, E., Belikov, R., and Martinache, F., "HIGH PERFORMANCE LYOT AND PIAA CORONAGRAPHY FOR ARBITRARILY SHAPED TELESCOPE APERTURES," *The Astrophysical Journal* **780**(2), 171 (2013).

[51] Guyon, O., Martinache, F., Belikov, R., and Soummer, R., "High Performance Piaa Coronagraphy With Complex Amplitude Focal Plane Masks," *The Astrophysical Journal Supplement Series* **190**(2), 220–232 (2010).

[52] Kasdin, N. J., Vanderbei, R. J., Spergel, D. N., and Littman, M. G., "Extrasolar Planet Finding via Optimal ApodizedPupil and ShapedPupil Coronagraphs," *The Astrophysical Journal* **582**(2), 1147–1161 (2003).

[53] Guyon, O., Pluzhnik, E. A., Kuchner, M. J., Collins, B., and Ridgway, S. T., "Theoretical Limits on Extrasolar Terrestrial Planet Detection with Coronagraphs," *The Astrophysical Journal Supplement Series* **167**(1), 81–99 (2006).

[54] Charpinet, S., Fontaine, G., Brassard, P., Green, E. M., Van Grootel, V., Randall, S. K., Silvotti, R., Baran, A. S., Østensen, R. H., Kawaler, S. D., and Telting, J. H., "A compact system of small planets around a former red-giant star," *Nature* **480**(7378), 496–499 (2011).

[55] Kalas, P., Graham, J. R., Chiang, E., Fitzgerald, M. P., Clampin, M., Kite, E. S., Stapelfeldt, K., Marois, C., and Krist, J., "Planet 25 Light-Years from Earth," *Science* **322**(November), 1345–1347 (2008).

[56] a. M. Lagrange, Gratadour, D., Chauvin, G., Fusco, T., Ehrenreich, D., Mouillet, D., Rousset, G., Rouan, D., Allard, F., Gendron, É., Charton, J., Mugnier, L., Rabou, P., Montri, J., and Lacombe, F., "A probable giant planet imaged in the $\{\beta\}$ Pictoris disk. VLT/NaCo deep L'-band imaging," *Astronomy and Astrophysics* **493**, L21–L25 (2009).

[57] Espaillat, C., Muzerolle, J., Najita, J., Andrews, S., Zhu, Z., Calvet, N., Kraus, S., Hashimoto, J., Kraus, A., and D'Alessio, P., "An Observational Perspective of Transitional Disks," in [*Protostars and Planets VI*], 497, University of Arizona Press (2014).

[58] Keppler, M., Benisty, M., Müller, A., Henning, T., van Boekel, R., Cantalloube, F., Ginski, C., van Holstein, R. G., Maire, A.-L., Pohl, A., Samland, M., Avenhaus, H., Baudino, J.-L., Boccaletti, A., de Boer, J., Bonnefoy, M., Chauvin, G., Desidera, S., Langlois, M., Lazzoni, C., Marleau, G.-D., Mordasini, C., Pawellek, N., Stolker, T., Vigan, A., Zurlo, A., Birnstiel, T., Brandner, W., Feldt, M., Flock, M., Girard, J., Gratton, R., Hagelberg, J., Isella, A., Janson, M., Juhasz, A., Kemmer, J., Kral, Q., Lagrange, A.-M., Launhardt, R., Matter, A., Ménard, F., Milli, J., Mollière, P., Olofsson, J., Pérez, L., Pinilla, P., Pinte, C., Quanz, S. P., Schmidt, T., Udry, S., Wahhaj, Z., Williams, J. P., Buenzli, E., Cudel, M., Dominik, C., Galicher, R., Kasper, M., Lannier, J., Mesa, D., Mouillet, D., Peretti, S., Perrot, C., Salter, G., Sissa, E., Wildi, F., Abe, L., Antichi, J., Augereau, J.-C., Baruffolo, A., Baudoz, P., Bazzon, A., Beuzit, J.-L., Blanchard, P., Brems, S. S., Buey, T., De Caprio, V., Carbillet, M., Carle, M., Cascone, E., Cheetham, A., Claudi, R., Costille, A., Delboulbé, A., Dohlen, K., Fantinel, D., Feautrier, P., Fusco, T., Giro, E., Gluck, L., Gry, C., Hubin, N., Hugot, E., Jaquet, M., Le Mignant, D., Llored, M., Madec, F., Magnard, Y., Martinez, P., Maurel, D., Meyer, M., Möller-Nilsson, O., Moulin, T., Mugnier, L., Origné, A., Pavlov, A., Perret, D., Petit, C., Pragt, J., Puget, P., Rabou, P., Ramos, J., Rigal, F., Rochat, S., Roelfsema, R., Rousset, G., Roux, A., Salasnich, B., Sauvage, J.-F., Sevin, A., Soenke, C., Stadler, E., Suarez, M., Turatto, M., and Weber, L., "Discovery of a planetary-mass companion within the gap of the transition disk around PDS 70," *Astronomy & Astrophysics* **617**, A44 (2018).

[59] Michelson, A. A., "Measurement of Jupiter's satellites by interference," *Nature* **45**(1155), 160–161 (1891).

[60] Monnier, J. D., "Optical interferometry in astronomy," *Reports on Progress in Physics* **66**(5), 789–857 (2003).

[61] Tuthill, P. G., Monnier, J. D., Danchi, W. C., Wishnow, E. H., and Haniff, C. a., "Michelson Interferometry with the Keck I Telescope," *Publications of the Astronomical Society of the Pacific* **112**(770), 550–565 (2000).

[62] HANBURY BROWN, R. and TWISS, R. Q., "A Test of a New Type of Stellar Interferometer on Sirius," *Nature* **178**(4541), 1046–1048 (1956).

[63] HANBURY BROWN, R., "Stellar Interferometer at Narrabri Observatory," *Nature* **218**(5142), 637–641 (1968).

[64] Boyajian, T. S., McAlister, H. A., van Belle, G., Gies, D. R., ten Brummelaar, T. A., von Braun, K., Farrington, C., Goldfinger, P. J., O'Brien, D., Parks, J. R., Richardson, N. D., Ridgway, S., Schaefer, G., Sturmann, L., Sturmann, J., Touhami, Y., Turner, N. H., and White, R., "STELLAR DIAMETERS AND TEMPERATURES. I. MAIN-SEQUENCE A, F, AND G STARS," *The Astrophysical Journal* **746**(1), 101 (2012).

[65] Zhao, M., Gies, D., Monnier, J. D., Thureau, N., Pedretti, E., Baron, F., Merand, A., ten Brummelaar, T., McAlister, H., Ridgway, S. T., Turner, N., Sturmann, J., Sturmann, L., Farrington, C., and Goldfinger, P. J., "First Resolved Images of the Eclipsing and Interacting Binary β Lyrae," *The Astrophysical Journal* **684**(2), L95–L98 (2008).

[66] Bracewell, R. N., "Detecting nonsolar planets by spinning infrared interferometer," *Nature* **274**, 780–781 (1978).

[67] Traub, W. a. and Oppenheimer, B. R., "Direct Imaging of Exoplanets," in [*Exoplanets*], Seager, S., ed., 111–156, Univ. Arizona Press, Tucson (2010).

[68] Serabyn, E., Appleby, E., Bell, J., Booth, A., Chin, J., Colavita, M. M., Crawford, S., Creech-Eakman, M., Dahl, W., Fanson, J., Garcia, J., Gathright, J., Hovland, E., Hrynevych, M., Koresko, C., Ligon, R., Mennesson, B., Moore, J., Palmer, D., Panteleeva, T., Paine, C., Ragland, S., Reder, L., Saloga, T., Smythe, R., Tyau, C., Tsubota, K., Vasisht, G., Wetherell, E., Wizinowich, P., and Woillez, J., "The Keck Interferometer Nuller (KIN): configuration, measurement approach, and first results," in [*Techniques and Instrumentation for Detection of Exoplanets II. Edited by Coulter, Daniel R. Proceedings of the SPIE, Volume 5905, pp. 272-283 (2005).*], Coulter, D. R., ed., **5905**, 59050T (2005).

[69] Serabyn, E., Mennesson, B., Colavita, M. M., Koresko, C., and Kuchner, M. J., "THE KECK INTERFEROMETER NULLER," *The Astrophysical Journal* **748**(1), 55 (2012).

[70] Defrère, D., Hinz, P., Mennesson, B., Millan-Gabet, R., Skemer, A., Bailey, V., and Rodigas, T., "Searching for Faint Exozodiacal Disks: Keck Results and LBTI Status," *Proceedings of the International Astronomical Union* **8**(S299), 332–333 (2013).

[71] Danchi, W., Bailey, V., Bryden, G., Defrère, D., Ertel, S., Haniff, C., Hinz, P., Kennedy, G., Mennesson, B., Millan-Gabet, R., Rieke, G., Roberge, A., Serabyn, E., Skemer, A., Stapelfeldt, K., Weinberger, A., Wyatt, M., and Vaz, A., "Enabling the direct detection of earth-sized exoplanets with the LBTI HOSTS project: a progress report," in [*Optical and Infrared Interferometry and Imaging V*], Malbet, F., Creech-Eakman, M. J., and Tuthill, P. G., eds., **9907**, 990713 (2016).

[72] Mennesson, B., Absil, O., Lebreton, J., Augereau, J. C., Serabyn, E., Colavita, M. M., Millan-Gabet, R., Liu, W., Hinz, P., and Thébault, P., "An interferometric study of the fomalhaut inner debris disk. II. Keck nuller mid-infrared observations," *Astrophysical Journal* **763**(2) (2013).

[73] Mennesson, B., Millan-Gabet, R., Serabyn, E., Colavita, M. M., Absil, O., Bryden, G., Wyatt, M., Danchi, W., Defrère, D., Doré, O., Hinz, P., Kuchner, M., Ragland, S., Scott, N., Stapelfeldt, K., Traub, W., and Woillez, J., "CONSTRAINING THE EXOZODIACAL LUMINOSITY FUNCTION OF MAIN-SEQUENCE STARS: COMPLETE RESULTS FROM THE KECK NULLER MID-INFRARED SURVEYS," *The Astrophysical Journal* **797**(2), 119 (2014).

[74] Defrère, D., Hinz, P. M., Skemer, A. J., Kennedy, G. M., Bailey, V. P., Hoffmann, W. F., Mennesson, B., Millan-Gabet, R., Danchi, W. C., Absil, O., Arbo, P., Beichman, C., Brusa, G., Bryden, G., Downey, E. C., Durney, O., Esposito, S., Gaspar, A., Grenz, P., Haniff, C., Hill, J. M., Lebreton, J., Leisenring, J. M., Males, J. R., Marion, L., McMahon, T. J., Montoya, M., Morzinski, K. M., Pinna, E., Puglisi, A., Rieke, G., Roberge, A., Serabyn, E., Sosa, R., Stapeldfeldt, K., Su, K., Vaitheeswaran, V., Vaz, A., Weinberger, A. J., and Wyatt, M. C., "FIRST-LIGHT LBT NULLING INTERFEROMETRIC OBSERVATIONS: WARM EXOZODIACAL DUST RESOLVED WITHIN A FEW AU OF η Crv," *The Astrophysical Journal* **799**(1), 42 (2015).

[75] Gabor, P., *A study of the performance of a nulling interferometer testbed preparatory to the Darwin mission*, PhD thesis, Université Paris Sud, Paris XI (12 2009).

[76] Penny, A. J., Leger, A. M., Mariotti, J.-M., Schalinski, C., Eiroa, C., Laurance, R. J., and Fridlund, C. V. M., "Darwin interferometer," in [*Proc. SPIE*], Reasenberg, R. D., ed., **3350**, 1–6 (1998).

[77] Beichman, C. A., Woolf, N. J., and Lindensmith, C. A., [*The Terrestrial Planet Finder (TPF) : a NASA Origins Program to search for habitable planets*], Jet Propulsion Laboratory, California Institute of Technology, Washington, D.C. (1999).

[78] Jet Propulsion Laboratory, "Tpf-i swg report." `https://exoplanets.nasa.gov/exep/resources/documents/` (2007). Accessed: 2019-01-13.

[79] ESA, "Darwin: Study ended, no further activities planned." `https://www.esa.int/Our_Activities/Space_Science/Darwin_overview` (2009). Accessed: 2019-01-13.

[80] Danchi, W. C. and Lopez, B., "The FourierKelvin Stellar Interferometer (FKSI)A practical infrared space interferometer on the path to the discovery and characterization of Earth-like planets around nearby stars," *Comptes Rendus Physique* **8**, 396–407 (apr 2007).

[81] Duigou, J. M. L., Ollivier, M., Lger, A., Cassaing, F., Sorrente, B., Fleury, B., Rousset, G., Absil, O., Mourard, D., Rabbia, Y., Escarrat, L., Malbet, F., Rouan, D., Cldassou, R., Delpech, M., Duchon, P., Meyssignac, B., Guidotti, P.-Y., and Gorius, N., "Pegase: a space-based nulling interferometer," in [*Space Telescopes and Instrumentation I: Optical, Infrared, and Millimeter*], Mather, J. C., MacEwen, H. A., and de Graauw, M. W. M., eds., **6265**, 495 – 508, International Society for Optics and Photonics, SPIE (2006).

[82] Kammerer, J. and Quanz, S. P., "Simulating the Exoplanet Yield of a Space-based MIR Interferometer Based on Kepler Statistics," *Astronomical & Astrophysical* **609**(A4), 1–14 (2018).

[83] Angel, J. R. P. and Woolf, N. J., "An Imaging Nulling Interferometer to Study Extrasolar Planets," *The Astrophysical Journal* **475**(1), 373–379 (1997).

[84] "National aeronautics and space administration presidents fy 2007 budget request," (2007). Accessed: 2020-08-20.

[85] Martinache, F. and Ireland, M. J., "Kernel-nulling for a robust direct interferometric detection of extrasolar planets," *Astronomy & Astrophysics* **619**, A87 (2018).

[86] Quanz, S. P., Kammerer, J., Defrère, D., Absil, O., Glauser, A., and Kitzmann, D., "Exoplanet science with a space-based mid-infrared nulling interferometer," in [*Optical and Infrared Interferometry and Imaging VI*], Mérand, A., Creech-Eakman, M. J., and Tuthill, P. G., eds., **107011I**, 37, SPIE (jul 2018).

[87] "Nancy grace roman space telescope."

[88] SpaceX, "Falcon 9." `https://www.spacex.com/falcon9` (2019). Accessed: 2019-01-13.

[89] Reach, W. T., Morris, P., Boulanger, F., and Okumura, K., "The mid-infrared spectrum of the zodiacal and exozodiacal light," *Icarus* **164**(2), 384–403 (2003).

[90] Burrows, A., Sudarsky, D., and Hubeny, I., "Spectra and Diagnostics for the Direct Detection of WideSeparation Extrasolar Giant Planets," *The Astrophysical Journal* **609**(1), 407–416 (2004).

[91] Deming, D., Seager, S., Richardson, L. J., and Harrington, J., "Infrared radiation from an extrasolar planet," *Nature* **434**(7034), 740–743 (2005).

[92] Burrows, A., Marley, M., Hubbard, W. B., Lunine, J. I., Guillot, T., Saumon, D., Freedman, R., Sudarsky, D., and Sharp, C., "A Nongray Theory of Extrasolar Giant Planets and Brown Dwarfs," *The Astrophysical Journal* **491**(2), 856–875 (1997).

[93] Zhu, Z., "ACCRETING CIRCUMPLANETARY DISKS: OBSERVATIONAL SIGNATURES," *The Astrophysical Journal* **799**(1), 16 (2015).

[94] Madhusudhan, N., Burrows, A., and Currie, T., "MODEL ATMOSPHERES FOR MASSIVE GAS GIANTS WITH THICK CLOUDS: APPLICATION TO THE HR 8799 PLANETS AND PREDICTIONS FOR FUTURE DETECTIONS," *The Astrophysical Journal* **737**(1), 34 (2011).

[95] Hu, R., Ehlmann, B. L., and Seager, S., "THEORETICAL SPECTRA OF TERRESTRIAL EXOPLANET SURFACES," *The Astrophysical Journal* **752**(1), 7 (2012).

[96] Pollack, J. B., Hubickyj, O., Bodenheimer, P., Lissauer, J. J., Podolak, M., and Greenzweig, Y., "Formation of the Giant Planets by Concurrent Accretion of Solids and Gas," *Icarus* **124**(1), 62–85 (1996).

[97] Gaudi, B. S., Seager, S., and MallenOrnelas, G., "On the Period Distribution of Closein Extrasolar Giant Planets," *The Astrophysical Journal* **623**(1), 472–481 (2005).

[98] Mayor, M., Marmier, M., Lovis, C., Udry, S., Ségransan, D., Pepe, F., Benz, W., Bertaux, J. L., Bouchy, F., Dumusque, X., Curto, G. L., Mordasini, C., Queloz, D., and Santos, N. C., "The HARPS search for southern extra-solar planets XXXIV. Occurrence, mass distribution and orbital properties of super-Earths and Neptune-mass planets," *arXiv e-prints* , arXiv:1109.2497 (2011).

[99] Batygin, K., Bodenheimer, P. H., and Laughlin, G. P., "IN SITU FORMATION AND DYNAMICAL EVOLUTION OF HOT JUPITER SYSTEMS," *The Astrophysical Journal* **829**(2), 114 (2016).

[100] Bodenheimer, P., "Models of the in Situ Formation of Detected Extrasolar Giant Planets," *Icarus* **143**(1), 2–14 (2000).

[101] Boley, A. C., Contreras, A. P. G., and Gladman, B., "THE IN SITU FORMATION OF GIANT PLANETS AT SHORT ORBITAL PERIODS," *The Astrophysical Journal* **817**(2), L17 (2016).

[102] Papaloizou, J. C. B. and Terquem, C., "Planet formation and migration," *Reports on Progress in Physics* **69**(1), 119–180 (2006).

[103] Brunini, A. and Cionco, R. G., "The origin and nature of Neptune-like planets orbiting close to solar type stars," *Icarus* **177**(1), 264–268 (2005).

[104] Ward, W. R., "Protoplanet Migration by Nebula Tides," *Icarus* **126**(2), 261–281 (1997).

[105] Terquem, C. and Papaloizou, J. C. B., "Migration and the Formation of Systems of Hot SuperEarths and Neptunes," *The Astrophysical Journal* **654**(2), 1110–1120 (2007).

[106] Nelson, R. P. and Papaloizou, J. C. B., "Possible commensurabilities among pairs of extrasolar planets," *Monthly Notices of the Royal Astronomical Society* **333**(2), L26–L30 (2002).

[107] Lee, M. H. and Peale, S. J., "Dynamics and Origin of the 2 : 1 Orbital Resonances of the GJ 876 Planets," *The Astrophysical Journal* **567**(1), 596–609 (2002).

[108] Kley, W., Peitz, J., and Bryden, G., "Evolution of planetary systems in resonance," *Astronomy & Astrophysics* **414**(2), 735–747 (2004).

[109] Peale, S. J., "Orbital Resonances in the Solar System," *Annual Review of Astronomy and Astrophysics* **14**(1), 215–246 (1976).

[110] Chatterjee, S., Ford, E. B., Matsumura, S., and Rasio, F. A., "Dynamical Outcomes of PlanetPlanet Scattering," *The Astrophysical Journal* **686**(1), 580–602 (2008).

[111] Nagasawa, M., Ida, S., and Bessho, T., "Formation of Hot Planets by a Combination of Planet Scattering, Tidal Circularization, and the Kozai Mechanism," *The Astrophysical Journal* **678**(1), 498–508 (2008).

[112] Seager, S., "The future of spectroscopic life detection on exoplanets," *Proceedings of the National Academy of Sciences* **111**(35), 12634–12640 (2014).

[113] Gordon, I., Rothman, L., Hill, C., Kochanov, R., Tan, Y., Bernath, P., Birk, M., Boudon, V., Campargue, A., Chance, K., Drouin, B., Flaud, J.-M., Gamache, R., Hodges, J., Jacquemart, D., Perevalov, V., Perrin, A., Shine, K., Smith, M.-A., Tennyson, J., Toon, G., Tran, H., Tyuterev, V., Barbe, A., Császár, A., Devi, V., Furtenbacher, T., Harrison, J., Hartmann, J.-M., Jolly, A., Johnson, T., Karman, T., Kleiner, I., Kyuberis, A., Loos, J., Lyulin, O., Massie, S., Mikhailenko, S., Moazzen-Ahmadi, N., Müller, H., Naumenko, O., Nikitin, A., Polyansky, O., Rey, M., Rotger, M., Sharpe, S., Sung, K., Starikova, E., Tashkun, S., Auwera, J. V., Wagner, G., Wilzewski, J., Wcisło, P., Yu, S., and Zak, E., "The HITRAN2016 molecular spectroscopic database," *Journal of Quantitative Spectroscopy and Radiative Transfer* **203**(1), 3–69 (2017).

[114] Mills, F. Personal communication (2019-06-18).

[115] Kreidberg, L., Bean, J. L., Désert, J.-M., Line, M. R., Fortney, J. J., Madhusudhan, N., Stevenson, K. B., Showman, A. P., Charbonneau, D., McCullough, P. R., Seager, S., Burrows, A., Henry, G. W., Williamson, M., Kataria, T., and Homeier, D., "A PRECISE WATER ABUNDANCE MEASUREMENT FOR THE HOT JUPITER WASP-43b," *The Astrophysical Journal* **793**(2), L27 (2014).

[116] Stevenson, K. B., Harrington, J., Nymeyer, S., Madhusudhan, N., Seager, S., Bowman, W. C., Hardy, R. A., Deming, D., Rauscher, E., and Lust, N. B., "Possible thermochemical disequilibrium in the atmosphere of the exoplanet GJ 436b," *Nature* **464**(7292), 1161–1164 (2010).

[117] Werner, M., "The spitzer space telescope mission," *Advances in Space Research* **36**(6), 1048–1049 (2005).

[118] Hu, R., Seager, S., and Yung, Y. L., "HELIUM ATMOSPHERES ON WARM NEPTUNE- AND SUB-NEPTUNE-SIZED EXOPLANETS AND APPLICATIONS TO GJ 436b," *The Astrophysical Journal* **807**(1), 8 (2015).

[119] Madhusudhan, N. and Seager, S., "HIGH METALLICITY AND NON-EQUILIBRIUM CHEMISTRY IN THE DAYSIDE ATMOSPHERE OF HOT-NEPTUNE GJ 436b," *The Astrophysical Journal* **729**(1), 41 (2011).

[120] Line, M. R., Vasisht, G., Chen, P., Angerhausen, D., and Yung, Y. L., "THERMOCHEMICAL AND PHOTOCHEMICAL KINETICS IN COOLER HYDROGEN-DOMINATED EXTRASOLAR PLANETS: A METHANE-POOR GJ436b?," *The Astrophysical Journal* **738**(1), 32 (2011).

[121] Moses, J. I., Line, M. R., Visscher, C., Richardson, M. R., Nettelmann, N., Fortney, J. J., Barman, T. S., Stevenson, K. B., and Madhusudhan, N., "COMPOSITIONAL DIVERSITY IN THE ATMOSPHERES OF HOT NEPTUNES, WITH APPLICATION TO GJ 436b," *The Astrophysical Journal* **777**(1), 34 (2013).

[122] Agúndez, M., Venot, O., Selsis, F., and Iro, N., "The puzzling chemical composition of GJ 436B's atmosphere: Influence of tidal heating on the chemistry," *Astrophysical Journal* **781**(2) (2014).

[123] Morley, C. V., Knutson, H., Line, M., Fortney, J. J., Thorngren, D., Marley, M. S., Teal, D., and Lupu, R., "FORWARD AND INVERSE MODELING OF THE EMISSION AND TRANSMISSION SPECTRUM OF GJ 436B: INVESTIGATING METAL ENRICHMENT, TIDAL HEATING, AND CLOUDS," *The Astronomical Journal* **153**(2), 86 (2017).

[124] Van Grootel, V., Gillon, M., Valencia, D., Madhusudhan, N., Dragomir, D., Howe, A. R., Burrows, A. S., Demory, B.-O., Deming, D., Ehrenreich, D., Lovis, C., Mayor, M., Pepe, F., Queloz, D., Scuflaire, R., Seager, S., Segransan, D., and Udry, S., "TRANSIT CONFIRMATION AND IMPROVED STELLAR AND PLANET PARAMETERS FOR THE SUPER-EARTH HD 97658 b AND ITS HOST STAR," *The Astrophysical Journal* **786**(1), 2 (2014).

[125] Besse, P. A., Bachmann, M., and Melchior, H., "New 1x2 MMI with Free Selection of Power Splitting Ratios," in [*20th European Conference on Optical Communication*], 669–672 (1994).

[126] Ma, P., Choi, D.-Y., Yu, Y., Yang, Z., Vu, K., Nguyen, T., Mitchell, A., Luther-Davies, B., and Madden, S., "High Q factor chalcogenide ring resonators for cavity-enhanced MIR spectroscopic sensing," *Optics Express* **23**(15), 19969 (2015).

[127] Kern, P., Malbet, F., Schanen-Duport, I., and Benech, P., "Integrated optics single-mode interferometric beam combiner for near infrared astronomy," *Integrated Optics for Astronomical Interferometry* **1**, 195 (1997).

[128] Jovanovic, N., Tuthill, P. G., Norris, B., Gross, S., Stewart, P., Charles, N., Lacour, S., Ams, M., Lawrence, J. S., Lehmann, A., Niel, C., Robertson, J. G., Marshall, G. D., Ireland, M., Fuerbach, A., and Withford, M. J., "Starlight demonstration of the Dragonfly instrument: an integrated photonic pupil-remapping interferometer for high-contrast imaging," *Monthly Notices of the Royal Astronomical Society* **427**(1), 806–815 (2012).

[129] Weber, V., Barillot, M., Haguenauer, P., Kern, P. Y., Schanen-Duport, I., Labeye, P. R., Pujol, L., and Sodnik, Z., "Nulling interferometer based on an integrated optics combiner," in [*New Frontiers in Stellar Interferometry*], Traub, W. A., ed., **5491**, 842 – 850, International Society for Optics and Photonics, SPIE (2004).

[130] Abuter, R., Accardo, M., Amorim, A., Anugu, N., Ávila, G., Azouaoui, N., Benisty, M., Berger, J. P., Blind, N., Bonnet, H., Bourget, P., Brandner, W., Brast, R., Buron, A., Burtscher, L., Cassaing, F., Chapron, F., Choquet, É., Clénet, Y., Collin, C., Coudé du Foresto, V., de Wit, W., de Zeeuw, P. T., Deen, C., Delplancke-Ströbele, F., Dembet, R., Derie, F., Dexter, J., Duvert, G., Ebert, M., Eckart, A., Eisenhauer, F., Esselborn, M., Fédou, P., Finger, G., Garcia, P., Garcia Dabo, C. E., Garcia Lopez, R., Gendron, E., Genzel, R., Gillessen, S., Gonte, F., Gordo, P., Grould, M., Grözinger, U., Guieu, S., Haguenauer, P., Hans, O., Haubois, X., Haug, M., Haussmann, F., Henning, T., Hippler, S., Horrobin, M., Huber, A., Hubert, Z., Hubin, N., Hummel, C. A., Jakob, G., Janssen, A., Jochum, L., Jocou, L., Kaufer, A., Kellner, S., Kendrew, S., Kern, L., Kervella, P., Kiekebusch, M., Klein, R., Kok, Y., Kolb, J., Kulas, M., Lacour, S., Lapeyrère, V., Lazareff, B., Le Bouquin, J.-B., Lèna, P., Lenzen, R., Lévêque, S., Lippa, M., Magnard, Y., Mehrgan, L., Mellein, M., Mérand, A., Moreno-Ventas, J., Moulin, T., Müller, E., Müller, F., Neumann, U., Oberti, S., Ott, T., Pallanca, L., Panduro, J., Pasquini, L., Paumard, T., Percheron, I., Perraut, K., Perrin, G., Pflüger, A., Pfuhl, O., Phan Duc, T., Plewa, P. M., Popovic, D., Rabien, S., Ramírez, A., Ramos, J., Rau, C., Riquelme, M., Rohloff, R.-R., Rousset, G., Sanchez-Bermudez, J., Scheithauer, S., Schöller, M., Schuhler, N., Spyromilio, J., Straubmeier, C., Sturm, E., Suarez, M., Tristram, K. R. W., Ventura, N., Vincent, F., Waisberg, I., Wank, I., Weber, J., Wieprecht, E., Wiest, M., Wiezorrek, E., Wittkowski, M., Woillez, J., Wolff, B., Yazici, S., Ziegler, D., and Zins, G., "First light for GRAVITY: Phase referencing optical interferometry for the Very Large Telescope Interferometer," *Astronomy & Astrophysics* **602**(1874), A94 (2017).

[131] Coude du Foresto, V., Perrin, G. S., Ruilier, C., Mennesson, B. P., Traub, W. A., and Lacasse, M. G., "FLUOR fibered instrument at the IOTA interferometer," in [*Astronomical Interferometry*], Reasenberg, R. D., ed., **3350**, 856 (1998).

[132] Scott, N. J., Millian-Gabet, R., Lhomé, E., Ten Brummelaar, T. A., Coudé du Forestro, V., Sturmann, J., and Sturmann, L., "JOUVENCE OF FLUOR: UPGRADES OF A FIBER BEAM COMBINER AT THE CHARA ARRAY," *Journal of Astronomical Instrumentation* **02**(02), 1340005 (2013).

[133] Tango, W. J., "Dispersion in stellar interferometry," *Applied Optics* **29**(4), 516 (1990).

[134] Cvetojevic, N., Lawrence, J. S., Ellis, S. C., Bland-Hawthorn, J., Haynes, R., and Horton, a., "Characterization and on-sky demonstration of an integrated photonic spectrograph for astronomy.," *Optics express* **17**(21), 18643–18650 (2009).

[135] Bland-Hawthorn, J. and Kern, P., "Astrophotonics: a new era for astronomical instruments," *Optics Express* **17**(3), 1880 (2009).

[136] Martinache, F., "Kernel phase in Fizeau interferometry," *Astrophysical Journal* **724**(1), 464–469 (2010).

[137] Soref, R. A., Emelett, S. J., and Buchwald, W. R., "Silicon waveguided components for the long-wave infrared region," *Journal of Optics A: Pure and Applied Optics* **8**(10), 840–848 (2006).

[138] Nedeljkovic, M., Khokhar, A. Z., Hu, Y., Chen, X., Penades, J. S., Stankovic, S., Chong, H. M. H., Thomson, D. J., Gardes, F. Y., Reed, G. T., and Mashanovich, G. Z., "Silicon photonic devices and platforms for the mid-infrared," *Optical Materials Express* **3**(9), 1205 (2013).

[139] Soref, R., "Mid-infrared photonics in silicon and germanium," *Nature Photonics* **4**(8), 495–497 (2010).

[140] Sinobad, M., Ma, P., Luther-Davies, B., Allioux, D., Orobtchouk, R., Moss, D. J., Madden, S., Boutami, S., Fedeli, J.-M., Monat, C., and Grillet, C., "Dispersion engineered air-clad SiGe waveguides with low propagation loss in the mid-infrared," in [*2017 European Conference on Lasers and Electro-Optics and European Quantum Electronics Conference*], CD_14_4, Optical Society of America (2017).

[141] Sinobad, M., Monat, C., Luther-davies, B., Ma, P., Madden, S., Moss, D. J., Mitchell, A., Allioux, D., Orobtchouk, R., Boutami, S., Hartmann, J.-M., Fedeli, J.-M., and Grillet, C., "Mid-infrared octave spanning supercontinuum generation to 85 μm in silicon-germanium waveguides," *Optica* **5**(4), 360 (2018).

[142] Xia, X., Chen, Q., Tsay, C., Arnold, C. B., and Madsen, C. K., "Low-loss chalcogenide waveguides on lithium niobate for the mid-infrared," *Optics Letters* **35**(19), 3228 (2010).

[143] Krasnokutska, I., Tambasco, J.-L. J., Li, X., and Peruzzo, A., "Ultra-low loss photonic circuits in lithium niobate on insulator," *Optics Express* **26**, 897 (jan 2018).

[144] Jackel, J. L., Rice, C. E., and Veselka, J. J., "Proton exchange for highindex waveguides in LiNbO 3," *Applied Physics Letters* **41**, 607–608 (oct 1982).

[145] Li, X. P., Chen, K. X., and Hu, Z. F., "Low-loss bent channel waveguides in lithium niobate thin film by proton exchange and dry etching," *Optical Materials Express* **8**, 1322 (may 2018).

[146] Hsiao, H.-K., Winick, K. a., Monnier, J. D., and Berger, J.-P., "An infrared integrated optic astronomical beam combiner for stellar interferometry at 3-4 microm.," *Optics express* **17**(21), 18489–18500 (2009).

[147] Parker, J. M., "Fluoride Glasses," *Annual Review of Materials Science* **19**(1), 21–41 (1989).

[148] Nasu, Y., Kohtoku, M., and Hibino, Y., "Low-loss waveguides written with a femtosecond laser for flexible interconnection in a planar light-wave circuit," *Optics Letters* **30**(7), 723 (2005).

[149] Gross, S., Jovanovic, N., Sharp, A., Ireland, M., Lawrence, J., and Withford, M. J., "Low loss mid-infrared ZBLAN waveguides for future astronomical applications," *Optics Express* **23**(6), 7946 (2015).

[150] Eggleton, B. J., Luther-Davies, B., and Richardson, K., "Chalcogenide photonics," *Nature Photonics* **5**(3), 141–148 (2011).

[151] Frerichs, R., "New Optical Glasses with Good Transparency in the Infrared," *Journal of the Optical Society of America* **43**(12), 1153 (1953).

[152] Schultz-Sellack, C., "Diathermansie einer Reihe von Stoffen für Wärme sehr geringer Brechbarkeit," *annalen der physik* **139**(182), 182–187 (1870).

[153] Hilton, A., "Optical properties of chalcogenide glasses," *Journal of Non-Crystalline Solids* **2**, 28–39 (1970).

[154] Madden, G. E., Choudhury, D., MacPherson, W. N., and Thomson, R. R., "Development of low-loss mid-infrared ultrafast laser inscribed waveguides," *Optical Engineering* **56**(7), 075102 (2017).

[155] Savage, J., "Optical properties of chalcogenide glasses," *Journal of Non-Crystalline Solids* **47**(1), 101–115 (1982).

[156] Ma, P., Choi, D.-Y., Yu, Y., Gai, X., Yang, Z., Debbarma, S., Madden, S., and Luther-Davies, B., "Low-loss chalcogenide waveguides for chemical sensing in the mid-infrared.," *Optics express* **21**(24), 29927–37 (2013).

[157] Li, F., Jackson, S., Magi, E., Grillet, C., Madden, S., Moghe, Y., Read, A., Duvall, S. G., Atanackovic, P., Eggleton, B. J., and Moss, D. J., "Low propagation loss silicon-on-sapphire integrated waveguides for the mid-infrared," *Optics Express* **19**(16), 15212–20 (2011).

[158] Carletti, L., Ma, P., Yu, Y., Luther-Davies, B., Hudson, D., Monat, C., Orobtchouk, R., Madden, S., Moss, D. J., Brun, M., Ortiz, S., Labeye, P., Nicoletti, S., and Grillet, C., "Nonlinear optical response of low loss silicon germanium waveguides in the mid-infrared," *Optics Express* **23**(7), 8261–71 (2015).

[159] Brun, M., Labeye, P., Grand, G., Hartmann, J.-M., Boulila, F., Carras, M., and Nicoletti, S., "Low loss SiGe graded index waveguides for mid-IR applications," *Optics Express* **22**(1), 508 (2014).

[160] Lawrence, M., "Lithium niobate integrated optics," *Reports on Progress in Physics* **56**(3), 363–429 (1993).

[161] Burns, W. K., Klein, P. H., West, E. J., and Plew, L. E., "Ti diffusion in Ti : LiNbO 3 planar and channel optical waveguides," *Journal of Applied Physics* **50**(10), 6175–6182 (1979).

[162] Tepper, J., Labadie, L., Diener, R., Minardi, S., Pott, J.-U., Thomson, R. R., and Nolte, S., "Integrated optics prototype beam combiner for long baseline interferometry in the L and M bands," *Astronomical & Astrophysical* **602**, A66 (2017).

[163] Gretzinger, T., Gross, S., Ams, M., Arriola, A., and Withford, M. J., "Ultrafast laser inscription in chalcogenide glass: thermal versus athermal fabrication," *Opt. Mater. Express* **5**(12), 2862–2877 (2015).

[164] Han, T., *Nano-Moulding of Integrated Optical Devices*, PhD thesis, Australian National University (2011).

[165] Yu, Y., Gai, X., Wang, T., Ma, P., Wang, R., Yang, Z., Choi, D.-Y., Madden, S., and Luther-Davies, B., "Mid-infrared supercontinuum generation in chalcogenides," *Optical Materials Express* **3**(8), 1075–1086 (2013).

[166] Smit, M., Leijtens, X., Ambrosius, H., Bente, E., van der Tol, J., Smalbrugge, B., de Vries, T., Geluk, E.-J., Bolk, J., van Veldhoven, R., Augustin, L., Thijs, P., Domenico D'Agostino, Rabbani, H., Lawniczuk, K., Stopinski, S., Tahvili, S., Corradi, A., Emil Kleijn, Dzibrou, D., Felicetti, M., Bitincka, E., Moskalenko, V., Zhao, J., Rui Santos, Gilardi, G., Yao, W., Williams, K., Stabile, P., Kuindersma, P., Josselin Pello, Bhat, S., Jiao, Y., Heiss, D., Roelkens, G., Wale, M., Firth, P., Francisco Soares, Grote, N., Schell, M., Debregeas, H., Achouche, M., Gentner, J.-L., Arjen Bakker, Korthorst,

T., Gallagher, D., Dabbs, A., Melloni, A., Morichetti, F., Daniele Melati, Wonfor, A., Penty, R., Broeke, R., Musk, B., and Robbins, D., "An introduction to InP-based generic integration technology," *Semiconductor Science and Technology* **29**(8), 083001 (2014).

[167] Ottaviano, L., Minhao, P., Semenova, E., and Yvind, K., "Low-loss high-confinement waveguides and microring resonators in AlGaAs-on-insulator," *Optics Letters* **41**(17), 3996–3999 (2016).

[168] Chiles, J., Nader, N., Stanton, E. J., Herman, D., Moody, G., Zhu, J., Skehan, J. C., Guha, B., Kowligy, A., Gopinath, J. T., Srinivasan, K., Diddams, S. A., Coddington, I., Newbury, N. R., Shainline, J. M., Nam, S. W., and Mirin, R. P., "Multi-functional integrated photonics in the mid-infrared with suspended AlGaAs on silicon," (may 2019).

[169] Adachi, S., "Model dielectric constants of GaP, GaAs, GaSb, InP, InAs, and InSb," *Physical Review B* **35**, 7454–7463 (may 1987).

[170] Phelan, R., Byrne, D., O'Carroll, J., Gleeson, M., Nawrocka, M., Lennox, R., Carney, K., Herbert, C., Somers, J., and Kelly, B., "Mid-Infrared InP-Based Discrete Mode Laser Diodes," in [*Optoelectronic Devices [Working Title]*], **i**, 13, IntechOpen (jun 2019).

[171] Gilles, C., Orbe, L. J., Carpintero, G., Maisons, G., and Carras, M., "Mid-infrared wavelength multiplexer in InGaAs/InP waveguides using a Rowland circle grating," *Optics Express* **23**, 20288 (aug 2015).

[172] Guignard, M., Nazabal, V., Smektala, F., Zeghlache, H., Kudlinski, A., Quiquempois, Y., and Martinelli, G., "High second-order nonlinear susceptibility induced in chalcogenide glasses by thermal poling," *Optics Express* **14**(4), 1524 (2006).

[173] Haguenauer, P., Berger, J.-P., Rousselet-Perraut, K., Kern, P., Malbet, F., Schanen-Duport, I., and Benech, P., "Integrated optics for astronomical interferometry III Optical validation of a planar optics two-telescope beam combiner," *Applied Optics* **39**(13), 2130 (2000).

[174] MacKenzie, F., Beaumont, C., Nield, M., and Cassidy, S., "Measurement of excess loss in planar silica X junctions," *Electronics Letters* **28**(20), 1919 (1992).

[175] Ladouceur, F. and Love, J. D., "X-junctions in buried channel waveguides," *Optical and Quantum Electronics* **24**(12), 1373–1379 (1992).

[176] Soldano, L. B., Veerman, F. B., Smit, M. K., Verbeek, B. H., Dubost, A. H., and Pennings, E. C. M., "Planar Monomode Optical Couplers Based on Multimode Interference Effects," *Journal of Lightwave Technology* **10**(12), 1843–1850 (1992).

[177] Benisty, M., Berger, J.-P., Jocou, L., Labeye, P., Malbet, F., Perraut, K., and Kern, P. Y., "An integrated optics beam combiner for the second generation VLTI instruments," *Astronomy and Astrophysics* **498**(2), 601–613 (2009).

[178] Errmann, R., Minardi, S., Labadie, L., Dreisow, F., Nolte, S., and Pertsch, T., "Integrated optics interferometric four telescopes nuller," *Applied optics* **54**(24), 7449–7454 (2015).

[179] Madden, S., Jin, Z., Choi, D., Debbarma, S., Bulla, D., and Luther-Davies, B., "Low loss coupling to sub-micron thin film deposited rib and nanowire waveguides by vertical tapering," *Optics Express* **21**(3), 3582–3594 (2013).

[180] Takagi, A., Jinguji, K., and Kawachi, M., "Wavelength characteristics of (2*2) optical channel-type directional couplers with symmetric or nonsymmetric coupling structures," *Journal of Lightwave Technology* **10**(6), 735–746 (1992).

[181] Milton, A. F. and Burns, W. K., "Tapered Velocity Couplers for Integrated Optics: Design," *Applied Optics* **14**(5), 1207 (1975).

[182] Wilson, M. and Teh, G., "Tapered Optical Directional Coupler," *IEEE Transactions on Microwave Theory and Techniques* **23**(1), 85–92 (1975).

[183] Kawachi, M., Yasu, M., and Edahiro, T., "Fabrication of SiO2-TiO2 glass planar optical waveguides by flame hydrolysis deposition," *Electronics Letters* **19**(15), 583 (1983).

[184] Takagi, A., Jinguji, K., and Kawachi, M., "Design and fabrication of broad-band silica-based optical waveguide couplers with asymmetric structure," *IEEE Journal of Quantum Electronics* **28**(4), 848–855 (1992).

[185] Hsiao, H.-k., Winick, K. a., and Monnier, J. D., "Midinfrared broadband achromatic astronomical beam combiner for nulling interferometry.," *Applied optics* **49**(35), 6675–6688 (2010).

[186] Thommas, G. Personal communication (2019-02-20).

[187] Synopsys, Inc., "Rsoft cad environment product overview." `http://optics.synopsys.com/rsoft/rsoft-cad-environment.html` (2019). Accessed: 2019-04-13.

[188] Talbot, H. F., "Facts relating to optical science. No. IV," *Philosophical Magazine* **9**(56), 401–407 (1836).

[189] Maese-Novo, A., Halir, R., Romero-García, S., Pérez-Galacho, D., Zavargo-Peche, L., Ortega-Moñux, A., Molina-Fernández, I., Wangüemert-Pérez, J. G., and Cheben, P., "Wavelength independent multimode interference coupler," *Optics Express* **21**(6), 7033 (2013).

[190] Halir, R., Cheben, P., Luque-González, J. M., Sarmiento-Merenguel, J. D., Schmid, J. H., Wangüemert-Pérez, G., Xu, D.-x., Wang, S., Ortega-Moñux, A., and Molina-Fernández, Í., "Ultra-broadband nanophotonic beamsplitter using an anisotropic sub-wavelength metamaterial," *Laser & Photonics Reviews* **10**(6), 1039–1046 (2016).

[191] Lord Rayleigh F.R.S, "XXV. On copying diffraction-gratings, and on some phenomena connected therewith," *The London, Edinburgh, and Dublin Philosophical Magazine and Journal of Science* **11**(67), 196–205 (1881).

[192] Bryngdahl, O., "Image formation using self-imaging techniques," *Journal of the Optical Society of America* **63**(4), 416–419 (1973).

[193] Bachmann, M., Besse, P. A., and Melchior, H., "General self-imaging properties in N N multimode interference couplers including phase relations.," *Applied optics* **33**(18), 3905–3911 (1994).

[194] Soldano, L. B. and Pennings, E. C. M., "Optical multi-mode interference devices based on self-imaging: principles and applications," *Journal of Lightwave Technology* **13**(4), 615–627 (1995).

[195] Bachmann, M., Besse, P. A., and Melchior, H., "Overlapping-image multimode interference couplers with a reduced number of self-images for uniform and nonuniform power splitting.," *Applied Optics* **34**(30), 6898–910 (1995).

[196] Hill, M. T., Leijtens, X. J. M., Khoe, G. D., and Smit, M. K., "Optimizing Imbalance and Loss in 2 X 2 3-dB Multimode Interference Couplers via Access Waveguide Width," *Journal of Lightwave Technology* **21**(10), 2305–2313 (2003).

[197] Saleh, B. E. A. and Teich, M. C., "Fiber optics," in [*Fundamentals of photonics*], ch. 8, 272–309, John Wiley & Sons, Inc. (1991).

[198] Liu, J.-M., "Symmetric slab waveguides," in [*Photonic Devices*], ch. 2, 95–99, Cambridge University Press, Cambridge (2005).

[199] Goos, F. and Hänchen, H., "Ein neuer und fundamentaler Versuch zur Totalreflexion," *Annalen der Physik* **436**(7-8), 333–346 (1947).

[200] Kapany, N. S. and Burke, J. J., [*Optical Waveguides*], Academic Press, INC., New York (1972).

[201] Jenkins, R. M., Devereux, R. W. J., and Heaton, J. M., "Waveguide beam splitters and recombiners based on multimode propagation phenomena," *Optics Letters* **17**(14), 991–993 (1992).

[202] Besse, P. A., Bachmann, M., Melchior, H., Soldano, L. B., and Smit, M. K., "Optical Bandwidth and Fabrication Tolerances of Multimode Interference Couplers," *Journal of Lightwave Technology* **12**(6), 1004–1009 (1994).

[203] Morrissey, P., Yang, H., Sheehan, R., Corbett, B., and Peters, F., "Design and fabrication tolerance analysis of multimode interference couplers," *Optics Communications* **340**, 26–32 (2015).

[204] Kenchington Goldsmith, H.-D., Ireland, M., Ma, P., Cvetojevic, N., and Madden, S., "Improving the extinction bandwidth of MMI chalcogenide photonic chip based MIR nulling interferometers," *Optics Express* **25**(14), 16813–16824 (2017).

[205] Hewak, D., Brady, D., Curry, R., Elliott, G., Huang, C., Hughes, M., Knight, K., Mairaj, A., Petrovich, M., Simpson, R., and Sproat, C., "Chalcogenide glasses for photonics device applications," in [*Photonic Glasses and Glass-Ceramics*], 29–102, Optoelectronics Research Centre (2010).

[206] Jensen, W. B., "A Note on the Term "Chalcogen"," *Journal of Chemical Education* **74**(9), 1063 (1997).

[207] Hilton, A. R., "Nonoxide chalcogenide glasses as infrared optical materials.," *Applied optics* **5**(12), 1877–1882 (1966).

[208] Lucas, P., "Energy landscape and photoinduced structural changes in chalcogenide glasses," *Journal of Physics: Condensed Matter* **18**, 5629–5638 (2006).

[209] He, H. and Thorpe, M. F., "Elastic Properties of Glasses," *Physical Review Letters* **54**(19), 2107–2110 (1985).

[210] Thorpe, M. F., "Continuous Deformation in Random Networks," *Journal of Non-Crystalline Solids* **57**, 355–370 (1983).

[211] Wang, J., Sheng, Z., Li, L., Pang, A., Wu, A., Li, W., Wang, X., Zou, S., Qi, M., and Gan, F., "Low-loss and low-crosstalk 8 8 silicon nanowire AWG routers fabricated with CMOS technology," *Optics Express* **22**(8), 9395 (2014).

[212] Luther-Davies, B., "Chalcogenide Materials for Nonlinear Photonics in the Near and Middle Infrared," in [*Oecc / Acoft 2014*], (July), 401–403 (2014).

[213] Bulla, D. a. P., Wang, R. P., Prasad, a., Rode, a. V., Madden, S. J., and Luther-Davies, B., "On the properties and stability of thermally evaporated Ge-As-Se thin films," *Applied Physics A: Materials Science and Processing* **96**(3), 615–625 (2009).

[214] Yang, Y., Zhang, B., Yang, A., Yang, Z., and Lucas, P., "Structural Origin of Fragility in Ge As S Glasses Investigated by Calorimetry and Raman Spectroscopy," *Journal of Physical Chemestry B* **119**, 5096–5101 (2015).

[215] Wang, R., Yan, K., Yang, Z., and Luther-Davies, B., "Structural and physical properties of Ge11.5As24S64.5·xSe64.5·(1x) glasses," *Journal of Non-Crystalline Solids* **427**, 16–19 (2015).

[216] Madden, S. J., Choi, D.-Y., Bulla, D. A., Rode, A. V., Luther-Davies, B., Ta'eed, V. G., Pelusi, M. D., and Eggleton, B. J., "Long, low loss etched As_2S_3 chalcogenide waveguides for all-optical signal regeneration," *Optics Express* **15**(22), 14414 (2007).

[217] Yu, Y., Gai, X., Ma, P., Vu, K., Yang, Z., Wang, R., Choi, D.-Y., Madden, S., and Luther-Davies, B., "Experimental demonstration of linearly polarized 210 μm supercontinuum generation in a chalcogenide rib waveguide," *Optics Letters* **41**(5), 958 (2016).

[218] Hô, N., Phillips, M. C., Qiao, H., Allen, P. J., Krishnaswami, K., Riley, B. J., Myers, T. L., and Anheier, N. C., "Single-mode low-loss chalcogenide glass waveguides for the mid-infrared," *Optical Letters* **31**(12), 1860–1862 (2006).

[219] Vigreux, C., Barthélémy, E., Bastard, L., Broquin, J.-E., Barillot, M., Ménard, S., Parent, G., and Pradel, A., "Realization of single-mode telluride rib waveguides for mid-IR applications between 10 and 20 μm," *Optics Letters* **36**(15), 2922 (2011).

[220] Han, T., Madden, S., Bulla, D., and Luther-Davies, B., "Low loss Chalcogenide glass waveguides by thermal nano-imprint lithography.," *Optics express* **18**(18), 19286–19291 (2010).

[221] Lucas, P., Boussard-Pledel, C., Wilhelm, A., Danto, S., Zhang, X.-H., Houizot, P., Maurugeon, S., Conseil, C., and Bureau, B., "The Development of Advanced Optical Fibers for Long-Wave Infrared Transmission," *Fibers* **1**(3), 110–118 (2013).

[222] Cui, S., Boussard-Plédel, C., Troles, J., and Bureau, B., "Telluride glass single mode fiber for mid and far infrared filtering," *Optical Materials Express* **6**(4), 971 (2016).

[223] Vigreux, C., Escalier, R., Pradel, A., Bastard, L., Broquin, J.-E., Zhang, X., Billeton, T., Parent, G., Barillot, M., and Kirschner, V., "Telluride buried channel waveguides operating from 6 to 20μm for photonic applications," *Optical Materials* **49**, 218–223 (2015).

[224] Zhiyong, Y. Personal communication (2015-03-30).

[225] LightPath Technologies, "Find your lens." `http://www.lightpath.com/` (2019). Accessed: 2019-04-17.

[226] Shiraishi, K., Yoda, H., Ohshima, A., Ikedo, H., and Tsai, C. S., "A silicon-based spot-size converter between single-mode fibers and Si-wire waveguides using cascaded tapers," *Applied Physics Letters* **91**(14) (2007).

[227] Kasap, S. O., [*Optoelecttronics and Photonics: Principles and Practices*], Pearson Education Limited, 2 ed. (2013). An optional note.

[228] Marcuse, D., "Curvature loss formula for optical fibers," *Journal of Optical Society of America* **66**(3), 216–220 (1976).

[229] Baets, R. and Lagasse, P. E., "Loss calculation and design of arbitrarily curved integrated-optic waveguides," *Journal of the Optical Society of America* **73**(2), 177 (1983).

[230] Love, J., Henry, W., Stewart, W., Black, R., Lacroix, S., and Gonthier, F., "Tapered single-mode fibres and devices. part 1: Adiabaticity criteria," *IEE Proceedings J (Optoelectronics)* **138**(5), 343–354 (1977).

[231] Tang, Z., Shiryaev, V. S., Furniss, D., Sojka, L., Sujecki, S., Benson, T. M., Seddon, A. B., and Churbanov, M. F., "Low loss ge-as-se chalcogenide glass fiber, fabricated using extruded preform, for mid-infrared photonics," *Opt. Mater. Express* **5**, 1722–1737 (Aug 2015).

[232] Luxel Corporation, "Radak and oled furnaces." `https://luxel.com/products/thermal-evaporation-equipment/radak-and-oled-furnaces/` (2019). Accessed: 2019-08-06.

[233] RD Mathis Company, "Technical library." `https://rdmathis.com/technical-library/` (2018). Accessed: 2019-05-27.

[234] Doemling, M. F., Rueger, N. R., and Oehrlein, G. S., "Photoresist erosion studied in an inductively coupled plasma reactor," *Journal of Vacuume Science and Technology B* **16**(4), 1998–2005 (1998).

[235] Yu, Y., *Mid Infrared supercontinuum generation in chalcogenides*, PhD thesis, Australian National University (2017).

[236] Cardinal, T., Richardson, K., Shim, H., Schulte, A., Beatty, R., Le Foulgoc, K., Meneghini, C., Viens, J., and Villeneuve, A., "Non-linear optical properties of chalcogenide glasses in the system AsSSe," *Journal of Non-Crystalline Solids* **256-257**, 353–360 (1999).

[237] Prasad, A., Zha, C.-J., Wang, R.-P., Smith, A., Madden, S., and Luther-Davies, B., "Properties of Ge_xAs_ySe_1-x-y glasses for all-optical signal processing," *Optics Express* **16**(4), 2804 (2008).

[238] Kolev, V. Z., Duering, M. W., Luther-Davies, B., and Rode, A. V., "Compact high-power optical source for resonant infrared pulsed laser ablation and deposition of polymer materials," *Optics Express* **14**(25), 12302 (2006).

[239] Santec Corporation, "Tunable lasers." https://www.santec.com/en/products/instruments/tunablelaser (2000). 2019-06-29.

[240] Thorlabs, Inc., "Holographic wire grid polarizers." https://www.thorlabs.com/newgrouppage9.cfm?objectgroup_id=1118 (2019). Accessed: 2019-04-13.

[241] Newport Corporation, "Reflective microscope objectives." https://www.newport.com/f/reflective-microscope-objectives (2019). Accessed: 2019-04-13.

[242] FLIR Integrated Imaging Solutions, Inc., "Firefly mv 1394a." https://www.ptgrey.com/firefly-mv-ieee-1394b-firewire-cameras (2019). Accessed: 2019-04-13.

[243] Gentec-EO, "Um9b-bl-d0." https://www.gentec-eo.com/products/um9b-bl-d0 (2019). Accessed: 2019-05-15.

[244] Ledemi, Y., El Amraoui, M., and Messaddeq, Y., "Transmission enhancement in chalco-halide glasses for multiband applications," *Optical Materials Express* **4**(8), 1725 (2014).

[245] Payne, F. P. and Lacey, J. P. R., "A theoretical analysis of scattering loss from planar optical waveguides," *Optical and Quantum Electronics* **26**, 977–986 (1994).

[246] Fallahkhair, A. B., Li, K. S., and Murphy, T. E., "Vector Finite Difference Modesolver for Anisotropic Dielectric Waveguides," *Journal of Lightwave Technology* **26**(11), 1423–1431 (2008).

[247] R. M. Knox, P. P. T., "Integrated circuits for the millimeter through optical frequency range," in [*in Proceedings, MRI Symposium on Submillimeter Waves*], Fox, J., ed., 497516, Polytechnic Press, Brooklyn (1970).

[248] Paiuk, A. P., Stronski, A. V., Vuichyk, N. V., Gubanova, A. A., Krys'kov, T. A., and Oleksenko, P. F., "Mid-IR impurity absorption in As2S3 chalcogenide glasses doped with transition metals," *Semiconductor Physics Quantum Electronics and Optoelectronics* **15**(2), 152–155 (2012).

[249] Young, P. A., "Optical properties of vitreous arsenic trisulphide," *Journal of Physics C: Solid State Physics* **4**(1), 93–106 (1971).

[250] Kanamori, T., Terunuma, Y., Takahashi, S., and Miyashita, T., "Transmission loss characteristics of As40S60 and As38Ge5Se57 glass unclad fibers," *Journal of Non-Crystalline Solids* **69**(2-3), 231–242 (1985).

[251] Kanamori, T., Terunuma, Y., Takahashi, S., and Miyashita, T., "Chalcogenide glass fibers for mid-infrared transmission," *Journal of Lightwave Technology* **2**(5), 607–613 (1984).

[252] UPS, "Characteristic ir absorption frequencies of organic functional groups." http://www2.ups.edu/faculty/hanson/Spectroscopy/IR/IRfrequencies.html (2019). Accessed: 2019-06-09.

[253] Churbanov, M. F., Scripachev, I. V., Snopatin, G. E., Shiryaev, V. S., and Plotnichenkoa, V. G., "High-purity glasses based on arsenic chalcogenides," *Journal of Optoelectronics and Advanced Materials* **3**(2), 341–349 (2001).

[254] MicroChem, "Su-8 2000: Permanent Epoxy Negative Photoresist," (2015).

[255] Maley, N., "Critical investigation of the infrared-transmission-data analysis of hydrogenated amorphous silicon alloys," *Physical Review B* **46**(4), 2078–2085 (1992).

[256] Norris, B., Cvetojevic, N., Gross, S., Jovanovic, N., Stewart, P. N., Charles, N., Lawrence, J. S., Withford, M. J., and Tuthill, P., "High-performance 3D waveguide architecture for astronomical pupil-remapping interferometry," *Optics Express* **22**(15), 18335–53 (2014).

[257] Martin, G., Heidmann, S., Rauch, J.-Y., Jocou, L., and Courjal, N., "Electro-optic fringe locking and photometric tuning using a two-stage MachZehnder lithium niobate waveguide for high-contrast mid-infrared interferometry," *Optical Engineering* **53**(3), 034101 (2014).

[258] Gleason, B., Richardson, K., Sisken, L., and Smith, C., "Refractive Index and Thermo-Optic Coefficients of Ge-As-Se Chalcogenide Glasses," *International Journal of Applied Glass Science* **7**(3), 374–383 (2016).

[259] Synopsys, Inc., "Multi-physics utility product overview." `https://www.synopsys.com/optical-solutions/rsoft/multiphysics-utility.html` (2019). 2019-05-06.

[260] Microchemicals GmbH, "Az®nlof 2000 series." `https://www.microchemicals.com/products/photoresists/az_nlof_2070.html` (2019). Accessed: 2019-05-06.

[261] AJA International, Inc., "Atc flagship series sputtering systems." `http://www.ajaint.com/atc-series-sputtering-systems.html` (2019). Accessed: 2019-06-25.

[262] Lozanova, V., Lalova, A., Soserov, L., and Todorov, R., "Optical and electrical properties of very thin chromium films for optoelectronic devices," *Journal of Physics: Conference Series* **514**(1), 012003 (2014).

[263] Besse, P. A., Gini, E., Bachmann, M., and Melchior, H., "New 2 x 2 and 1x3 ultimode Interfere with Free Selection of Power Splitting Ratios," *Journal of Lightwave Technology* **14**(10), 2286–2293 (1996).